The Drying Shrinkage in Three-Dimensional Printing and its Dependence on the Properties of the Powder and the Binder

by

Jain Charnnarong

B.Eng. Mechanical Engineering
Chulalongkorn University, 1988

M.S.M.E., Mechanical Engineering
Massachusetts Institute of Technology, 1991

Submitted to the Department of Mechanical Engineering in Partial Fulfillment of the Requirements for the Degree of

DOCTORAL PHILOSOPHY

AT THE

MASSACHUSETTS INSTITUTE OF TECHNOLOGY

June 1996

Signature of Author:_____
Department of Mechanical Engineering
May 31, 1996

Certified by:_____
Emanuel M. Sachs
Associate Professor of Mechanical Engineering
Laboratory for Manufacuring and Productivity
Thesis Supervisor

Accepted by:_____
Ain A. Sonin
Professor of Mechanical Engineering
Chairman, Committee for Graduate Students

The Drying Shrinkage in Three-Dimensional Printing and its Dependence on the Properties of the Powder and the Binder

by
Jain Charnnarong

Submitted to the Department of Mechanical Engineering on June 7, 1996
in Partial Fulfillment of the Requirements for the Degree of
Doctoral Philosophy in Mechanical Engineering

ABSTRACT

Although Three-Dimensional Printing appears to have only a slight amount of shrinkage, it sometimes leads to issues such as distortion and delamination where layers crack or disintegrate upon drying and sintering of the binder. It is imperative to reduce the amount of shrinkage to enhance dimensional control and part integrity. Current Three-Dimensional Printing of ceramics yields approximately 0.5 percent linear shrinkage after heat treatment to 900°C. Half of the shrinkage occurs during binder drying and the rest takes place during sintering at elevated temperature. This thesis work explored drying shrinkage and subsequently employed the knowledge of drying shrinkage to identify the shrinkage interaction between the powder and the binder.

Drying shrinkage takes place during saturated drying and begins when the liquid-vapor interface reaches the pore entrances. Wetting curves the liquid-vapor interface and forces the liquid phase under tension. The network contracts under the tensile stress forcing the liquid to flow from the interior to the liquid-vapor interface at the exterior. The deformation continues until the network strength is sufficiently to withstand the liquid tension. There are a few strategies to minimize drying shrinkage, but an immediate and appropriate solution for Three-Dimensional Printing is to minimize the amount of liquid captured at the point of gellation which determines shrinkage potential of the body. It is achievable by gelling the silica binder by drying.

As binder deforms, it pulls along attached powder particles which are constrained to their neighbors. The particle movement induces compressive stress in the powder and also places the binder under tensile stress. At all times, the forces developed from the binder tension and the powder compression must be equal to remain under static equilibrium. It was found that powder shrinkage strain varies with the level of isostatic stress, initial packing density, and the morphology of particles. Equiaxed powders allow for tighter particulate formation than those of high aspect ratio due to less intergranular friction and geometrical advantage. As a consequence, equiaxed particles provide less shrinkage.

A new powder-binder system consists of spherical alumina powder with high solid loading colloidal silica gelled by drying was proposed. The new materials decrease the shrinkage by almost an order of magnitude. Shrinkage could also be reduced with lower printing saturation level because of tri-axial stress effect at the binder necks and the reduction of shrinkage force with lower binder content in the powder bed. Improper printing saturation level and binder distribution may result in a reduction of shrinkage deformation at a cost of low part strength.

Thesis Committee: Prof. Emanuel M. Sachs, Chairman
Prof. Michael J. Cima
Prof. Mary C. Boyce

Acknowledgments

Switching from a research on papers to a hand-on one with practical applications is an excellent experience that I have learned. The lessons acquired from Three-Dimensional Printing not only broaden my technical knowledge, but also teach me the wisdom of life. I am more matured than when I first stepped to MIT several years ago.

I would like to thank Ely Sachs for giving me the opportunity and the support throughout the program. To me, Ely is more than a thesis advisor. His bicycle example will be ringing in my ears for a long time. Special thanks to my thesis committee members, Prof. Michael Cima and Prof. Mary Boyce, for their marvelous advice and guidance.

I thought I knew some machining, until I met Fred Cote. From that day, Fred has straightened me up as well as Kelvin Baron and Jerry Wentworth. I never though that I could do electron microscope either until Lenny Rigione gave me a good tutorial. John Centorino also gave me a very thorough tutorial when I melt glass into the insulator in one of his furnaces. Thank you so much all of you!

Special thanks to the dedicated Three-Dimensional Printing staffs, Dave Brancazio and Michael Rynerson who have given so much of their time to keep the machine running days and nights. In the past four years, I have interacted and learned so much from all the students in the lab. John Lee made several wonderful file processing algorithms for the shrinkage bars. Alain Curodeau for his electronic wizard. Steve Micheals for his knowledge on powder packing. There are numerous others which I could not just list their names on a single sheet of paper. I would like you to know that I am so grateful.

Getting through a doctoral program requires quite an effort and determination. There are always hard times during the course of a doctoral thesis. I would like to thank Lucille Blake for her moral support for the past several years, Satbir Khanuja for his friendship and understanding. Jim and Jennifer Serdy are more than friends to me. I really enjoy your warm support and the way you appreciate and interpret the philosophy of life and society.

The lasting friendship of ATSIST add up to the rich experiences I have had from living in the States. I strongly believe that we, as a team, will be able to build our beloved country in the near future. Special thank to my best friend, Sarote Phornprapha, whose remarkable support and care always remind me of a true friendship.

There is no way that I can express my deeply appreciation to Uncle Suchin Laman-Udom for his support. Your sincere help, guidance, and care for several past few years are truly inestimable. You really taught me to be a better and matured person.

I am wholeheartedly gratitude to my parents, Harn and Prayoonsri, and both of my sisters, Sirima and Nopporn, for their sincere, unconditional, and everlasting support. You may never know that it was your love and care that propelled me through the hardship. And it was your support that brought me to this achievement. I love you all !!

Lastly, I would like to praise a sincere thank to my fiancé, Nijasri Suwanwela, who always stands on my side sharing the good and the difficult moments. You may never realize that I will not be able to make it this far without your care and companionship.

To

His Majesty King Bhumibhol Adulyadej
and
My Parents, Harn and Prayoonsri

May Dharmma and Peace Be with You, Always

Content

Chapter 1. Introduction

Chapter 2. Powder in Three-Dimensional Printing of Ceramics

Chapter 3. Binders in Three-Dimensional Printing of Ceramics

Chapter 4. Mechanics of Drying Gels

Chapter 5. Drying of Gels

Chapter 6. Stress-Strain Relationship of Drying Gels

Chapter 7. Powder Deformation Response to Shrinkage Stress

Chapter 8. Powder-Binder Shrinkage Interaction

Chapter 9. Conclusion

Appendices

Executive Summary

• GENERAL VIEW OF SHRINKAGE ISSUE IN THREE-DIMENSIONAL PRINTING OF CERAMICS

The amount of shrinkage in Three-Dimensional Printing of ceramics is generally much less than other rapid prototyping processes. Although the shrinkage strain is in a fraction of a percent, it does not only lead to dimensional control but also some serious issues such as cracking, distortion, and delamination which affect the integrity of printed parts.

Current shrinkage of Three-Dimensional Printing of ceramics using acid gelled silica binder (Binder B) and a lamella alumina powder (Norton 7920) takes place in drying and in heat treatment process. The final shrinkage strain after heat treatment to 900°C is approximately 0.4 percent where half of the shrinkage occurs during drying and the other half appears during the heat treatment.

While the shrinkage during sintering of binders is well documented, drying shrinkage is not very well understood. Therefore, this research hopes to explore the fundamental physics of drying of deformable bodies and to quantify the coalescent characteristics and interaction between the powder and the binder. These findings will not only benefit Three-Dimensional Printing of ceramics, but could also generally be applied to various materials using Three-Dimensional Printing fabrication.

• BINDER

Shrinkage was found to be originated at the binders as they dry and undergo heat treatment process. Therefore, it is very important to investigate the underlying physics of shrinkage of the binders.

Binders join powder and provide strength for printed parts in green and after heat treatment. Colloidal silica was selected as a primary binder to provide equivalent

mechanical properties and degree of leachability with current investment casting. Current binder (Binder B) is a mixture of amorphous silica colloid (Nyacol 9950) with several organic stabilizers including a coagulation surfactant. Binder B was made to gels rapidly when its pH is lower below 7.5. The organic stabilizers are designed to burn out in the early stage of the heat treatment process.

During gellation, sol particles form into a giant network known as gel which encloses solvent liquid between its interconnected pores. As the gel dries, the liquid-vapor interface reaches the pore entrances. Due to the physics of wetting, the liquid-vapor interface is curved such that the radius of curvature is on the vapor side. This places the liquid under tensile stress. The liquid tension squeezes the network and causes the solid phase to be under compression. If the network is deformable, it will contract due to the compressive stress and the liquid will flow out from the interior to the exterior. This marks the beginning of drying shrinkage.

The network contraction continues as the network builds up its strength. When the network strength is sufficient to resist the compressive stress induced by the liquid tension, the contraction ceases marking the end drying shrinkage. At this point, the liquid-vapor interface reaches its smallest radius and the network is at its maximum compression. As drying continues, the liquid-vapor interface moves into the network interior after which drying is governed by a diffusion process. Since drying shrinkage occurs during saturation drying, there are three strategies to minimize the shrinkage: 1) minimize the amount of liquid enclosed at the point of gel 2) maximize the network strength 3) minimize the magnitude of liquid tension.

Minimization of drying shrinkage with lower pore liquid at the point of gellation was put to test. A drop of binder is detained between a set of parallel flat plates made out of dense alumina. One side of the plate is grounded to the frame while the other is mounted on an elastic leaf spring which presents the shrinkage resistance of the powder. As the binder consolidates, it pulls on the movable plate and exerts tension force to the spring. The movement can be monitored by an optic sensor system. Stress is calculated from the ratio of the tension force in the spring and the cross-section of the *initial* neck area of the binder. It is very important to point out that this is not a true stress on the binder's neck due to reduction in the cross-section area, but more as an engineering stress. Strain is

calculated from the ratio of the boundary movement to initial binder height. Since the boundary is elastic, the stress varies linearly with the strain according the stiffness of the spring. But, more importantly, are the maximum shrinkage values corresponding to various spring stiffness. These maximum shrinkage values identify the shrinkage locus of the binder as a function of resistant stress of the powder which is shown in Figure 1.

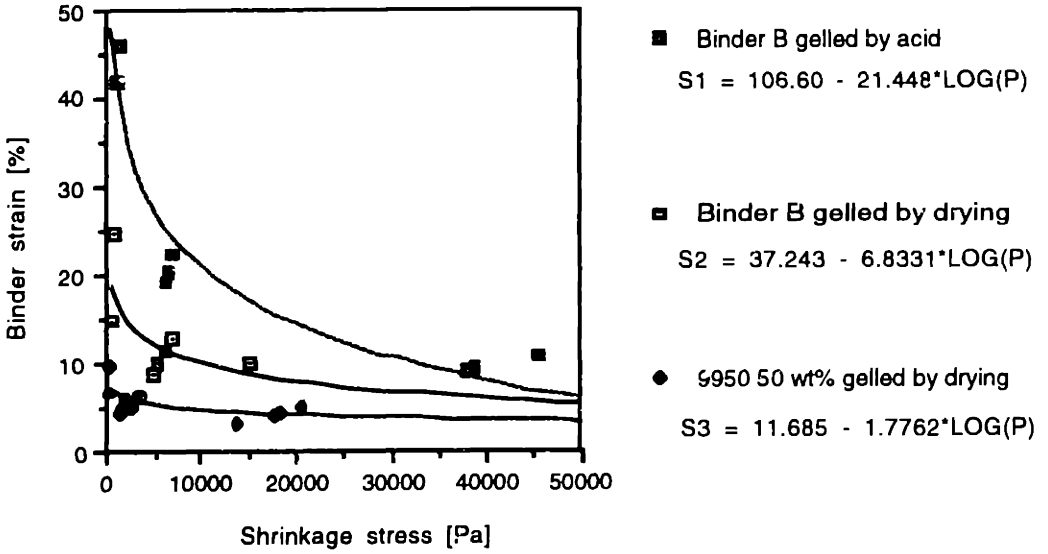

Figure 1. Shrinkage Strain Loci

Acid gelled Binder B rapidly coagulates, thus, containing a large amount of liquid at the point of gel. The liquid volume defines maximum possible deformation known as shrinkage strain potential. There will be less shrinkage with low liquid content at the gel point. Nyacol 9950 gelled by drying was proposed as a solution. It allows a large fraction of water to evaporate before gelation takes places. Compared to acid gelled Binder B, Nyacol 9950 reduces drying shrinkage by a factor of three. On the other hand, reducing shrinkage by maximizing the network strength was proven feasible by increasing the degree of 'dissolution and deposition'. But, it was not fully explored due to complex chemistry involvement.

• POWDER

The thesis work includes the study of powder and its deformation under stress because it has substantial impact on shrinkage resistance driven by the binder. In addition,

the nature of particle formation in the powder bed has a significant role in controlling the ratio of shrinkage strain between the binder and the powder.

Alumina was selected as the powder in Three-Dimensional Printing for its refractoriness and its surface compatibility with special metals in directional and single crystal castings. Current process utilizes electronics grade lamella alumina powder with an average size of 28 μm based on cost, availability, and surface smoothness requirement. This research work incorporates a spherical alumina powder (CB-A30S) of equivalent particle size into the test to compare the morphological effect on the shrinkage deformation. Spherical alumina is known for low intergranular friction which allows for higher apparent packing fraction and flowability.

To achieve low shrinkage, powder must be packed at maximum bulk densities. Current spreading technique reviewed that the lamella powder (Norton 7920) exhibited strong packing degradation as a function of time. It was found that the packing fraction was very sensitive to intergranular cohesion caused by absorbed moisture. Moisture has been collected into the powder during the recycle process from various points. With only a small amount, moisture could lower the packing fraction as much as ten percent. Misting was the primary cause of packing degradation while seeping moisture from the previous layer was the secondary. In terms of morphology, particles with low aspect ratio (spherical or equi-ax) had far superior packability than that of high aspect ratio (lamella or plate like) due to less intergranular friction.

An intensive test was conducted on Norton 7920 lamella powder and CB-A30S spherical powder to test for their deformation characteristics and morphological effect under isostatic stress (Chapter 7). It was found that shrinkage of powder in Three-Dimensional Printing is governed by particle rearrange.nent and restacking at very low stress. The amount of powder strain was a strong function of initial packing fraction and the aspect ratio. Powder with lower initial packing fraction deformed at a higher strain than that with higher packing fraction for the same isostatic pressure increment, Figure 2. Powder with low aspect ratio naturally packed to higher densities and deforms at a smaller magnitude than that of high aspect ratio.

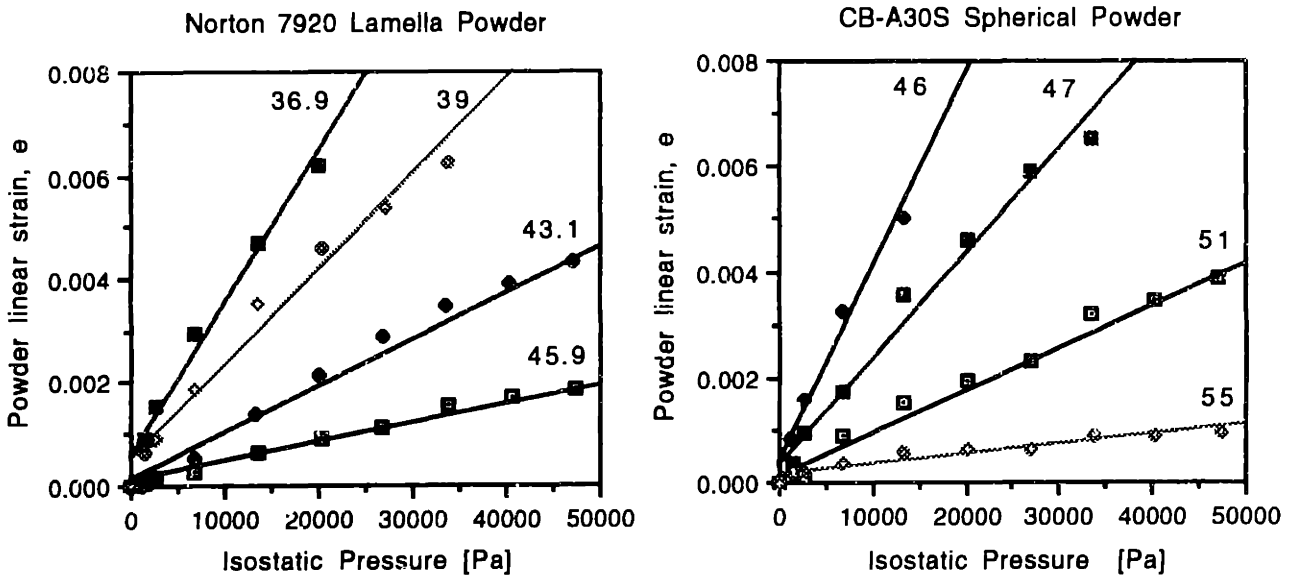

Figure 2. Yield Response to Isostatic Stress of (a) Norton 7920 (b) CB-A30S

• POWDER-BINDER SHRINKAGE INTERACTION

Finally, the focus on powder-binder shrinkage interaction identifies the linkage between powder and binder deformation which determines the total shrinkage of Three-Dimensional Printing parts when the binder is printed on the powder.

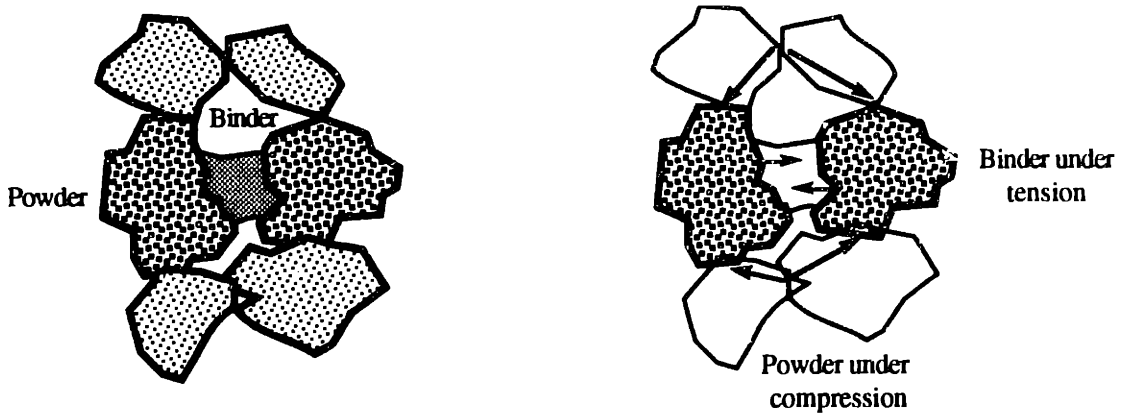

Figure 3. Binder Shrinkage and Powder Resistant Stress
(a) Powder and Binder in Assembly (b) Force Balance Between Powder and Binder

Binder consolidates during drying and heat treatment and pulls attached particles along with its shrinkage stress. The particles are, however, mechanically constrained with

their neighbors, thus their movement induced compressive stress in the powder known as resistant stress. At all time, the *forces* developed from both shrinkage and resistance stress must be equal such that the powder and the binder always remain under static equilibrium, Figure 3. The ratio of binder strain to powder (or composite) strain is governed by the magnitude of mean particle separation which is the average free distance from one particle to others in the first-layer neighbor. A particulate system with less mean particle separation should provide less shrinkage deformation.

An experiment was conducted by depositing binders with known shrinkage behaviors to saturate the powder which was packed at various densities. The shrinkage strain were plotted as a function of initial packing densities which appear as the slope on the stress-strain map of Norton 7920 and CB-A30S powders. Then the binder shrinkage strain from Figure 1 was adjusted and rescaled to fit with the measurement data of each powder, Figure 2. The scaling factor can further be calculated to identify the mean particle separation of associated powder, Figure 4.

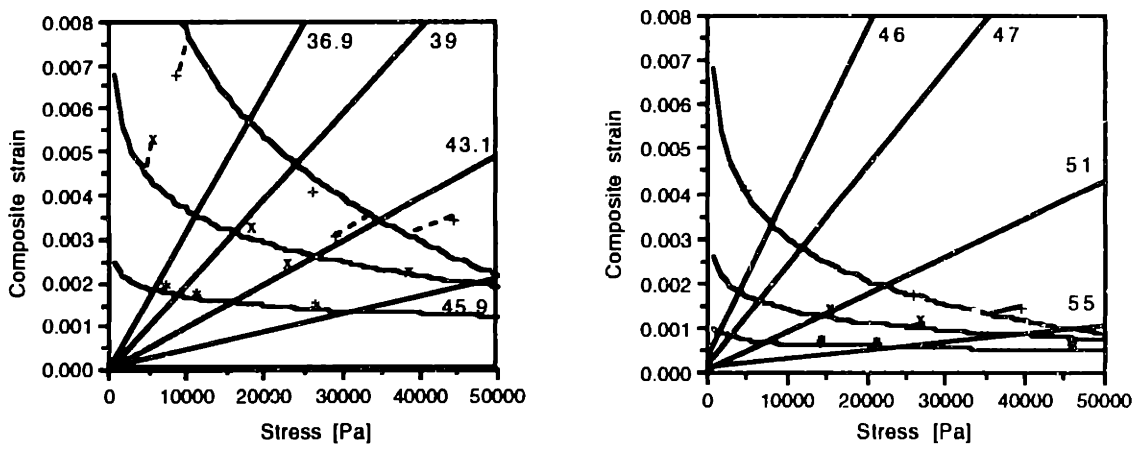

Figure 4. Measured Shrinkage Strain as a Function of Initial Packing Density of (a) Norton 7920 and (b) CB-A30S. The Plot is Fitted with Adjusted Binder Shrinkage Loci (Figure 1) to Identify the Strain Ratio Between the Powder and the Binder

\+ Binder B acid gelled x Binder gelled by drying * Nyacol 9950 @ 50 wt % gelled by drying

It was found that the mean particle separation of Norton 7920 and CB-A30S were 0.0769 and 0.0290 of the particle radius, respectively (detail in Chapter 8). The numbers were reconfirmed with the heat treatment shrinkage as well. Since CB-A30S spherical powder naturally packs to a tighter formation than Norton 7920, its shrinkage level is approximately half of the lamella powder. And with the extremely low shrinkage strain of

Nyacol 9950 at 50 weight percent gelled by drying, this powder-binder system was proposed as a new material system for the Three-Dimensional Printing of ceramic process. At a printing saturation level of 65 percent, the overall heat treatment and drying shrinkage strain of the system was found to be less than 0.05 percent - an improvement of more than 8 fold over the current standard material system of acid gelled Binder B on Norton 7920 powder.

Nomenclature

$\alpha.$	Shrinkage strain potential
A	Cross section area
A_b	Cross section area of the binder
AL	Cross section area of liquid phase
As	Cross section area of solid phase
β	$\beta = \frac{\mu}{DK_G}$
C_D	Coefficient of drag
D	Specific permeability of a porous medium
D_p	Diameter of a tube
D_{sp}	Diameter of a sphere
δ	Binder Strain
ε	Porosity or pore fraction = $\frac{\text{Pore volume in the powder bed}}{\text{Total volume of the powder bed}}$
$\varepsilon(t)$	Pore fraction of drying body at time t
ε_i	Strain in i-direction
$\varepsilon_{\text{powder}}$	Linear powder strain
ε_v	Volumetric strain
$\dot{\varepsilon}_f$	Free strain rate
$\dot{\varepsilon}_i$	Strain rate in i-direction
$\dot{\varepsilon}_v$	Volumetric strain rate
$\dot{\varepsilon}_s$	Syneresis strain rate
$\langle \dot{\varepsilon}_x \rangle$	Average strain rate across the thickness in x-direction
E_p	Young modulus of a porous material
f	Fanning's friction factor
$f(\varepsilon)$	A function of porosity volume fraction
f_s	Factor to account for non-circular of the path in Channel Theory
f_t	Factor to account for non-linearity of the path in Channel Theory
F	Uniaxial viscosity

F_N Normal force component

F_T Tangential force component

F_x External force acting in x-direction

F_{xL} Resultant force from liquid phase in the network in x-direction

F_{xS} Resultant force from solid phase in the network in x-direction

γ_{LV} Liquid-vapor specific energy

g Gravitation acceleration (9.81 m/s^2)

$g(r)$ Radial distribution function

G_p Shear modulus

h Capillary height

H_r Hydraulic radius $= \dfrac{\text{cross section area of a channel}}{\text{Wetted periphery}}$

$i(r,\theta)$ Toggle variable representing particles or pores where

$i(r,\theta)$ = 0 over the area represented by the pores

= 1 over the area represented by the particles

J Fluid flux = $\dfrac{\text{Volume flow rate of a fluid}}{\text{Area that the fluid pass through}}$

k Equivalent stiffness of powder under isostatically compression

K_G Bulk viscosity

K_p Bulk modulus of the porous body

l_o The initial binder height

L Length of a tube

L_e Equivalent length of tube

m_a Mass of air phase

m_L Mass of liquid phase

m_S Mass of solid phase

μ Viscosity

ν Poisson ratio

ν_{sp} Specific volume

N Poisson ratio for viscous porous network

P Hydrostatic pressure in fluid. P is positive when the fluid is under tension and vice versa.

P_E	Liquid tension at the pore entrance at associated drying rate $\dot{V}_E$
P_R	Maximum liquid tension at the pore entrance
R_{mi}	Fluid drag experienced by ith particle
P_{iso}	Isostatic pressure
$\langle P \rangle$	Average liquid pressure along the film thickness, $\langle P \rangle = \frac{1}{L}\int_0^L P dz$
Δp_d	Pressure drop
ϕ	Packing volume fraction = $1-\varepsilon$ = $\frac{\text{Powder volume in the powder bed}}{\text{Total volume of the powder bed}}$
$\dot{Q}$	Volume flow rate
ρ	Density of a fluid
ρ_a	Density of air phase
ρ_L	Density of liquid phase
ρ_{par}	Particle density
ρ_{skel}	Skeleton density
ρ_{solid}	Solid density
r	Radius at the pore entrance
R_{pore}	Pore radius
R	Meniscus radius of curvature
Re	Reynolds number
R_{mi}	Fluid drag experienced by ith particle
θ	Contact angle
S	Saturation
S_B	Specific area based of packed powder bed volume
S_v	Specific area based of particle volume
Sh_v	Volumetric shrinkage
$Sh_{spec.v}$	Specific volumetric shrinkage (per unit mass)
σ	Total normal stress on the plane of soil mass
σ_b	Binder shrinkage stress
σ_x	Bulk stress
σ_f	Normal stress on the powder

$\tilde{\sigma}_{soil}$	Effective normal stress of soil
$\tilde{\sigma}$	Effective normal stress of gel
$\tilde{\sigma}_x$	Stress of the solid phase in a network in x-direction
$\tilde{\sigma}_y$	Stress of the solid phase in a network in y-direction
$\tilde{\sigma}_z$	Stress of the solid phase in a network in z-direction
τ_f	shear strength of powder
T_s	Surface tension
u	Flow velocity
u_e	Equivalent flow velocity
V	Volume of a network
V_a	Volume of air
V_L	Volume of liquid phase
V_p	Volume of pore
V_S	Volume of solid phase
$\dot{V}_E$	Volumetric drying rate
w	Moisture content is mass of liquid to mass of solid in powder

List of Tables and Figures

Chapter 1. Introduction

Chapter 2. Powder for Three-Dimensional Printing of Ceramics

Chapter 3. Binders in Three-Dimensional Printing of Ceramics

Chapter 4. Mechanics of Drying Gels

Chapter 5. Drying of Gels

Chapter 6. Stress-Strain Relationship of Drying Gels

Chapter 7. Powder Deformation Response to Shrinkage Stress

Chapter 8. Powder-Binder Shrinkage Interaction

Chapter 1.

Introduction

1.0 THESIS OBJECTIVE

The objective of this thesis is to understand the causes and the physics of shrinkage during drying in The Three-Dimensional Printing, and to identify key process parameters concerning shrinkage reduction. The impetus for this thesis work is to enhance the dimensional tolerances of the Three-Dimensional Printing ceramic process.

1.1 INVESTMENT CASTING

1.1.1 Process Description

The investment casting process, also known as lost wax process, is probably the most commonly used casting process for producing, high precision, high surface quality castings. Archaeological evidence so far points to the first use of investment in Thailand around 4500 BC [1]. In the US, investment casting was extensively developed for aircraft turbo-supercharger parts by General Electric in the 1940's. By the end of that decade, investment casting was also used extensively by the aero-engine industry, especially for heat resisting alloy components in turbines [2].

The starting point for investment casting is the production of an expendable (usually wax) pattern. This pattern is often made from a precision die by injection process. Complex features might well be obtained with multi-part dies or the use of complex ceramic cores. The wax patterns are assembled with a gating and feeding system and cleaned prior to their first coating. The primary dip coat contains fine refractory powder mixed with a binder.

The assembly is dipped and allowed to drain off excess slurry over the tank while being rotated. The wet assembly is immediately stuccoed with relative coarser ceramic particles either by sprinkling the stucco particles from above or by being submerged into a

fluidized bed. The fine ceramic layer forms the inner surface of the mold and reproduces every detail of the pattern. The stucco particles retard draining and improve strength and bond. Following the coating, the assembly will be allowed to gel by temperature and humidity controlled air. Gelation can be done by drying or with the used of chemicals. Successive layers are made with coarser ceramic powder and stucco. This speeds up the thickness built rate and also reinforces the shell.

After the thickness reaches 0.25 inches or more, the assembly is ready for wax removal. The assembly is inverted and heated in an autoclave with steam and molten wax is drained out from the mold by gravity. After the wax is removed, the ceramic shell is fired to approximately 1000°C to sinter the binder and the refractory. Once the assembly is ready, it is poured with molten metal. After it cools, the shell is knocked out leaving the casting with runners. Castings are cut from the runners and the ceramic cores are leached out by a hot caustic solution such as sodium or potassium hydroxide in an autoclave. The castings require final machining/finishing and inspection before they are complete.

Required part

Step 1: Ceramic core making

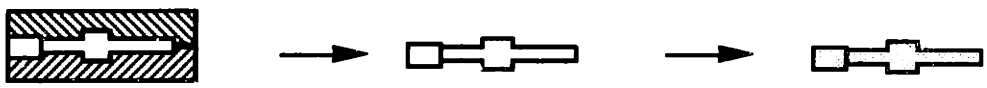

Core tooling | Injected core | Sintered core

Step 2: Making wax pattern assembly with inserted cores, runners, and gate

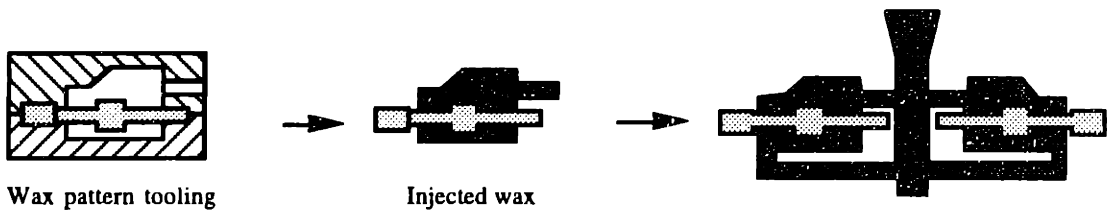

Wax pattern tooling with inserted core | Injected wax pattern | Assembly with gate and runners

Step 3: Slurry dipping and stuccoing

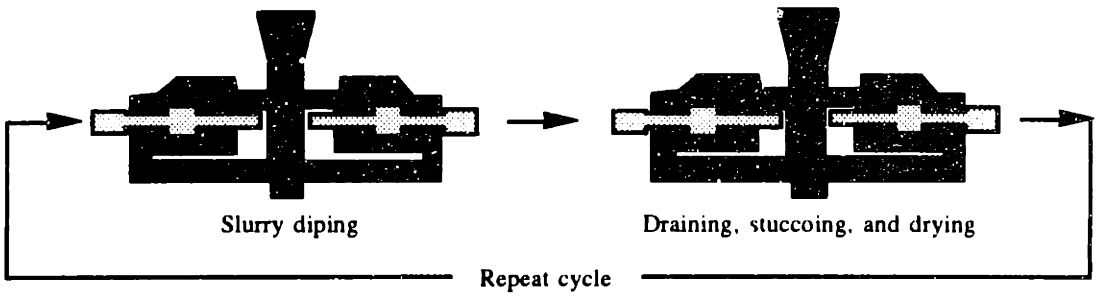

Step 4: Dewaxing, shell firing, and pouring

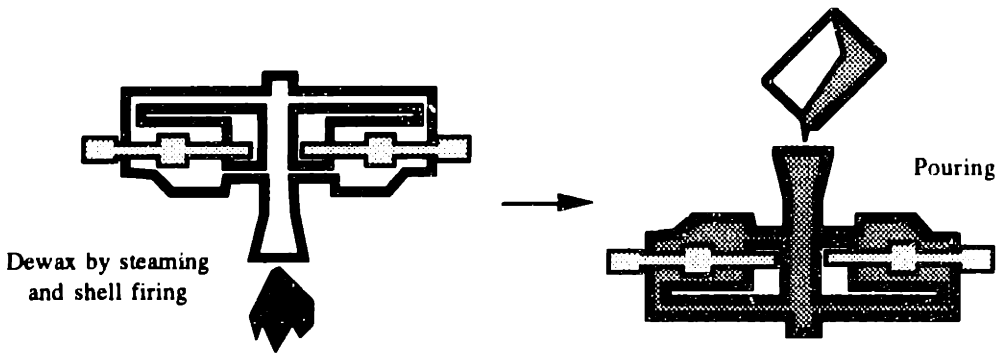

Step 5: Knocking out, cutting from gate and runners, and core removal

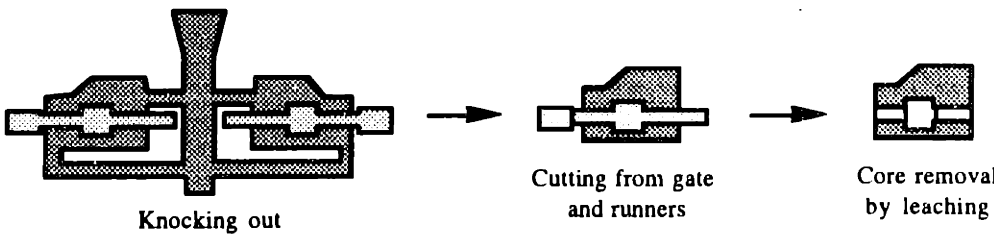

Step 6: Final machining and finished product

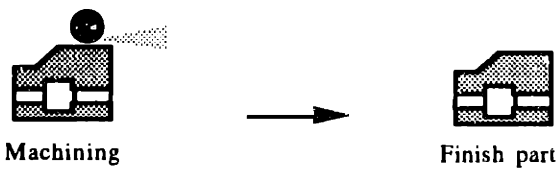

Figure 1.1 Investment Casting Process from Required Part to Finished Product

There are several tedious steps involved in investment casting. Figure 1.1 shows complete investment casting process in schematic.

There are three main groups of materials in investment casting.

1) Waxes

Expendable patterns are made of waxes generally with precision die injection process. More details of waxes in investment casting is in Appendix A.

2) Refractories

Powder refractories reproduce the shape and surface quality of the wax pattern and hold up excess binder from dripping. Details of refractories are discussed in Chapter 2.

3) Binders

Binders serve to bond stucco materials which reproduce the surface and geometry of the wax patterns. Binders sinter during heat treatment and strengthen the shells. Binder is discussed in detail in Chapter 3.

1.2 THREE-DIMENSIONAL PRINTING PROCESS

1.2.1 Process Description

Two needs which are important to industrial productivity and competitiveness are 1) the reduced lead time to market of new products, and 2) the flexible manufacture of products in small quantity. A major contributor to the time to market is the time required to develop tooling. The long lead times are due to the fact that tooling is normally one of a kind and because tools of extreme complexity require a great deal of human. Long lead time for tooling development also means high manufacturing cost which directly determines the minimum economic batch size. These issues of tooling production in conventional manufacturing processes truly limit the development of complex geometry products in small batch size.

An answer to this manufacturing impedance is a rapid and flexible manufacturing process which can produce complex three-dimensional parts directly from a computer model. The process, called Three-Dimensional Printing (3DP®), was developed at MIT to produce both functional parts and tooling required for prototypes and small batch production [3].

Three-Dimensional Printing creates parts in a layered printing fashion. The cross section information for each layer is obtained by a slicing algorithm applied to the computer model of the part. The information is fed to an 'ink-jet' printhead which selectively deposits binder material/s onto a thin layer of powered material to join them. The piston is then lowered and a new layer of powder is spread out, packed, and joined with the binder. This layering process is repeated until the part is completely printed, from bottom to top. Following a heat treatment to strengthen the binder, the unbounded powder is removed, leaving the fabricated part. The process sequence is depicted in Figure 1.2.

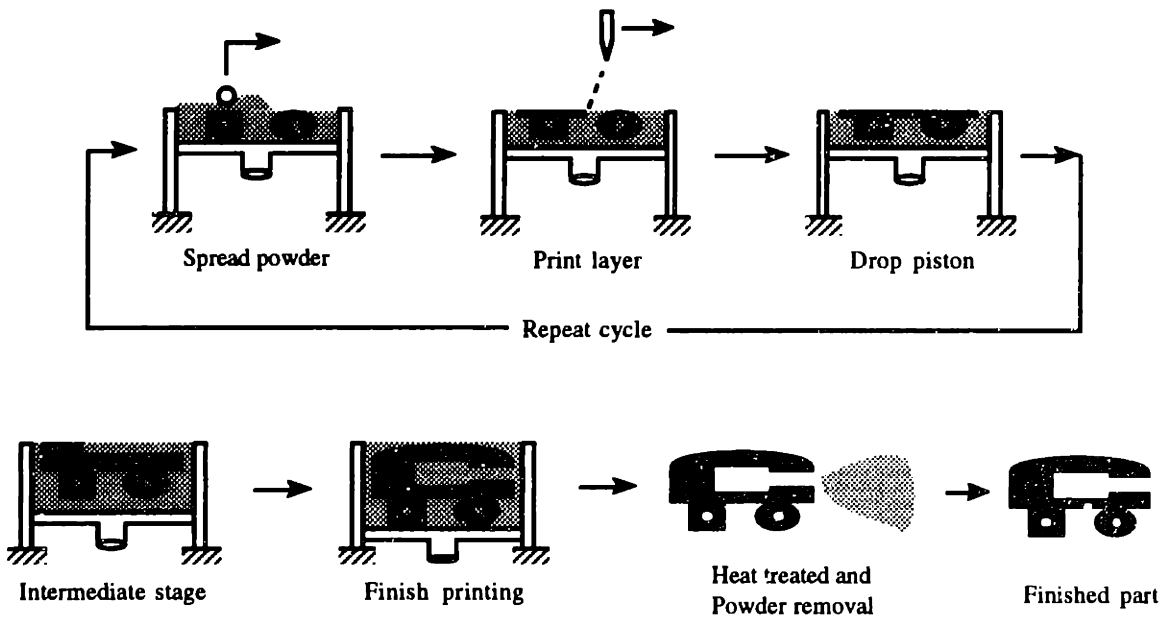

Figure 1.2 Sequences of Operation in Three-Dimensional Printing Process

Three-Dimensional Printing can fabricate parts in a wide variety of materials, including ceramics, metals, metal ceramic composites, and polymers. The printhead is made of several separated jets which could deposit multi binder materials at the same time.

1.2.2 Three-Dimensional Printing of Ceramics

Three-Dimensional Printing can be applied to an ever increasing variety of materials. But, in this thesis, Three-Dimensional Printing is generally defined for Three-Dimensional Printing fabrication of ceramic powder with binder materials. Still, there are several choices of applicable ceramics such as alumina, zircon, zirconia, silica, and silicon carbide. These ceramic materials are identical to those currently deployed in investment casting. Alumina powder has been used with colloidal silica binder in Three-Dimensional Printing of Ceramics since the beginning. Both materials have set benchmarks and standards for the process for several years. This thesis work will discuss, in detail, both of these materials in Chapter 2 and 3, as well as subsequent chapters.

The initial investigation of Three-Dimensional Printing of ceramic process has produced parts with good dimensional control but with low part strength. Together with the process' extreme flexibility in fabrication of complex-three dimensional objects, Three-Dimensional Printing has found a niche in the direct fabrication of ceramic cores and shells for metal casting.

In current practice, complex and high precision castings are made by investment casting which has long lead time and is not economically suitable for small batch production. Three-Dimensional Printing could offer its process capability to investment casting in this area of special demand. Three-Dimensional Printing can be applied to metal molding with various benefits. First, there is no requirement for wax patterns and the ceramic shells can be made to the final shape. Second, cores are directly printed with the shells in the same process. This offers great time and cost saving.

1.2.3 Printhead and Binder Technologies

• PRINTHEAD TECHNOLOGY

There are two categories of current ink-jet technology: Drop-on-Demand (DOD) and Continuous-Jet (CJ). A DOD printhead generates a single drop of ink only when it

receives a control signal from the electronic system. But a CJ printhead generate a stream of droplets continuously from a pressurized nozzle [4].

Drop-on-demand systems are classified into two types, piezo-driven and evaporative-bubble driven. In piezo-driven system, a small piezo crystal generates a pressure wave in the ink. In evaporative-bubble system, a small resistive element is energized causing nearby ink to evaporate and form a bubble. In both cases, a droplet is generated by a pressure wave pulse (and probably their reflection and harmonics in the ink chamber). DOD systems are depicted in Figure 1.3.

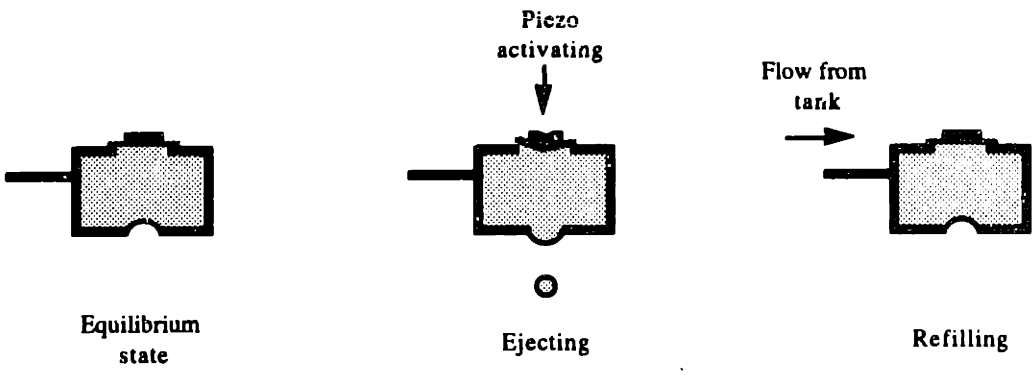

Piezo-Driven Drop-on-Demand System

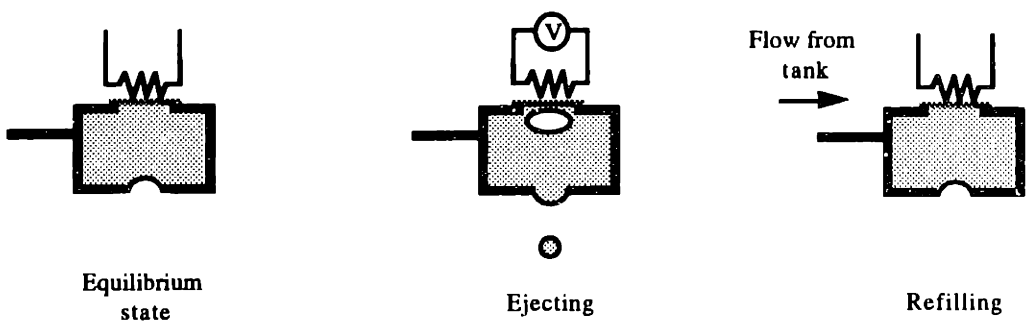

Evaporative-Bubble Drop-on-Demand System

Figure 1.3 Piezo-Driven and Evaporative-Bubble Drop-on-Demand Ink-Jet Systems

Continuous-jet systems deliver a cylindrical stream of liquid from a small nozzle with pressure. The reduction of surface energy breaks up the cylindrical jet into spherical droplets of equal mass. The break up takes place at a characteristic frequency first studied by Rayleigh [5]. However, it could be assisted by the addition of a piezo crystal that produces vibration at the nozzle tip in the ball park of Rayleigh's frequency. Since the droplets are jetted in continuous mode, they will have to be selected such that some will reach the target (or be printed) and the others will be recirculated back to the tank. The selection process is performed electrostatically. Following the formation, the droplets are charged. The amount of charges on a droplet can be varied electronically. The charged droplets are passed through a constant electric field. The amount of deflection of each droplet depends on the amount of charge each one possesses. Highly charged droplets are deflected into a catcher and recirculated, while others reach different target positions according to the charge level. The printing method is called proportional deflection, Figure 1.4. However, binary control could also well be utilized where charged droplets are deflected to the catcher and uncharged ones get to the target.

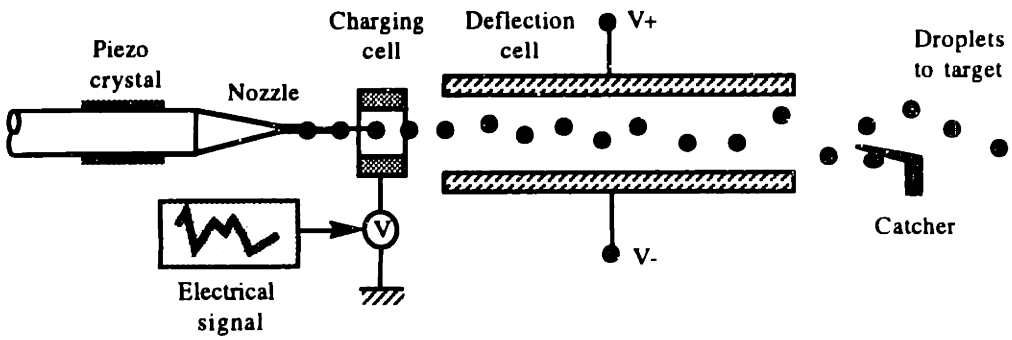

Figure 1.4 Continuous-Jet (CJ) System with Proportional Deflection

Both DOD and CJ can be operated with droplets ranging from 15 μm to several hundred microns. DOD systems are limited to droplet rates of approximately 10 kilohertz due to long delay time in cavity refilling by capillary action [6]. However, CJ systems have droplet rates up to 1 megahertz.

• BINDER TECHNOLOGY

Inorganic binders for Three-Dimensional Printing of ceramic process are typically silicate compounds. Silicate binders are manufactured from partial polymerization of silicic acid or its salts in aqueous solution. The resulting solution is call a sol. Silica and Zirconia sols are mostly water based containing up to 50 weight percent silica with less than 10 centipoise in viscosities. Others kind of binders can be manufactured with other liquid base such as alcohol, for example.

Silica is chosen as a principle Three-Dimensional Printing ceramic process because of its long proven application and material compatibility with investment casting. Silica has been used successfully in directional solidification castings with a good degree of leachability allowing cores to be removed from the castings. More details of silica will be discussed in Chapter 3.

Polymerization of these hydrolyzed silica sols makes them gel and provide strength for green parts. Gellation can be performed with several methods such as drying, freezing, or heating. These mechanisms coagulate the colloid by allowing the particles to collide to one another more frequently. Drying forces the electrostatic fields of the silica particles to overlap. Ice crystals confine the particles in a small volume while heating increases the collision rate of the particles. In addition, silica can be gelled chemically by lowering its surface charge with ion or salts.

Special surfactants such as polymeric additives presented in the binder solution can be tailored to bridge and confine silica particles. This increases the rate of particle collision thus assists gellation. Furthermore, reactive gases such as ammonium compounds or sulfur dioxide can be blown to cure silica binder by being absorbed into the solvent to alter the electrostatic fields. Details of silica can be found in 'The Chemistry of Silica' by Iler [7]. And the development of silica binder for Three-Dimensional Printing of ceramic process was studied by James Bredt [8].

1.3 RELATED RAPIDPROTOTYPE PROCESSES

Recently there has been much interest in rapidprototype processes referred to as desktop manufacturing where parts can be produced directly from electronic information with no tooling required. There are a variety of rapidprototype processes available. In general, these processes can be categorized into three main areas:

1) Chemical Structure transformation of a liquid or solid using light energy
2) Sintering of a powder using light energy
3) Selective addition of material particles or layers to an existing surface

• STEREOLITHOGRAPHY

The most advanced system in chemical structure transformation of a liquid or solid system is Stereolithography. The process works on a principle of polymerizing of an ultraviolet photosensitive liquid. A focused UV laser is vector scanned on the surface of a photopolymerizable liquid polymer bath. The UV light breaks down double bond between carbon atoms at the end of monomer chains (C=C) into single bond (C-C) and free electrons. The electrons from one monomer then pair up with free electrons from nearby chains resulting in polymerization. Photosensitive polymers in stereolithography are designed such that they turn into a solid phase after polymerization. Therefore, after UV curing, exposed area turns into a solid layer adding to the top of the part being created. The part is then lowered to submerge the last created layer and the UV laser draws the next layer. Stereolithography has some limitations. A newly created layer floats freely unless fixed to the layer below or to a support. Consequently, overhangs and undercuts must be accommodated and must be subsequently machined away. In order to minimized total process time, the part is not fully polymerized and must be post-cured in an UV chamber. Another limitations is that there are very limited classes of photosensitive polymers, thus, making them very expensive. They also have low strength and limited shelf life.

Stereolithography has been used to create parts for aesthetic judgment in the past. Recently, a new class of photosensitive polymer is being used as a substitute for wax

patterns in investment casting. Shells can be made on the polymer which will be subsequently melted away prior to pouring. [9]. At the current time, the level of precision has much improved but not attainable part strength, which limits the products from being functional parts.

Another mutation from Stereolithography is a system developed by Cubital. The process still uses photosensitive polymer but depends on sets of masks to block high-powered mercury light instead of vector scanned UV laser. Photosensitive polymer is wiped on top of previously created layer and exposed to masked mercury light. Solidified polymer is consequently machined flat.

• SELECTIVE LASER SINTERING

Developed by University of Texas at Austin, selective laser sintering (SLS) uses a high-powered laser to sinter powder in layer fashion. The powder can be polymers, waxes, metals, and coated ceramics powders. The powder is applied by a counter-rotating roller with typical layer spacing of 0.004 inches [10].

SLS process is limited from high precision applications due to high amount of part shrinkage and distortion during sintering. The bottom layers of SLS parts always warp upward at the corners indicating large shrinkage anisotropy within and between layers.

• MATERIAL ADDITIVE PROCESSES

There are quite a number of material additive processes for rapidprototyping.

- Laminated Object Manufacturing

Developed by Hydronetics Inc. of Chicago, Laminated Object Manufacturing (LOM) cut sheets of papers and foil like materials and laminate them (by glue or weld) to form a three-dimension part [11], [12]. LOM has strategically advantage to other

competitors in rapidprototyping in terms of cost and the process ability to make a wide variety of materials and porosities.

- Fused Deposit Manufacturing (FDM)

Fused Deposit Manufacturing (FDM) in developed by Stratasys Inc. (Eden Prairie, MN). The process constructs a layer by delivering thermal plastic filament materials from a heat extrusion nozzle which hardens immediately at the temperature of the environment. Each finished layer may be machined by a special cutter at a specified height. FDM is suitable for small parts.

- Ballistic Particle Manufacturing (BPM)

The process uses three-dimensional solid model to direct streams of material (photocurable polymer, waxes, plastic, ceramics, or metals) to the target. Three dimensional parts are created in layer basis similar to ink-jet printing. Current BPM machines shoot photocurable polymer onto the target by a piezoelectric ink-jet mechanism and consequently cured by continuos ultraviolet flooding [13].

1.4 SHRINKAGE IN RAPID PROTOTYPE PROCESSES

1.4.1 Shrinkage in Three-Dimensional Printing of Ceramics

Three-Dimensional Printing generally has a very good dimension control relatively to other rapid prototype processes. Although the process appears to have only a very slight amount of shrinkage, the shrinkage sometime leads to issues such as distortion and delamination. Prior to October of 1994, a large fraction of Three-Dimensional Printing ceramic product was damaged during build process. One of the common failure modes is delamination where layers crack or disintegrate upon sintering of the binder. A further study reviewed that parts undergo 0.3 to 0.5 percent linear shrinkage. Since Three-Dimensional Printing is layer-by-layer manufacturing, shrinkage not only effects the final dimensions but also part integrity.

• CAUSES OF SHRINKAGE IN THREE-DIMENSIONAL PRINTING OF CERAMICS

Shrinkage in Three-Dimensional Printing of ceramics begins in the green state and subsequently increases during post-processes, namely drying, firing, and postdipping-refiring. The final shrinkage strain after postdipping is roughly 0.4 and 3.5 percent when heat treated to 900°C and 1500°C and cooled to room temperature, respectively. Origin of shrinkage for Three-Dimensional Printing parts can be categorized as follows:

1) Drying shrinkage due to capillary stress
2) Heat treatment shrinkage due to sintering

• DRYING SHRINKAGE

Shrinkage from capillary stress occurs as binder dries (between green state and dried). When liquid-vapor interface starts to enter the pores of the binder, it develops concave menisci with the center of curvature in the vapor side. This phenomena places the liquid under tension (suction). In the case of drying gel, the liquid tensile stress is

supported by the solid phase of the binder so called **network**, which therefore undergoes compression. If the network in the binder is compliant, the compressive force causes it to contract into the liquid. The magnitude of liquid tension depends on the pore size, properties of the fluid, and contact angle. As drying proceeds, the network becomes stiffer and the tension in the liquid rises accordingly. Once the stiffness of the network is sufficient to resist the capillary stress, shrinkage stops and the radius of the meniscus becomes approximately equal to that of the pores. At this point, the tension in the liquid could be as high as 1-3 MPa. Beyond this point, the liquid-vapor front recedes into the interior leaving air-filled pores behind. Details of drying mechanism will be elaborated in Chapter 4 and 5.

Typical shrinkage of Three-Dimensional Printing of ceramic parts is illustrated in Figure 1.5. Note that in green, dried, and after heat treatment, shrinkage shows a strong non-linearity to part length which may be explained by traction between the printing region and the unbounded powder bed.

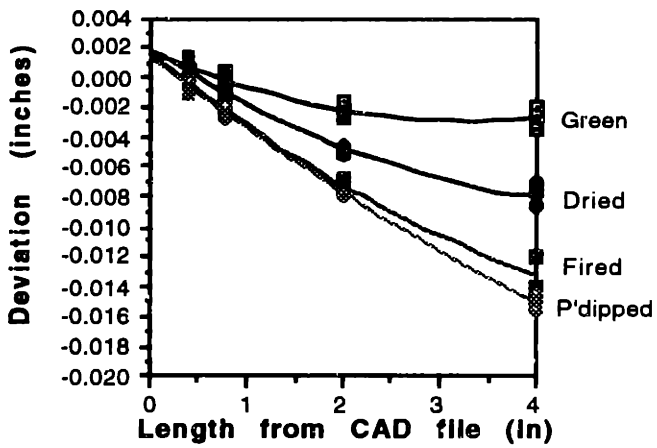

Figure 1.5 Shrinkage of Three-Dimensional Printing of Ceramic parts
(Powder: Norton 7920 rinsed with 0.3 percent citric acid | Binder B at 1.2 cc/min)

- HEAT TREATMENT SHRINKAGE

Particle consolidation during sintering is another important source of shrinkage. The degree of consolidation depends on materials, particle shape and size and distribution, and firing temperature. Figure 1.6 illustrates shrinkage (in percent) of test samples built on

the slow axis, as a function of temperature. Shrinkage strain linearly varies with temperature to about 0.3 percent at 900°C and 0.5 percent 1100°C, then abruptly increases to 3.5 percent at 1500°C.

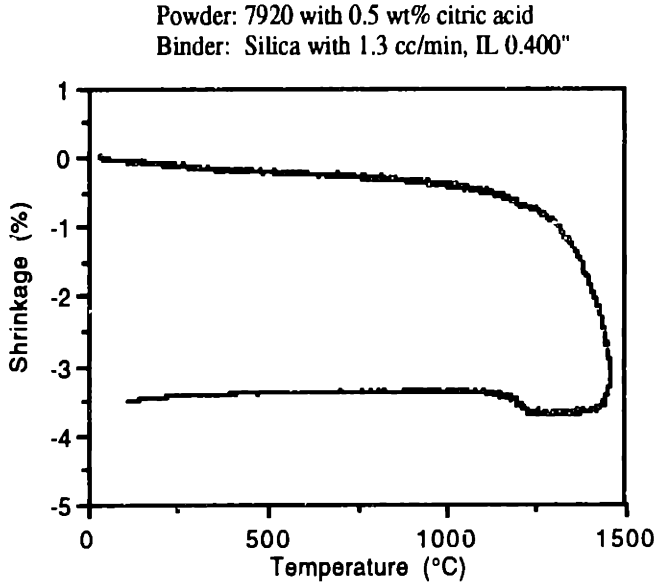

Figure 1.6 Shrinkage in Firing Caused by Particle Consolidation

Sintering of amorphous silica is governed by viscous flow. Sintering is driven by the energy relief from reduction of surface area of the binder. Figure 1.7 illustrates the reduction in surface area and shrinkage of two spheres in contact at elevated temperature.

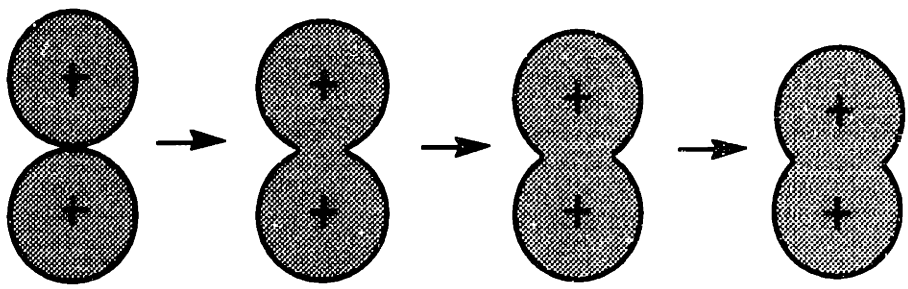

Figure 1.7 Reduction of Surface Area Brings Particles Closer (center to center) and Causes Shrinkage

• PROCESS ISSUES RELATED TO SHRINKAGE

Shrinkage directly effects the dimensional control and tolerance of printed parts. Without shrinkage compensation printed parts are always smaller than intended. Shrinkage characteristics must be well understood before a compensation scheme can be built into the CAD file to scale the electronic information and to compensate for, Figure 1.8.

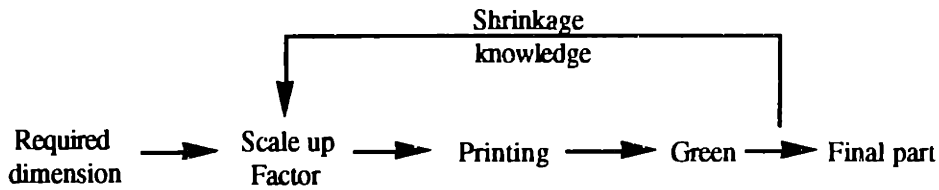

Figure 1.8 Shrinkage Compensation Scheme

Interlayer shrinkage anisotropy causes part distortion. A typical phenomena is upward distortion of corners especially when layers with large cross section are printed. Although the amount of distortion is small, it can be visibly observed on thin slabs. Distortion tends to concentrate especially during the first few layers of printing because created part has minimal number of layers (or thickness to counter the bending moment from shrinkage anisotropy). Figure 1.9 shows distortion for thin and thick slabs (exaggerated for purpose of illustration).

Figure 1.9 Part Distortion on Thin and Thick Slabs

In addition, upward distortion may interfere with powder spreading and packing process. The roller may shear and shift the created part resulting in lost of the registration between previous and new layers. Figure 1.10 illustrates how the shifting takes place.

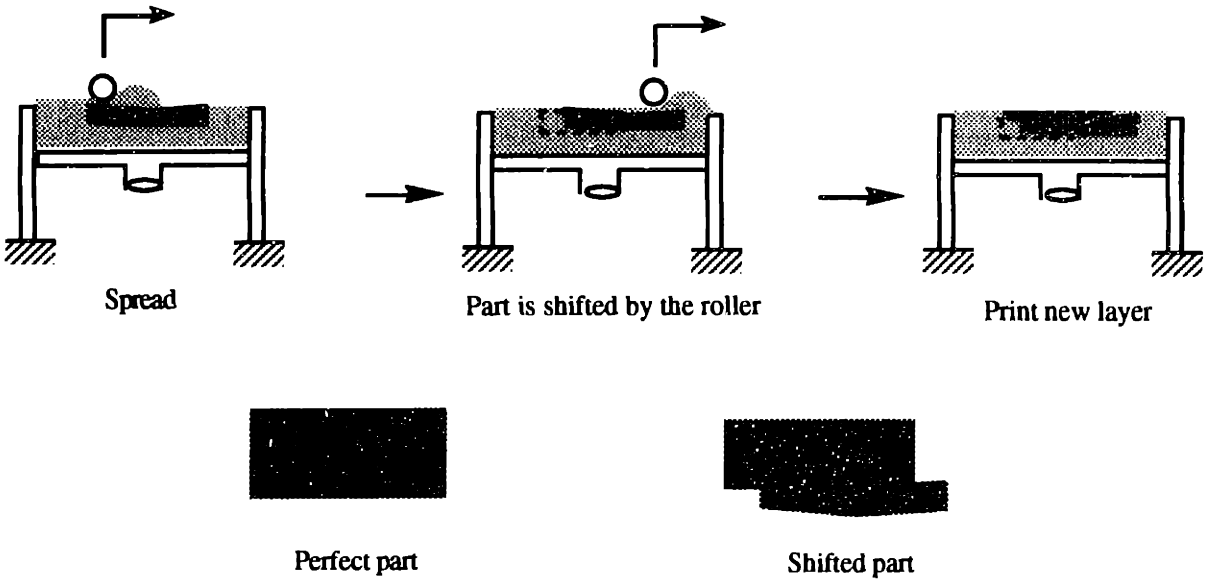

Figure 1.10 Shifted Part Induced by Upward Distortion

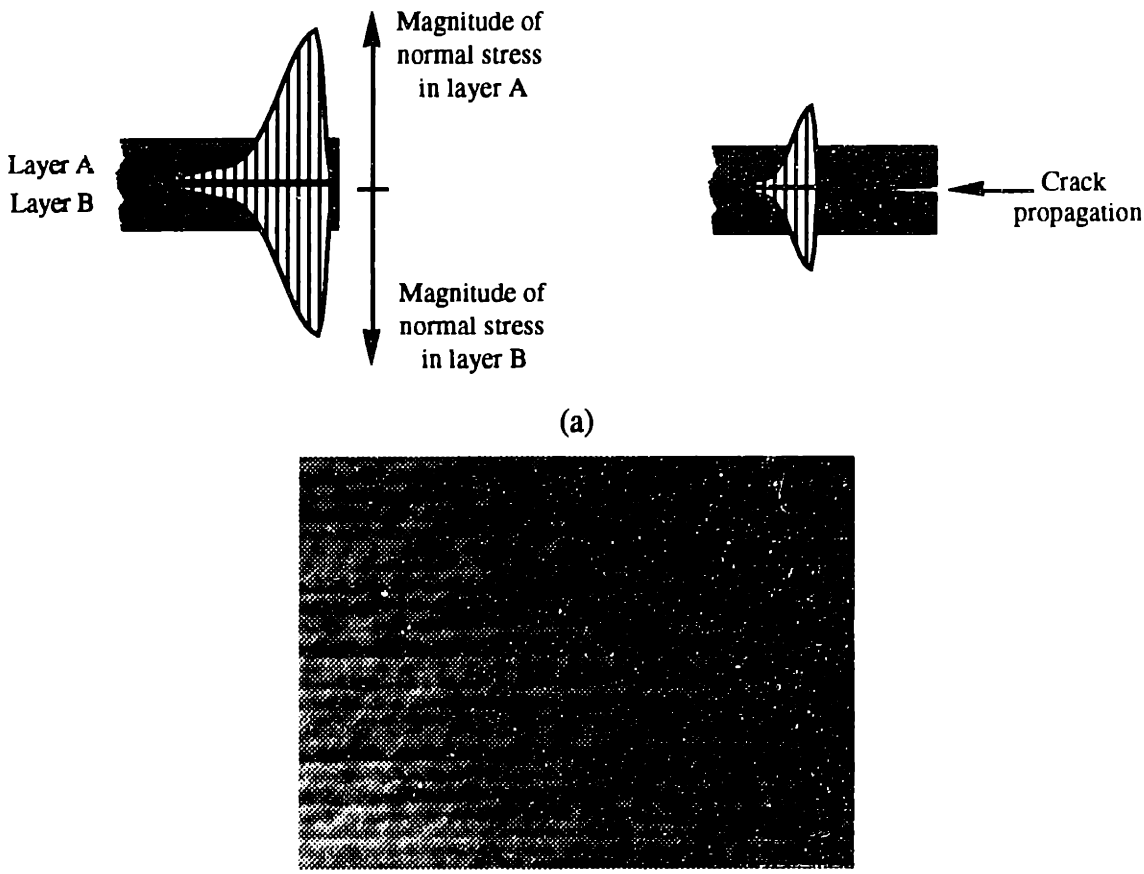

Figure 1.11 Peeling Stress at the Interface and Crack Propagation into the Interior

The most critical issue related to shrinkage is delamination. Internal stress is induced by shrinkage anisotropy between layers resulting in a shear stress that concentrates along layer interfaces and a normal stress in the direction perpendicular to the layer. The normal stress maximum near the edge of the part striving to peel layers from their interfaces. If the magnitude of this normal force is high, cracks propagate along the interface plane starting from the edge into the interior. The cracks stop after some elastic energy has been released while the remaining energy reaches a new equilibrium with the interface strength. Figure 1.11 (a) and (b) show crack propagation into the interface plane. Interface cracks reduce the cross section area resulting in higher stress density at the defected layer interface when subjected to external force. If the interface can not bear the stress, the cracks propagate until the entire interface fails (or delaminates) causing part disintegration as shown in Figure 1.12. This failure mode seriously affected Three-dimensional Printing of ceramics prior to October of 1994. Part survivability at that time was less than 60 percent.

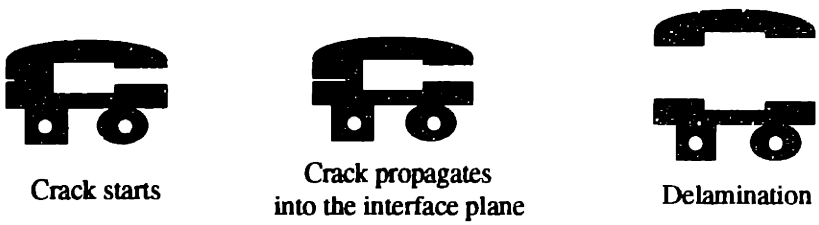

Figure 1.12 Progress of Crack Propagation and Delamination

1.4.2. Related Work on Shrinkage of Three-Dimensional Printing of Ceramics

Marcos Esterman, Jr. investigated heat treatmcnt shrinkage of Three-Dimensional Printing ceramic part as a function of firing temperature in a dilatometer [14]. He found that heat treatment shrinkage increased linearly with temperature upto about 0.7 percent at 1200°C. Above this threshold, shrinkage rapidly increased to 2.5 percent at 1400°C. Esterman also found that flatness of ceramic plates remained within 1-3 mils over 1.25 square inch after being heat treated to 1000°C. But when the slat was heat treated to 1500°C, the flatness was found to be 9 mils over the same area. Esterman also investigated the relation between the amount of binder per unit volume of ceramic powder, (B/V). He found that distortion increased with B/V ratio. However, his measurement techniques could not detect shrinkage during drying.

Christopher L. Harris first investigated shrinkage of bars after drying and firing using a Pratt and Whitney supermicrometer with constant contact force [15]. Printed binder was Nyacol 830 gelled by drying. He found that there was no shrinkage during the green state, and only 0.01 percent after firing to 1000°C. However, the shrinkage increased to 1.4 percent, if fired at 1500°C. So, he concluded that Three-Dimensional Printing had quite a remarkable dimensional control below 1000°C.

Khalil Sardouk conducted an intensive study of dimensional control of Three-Dimensional Printing bars as function of printing axes, acidity of the powder, misting, and firing temperature [16]. Sardouk observed some degree of shrinkage non-linearity as a function of length. He also noticed shrinkage anisotropy at different areas on the powder bed. However, some of his data were scattered due to lack of precision in his contact measurement technique. Khalil concluded that the shrinkage was, in average, 0.5 percent for parts built with slow and fast axes.

Richard Li-Chao Yu investigated shrinkage of ceramic parts printed with a co-dispersion of silica binder [17] and polymer from green to dried, fired, and postdipped using a non contact measurement techniques· Yu mounted a microscope CCD camera on the tip of a coordinate measuring machine (CMM). The accuracy, resolution, and

repeatability was greatly improved over the contact measurement technique. Yu found that shrinkage with co-dispersion binder is slightly more with silica binder.

Esterman and Yu both tried to quantify the strength of parts. Esterman related modulus of rupture to B/V ratio and line spacing, whereas Yu compared strength of Three-Dimensional Printing parts at different firing temperatures using several types of binders.

So far, no study has systematically reviewed shrinkage of Three-Dimensional Printing of ceramic process to a point that clarifies a basic understanding of shrinkage and distortion. Shrinkage is a very complex phenomena and should well be understood before Three-Dimensional Printing can be applied to precision applications.

1.4.3 Shrinkage of Stereolithography

Stereolithography builds solid parts by curing of photopolymer liquid with a UV laser. A layer is created by knitting strands of cured photopolymer and binding them onto the previous layer.

Iwanaga et. al. [18] investigated the relationship between material characteristics and warpage of several acrylate polymers. It was found that the warpage which occurred during laser curing was greatly influenced by the shrinkage stress and the modulus of elasticity of the solidified part. To minimize shrinkage, shrinkage stress (or curing stress) had to be minimized while maximizing the modulus of elasticity. Iwanaga could not find the relationship between curing temperature immediately following laser scanning and the amount of shrinkage.

Arney et. al. [19] studied the relationship between and shrinkage and the molar shrinkage constant, which is the difference of specific volume before and after polymerization of several structures of acrylic monomers. They found that there appears to be no significant relationship.

Laser scanning techniques that improve dimensional control of acrylic base resin were developed at 3D Systems during 1990-1992 [20]. The new scanning schemes (WEAVE™ and STAR-WEAVE™) improved the accuracy by 40 percent.

In 1993, a new class of Stereolithography resins was developed by Ciba-Geigy (Switzerland) and 3D systems (CA) based on epoxy technology. The new resin (XB-5170) provides significant improvement of overall part accuracy and dimensional stability relative to earlier resins (acrylate base). Not only does the new resin improves the mechanical properties, but it also has very low shrinkage which results in low curl and distortion [20].

Flach and Chartoff [21] developed a linear shrinkage prediction for the process model. The prediction is a simplified computation of specific volume changes from the extent of conversion of monomer (C=C) to polymer (C-C) and allows for shrinkage to lag behind conversion by a specified amount. It is found that faster shrinkage resins should result in lower overall linear shrinkage and dimensional inaccuracy.

In March of 1994, a new epoxy-base resin (SL-5180) was released by 3D system. This resin has smaller laser-cure and post-cure shrinkage than 5170 epoxy resin, resulting in tighter dimensional control and less distortion. In addition, the modulus of rupture of this new resin is four times that of conventional acrylate base resins. Therefore, parts built with this resin are much stronger and tougher. These outstanding properties allow stereolithography to build thin wall structures with minimal creep and distortion.

Ullet J. S., Rodrigues S. J., and Chartoff R. P. [22], investigated linear shrinkage of acrylate (XB5149) and epoxy (XB5170) resins during curing. The resins were cured with a helium-cadmium (He-Cd) laser using two exposures. The exposure time was held constant while the delay time between exposures was varied. Both resins showed that the final cure depth and linear shrinkage was a function of delay time. For the acrylate resin, long delay time resulted in swelling of the partially cured strands during the delay and after the second exposure. Maximum shrinkage was found with short delay time around (1.34 percent). In addition, long delay time resulted in smaller final cure depths. For the epoxy resin, long delay time resulted in minimum shrinkage. Unlike the acrylate

resin, epoxy strands made with long delay times had greater final cure depth value than that of short delay time exposures.

One of the most thorough studies of shrinkage and stress relaxation of stereolithography was conducted at Sandia National Lab by Guess T. R. et al. [23]. The experiment called for two resins developed by Ciba-Giegy, Cibatool® SL 5170 (epoxy base) and SL 5149 (acrylate base). Strand specimens were drawn with single pass of He-Cd laser beam using PatternDraw copyright software on 3D System's SLA-250 machine. Shrinkage was measured in-situ with an optical video microscope as a function of time. Linear shrinkage is found to be 1.0 percent for SL 5149 acrylate and 1.6 percent for SL 5170 epoxy. When strands were made of multiple laser exposures, it was found that both SL 5149 and SL 5170 continued to shrink, contradicted to the finding from Ullet's finding [22]. Shrinkage force and stress relaxation were measured by making strands anchored one end to a force gage and the other to an electronically-driven micrometer. No force was detectable for both resins after the first exposure probably due to the force gage resolution of 0.02 gm. But, when 0.5 percent step strain is applied after different delay times. Epoxy shows an increase of modulus with elapsed time. This modulus increment occurs after linear shrinkage has stopped. On the other hand, acrylates show no sign of modulus evolution. The modulus remains stable after the shrinkage has shopped. Therefore, epoxy resin accumulates less shrinkage than acrylate resin for multiple laser exposures. In terms of stress relaxation, epoxy resins show that response times get larger with elapsed time after laser draw. But, acrylate resins indicate that stress relaxation times are not a function of elapsed time after the strand is hit with the laser.

1.5 RESEARCH SCOPE AND APPROACH

1.5.1 Problem Statement

Current Three-Dimensional Printing process parameters yield approximately 0.5 percent linear shrinkage. Half of the linear shrinkage occurs during drying of binder and the rest (if fired to 900°C) takes place during sintering at elevated temperature. There is a strong evidence that shrinkage interaction among layers cause distortion, crack, and delamination in Three-Dimensional Printing parts. The fundamental mechanisms of linear shrinkage and shrinkage related issues such as distortion are not fully understood.

1.5.2 Scope of Study and Approach

An intensive set of experiments was conducted during January-June 1994 which led to a conclusion that binder consolidation is a primary cause of linear shrinkage of Three-Dimensional Printing of ceramics. According to the nature of the process, half of total linear shrinkage occurs during drying of the binder, while the other half takes place as the binder sinters at high temperature.

While shrinkage during sintering of binders is well documented, drying shrinkage is not very well understood due to the complexity of the physics and chemistry of drying. This research work hopes to develop a fundamental understanding of the mechanics of drying of a liquid-filled deformable solid. In addition, the linkage between powder and binder interaction shall be identified. The knowledge will be applied to reduce shrinkage and distortion in the Three-Dimensional Printing ceramic process.

Materials of this research will be limited to alumina as the powder and colloidal silica as the binder. Both materials have been standards for Three-Dimensional Printing of ceramics and we have gained some knowledge working with them for a number of years.

There are a few areas which this research work will focus on:

1) Mechanics of Drying and Deformation

George Scherer [24-27] has developed a drying stress model for sol-gel bodies. According to Scherer, liquid tension driven by the capillary and the network's strength are responsible for shrinkage during drying. This research will apply Scherer's model to gel bodies in order to identify important factors that effect drying shrinkage for Three-Dimensional Printing binders.

2) Stress-Strain Map of Binders

It is very important to understand the nature of shrinkage of binders in Three-Dimensional Printing. This scope of work proposes an approach to isolate the binder from the powder and study their stress-strain relationship. Ideally, microscopic deformation of a binder meniscus bounded by two particles shall be studied during drying and consolidation. However, there are a few limitation to the approach. First, if 30μm platelet particles are used, the total volume of binder to bond two particles is in the order of $8x10^{-8}$ μl which is unrealistically small. Second, the jagged nature of platelet powders makes contact angle to be a complex 3-dimensional problem.

In order to simplify the problem, the volume of the experiment binder should be about 2 to 5 μl or 3 to 5 mg. This allows a practical measurement of how much liquid evaporates and leaves the body. In addition, the binder shall be bounded by two parallel flat boundaries with a gap space of 125 to 250μm. Flat boundary allows the contact angle to be independent of binder volume.

The boundary movement as the binder deforms during drying will be monitored by a high resolution optical sensor. Maximum stress and strain of binders as a function of boundary compliance will be recorded and illustrated as a stress-strain map. The compliance will be varied to cover equivalent powder bed stiffness. Figure 1.13 a) presents a schematic while 1.13 b) shows a sketch of the proposed setup.

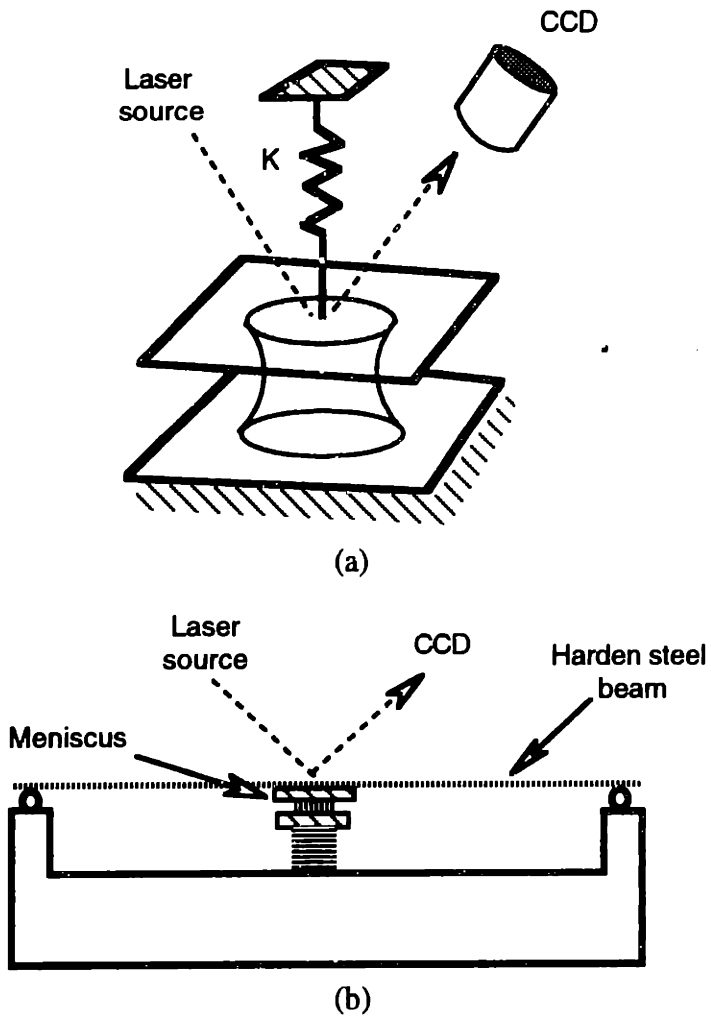

Figure 1.13 Boundary Stress-Strain Map Setup

3) Mechanics of Powder under Isostatic Stress

Mechanics of powder has important roles in Three-Dimensional Printing process including shrinkage. As the binder consolidates and exerts shrinkage stress on powder particles, the particles move closer and increase their coordination numbers. As more and more particle contact points are made, the powder bed resists the coalescence. Finally, the shrinkage ceases at the point where the shrinkage force reaches an equilibrium with the packing resistance force.

This study will provide a fundamental understanding of the mechanics of powder such as yielding criteria in relation to shear, tensile, and compressive stresses as a function of porosity. The research is hoping to identify the coalescent character of powder and also to determine that equilibrium point where the coalescent and shrinkage stress come into balance. These finding will not only benefit Three-Dimensional Printing ceramic process, but also generally apply to other Three-Dimensional Printing material systems.

1.6 THESIS ORGANIZATION

Before shrinkage mechanism can be well explain, Chapter 2 and 3 serve as an introduction to powder and binder materials in Three-Dimensional Printing of ceramics. Powder is a major build material for Three-Dimensional Printing such that an average part contains 92 weight percent of powder. Typical powder materials are listed in chapter 2 together with some useful result and problems on their packing. Chapter 3 introduces common binder in the focus of this thesis work as well as some key requirements for binders in the process.

Shrinkage mechanism during drying are discussed in detail in Chapter 4 with mathematical explanation. It is a summary of George Scherer's theoretical work on drying of deformable bodies. Interaction of solid network under compression and liquid tension due to capillary tension is specified. Chapter 5 shows how these theories can be applied to drying of gel in various shapes, geometry, and boundary constraints as well as some useful strategies to minimize drying shrinkage.

Actual shrinkage measurement of printed parts in Three-Dimensional Printing are listed in length in Chapter 6 with observed important process parameters affecting the magnitude of drying shrinkage. Some shrinkage reduction strategies were tried out on binders. The second part of the chapter focuses on creating stress-strain map for Binder B and Nyacol 9950 experimentally.

Mechanics of powder deformation under equivalent binder stress are written in Chapter 7. Characteristics of plastic deformation of powder in Three-Dimensional Printing are identified with a mathematical model based on an experiment.

Last, but not least, binder stress-strain characteristics from chapter 6 and powder strain behavior under stress from Chapter 7 are combined in Chapter 8. This chapter is a highlight of this thesis work. Powder-binder shrinkage interaction was identified when printing at, or close to, saturation level. The findings in this chapter point to a new powder-binder system which could reduce overall shrinkage in Three-Dimensional Printing of ceramics by a factor of 5-8.

Bibliography

[1] Taylor, P. R., *Lost was casting - a short illustrated review*, Metal and Materials, 2, 11, pp.705-710, 1986.

[2] Smart, R. F., *High Strength and integrity investment castings*, Materials and Design, 10, 6, pp.301-305.

[3] Sachs, E., Cima, M., Williams, P., Brancazio D., and Cornie, J., *Three Dimensional Printing: Rapid Tooling and Prototypes Directly from a CAD Model*, Journal of Engineering for Industry, Vol. 114, pp. 481-488, Nov. 1992.

[4] Kyser, E., Drive Pulse Optimization, *Journal of Advance in Non-Impact Printing Technologies*, Gaynor, ed., pp. 1175-1189, 1981.

[5] Rayleigh, F. R. S., *On the Instability of Jets*, Proc. London. Math Soc., Vol. 10, No. 4, pp. 4-13.

[6] Arndt, P., *Pulsed Droplet Ejecting System*, US Patent #3,683,212, 1974.

[7] Iler, R. K., *The Chemistry of Silica*, John Wiley & Sons, 1979.

[8] Bredt J., *Binder Stability and Powder\Binder Interaction in Three Dimensional Printing*, MIT PhD Thesis, Dept. of Mechanical Engineering, Supervised by E. M. Sachs, 1995.

[9] Weiss, I., Levent-Gursoz, E., Prinz, F., Mahalingham, S., Fussel, P., and Patrick, E., *A Rapid Tool Manufacturing System based on Stereolithography and Thermal Spraying*, ASME Manufacturing Review, Mar, 1990.

[10] Deckard, C., Beaman, J., *Recent Advances in Selective Laser Sintering*, Fouteen Conference on Production Research and Technology, University of Michigan, pp.447-452, Oct. 1987.

[11] Fallon, M., *Desktop Manufacturing Takes You from Art to Part*, Plastics Technology, pp. 78-82, Feb 1989.

[12] Belford, D., *Laser Modeling Reduces Engineering Time*, Laser Focus World, pp. 103-108, June 1989.

[13] Kochan, D., *Solid Freeform Manufacturing*, pp. 121, Elsevier, Amsterdam, 1993

[14] Esterman M.,Jr., *Characterization of the Powder/Binder Interaction in the Three Dimensional Printing Process*, 1990, MIT ME Thesis MS, Supervised by E. M. Sachs.

[15] Harris C. L., *Characterization of Dimensional Variability and Part Bleeding Using The Three Dimensional Printing Process*, MIT ME Thesis BS, Supervised by E. M. Sachs, 1991.

[16] Sardouk K., *Analysis of Dimensional Control in 3D Printing*, MIT ME Thesis BS, Supervised by E. M. Sachs, 1993.

[17] Yu R. L., *Development of a Co-Dispersion Binder for the Three Dimensional Printing Process to Facilitate Handling of Ceramic Casting Shells in the Green State*, MIT ME Thesis MS, Supervised by E. M. Sachs, 1994.

[18] Iwanaga S. . Ohkawa M., Igarashi K., *Influence of Material Characterization on Dimensional Stability*, Third International Conference on Rapid Prototyping, Dayton, OH, pp.77-88, 1992.

[19] Arney J. S., Sanders L., Hardesty R., *The Impact of Molecular Structure and Crosslink Formation on the Shrinkage of Acrylic Monomer*, The Fourth International Conference on Rapid Prototyping, Dayton, OH, pp.169-174, 1993.

[20] Pang T. H., *Stereolithography Epoxy Resin Development: Accuracy and Dimensional Stability*, Solid Freeform Fabrication Proceedings, September, pp.11-18, 1993.

[21] Flach L., Chartoff R., *Stereolithography Process Modeling: Shrinkage Prediction*, The Fifth International Conference on Rapid Prototyping, Dayton, OH, pp.181-189, 1994

[22] Ullett J. S., Rodrigues S. J., Chartoff R. P., *Linear Shrinkage of Stereolithography resins*, The Sixth International Conference on Rapid Prototyping, Dayton, OH, pp.57-67, 1995

[23] Guess T. R., Chambers R. S., Hinnerichs T. D., McCarty G. D., Shagam R. N., *Epoxy and Acrylate Stereolithography Resins: In-situ Measurements of Cure Shrinkage and Stress Relaxation*, The Sixth International Conference on Rapid prototyping, Dayton, OH, pp. 69-80, 1995

[24] Scherer G.W., *Drying Gels I. General Theory*, Journal of Non-Crystalline Solids 87, pp.199-225, North-Holland, Amsterdam, 1986

[25] Scherer G.W., *Drying Gels II. Film and Flat plate*, Journal of Non-Crystalline Solids 89, pp.217-238, North-Holland, Amsterdam, 1987

[26] Scherer G.W., *Drying Gels III. Warping plate*, Journal of Non-Crystalline Solids 91, pp.83-100, North-Holland, Amsterdam, 1987

[27] Scherer G.W., *Drying Gels IV. Cylinder and Sphere*, Journal of Non-Crystalline Solids 91, pp.101-121, North-Holland, Amsterdam, 1987

Chapter 2.

Powder in Three-Dimensional Printing of Ceramics

2.0 INTRODUCTION

A typical Three-Dimensional Printing ceramic part consists, by weight, of 92 percent powder and 18 percent binder. This fact makes powder a very important build material in Three-Dimensional Printing of ceramics. Powder plays several important roles in the fundamental physics of Three-dimensional Printing such as to control binder migration and primitive formation into lines and layers. Additionally, it has much influence on surface roughness as well as shrinkage and deformation of parts. Powder dictates several key properties of Three-Dimensional Printing product such as, thermal, mechanical, and chemical properties. Whether Three-dimensional Printing is applicable for directional or single crystal solidification or not depends on refractoriness of the powder. Therefore, selecting an appropriate powder for Three-Dimensional Printing of ceramics is a very important decision.

2.1 POWDER SELECTION

Since powder has strong impacts on Three-Dimensional Printing process limitations and capacities, selection of powder for Three-Dimensional Printing ceramic process requires a thoughtful consideration.

The very first thing a designer would have to find out before working on the drawings are the customer needs. In order to satisfy the needs, the designer must be able to under the customer and convey the solutions into product design. For a process designer, the same process shall be applied as well. So, the first thing to do at this step is to identify Three-Dimensional Printing customers and what are their expectations.

Three-Dimensional Printing consortium members in casting business involve with complex 3-dimensional shapes. For example, Pratt & Whitney Aircraft Engine Division, Howmet, as well as General Electric Power Plant Division make state-of-the-arts castings of gas/steam turbine/engine components. While Johnson & Johnson Orthopedics is leading manufacturer of fine features casting of prostheses. Therefore, the market niche that Three-Dimensional Printing ceramic process has involved is the casting of complex 3-dimensional bodies in a small batch size which relies on the flexibility and fast turn around of Three-Dimensional Printing process for a much shorter design and manufacturing cycle. Three-Dimensional Printing offers a solution to make complex castings with an ability to evaluate them in a matter of days to rapidly complete the design cycle.

Current manufacturing standard for casting of complex 3-dimensional shapes with highest surface finish is investment casting. From material selection perspective, it is essential to review choices of powdered refractory in investment casting at this point.

2.1.1 Powdered Refractory in Investment Casting

Investment shell molds are made by applying a series of ceramic slurry coatings to the patterns usually grouped in clusters. Slurry coatings consist of fine ceramic particles with ceramic binder. A cluster is first dipped into a bath of slurry coating. Then it is taken out and manipulated to drain off the excess slurry. The wet slurry layer is immediately deposited with stucco with relative coarser ceramic particles by either dipping the cluster into a fluidized bed of particles or by sprinkling the particles onto it. Following the coating, the assembly is let to dry off. This series of slurry dipping, stuccoing, and drying are repeated for several times until the patterns have sufficient ceramic shell thickness which is approximately a quarter of an inch.

Ceramic powder is used in investment casting in two general forms - slurry mixture and stucco. Fine ceramic particles are mixed with the slurry to conform to the surface of a pattern and to reproduce every details of the pattern surface including the smoothness. The stuccoes are larger particles to arrest further dripping and run off of excess slurry, prevent mold cracking, and speed up the material building rate.

Most common refractories for investment casting are siliceous such as silica, zircon, alumina, and various alumina silicate, such as mullite [1]. Physical properties of most common refractories are illustrated in Table 2.1.

Refractory	Melting pt. (°C)	Density [kg/cu.m]	Coef. Of Thermal Expansion [x10^{-6}/K]
Fused silica	1710	2070	.015
Zircon	2538	4650	0.23
Chromite	2093	4400	0.27
Alumina	2050	4000	0.7
Olivine	1875	3320	0.8
Quartz	1710	2660	1.4
Mullite	1550-1830	3120	0.4
Kyanite	1325	3620	0.4

Table 2.1 Physical Properties of Common Ceramic Refractories[1]

Silica is generally used in form of silica glass (fused silica) which in made by melting and solidifying of quartz sand. Silica is grounded to powder to mix into slurry or crushed and screened to make different grades of stuccos. It has extremely low thermal coefficient of expansion, therefore resists thermal shock load for the mold. Silica is soluble in molten or solution of caustic allowing chemically removal of shell that are difficult to clean by other methods. Silica may also be used in nature form of quartz. Quartz is probably the least expensive material among other refractories. But its use is purely limited by its high thermal coefficient of expansion which increases abruptly at 573°C (1073°F) as phase transition from α to β. As a consequence, shells made with quartz are susceptible to thermal shock and must be fired slowly. Most foundries consider the slow firing requirement of quartz not practical.

Zircon appears naturally as a sand. Zircon is normally used as a stucco of primary coats because it does not naturally occurs in a size coarse enough for backup stucco. It is also ground to powder and mixed with slurry, often with fused silica and/or aluminum silicates. Zircon is more expensive than silica, but it has more refractoriness and resistance to be wetted by molten metals.

[1] See Detail in Appendix B.

Alumina is a form of oxide of aluminum with the chemical formula Al_2O_3. It is more refractory than silica or mullite and less reactive to metal alloys than any siliceous refractories. Alumina is primarily used for superalloy casting and high temperature casting.

Aluminum Silicates are made by calcining fireclays to produce a series of products with 42-72% silicate content with the remainder being silica and impurities. Cost and refractoriness increases with alumina content. Mullite ($3Al_2O_3 \cdot 2SiO_2$), with 72 percent by weight alumina at the eutectic point, is the only compound stable at high temperature. Mixture containing less than 72 percent alumina produces mullite and free silica (in form of silica glass). Alumino silicates are used as powders for slurry and stuccos.

Materials and manufacturing processes for making of ceramic cores in investment casting are different from the shells. Ceramic cores are widely used to produce internal passage ways in castings. Traditionally, there are two ways to produce ceramic cores: self-forming and pre-forming. Self-formed cores require that the wax patterns already have the openings corresponding to desired passageways. Therefore, self-formed cores are made at the same time and with the same materials as the shells in dipping and stuccoing process. This self-forming process is only applicable to simple geometry with large openings. For deep and small openings, special attention must be given to slurry viscosity, stucco particles, and drying. Vacuum dipping and the use of Ethyl silicate as the binder assist in slurry filling and drying. Pre-formed cores require separate toolings and normally made by casting or injecting silicate slurries similarly to ceramic molding processes. Other cores are made by ceramic injection molding. Fine ceramic powder (often fused silica or with addition of zircon) is mixed with an organic vehicle (in most cases, thermoplastic such as polyethylene, ethyl cellulose, shellac resins, waxes, and subliming organic compounds such as naphthalene and paradichlorobenzene) and injected into hardened steel dies. The organics which serve as a green binder are then burned out and ceramic powder is allowed to sinter to its final length and dimensions.

In order to choose an appropriate powder for Three-Dimensional Printing process, there are a few considerations, or functional requirement, to be examined. Functional requirement for Three-Dimensional Printing of ceramic powder are discussed in the next section.

2.1.2 Functional Requirements for Powder in Three-Dimensional Printing of Ceramics

Parts fabricated by Three-Dimensional Printing ceramic process are subjected to many requirements and expectations. Those important ones are listed below:

HIGH REFRACTORINESS AND LOW SURFACE REACTIVITY

According to thermodynamic law, theoretical efficiency of a reversible cycle (or Carnot cycle) is [2]:

$$\eta_{rev} = 1 - \frac{T_L}{T_H} \tag{2.1}$$

where η_{rev} is the thermodynamic efficiency of a reversible cycle

T_L is the temperature of heat sink reservoir

T_H is the temperature of heat source reservoir

The temperature of the heat sink reservoir of a gas turbine is usually fixed as ambient temperature. So, the only way to increase thermal efficient of Carnot engine is to increase the temperature of the heat source reservoir. This is equivalent to increasing the combustion temperature in most engines.

For gas turbines, the same thermodynamic law is applicable. The airline industry is very sensitive to fuel price. It is estimated that half of the cost for a typical flight is from the fuel. Therefore, a small increase in turbines' thermal efficiency could save millions of dollars for the industry. So, there has long been a great effort to increase the temperature of turbine inlets to gain higher thermal efficiency. However, the only major impedance to the concept is how to build turbine blades that withstand the heat while maintaining good mechanical properties. If consider only for refractoriness alone, ceramics are such wonderful candidates. But, ceramics are known to be brittle and have low toughness strength. Ceramic turbine blades will be shattered in case of foreign material ingestion (such as birds or debris from upstream compressors and combustion chamber). An alternative choice of material is nickel-base alloys. But new fabrication technique must be

employed since tradition investment casting for nickel-base alloy has reached its temperature ceiling.

Leaders in commercial aircraft engines such as Pratt & Whitney and General Electric have a few practical solutions. Mechanical design approach is to build turbines blades with internal cooling passages that remove build up heat when blown internally with compressed air. On the other hand, material approach is to rearrange the microstructures of the turbine blades. Strength of nickel-base alloy depend on their grain boundary properties. Therefore, one solution is to directionally solidify turbine blades and force the grain boundaries to run parallel to the direction of principle stress (longitudinal). This method is called directional solidification (DS). Turbine blades of this types have higher strength in the stress direction and the grain boundaries effect on mechanical properties is minimal. Another solution is to completely get rid of the grain boundaries by making the turbine blade out of a single grain. The technique is known as single crystal solidification (SC). The lack of grain boundaries significantly improves mechanical properties and enhances corrosion resistance. SC turbine blades can be further strengthen by a process called solution heat treatment which precipitates out a greater amount of γ phase and further augments the alloy strength.

For both directional and single crystal solidification, shells will be preheated to just a few hundred Celsius below the temperature of the molten metal. After the metal is poured, occupied shells are allowed to cool down slowly. Heat is removed from the bottom of the shell and solidification is allowed to start longitudinally from the bottom to the top. Directional solidification requires a strong longitudinal thermal gradient. This forces the grains to be columnar and align with the direction of the thermal gradient. For single crystal solidification, the grains are nucleated at the grain selector unit which is a spiral cavity attached to the bottom of the shell. Several grains will grow simultaneously and slowly inside the spiral unit. But only the last grain will be allowed to grow into the shell cavity. In this way, the casting will be made of a single grain and becomes grain-boundary free. Figure 2.1 illustrates a typical temperature profile experienced by the shell in single crystal solidification process.

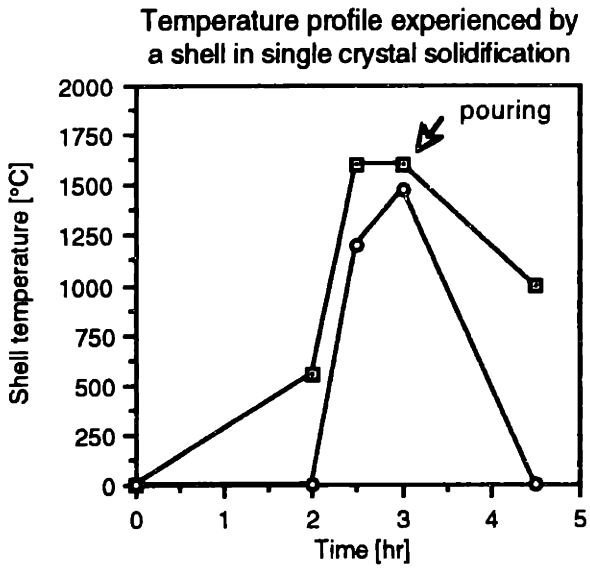

Figure 2.1. Typical Temperature Profile Experienced by a Shell in Single Crystal Solidification

According to Figure 2.1, single crystal solidification shells are reheated to approximately 1500°C within 1 to 2.5 hours. This rapid heating rate requires materials with low coefficient of thermal expansion to prevent thermal shock and cracking. In addition, the shells have to withstand the immense heat for 4-6 hours which clearly indicates the need for high refractoriness.

CONTROLLED PACKING

The powder bed packing fraction of Three-Dimensional Printing ceramic process must be well controlled. Under most circumstances, the highest possible powder packing fraction is sought to maximize dimensional control. Powder must exhibit good compaction while being spread and packed by a vibrated roller. Under no circumstance should previous layers be disturbed or deformed during the deposition and packing of the top layer. Packing will be elaborately discussed in the Section 1.6.

Packing controls permeability which is the ability of the mold to allow gases generated during pouring to escape through the mold surface. Low permeability traps gases and prevent molten metal from filling the mold cavity. On the other hand, if the permeability is too great, metal may penetrate the mold and cause burn-in defect.

FINE SURFACE FINISH

There are several key factors effecting the surface finish such as the accuracy of binder droplet placement, ballistic effect from the impact, and powder/binder interaction, etc.

There are two major sources of surface roughness concerning powder. One is the stratification or stair step effect from layering. Stratification can be reduced with thinner layers. Next is the distance between peaks and crevices of the particles. To minimized the surface roughness due to both factors requires fine particle size.

But, there are many trade off using fine particles. First, fine particles have more contact points per a unit volume. Therefore, the intergranular friction is higher than coarse grains. Any shear force applied on the powder bed (such as during spreading) will be transferred down and probably disturb layers beneath. Second, fine particles sinter at a lower temperature and limit the heat treatment temperature ceiling of the binder. Third, fine particles less than 10 μm present a health hazard. Fourth, fine particles may not pack to a higher densities due to excess intergranular friction. Fifth, powder/binder interaction including the ballistic effect is an extremely complex phenomena. Finer particles do not always guarantee a better surface finish.

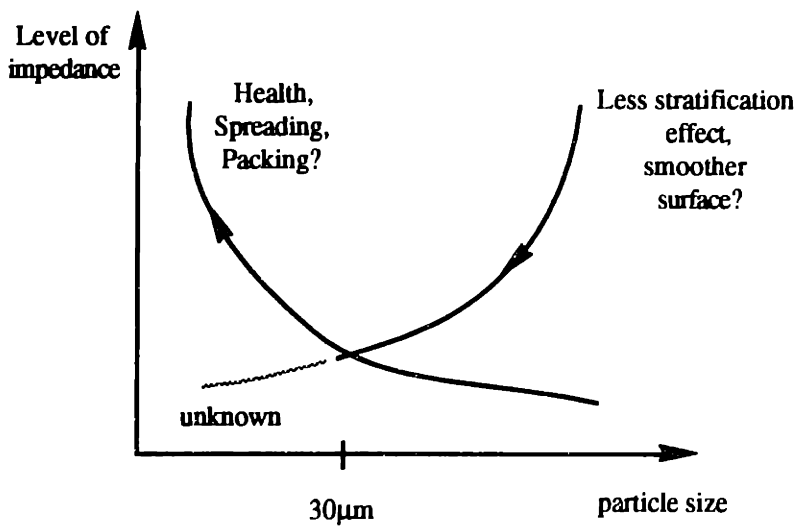

Figure 2.2 Motive and Impedance Concerning Particle Size in Three-Dimensional Printing

Figure 2.2 illustrates constraints and relevant issues concerning particle sizes. Three-Dimensional Printing has good experience with powder in a range of 30 ± 10 μm. This is proven a good operating point, but may not be an optimum.

DIMENSIONAL ACCURACY

Particle arrangement must remain constant throughout the process in order to preserve the tolerance and accuracy of printed parts. Powder shall not disintegrate, or sinter upon heat treatment of the binder.

LEACHABILITY AND CORE REMOVAL

Casted shells will be knocked out to recover the casting. Some shell materials may spall off during cooling, but a good portion still remain with the casting and will have to be knocked out by impact tools. Whatever remaining must be washed out by hot caustic such as molten sodium or potassium hydroxide in air or at high pressure. Selected powder materials shall facilitate binder leaching to assist core removal and knock out process

COST, AVAILABILITY, AND ENVIRONMENTAL CONSIDERATIONS

Slurry and stucco particles in investment casting are not reclaimable or recyclable. Therefore, they must be widely available with short lead time and at low cost. Equally important, used or processed particles must not present an environmental hazard.

2.2 ALUMINA AS SELECTED POWDER

It is very difficult to find a low cost powder which is commercially available and satisfies all the functional requirement in Section 2.1.2. In fact, each functional requirement will have to be prioritized.

There must be no compromise to the requirement of high refractoriness of the powder. If not, the shells will fall apart during reheating and pouring. The next requirement is castability which includes surface compatibility with the metals, level of reactivity with the metal, and permeability. Third is the leachability requirement. If the castings are not recoverable, then there is no point to pursue on them. The rest of the functional requirement are spreading and packing, dimensional accuracy, surface finish, and cost/ availability. Note that these three top priorities involve mainly with the physical and chemical properties of selected materials. All other functional requirement are adjustable process parameters. Hopefully, by fine tuning these parameters, Three-Dimensional Printing will find a local optimum to which shells can be made.

In investment casting, alumina is usually used as preferred refractory powder for slurry and stucco of directional and single crystal solidification. In other words, alumina is compatible with the casting techniques. Alumina is proven satisfactory with the top prorate of the functional requirement such as low coefficient of thermal expansion for good dimensional control, castability, and lastly leachability. Alumina[2] is cheap and commercially available. For the good reasons listed above, alumina is an appropriate choice of material for Three-Dimensional Printing ceramic powder. Properties of alumina are shown in Table 2.2.

---

[2] Alumina is found in abundant all over the world making it highly available at low cost. In addition to its high refractoriness, alumina is a good electrical insulator with very high resistivity and dielectric strength. As a result, alumina is normally used as substrates for integrated circuits and high voltage-high temperature equipment such as spark plugs. Alumina is also among one of the hardest materials available. Its strength per weight is just slightly less from diamond. Therefore it is also found as an excellent abrasive material for grinding wheels and cutting tools.

Properties	Value
Density [g/cc]	3.90-3.99
Bending strength [MPa]	350-450 (Room temp) 150 (1000°C)
Thermal Conductivity [W/m•K]	20
Thermal expansion coeff [$x10^{-6}$/K]	8-9
Hardness [Hv]	1500
Rockwell Hardness[15N scale]	95.5
Elastic modulus [MPa]	320-370
Fracture toughness [$MPa•m^{1/2}$]	2-3
Resistivity [Ω • cm]	$>10^{14}$
Dielectric strength [kV/mm]	23.6

Table 2.2 Properties of Alumina

2.3 PREPARATION OF ALUMINA POWDER

The principle source for high alumina ceramics is bauxite which is available in almost unlimited amount throughout the world. Bauxite extraction is performed in wet alkaline process called Bayer process. The process produces different grades of alumina hydrates depending on amount of the deposited minerals. The compounds are dehydrated by thermal treatment to about 1000°C. After passing through a number of phase transitions, the compound ends in α-alumina which is the starting material for all fabrication processes of high alumina ceramic. The Bayer process also introduces relative high amount of Na_2O which may need to be extracted if higher purity alumina is needed [3].

Alumina powder are commercially available in various grades, sizes, and shapes. A typical way of making fine alumina powder is to melt α-alumina in an electric arc furnace with graphite electrodes followed by an extensive grinding processes. Purity may be maintained by using grinding balls made out of alumina. However, coarser alumina particles may be crushed using metal grinding balls which are more effective than alumina due to higher specific gravity. In this case, subsequent purification with suitable acid is needed to take out the metal debris. Despite that fact that grinding is time-consumed, it is an effective method to achieve homogeneous powder size distribution. The shape of alumina powder made with grinding processes is highly irregular with sharp corners.

Particles normally have high aspect ratio such as lamella or tabular suitable for abrasive materials. Figure 2.3 illustrates irregularity of tabular alumina powder from Alcoa.

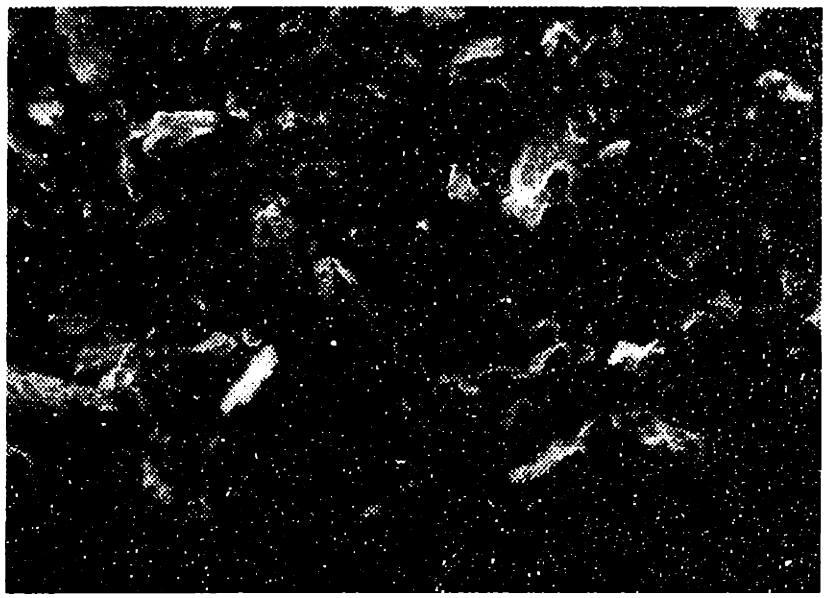

Figure 2.3 Tabular Alumina Powder (T-64 48-200)

Instead of breaking down by grinding, alumina powder may be manufactured with an evaporation-condensation process. This requires high temperature and rapid cooling. In order to achieve the high temperature required, high intensity arcs (plasma spray) with graphite electrodes under controlled atmospheres are used. The temperatures may reach 7,000-10,000 Kelvin as alumina vaporizes at the tail of the plasma arc flame from the anode. Once leaving the flame, the vapor cools down rapidly and condenses. In the liquid state, surface tension turns molten alumina into spheres. As the temperature of the molten alumina drops down, they solidify into solid balls. Spherical alumina powder is generally manufactured this way. However, the energy and process cost of plasma process is much higher than grinding. Therefore, spherical alumina powder generally costs about 2 orders of magnitude than that of the grinding process. Figure 2.4 shows a micrograph of CB-A30S spherical alumina (aluminabeads) made by Showa denko.

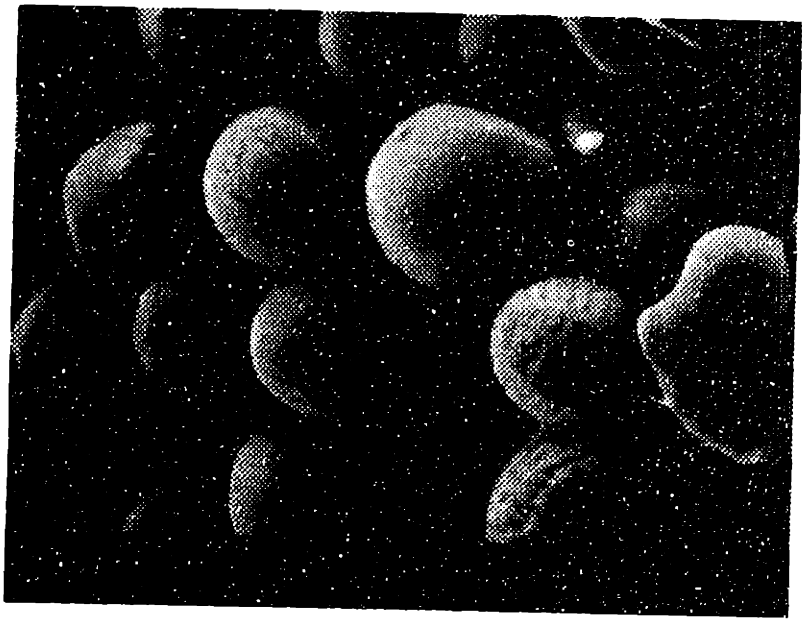

Figure 2.4 Showa Denko's CB-A30S Spherical Alumina Powder

Powder may also be fabricated chemically by particle growth process in a suspension. Nuclei may be originated homogeneously with supersaturation or heterogeneously with foreign particles and catalyst. As nuclei exceed the critical size they will continue to grow at a rate which could be controlled by the supplied rate of fresh material. Growth particles can be nearly spherical with few round corners or crystalline.

2.4 CURRENT ALUMINA POWDER IN THREE-DIMENSIONAL PRINTING

The requirement for smooth surface forces Three-Dimensional Printing to utilize fine alumina particle powder. The need is however balanced by the fact that small particles are difficult to manipulate by the rollers in spreading and packing process. Three-Dimensional Printing has found a workable alumina particle size of around 30 ± 10 μm which gives good surface finish. Beyond this range, the surface is either too rough or the powder can not be spread and packed successfully. Powders in Three-Dimensional Printing are selected according to several findings and researches. In 1992, Alan Lauder

studied the microstructure and particle arrangement of four types of alumina powder[3] [4]. During the same year, Sang-Joon (John) Lee indicated some key factors that govern packing density and layer accuracy of selected alumina powder [5].

Current Three-Dimensional Printing alumina powders are:

• Norton[4] 7920

Norton 7920 is the standard alumina powder for Three-Dimensional Printing of ceramics. It is 99.7 percent purity consisting of lamella or hexagonal platelets. Jim Breadt has described the powder as "tiny bathroom tiles" in his Ph.D. thesis [6]. The length and the width of Norton 7920 is approximately 28-30 μm while the thickness is about 1/5 of the former dimension, Figure 2.5.

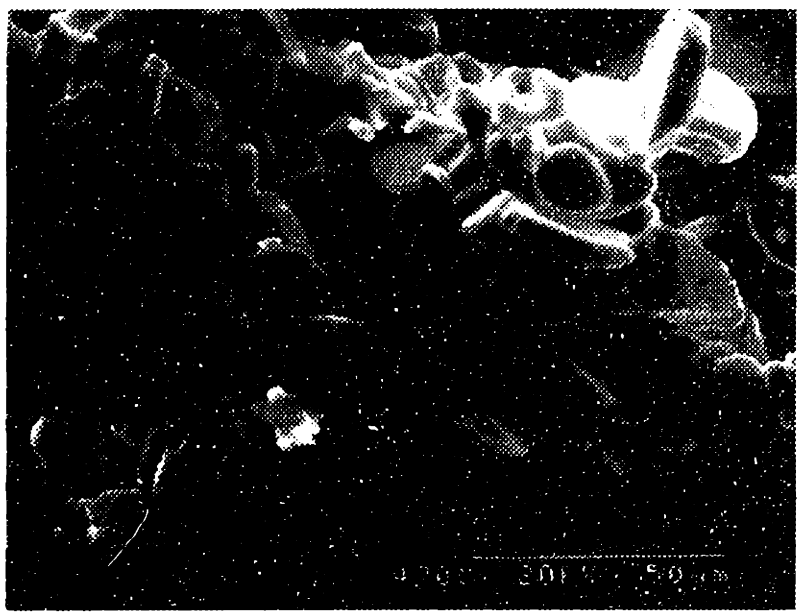

Figure 2.5 SEM Micrograph of Norton 7920

The particle size distribution of Norton 7920 ranges from 10 to 50 μm with the mean around mid 20's μm. Figure 2.6 shows size distribution of Norton 7920 batch 013-94 which has been used in the Three-Dimensional Printing process after January 1994.

---

[3] Norton 38 alumdum flour, Norton 30μm electronic grade, Showa denko's CB-10S aluminabeads, and a Spray dried alumina powder made in house at MIT

[4] Norton Industrial Ceramics, Worcester, MA

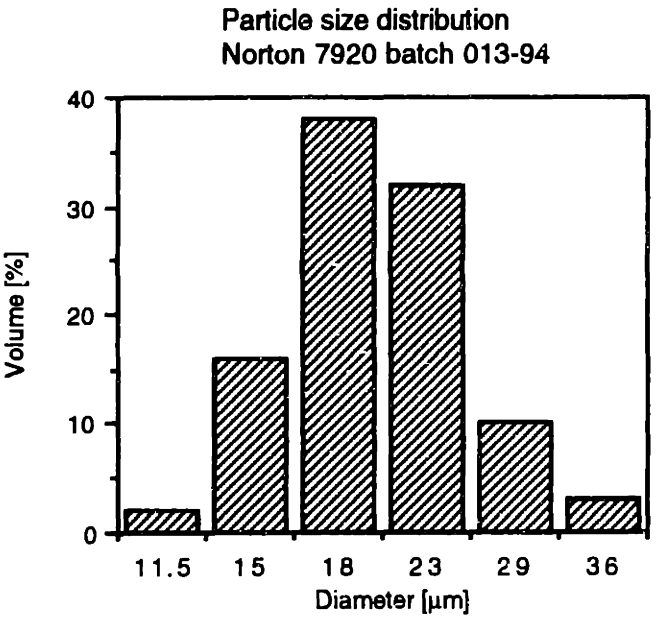

Figure 2.6 Particle Size Distribution of Norton 7920 Batch 013-94
(used in Three-Dimensional Printing process after Jan 1994)

• Norton 7921

Norton 7921 is nearly identical to Norton 7920. The different being the former is mixed with some amount of sodium silicate added to enhance flowability. Since sodium

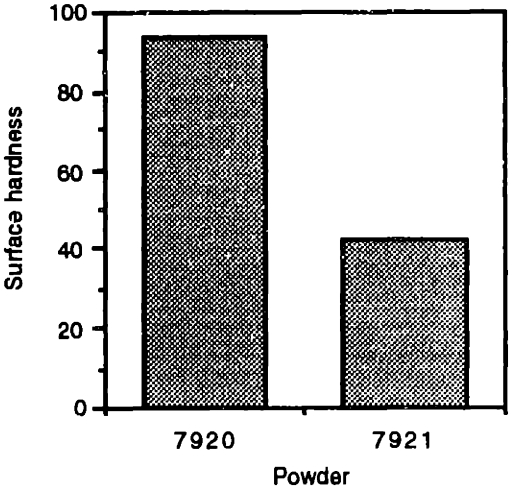

Figure 2.7 Loose powder strength of Norton 7920 vs 7921.
Hardness is quantified by the diameter of radical unit
(1 radical unit is 25 microns) of 90° stainless steel cone at 1 gm force

silicate melts during the heat treatment process, it is responsible for difficulties in powder removal from internal cavities, Figure 2.7. A special procedure was added in house at MIT where Norton 7921 powder was rinsed with deionized water to decant off the soluble surface coating and additives.

• Showa Denko CB-A30S (aluminabeads)

Showa Denko manufactures CB-A30S powder with plasma spray process. The powder consists of spherical balls at 30 μm in average with a narrow size distribution. Aluminabeads have very good fluidity and filling properties owing to less interparticle friction. As a consequence, it always packs to a higher density than Norton 7920 or 7921. CB-A30S is a very expensive powder with a price tag of $120/kg compare to about $4/lb of Norton 7920. As a result, Three-Dimensional Printing does not utilize the spherical powder for production, but solely for research purposes.

Table 2.3 shows properties of CB-A30S spherical powder.

Properties	Value
Average diameter [μm]	29±3
Impurities [wt %] SiO_2 Fe_2O_3 T-Na_2O	 0.01 0.05 0.04
Electrical Conductivity [μs/cm @25°C]	5.0
Na^+ [ppm]	1.5
Cl^- [ppm]	0.5
pH [±0.5]	8.5
Bulk Density [±0.1g/cc]	2.1

Table 2.3 Properties of Showa Denko CB-A30S spherical powder

A micrograph of the spherical alumina is shown in Figure 2.8

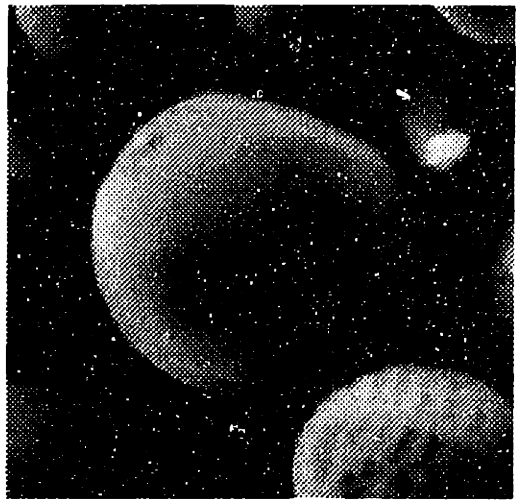

Figure 2.8. Micrograph of Showa Denko CB-A30S Spherical Powder

• Sumitomo Equi-ax 18 μm powder

Sumitomo Equi-ax powder is manufactured with a particle growth process. The powder is almost spherical with some rounded off corners as shown in Figure 2.9. Three-Dimensional Printing has not used this powder intensively since the manufacturer has not yet put the powder into full production. This powder has equivalent flowlability of Showa Denko's spherical powder so it can be packed to the same density.

Figure 2.9. Micrograph of 18 μm Sumitomo Equi-Ax Powder (Lot no TN4352)

2.5 PACKING OF POWDER

2.5.1. Phase Relation

Liquid filled powder can be either two-phase or three phase composition depending on level of liquid saturation. Completely dry powder has two phases namely solid powder and pore air. A fully saturated powder also has two phases of solid and liquid which totally occupies the pore volume. A partially filled powder, or unsaturated, has three phases: solid, liquid, and air which are shown in Figure 2.10.

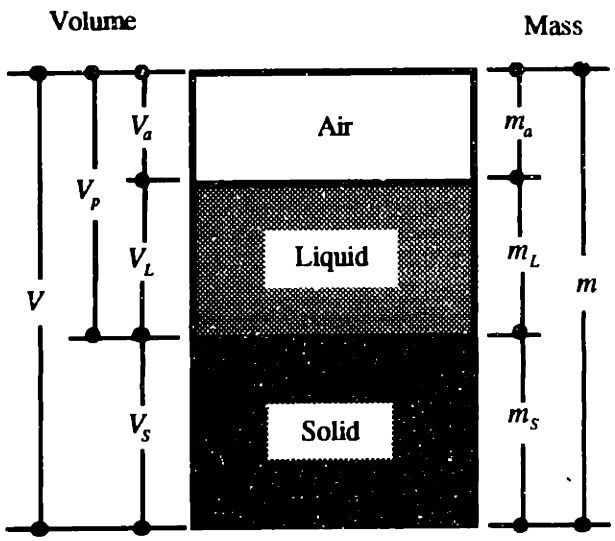

Figure 2.10. Phase Diagram of Liquid-Air Filled Powder

There are two common ways to describe phase composition of powder: one is by volume and the other is by mass basis. Volume and mass composition are normally related by densities or specific volumes and are always referred to interchangeably. Following are useful definitions and relationships of phase composition:

MOISTURE CONTENT, w, is the ratio of mass of liquid to the mass of solid in the powder

$$w = \frac{m_L}{m_S} \tag{2.2}$$

Moisture content is determined by weighing a powder sample and then drying the sample in an oven at 105°C to 110°C and reweighing. Drying is continued until the differences between successive weighing at four-hourly interval is no greater than 0.1 percent of the original mass of the sample.

SATURATION, S, is the ratio between the volume of liquid to the volume of pore. Pore volume is always equal to the sum of air and liquid volume combined. Saturation ranges from zero for completely dry soil to one for fully saturated (or supersaturated) powder.

$$S = \frac{V_L}{V_p} = \frac{V_L}{V_L + V_a} \tag{2.3}$$

SOLID DENSITY, ρ_{solid}, is defined as the ratio of the mass of the solid phase assuming that it has *no internal void* to the solid phase volume.

$$\rho_{solid} = \frac{m_S}{V_S} \tag{2.4}$$

In some cases, the solid phase contains internal or air-locked pockets. In this case, the assumption for solid density fails and the density is called PARTICLE DENSITY [7].

PARTICLE DENSITY, ρ_{par}, applies only to particles with closed pores. The density is defined as the ratio of the mass of the solid phase to the volume for particle includes the closed pores, but not intergranular ones. Figure 2.11 illustrates several types of inter and intra particle volume.

$$\rho_{par} = \frac{m_S}{V_S + V_{\text{closed pores}}} \tag{2.5}$$

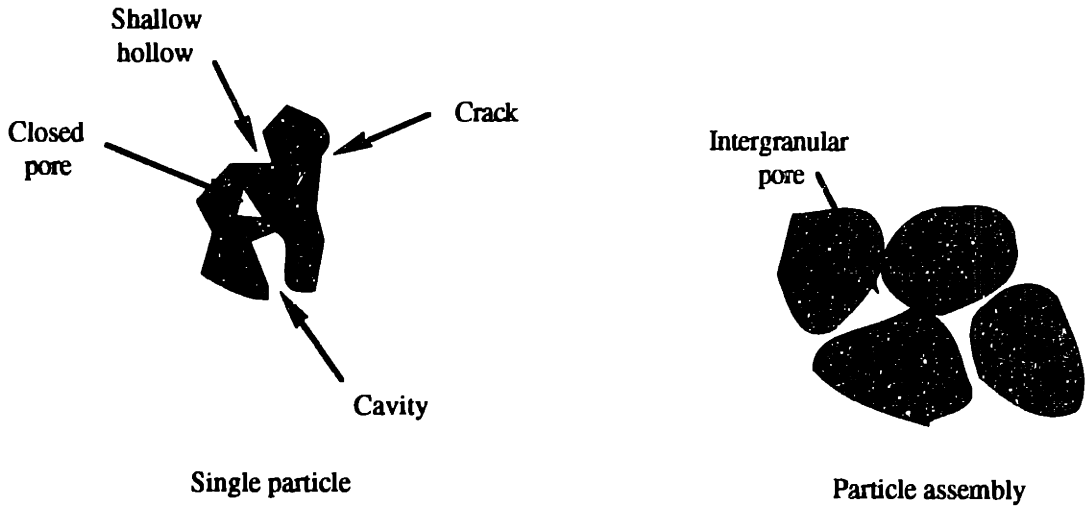

Figure 2.11 Intra and Inter Particle Volume

BULK DENSITY, ρ_{bulk}, is the ratio of the total mass to the total volume

$$\rho_{bulk} = \frac{m}{V} = \frac{m_S + m_L + m_a}{V} \approx \frac{m_S + m_L}{V} \tag{2.6}$$

if the powder has liquid in the pores, then the total mass of the powder includes the liquid mass. If the powder is dry, then only the mass of solid phase will be taken into account. It is assumed that air mass is negligible for most applications.

In general, bulk density of multiphase can be derived by densities and volume fraction of the mixtures. For example, with regard to powder, if ρ_L is the density of liquid phase and ρ_a is the density of air, the bulk density of powder is:

$$\rho_{bulk} = \frac{m_S + m_L + m_a}{V}$$

$$\rho_{bulk} = \frac{\rho_{solid} V_S + \rho_L V_L + \rho_a V_a}{V}$$

$$\rho_{bulk} = \left(\frac{V_S}{V}\right)\rho_{solid} + \left(\frac{V_L}{V}\right)\rho_L + \left(\frac{V_a}{V}\right)\rho_a \tag{2.7}$$

generalized bulk density for n mixtures is $\rho_{bulk} = \sum_{i=1}^{n} (\text{volume fraction}_i)(\rho_i)$

SPECIFIC VOLUME, v_{sp}, is the ratio of the total volume to the total mass. In other words, it is the inverse of bulk density.

$$v_{sp} = \frac{V}{m} = \frac{1}{\rho_{bulk}} \tag{2.8}$$

Specific volume is very useful to compare the volume change or shrinkage of materials at various stages since it is normalized on a unit mass.

PORE FRACTION or **POROSITY**, ε, is the ratio between the volume of voids to the total volume of the powder (only applicable to dry powder).

$$\varepsilon = \frac{V_p}{V} = \frac{V - V_S}{V} \tag{2.9}$$

In the case of dry powder, pore fraction can also be defined from bulk and solid densities:

$$\varepsilon = \frac{V_p}{V} = \frac{V - V_S}{V} = 1 - \frac{V_S}{V} = 1 - \frac{\rho_{solid} V_S}{\rho_{solid} V} = 1 - \frac{\rho_{bulk}}{\rho_{solid}} \tag{2.10}$$

PACKING FRACTION or **SOLID FRACTION**, ϕ, is the ratio of the solid volume to the total volume of the powder, or bulk density to solid density (only applicable to dry powder).

$$\phi = \frac{V_s}{V} = \frac{\rho}{\rho_{solid}} \tag{2.11}$$

Packing fraction relates to pore fraction as follow:

$$\phi = \frac{V_s}{V} = \frac{V - V_p}{V} = 1 - \varepsilon$$

or

$$\varepsilon = 1 - \phi \tag{2.12}$$

Packing fraction, ϕ, is normalized. When $\phi = 0$, there is no powder in the powder bed and when $\phi = 1$, then there is no pore in the powder bed.

2.5.2 Tap Packing Fraction

Tap density is the bulk density of a powder after being compacted by its own weight from being repeatedly dropped from a standard height. The density may be normalized with the solid density to obtain tap packing fraction. According to ASTM standard B 527-85, the stroke height must be 3.2 mm with a minimum of 3000 drops at the frequency of 250 cycles per minute. The compacting method allows particles to densify by rearrangement and restacking. Therefore, tap density is relatively high and is always being referred to as a limit for indirect compression methods.

A 50 grams of powder is poured into the graduated glass at a time. The motor, with a cam attached to the shaft, lifts and drops the gradual glass at a speed of 250 rpm. It takes about 12 minutes to complete the compaction. Figure 2.12 illustrates a schematic of the machine used in Three-Dimensional Printing lab to collect tap packing fraction.

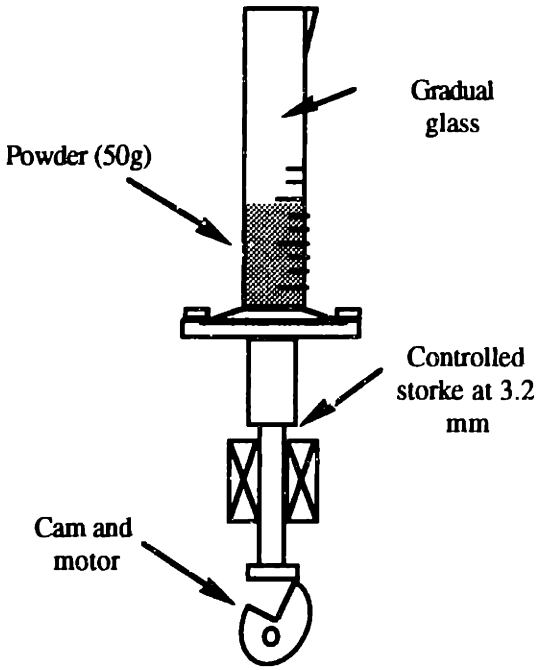

Figure 2.12 Tap Machine

Tap packing fraction of powder in Three-Dimensional Printing are shown in Table 2.4 and Figure 2.13. Fresh Norton 7920 powder can be packed to 51.7 percent packing fraction. Although this fresh powder loses some of its fines in the rinse process to take out soluble surfactants, it does not alter the tap density. However, there is a clear degradation in tap packing fraction as the powder is recycled in Three-Dimensional Printing process. Norton 7920 may lose about 10 percent of packing fraction if recycled for several times. An explanation to packing degradation is that powder collects moisture from the environment and during printing. The moisture forms liquid bridges in the powder thus making it cohesive. As a consequence, powder mobility is drastically reduced and the powder loses its packability.

Run no.	Powder	Tap packing fraction ϕ [%]	Condition
1	7920 fresh	51.7	28μm fresh from manufacturer
2	7920 recycled	40.2	30μm no citric acid
3	7920 recycled + acid	39.6	30μm 0.3 wt % citric acid
4	7921 fresh	55.0	22μm fresh from manufacturer
5	7921 fresh + moisture	47.8	22μm fresh + 1 wt % moisture
6	CB-A30S spherical	61.8	30μm fresh
7	Equi-ax powder 18μm	60.3	18μm fresh

Table 2.4 Tap Packing Fraction of Three-Dimensional Printing Powder

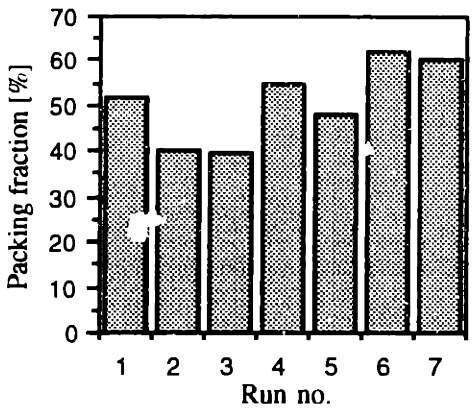

Figure 2.13 Plot of Tap Packing Fraction of Data in Table 2.4

Powdered citric acid mixed into the powder is very hydroscopic, thus, facilitating powder absorption of moisture from the air and the process. Figure 2.14 illustrates flow of powder in Three-Dimensional Printing process and how moisture accumulates and partially leaves the system.

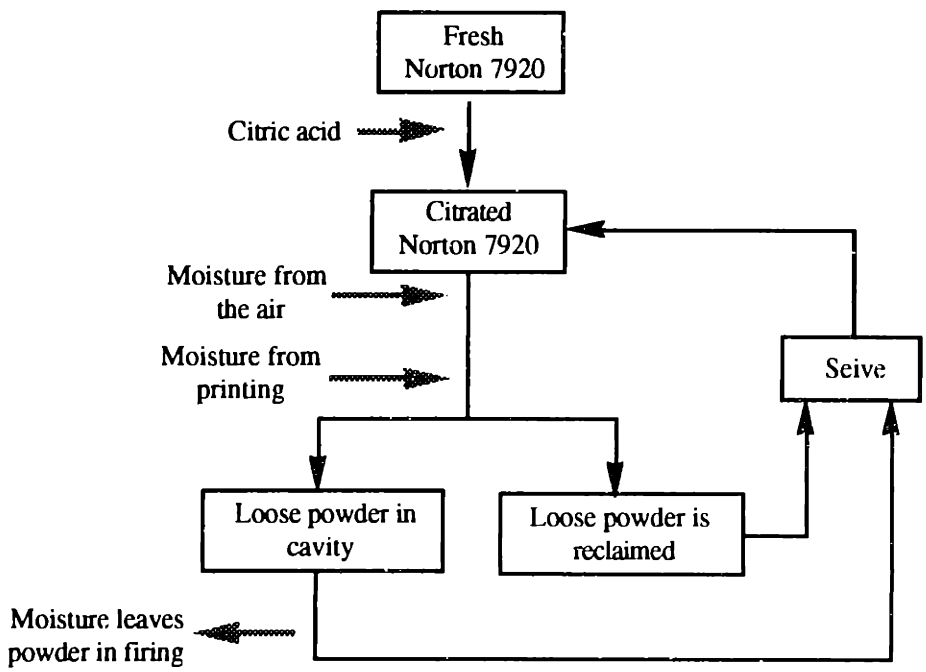

Figure 2.14 Flow of Moisture in and out of Powder

Norton 7921 usually packs to 55 percent which is slightly higher than Norton 7920 because of sodium silicate surfactant. However, it loses 10 percent of tap packing fraction immediately if mixed with only 1 weight percent of moisture. This is a strong evidence to support the hypothesis that moisture presence in the powder greatly degrades packing density.

CB-A30S spherical powder has significant higher flowability than lamella powder (7920 and 7921) to due its sphericity. Its packing fraction are always in high 50's to low 60's percent. For the same reason, Showa denko's equi-ax powder behaves similarly to the spherical powder in terms of packability.

It is observed that particles with high aspect ratio (such as Norton 7920 and 7921) have a wide packing variation than those of low aspect ratio (such as spherical powder) even if the same set of powder is reused in the test. This may be due to the fact that there are three extra rotational degrees of freedom and a set of shape factor to specify the arrangement of high aspect ratio particles These extra freedoms, if not well controlled, contribute to wider packing variation.

2.5.3 Spread Packing Fraction

Spread packing fraction is the packing fraction generated by the roller on the Three-Dimensional Printing machine. Standard spreading and packing is shown in Figure 2.15. First the piston drops down for 9 mils and then new powder is piled on one side. The roller counter rotates as it advances and spreads the powder on top of the previous layer. During this step, the roller is vibrated with an electro-magnetic actuator to pack the new layer. The magnitude and frequency of the vibration are about 30 μm and 800 Hz respectively. These process parameters are optimized from our experience. At the end of the roller's transverse, the piston moves up 2 mils. Then, the roller reverses its direction and rotation and counter rolls on 2 mil-thick powder layer, once again with vibration.

Since spread packing does not allow for powder particles to fully rearrange and restack due to a much shorter agitation period of the roller over the powder the packing fraction is less than that obtained from tap method.

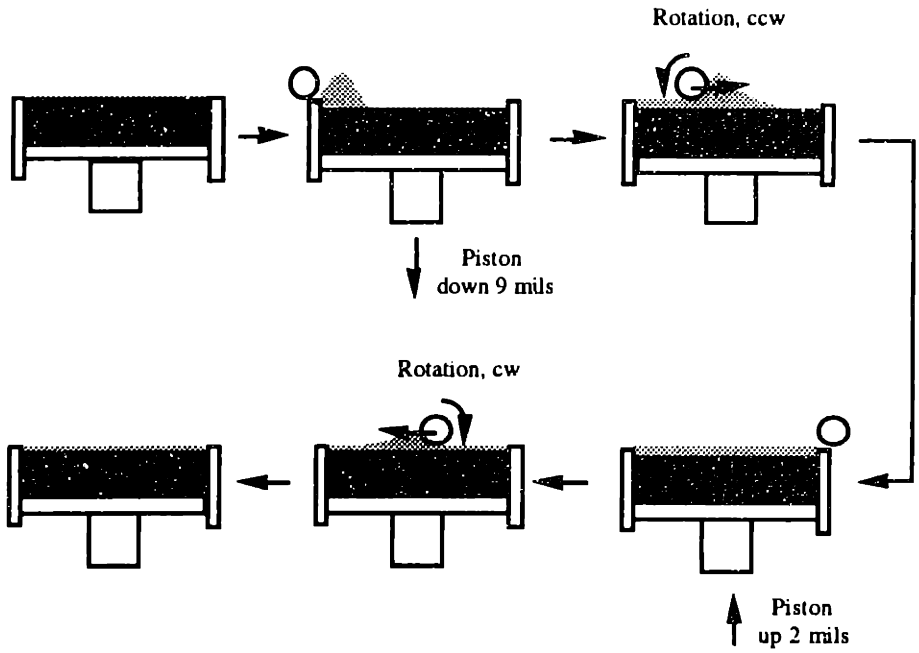

Figure 2.15 Spreading and Packing by Roller on Three-Dimensional Printing Machine

In spread packing fraction study, 50 layers of powder were spreaded and packed, layer by layer. After the machine finishes the last layer, powder is scooped out and weighted. Knowing the volume of the powder from the width and length of the piston and the thickness by the number of layers, spreading packing fraction is calculated from the ratio of its weight to the volume and normalized with the solid density.

Spreading packing fraction of fresh Norton 7920 is about 44 percent. It is lower than tapping packing density due the fact that powder doesn't have an opportunity to rearrange and restack as with tapping. After the powder is used and reprocessed, it picks up moisture from the process and the environment. Once again, recycled powder exhibits lower spread packing fraction. It does not take much moisture to lower the packing fraction as shown in Run no. 4 in Table 2.5. Here, powder were misted with a humidifier on the surface prior to spreading. It was found that only 0.25 weight percent of moisture could result in 5 percent drop in packing fraction. The mist from the ultrasound humidifier is not vapor but clouds of small tiny droplets of water. When each of these tiny droplets touches the powder particles, a portion is absorbed into intergranular pores while the rest remain as minute dew drops on the surface. Once the new layer is laid down, the moisture absorbs the 'free' moisture and forms liquid bridges. Collected moisture makes powder

Run no.	Powder	Spread packing fraction ϕ [%]	Condition
1	7920 fresh	44.0	Fresh from manufacturer
2	7920 recycled 1mo.	40.4	Recycled for 1 month
3	7920 recycled 3mo.	36.9	Recycled for 3 months
4	7920 recycled 3mo. misted while spreading	31.9	Recycled for 3 months total mist is 0.25 wt %
5	7920 recycled 3mo. print water every layer	35.2	Recycled for 3 months total water 6 wt %
6	7921 fresh	45.3	Fresh from manufacturer
7	CB-A30S spherical	56.9	Fresh from manufacturer

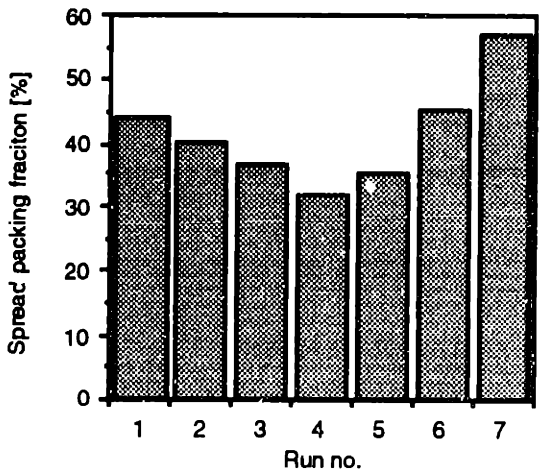

Table 2.5 and Figure 2.16 Spread Packing Fraction

cohesive and prevents the particles to move freely in the wet region near the layer interfaces causing a substantial drop in packing fraction. Figure 2.17 illustrates how the cohesion force prohibits packing.

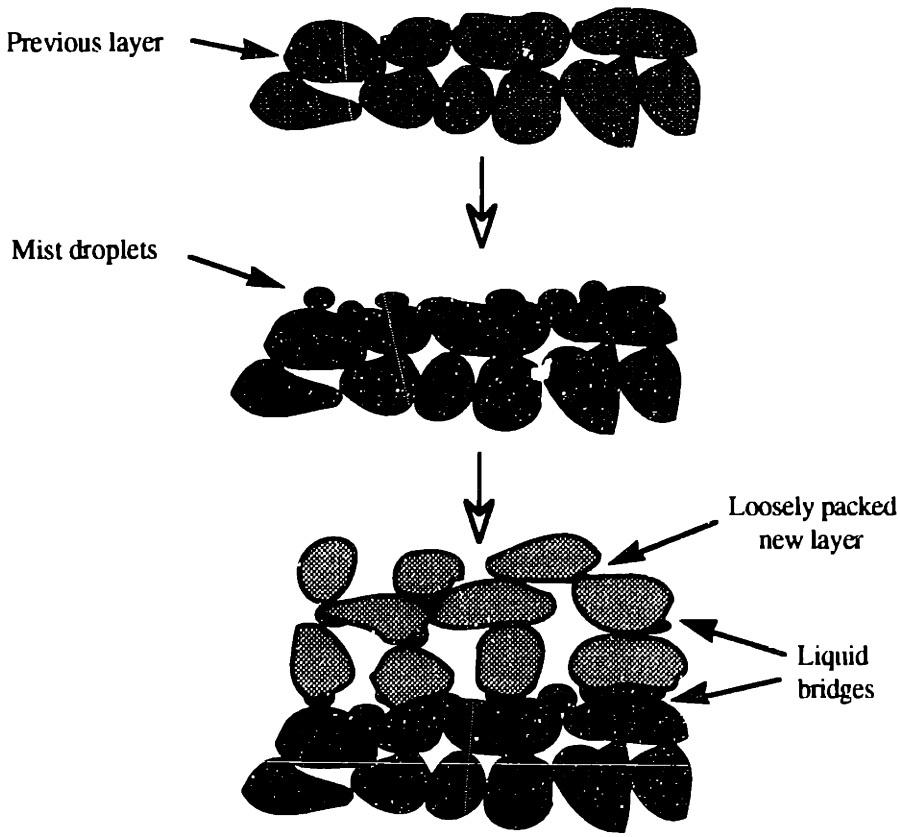

Figure 2.17 Liquid Bridge Makes Powder Cohesive and Prevents Packing

However, it is more forgivable for the moisture seeping out from the previous layer. Run no 5 in Table 2.5 was conducted by printing water onto almost the entire powder bed (4"x11") on every layer without ultrasound misting to simulate the moisture interlayer seeping. Printing saturation was 80 percent of the pore volume and the moisture content in the powder bed at the end of printing was 6 weight percent of the powder. However, it was found that powder packing was slightly lowered from dry spreading and was not as severe as the misted case. This indicates that liquid seeping across the layer interface is very limited.

Misting is often used in Three-Dimensional Printing process to lock up the powder surface from being ejected by the ballistic impact. Therefore, a new locking alternative that does not degrade powder packing may have to be identified to replace misting.

The spread packing fraction of Norton 7921 powder is slightly higher than that of 7920 powder because of sodium silicate surfactant. For CB-A30S spherical powder, the spreading packing fraction is much higher than Norton 7920 because of its higher flowablity due to less intergranular friction.

2.5.4 Packing of Mixed Powders

This experiment was conducted to find out the packing profile of mixtures of Norton 7920 and CB-A30S spherical powder. The mass ratio of both powders were varied from 0 to 100 percent by an increment of 20 percent. The mixtures were tap densified according the process in Section 2.5.2. Profile of the packing fraction can be shown in Figure 2.18.

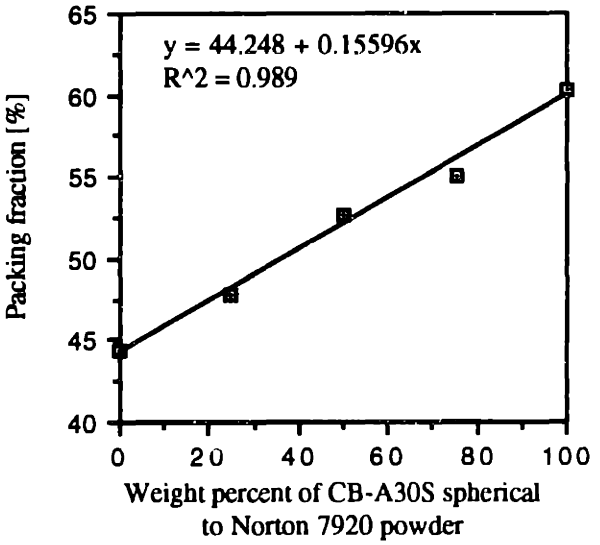

Figure 2.18 Tap Packing Fraction of Mixtures of Spherical to Norton 7920 Powder

The packing fraction of mixed powders was found to vary linearly with the mass ratio of spherical powder. This may be an alternative to increase packing fraction of Norton 7920.

2.6 CHAPTER SUMMARY

Alumina was selected as the powder for Three-Dimensional Printing of ceramics mainly because of its high refractoriness, low surface reactivity, and low coefficient of thermal expansion. Alumina has been long proven a practical refractory for high temperature investment casting of nickel-base alloys as well as directional and single crystal solidification applications.

Norton 7920 electronic grade lamella alumina powder was chosen as a standard powder for Three-Dimensional Printing according to cost and availability. Three-Dimensional Printing machine can spread and pack this powder to about 40 percent packing fraction. Though this packing fraction is not as high as other powder such as spherical or equi-ax. It serves the casting proposes for Three-Dimensional Printing. Packing fraction can still be improved with new powder and compacting methods.

Tap packing produces higher packing densities than spreading because powder is allowed to rearrange and restack at a greater extend. Spread packing compacts powder by mean of shear and vibration against its interparticle friction with only limited amount of densification exposure under the roller. It was found that powder with high aspect ratio has wider packing variation than that of lower aspect ratio which is probably because of the effect of three extra rotational degree of freedom and shape factor that specify the particles in assembly.

Norton 7920 exhibits strong packing degradation as a function of time. It is found that the packing fraction is very sensitive to intergranular cohesion caused by absorbed moisture. Moisture is collected as powder is recycled from various process points and can lower packing fraction as much as 10 percent with only a small amount. Misting is the primary cause of packing degradation while seeping moisture from the previous layer is the secondary.

Bibliography

[1] Horton R. A., *Investment Casting*, Metals Handbook, ASM International, Vol.15, p.253-269, 1988

[2] Cravalho E, Smith, Jr., J., *Engineering Thermodynamics*, Massachusetts Institute of Technology, 1981

[3] E. Dörre, H. Hübner, *Alumina: Proceesing*, Properties, and Application, Springer-Verlag, New York, 1984

[4] Lauder A , *Microstructure and Particle arrangement in Three Dimensional Printing*, Master thesis, Department of Materials Science and Engineering, Supervised by M. J. Cima, 1992

[5] Lee S., *Powder Layer Generation for Three Dimension Printing*, MIT Master Thesis, Dept. of Mechanical Engineering, Supervised by E. M. Sachs, 1992

[6] Bredt J., *Binder Stability and Powder\Binder Interaction in Three Dimensional Printing*, MIT PhD Thesis, Dept. of Mechanical Engineering, Supervised by E. M. Sachs, 1995

[7] Miwa S., *J. Soc. Powder Technology*, Japan, 1969, 6:115

Chapter 3.

Binders in Three-Dimensional Printing of Ceramics

3.0 INTRODUCTION

Powder can not be formed into Three-Dimensional Printing parts unless being joined by a binder. Binders in Three-Dimensional Printing are deposited into the powder bed by means of ink-jet printing. Upon impact, they penetrate into the powder bed and are absorbed in the pore volume by capillary suction. For Three-Dimensional Printing of ceramics, binders later undergo polymerization known as gellation. Gellation turns liquid binder into networks of solid phase which provide green strength for printed parts. The parts are then transported to furnaces to cure and strengthen the binder by heat treatment where water and other organic additives evaporate or burn out during the initial phase of heating.

Not only do binders provide strength to the solid freeform, but they also play critical roles in mechanical, thermal, and chemical properties of the shells. For example, shells can not withstand immense heat of directional or single crystal solidification without refractory binders. Binders have absolute control of shells integrity and strength. Destroying these bonds resulting in cracks, delamination, and disintegration.

This chapter is aimed to provide a brief background on current binders in Three-Dimensional Printing of ceramics. Much detail on binder was investigated by James Bredt [1] and his thesis on binder stability and powder-binder interaction. Jim has done a wonderful job developing binders from a commercial colloidal silica by adding several organic additives. His work yields a stable binder that rapidly gels at low pH.

Binders in investment casting is discussed in the first section following by their functional requirements in Three-Dimensional Printing of ceramics. Properties and the development of Binder B from Nyacol 9950 are discussed in the next few sections.

3.1 BINDING MATERIALS IN INVESTMENT CASTING

3.1.i Binders

Common binders in investment casting include silica compounds such as colloidal silica, hydrolyzed ethyl silica, and sodium silicate. Colloidal silica is the most widely used binder in investment casting [2]. Silica provides excellent thermal stability with a melting point of approximately 1,700°C with outstanding bonding properties. Colloidal silica are made with spherical silica particles in water. The particles are dispersed and stabilized from being polymerized by ionic charges with alkaline ions such as sodium or ammonia. The ionic stabilizer can be suppressed by adding ionic salts that neutralize the surface charges of silica particles, by concentrating the binder such as drying or freezing, or by adding coagulants that bridge and knit silica particles into a **network**. Destabilized colloidal silica **polymerizes** or **gels** and turns from liquid to solid to provide green strength for printed parts.

Next on popularity is Ethyl silicate which is a product of silicon tetrachloride and ethyl alcohol known as Tetraethylorthosilicate (TEOS) [3]. TEOS by itself is not reactive binder unless being hydrolyzed with water. The hydrolysis reaction is carried out with ethyl alcohol and water and perhaps with some acid catalyst such as hydrochloric acid. Hydrolyzed TEOS produces silicic acids which are capable of being polymerized into gels. Gelation can be initiated by concentration or by chemicals such as alkali salts, ammonia, or high positive charge ion. The gels made with ethyl silicate are, in many ways, similar to colloidal silica but differ in details such as strength and rate of reaction. Ethyl silicate can also be gelled with ammonia or sulfur dioxide atmospheres. Being an alcohol base binder, ethyl silicate dries much faster than colloidal silica shortening the cycle time and allowing subsequent dips to be applied more quickly.

Hybrid binders of colloidal silica and ethyl silicate have been developed to combine the advantages of both materials. Water required for hydrolysis reaction of ethyl silicate is supplied by colloidal silica. Having two resources of silica strengthens the cohesive bonds [4].

Liquid sodium silicate may be used as an inexpensive binder. This binder gels upon evaporation. However, the presence of sodium lower refractoriness by reducing the melting temperature which greatly limits its application. In addition, sodium silicate is vulnerable to steam atmosphere of dewaxing autoclaves.

Higher refractoriness could be obtained by colloidal alumina or colloidal zirconia binders. These binders were developed as a response for the need of high temperature casting of superalloys and directional solidification. However, both have a low degree of leachability and will be difficult to remove from the castings if made into cores.

3.1.2 Slurries

Slurries are made by mixing fine refractory powder with a binder. Typical slurry mixtures are shown by weight composition in Table 3.1.

Ingredient	Composition, wt. %
1. Solid phase in binders	5-10
2. Liquid phase in binders	15-30
3. Refractory powder	60-80

Table 3.1 Composition of Typical Slurries in Investment Casting

According to Table 3.1, a major component for slurries is refractory powder. These fine refractory particles coat and reproduce shapes and surface qualities of the wax patterns. The liquid phase in the binder provides vehicles to disperse the solid phase and stabilize the sols and also provides liquid bridge cohesion to hold up the refractory to the wax pattern. The solid phase is initially dispersed in the liquid phase. Once polymerized, it serves to bond the refractory particles together into a shell.

Table 3.2 reviews a few more formulae of slurry mixtures in investment casting. However, actual formula for specific castings are not publicly accessible but remain as tricks of trade for most foundries.

No.	Materials	Amount	Purpose
1	Silica	67% Tetraethyl silicate, 8 parts by volume Water, 1 volume part	Precoating for high melting alloys
	Liquids	33% Ethyl alcohol, 1-2 parts by volume	
2	Solids	187 parts 94 parts 325-mesh silica 56 parts 325-mesh alumina 37 parts 40-mesh silica	Precoating for high melting alloys
	Liquids	81 parts 80 parts 20% sodium silicate 1 part 2% polyvinyl alcohol	
3	Solids	60% plaster of paris 25% 50-mesh or finer silica 15% talc	Plaster molding for nonferrous alloys
	Liquids	Water to creamy consistency	
4	Solids	90% silica 6% magnesia 3% monobasic ammonium phosphate 1%monobasic sodium phosphate	Precoating for high-melting alloys
	Liquids	Water or 10% hydrochloric or nitric acid	
5	Solids	1464.6 g powder 3 parts china clay 17 parts 140-mesh silica flour	Precoating for high-melting alloys
	Liquids	800 ml 37.6% no. 40 ethyl silicate 59.8% 190-proof ethyl alcohol 2.6% hydrochloric acid in a 3% water solution	

Table 3.2 Coating Formulas for Investment molding [5], [6]

3.1.3 Other Ingredients in Slurries

WETTING AGENTS

Slurries often contain wetting agents such as sodium alkyl aryl sulfonates, sodium alkyl sulfates, or octylphenoxy polyethoxyethanol to promote wetting of the coats onto the wax patterns. Slurries generally contains 0.03 to 0.3 weight percent of wetting agents. For ethylsilicate binder, wetting agents are sometime omitted.

ANTIFOAM AGENTS

Antifoam may be included to get rid of air bubbles on the coat after dipping. Commonly used agents are aqueous silicone emulsions and liquid fatty alcohol such as n-octyl alcohol and 2-ethyl hexyl alcohol. Slurries typically contain very low concentration of defoamers (0.002 to 0.1 weight percent).

ORGANIC FILM FORMERS

Sometime aqueous polyvinyl acetate emulsions, polyvinyl alcohol, and ammonium alginate are used to increase green strength and resilience of the dried coating.

NUCLEATING AGENT

When close control of grain size is required such as equiaxed superalloy casting, nucleating agent (grain refiner) is added to the primary slurry in amounts of 0.5 to 10 weight percent of the refractory in the slurry. Popular grain refiner are refractory cobalt, compounds such as aluminates, silicates, titanates, and oxides.

3.1.4 Drying of Binders in Investment Casting

Between coats, slurries are hardened by drying or gelling. Warm air with humidity and temperature controlled is blown at the slurry coated assembly right after stuccoing. Drying of coats are quite complicated by thermal expansion of the wax pattern. If drying is too rapid, the chill from water evaporation causes the pattern to contract while the coat is still wet. As the coating develops strength and starts to shrink at the end of drying, the wax expands. This can crack the coating. In practice, relative humidity of blown air is generally kept above 40 percent. Some references recommend 50 percent relative humidity. The temperature different between in-coming air and the wax should not be excessive. Experience indicates 4 to 6°C is a practical maximum [2].

Slurry does not need to be totally dried between coats. But, it must be just dry enough for the next coat to be applied without washing off the previous one. An alternative to shorten drying cycle is to harden slurry by chemical gelation which can be accomplished without much drying. For example, Ethyl silicate can be gelled with ammonia atmosphere. Gelling can be accomplished by adding gelling agents to the stucco, or by alternating alkaline and acidic slurries, or negatively/positively charged slurries in the dipping sequence. Shells that were gelled with chemicals are generally weaker when subsequently dried.

3.2 FUNCTIONAL REQUIREMENTS FOR BINDERS IN THREE-DIMENSIONAL PRINTING

The functional requirements for binder shares many similarities to that of refractory powder.

• LONG SHELF LIFE

Binder shall not coagulate or settle while being stored. Good binder must exhibit long shelf life.

• STABILITY UNDER FLUID HANDLING WITH INK-JET PRINTING

The most demanding and probably the most difficult requirement for Three-Dimensional Printing is to have stable and robust binders when being exposed to the fluid handling system in ink-jet printing.

One of the key factors that govern part accuracy is the size of binder droplets that penetrate into the powder bed and form primitives. Ideally, the accuracy increases with the reduction in droplet size. Therefore, Three-Dimensional Printing printheads deploy very small orifices to create tiny binder droplets in continuous-jet (CJ) fashion (Section 1.2.3,

printhead and binder technologies). The orifice openings are in the order of 30-70 μm to generate droplets of approximately 80 μm in diameter.

Jetting colloids through these small orifices has been a major impediment for process development in Three-Dimensional Printing since the beginning. Electrostatically stabilized colloid particles by ionic surface charge works well for minimum binder movement, but not under vigorous shear activities in the fluid channels and at the printhead orifices. The fluid shear enhances the rate of particle collision and therefore induces particle aggregation into three dimensional networks. If these networks are large enough to partially block the orifice opening, the jet is diverted or blocked.

• RAPID GELLATION UPON REACHING IN THE POWDER BED

Binder leaves the orifice and forms into droplets. These droplets reach the powder bed with terminal velocity of approximately 10 m/s. Their impact on soft powder creates craters slightly bigger than the droplet diameter. Powder particles directly under the impact point are drawn into the droplets as they slowdown to conserve the momentum[1] Finally, the coalescence terminates its motion and the binder is absorbed to the pores volume by capillary action. The time constant for the liquid migration into the pores is on an order of second [1].

Next, it is required that the binders gel as soon as their migration ceases. The gelation has to be fast enough to prevent gravitational bleeding which is a macroscopic flow of binder in droplet like features at high saturation that usually hang off the bottom of a large part.

This rapid gelation requirement of the binder conflicts with the stability requirement during fluid handling. Binders are required to swing from stable to gel upon being absorbed into the pores.

---

[1] Tailin Fan and his research on Ballistic impact of binder droplets on powder bed

• HIGH GREEN STRENGTH

After printing is finished, green parts are held together by gelled binder. Green strength depends directly on the strength of the gel and the interface strength between the powder and the binder. Green strength shall be sufficient to allow parts being transferred to the furnace.

• STRENGTH AND HIGH REFRACTORINESS

High refractory are needed for turbine casting technology which employs directional and single crystal solidification for better mechanical properties at higher working temperature. Binder for Three-Dimensional Printing of ceramics shall have good shell strength at 1500°C approximately for 3-5 hours. Details of the required heat profile is shown in section 2.1.2

As poured shells are cooling down, the shell strength must not prevent the metal from contracting, causing hot tear. It is preferable that shells crack and break to facilitate metal contraction.

• LEACHABILITY AND CORE REMOVAL

Cast shells will be knocked out to recover the castings. Some of the shells may fall off during casting, but a large portion still remains. The remaining shells and cores must be easily leached out by hot caustic solution to complete the cleaning process.

• COST, AVAILABILITY, AND ENVIRONMENT CONSIDERATION

Binders should be widely available with short lead time and low cost. Processed binder shall not be hazardous to environment and human.

3.3 COLLOIDAL SILICA AS SELECTED BINDER

3.3.1 Colloidal Silica

To guarantee equivalent shell properties with current investment casting, Three-Dimensional Printing should focus on using binder materials typically utilized in investment casting. There are two choices available for the ceramic binder: Colloidal silica and Ethyl silicate.

Ethyl silicate has ethyl alcohol as a cosolvent and are very flammable by nature. This makes ethyl silicate not suitable for unattended operation. Processwise, ethyl silicate dries out much faster than colloidal silica due to high vapor pressure of the alcohol. As a consequence, it is easily build up on the catcher and clog the fluid returning lines. Ethyl silicate may accumulate on the charging and deflection cell, and even on the exterior of printhead orifice. This could be a serious problem for the machine operation. In addition, ethyl alcohol is corrosive to several types of plastics in the fluid handling system. It can not be used without careful consideration. Lastly, ethyl alcohol vapor posts significant health hazard for human respiratory systems and the environment.

Colloidal silica seems to be a better choice for binder. Water-base colloidal silica dries slowly at a controllable rate. Water makes it compatible with most of materials in the fluid handling system. And small amount of colloidal silica is environmental friendly. It is actually added to some food as well as juices for preservation.

The form of silica that is of interest in Three-Dimensional Printing have silica particles ranging from 5 nm to 100 nm. It has been available as commercial product as early as 1950's to stiffen corrugated cardboard. Colloidal silica is available with solid loading up to 50 weight percent while the viscosity remains quite low over the full range of stability. Commercial colloidal silica are available in a variety of grades:

- Nyacol 830 is a colloidal silica with amorphous silica particles size of 10 nm and a solid loading of 30 percent by weight. This product is designed for ceramic investment casting with suitable viscosities to yield superior coats [7]

- Ludox HS-30 from Dupont is an equivalent product to Nyacol 830.
- Nyacol 9950 is a product with 100 nm amorphous particles with 50 percent by weight silica loading [8].
- Ludox DI is a colloidal silica without Na_2O.
- Ludox AM has alumina as the surface coat to silica particles and is positively charged to stabilize at low pH [9]. This product is stable in acidic slurries.

3.3.2 Gelation of Colloidal Silica

When colloidal silica concentration reaches critical point of stability by drying, or the pH is lowered between 5 and 7 for a period of time, or by adding of salts or polymeric coagulants; the silica particles adhere to one another forming strands and three-dimensional networks. The network is supersaturated meaning that there is more water to fill all the interconnected voids.

The gelation rate of colloidal silica by lowering pH alone is too slow to stop bleeding. Three-Dimensional Printing practice calls for a polymer (polyethylene glycol, PEG) that bridges and gel silica particles when pH is below 7.5. Powdered citric acid is ground and mixed to alumina powder up to about 0.5 weight percent to facilitate pH lowering and gelation. There are a number of alternatives to gel silica binder according to Iler [3] and Bredt [1] such as freezing, Ion-exchange, etc.

3.3.3 Development of Colloidal Silica for Three-dimensional Printing

This is a remarkable work of Jim Bredt [1]. Jim has developed a colloidal silica binder which has proven sufficiently stable and also pH sensitive for rapid gelation .

Three-dimensional Printing's colloidal silica in made from Nyacol 9950 manufactured by Nyacol Products Inc[2]. Nyacol 9950 is a product with large amorphous particles of 100 nm particles at 50 weight percent. It has been designed for polishing of silicon wafers or other semiconductor materials. It is also designed to work in paper anti-slip or seam strength applications as well. The product has a milky appearance with no odor. Details of the product is shown in Table 3.3 [8]

Properties	Value
Silica content wt % vol %	50 33
Particle size [nm]	100
Impurity: Sodium oxide %	0.12
pH	9.5
Viscosity, cPs	15
Specific gravity	1.40

Table 3.3 Properties of Nyacol 9950

Jim dilutes Nyacol 9950 with distilled water to about half of its initial concentration. Jim's research has found that some organic additives are useful to enhance stability as well as to trigger rapid gelation with low pH. The binder mixture is known, in house, under a code name '**Binder B**'. Organic additives to Binder B include:

- GLYCOL (ETHYLENE OR PROPYLENE)

  Glycol slows down catcher buildup and enables the printhead to stop and start for a short period of time without difficulties.

- TEA (TRIETHANOLAMINE)

  TEA serves to hold pH of the binder at about 9-9.5 to stabilize colloidal silica.

- BUTYL CARBITOL

  Butyl carbitol keeps organic impurities from precipiting onto the printhead component. This additive seems to foam binder. But the problem could be alleviated by an antifoam agent.

---

[2] Nyacol Products Inc., P.O. Box 349, Megunco Road, Ashland, MA 01721

• PEG (Polyethylene Glycol)

Above pH 7.5, PEG provides strearic barrier on the surface of silica particles that repels and prevents them from making contact, thus stabilize the binder from being polymerized. Below pH 7.5, PEG strands attract one another at the end of their strand. Silica particles are brought in close proximity where polymerization takes place.

• THYMOL BLUE

This additive serves as a pH indicator to monitor the pH level during storage and to assess the citric acid content in the powder.

Ratio of organic additives of Binder B is shown in weight percent in Figure 3.1

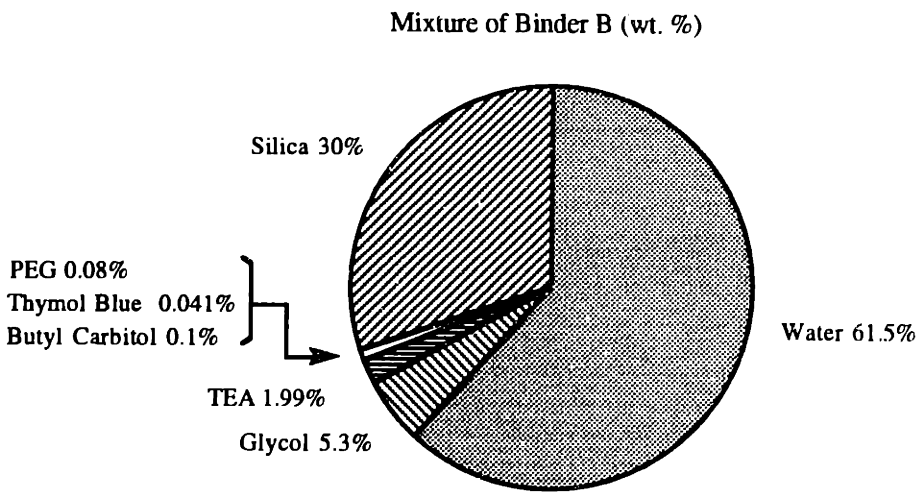

Figure 3.1 Composition of Binder B in Weight Percent

Binder B has proven a very stable binder for Three-dimensional Printing. It is very compatible with the fluid handling system with little degradation after recycling. Upon contact with the acidic powder bed, it gels almost immediately. Printed parts with Binder B dry very little and no layer curling is observed. The fact that it has about 8 weight percent of organic additives may account for small distortion during heat treatment. The organic burn out causes some smoke during firing, but this is not a big problem with sufficient ventilation.

3.3.4 Coagulation of Colloidal Silica with Citric Acid

Binder B gels rapidly when its pH is lowered from 9 to about 7.5. This is achieved by mixing citric acid into the powder bed. Practical citric content in the powder bed ranges from 0.2 to 0.5 percent by weight of the powder. Citric acid is very hydroscopic. It really loves water that is plentiful in binder and in air. Once the binder infiltrates the powder bed, it wets out citric grains and gels rapidly.

Citric acid is organic, composed of carbon, hydrogen, and oxygen. These elements are oxidized during early stages of heat treatment and turn into gases. Citric acid burns out in the furnace while the parts are cured allowing unbounded powder to fresh of acid once fired. Citric acid occurs naturally in fruits and it is not harmful but may slightly irritate soft tissues such as eyes or respiratory system if inhaled in large quantity.

3.4 SYNERESIS

Studies based on nuclear magnetic resonance (NMR) [10] and Raman spectroscopy [11,12] show that condensation continues for months at room temperature after gelation of silica because of large concentration of hydroxyl groups. The reaction creates new bridging bonds which stiffen and strengthen the network.

Not only does prolonged condensation strengthen the gel, it causes shrinkage of the network resulting in expulsion of liquid from the pores. This process is known as **syneresis**. Syneresis can be observed in everyday life. Cheese sweats and expels water onto its surface. Figure 3.2 presents syneresis of titania gel [13] that first occupied the whole volume, but shrank to about 1/3 of its initial volume leaving water outside the network.

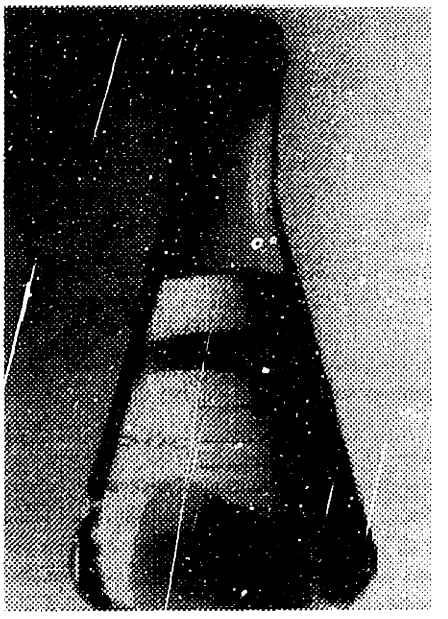

Figure 3.2 Shrinkage of Titania Gel from Syneresis [13]

Syneresis is driven by the tendency to reduce the solid-liquid interfacial area of the gel. This is accomplished by bringing solid surfaces into contact with the formation of new bonds due to condensation. Syneresis is a slow process which could take months to squeeze out internal water from the network. Therefore, it may be negligible compared to the time constant of Three-Dimensional Printing (a matter of hours or days).

3.5 CHAPTER SUMMARY

Colloidal silica was selected as a primary binder for ceramic process in Three-Dimensional Printing to guarantee equivalent shell properties with current investment casting. Ethyl silicate was inappropriate for Three-Dimensional Printing since its alcohol cosolvent is not well suit for fluid delivery system, human contact, and safety concerns. On the other hand, Nyacol 9950 colloidal silica was selected as primary binder for Three-Dimensional Printing. Among other commercial colloidal silica products, Nyacol 9950 contains largest amorphous silica particle of 100 nm with highest solid loading of 50 percent. Large particle size minimizes interparticle collision and increases the stability of the binder while high solid loading increases part strength.

Nyacol 9950 was not sufficiently stable to be used with Diconix printhead and fluid delivery architecture at that time. Development of Nyacol 9950 was carried out by James Bredt [1] by adding several selected organic additives. The product is known in house as 'Binder B'. Binder B is proven a stable binder. It is very stable and could rapidly gel as pH is lowered below 7.5. In order to facilitate binder gelation, powdered citric acid is mixed. Citric acid content ranges from 0.2 to 0.5 weight percent of the powder bed. It is an organic compound which will burn out completely at the early stage of heat treat process. However, the acid is very hydroscopic thus absorbs moisture from the binder and the environment which greatly degrades powder packability.

In gelation, silica particles adhere to one another forming strands and network of solid phase which contain water in its interconnected pores. Particle bonding continues long after gelation due to excess hydroxyl group and causes the network to shrink, known as syneresis. However, syneresis is a slow process which may be negligible due to the much shorter time constant of Three-Dimensional Printing process.

BIBLIOGRAPHY

[1] Bredt, J., *Binder Stability and Powder\Binder Interaction in Three Dimensional Printing*, MIT PhD Thesis, Dept. Of Mechanical Engineering, Supervised by E. M. Sachs, 1995.

[2] Horton R. A., *Investment Casting, Metals Handbook*, ASM International, Vol. 15, pp. 253-269, 1988.

[3] Iler R. K., *The chemistry of Silica*, John Wiley & Sons, 1979

[4] Ulaskas D. J., *Hybrid Binder Systems*, Paper presented at 29th Annual Meeting, Scottsdale, AZ, Investment casting institute, 1981.

[5] Heine R., Loper C., Jr., Rosenthal P., *Principles of Metal Casting*, 2nd Ed., McGraw-Hill, 1967.

[6] Geist K., Kerr R., Jr., *Principles of Precision Investment Castings*, Trans. AFS, vol. 55, pp. 17, 1947

[7] Nyacol Products Inc., *Nyacol ® 830 colloidal Silica Typical Properties*, P.O. Box 349, Ashland, MA 01721

[8] Nyacol Products Inc., *Nyacol ® 9950 colloidal Silica Typical Properties*, P.O. Box 349, Ashland, MA 01721

[9] Dupont, *Ludox product literature*

[10] Vega, A., Scherer, G., *J. Non-Cryst. Solids*, 111 [2,3], pp.153-166, 1989

[11] Quinson, J., Tchipkam, N., Dumas, J., Bovier, C., Serughetti, J., Guizard, C., Larbot, A., and Cot, L., *J. Non-Cryst. Solids*, 99, pp. 151-159, 1988

[12] Brun, M., Lallemand, A., Quinson J., Eyraud, C., *Thermochimica Acta*, 21, pp.59-88, 1977

[13] Yoldas B, J. Mater. Sci., 21, pp. 1087-1092, 1986

Chapter 4.
Mechanics of Drying Gels

4.0 INTRODUCTION

There are two shrinkage origins in Three-Dimensional Printing ceramic process: 1) drying and 2) sintering. Drying shrinkage is driven by tension in the liquid phase during saturation. Liquid tension gradient tries to drive liquid out from the interior to the exterior by compressing the **network**. If the network is not allowed to contract, there will be no liquid transportation nor shrinkage deformation. Drying shrinkage ceases as the network develops adequate strength to withstand the liquid tensile stress. On the other hand, sintering or heat treatment shrinkage takes place at elevated temperature as binder sinters and viscously flows to deposit at interparticle neck area. Both underlying mechanisms of drying and heat treatment shrinkage are distinct by their nature and should be discussed separately.

Drying is such an amazingly interesting phenomena. There are numerous examples of porous substances that repeatedly take up water and dry out. Shirts and jeans are good example. They always wrinkle in the drier after being washed. Wet papers curl in drying. Even our skin wrinkles if it is dehydrated. This chapter discusses the mechanics of drying of deformable porous bodies. It starts with concept of phase relation and the connection of liquid pressure drop and flow in porous media. The chapter also covers a topic of network-liquid interaction under capillary stress and, finally, how these two phases govern shrinkage deformation. Lastly, mathematical models are derived to describe the beauty of drying phenomena.

4.1 PHASE RELATIONSHIP OF SOLS AND GELS

There are three basic phases in drying business: liquid, solid, and air. However, when stresses in the liquid and the solid are specified in gage pressure, the role of air or gas

phase is negligible. Therefore, only the liquid and the solid phases are to be focused at this point.

There are several morphologies to describe the co-existence of the liquid and solid phases in sols and gels. **Liquid** refers to the systems that only contain liquid phase. **Sols** stand for colloidal suspensions of solid particles which remain dispersed inside liquid vehicles. **Gels** describe the systems that have liquid filled in between strands of solid network. Figure 4.1 illustrates phase relation of liquid, sol, and gel.

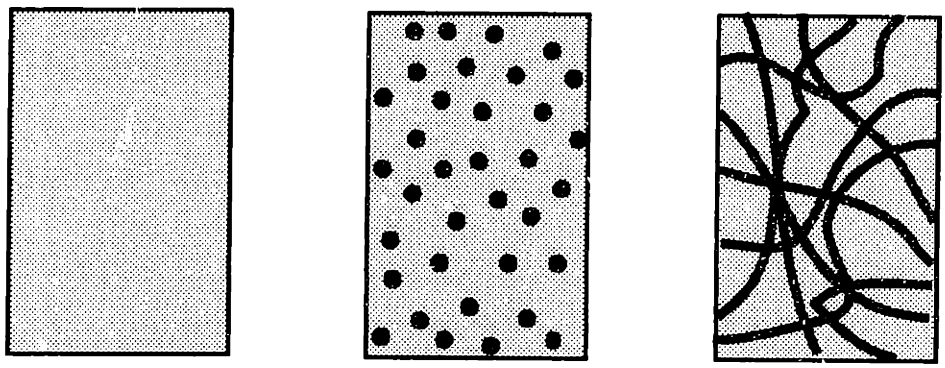

Figure 4.1 Phase Relation of Liquid, Sol, and Gel

Liquid phase is very essential to sol-gel process. First, liquid provides the medium or vehicle that suspends the solid particles against gravitation. Thus, the particles are slow or never fall down to the earth. Second, the liquid molecules help transferring momentum from one solid particle to its neighbors via molecular collisions in Brownian motion. Third, the liquid molecules buffer a solid particle from colliding and adhering to its neighbor particles. This stabilize reactive particles from being polymerized. Fourth, the liquid is directly involved with several important chemical reactions both to stabilize or to destabilize the suspension (such as hydrolysis, condensation, and coagulation). In addition, liquid is a transport vehicle that carries particles as it flows.

Gels can be made from sols by joining the solid particles into networks. This mechanism is called **gellation**. Gellation can be viewed as polymerization where each solid particle serves as a monomer. When these monomers join, they turn into a network of monomers, or polymer. A good example of sol-gel transition is gelatin made from water

and flour. Mixture of water and flour is a sol where flour particles are suspended in the water. When the mixture is heated, flour particles link and join into a network (starch) which contains water between the network strands.

Trapped liquid between the network strands assist further chemical reaction which last for a long time. The reaction includes polymerization and strengthening of existing bonds and further reduction of network surface area. However, the presence of liquid inside the body posts a severe threat to dimension stability and integrity of the gel body. Water eventually has to leave or dry from the gel by mean of evaporation. When curved liquid-vapor interface forms at the network exterior, liquid is under tensile stress. Liquid tension consequently compresses the network. The magnitude of the hydrostatic tension is approximately 50 to 100 MPa depending on the wetting characteristic and the pore radius. Although there exists liquid pressure gradient between the interior and the exterior of the gel, the liquid can not transport from the interior to the exterior unless the network is deformable. If it does so, the body is under contraction squeezing out liquid from the interior to the exterior. The network continues to deform until it can withstand the compression force. At that point the deformation ceases and the liquid reaches its maximum tension. Then the liquid-vapor interface recedes into the network interior. The rest of the drying is governed by diffusion mechanism and will not change the gel volume.

Drying of liquid phase from a gel places another danger to the integrity of the body. The difference in compression stress on the network in front and behind of the liquid-vapor interface can be significant as the interface moves inside the body. This causes gel to crack to release the elastic energy. The crack propagates from the exterior of the body following the liquid-vapor front into the interior. Cracking has been a very serious impediment to the sol-gel process.

4.2 CAPILLARITY

Capillarity is a phenomenon where fluid is under tension as its liquid-vapor interface is inside a small tube or gap. It is the same mechanism whereby trees transport underground water from the tip of the root to the topmost leaves. This capillary behavior is governed by surface tension and wetting characteristic of the solid-liquid in contact.

Consider a small glass tube in Figure 4.2 that is inserted into a pool of water under atmospheric pressure. The water rises up inside the tube as a result of surface tension and the wetting property between water and the glass surface. The surface tension exists everywhere along the liquid surface, but contributes to capillary rise at the point where liquid, vapor, and solid join. In this case, it is the point where the liquid-vapor interface touches the internal perimeter of the tube. Surface tension acts in the tangential direction to the liquid-vapor interface at the contact point. In this case, it poses at an angle θ from the solid surface, known as **contact angle**. Contact angle depends on the molecular adhesion between the liquid and the solid. The magnitude of surface tension can then be calculated by balancing the weight of this rising fluid column with the surface tension force, Figure 4.2.

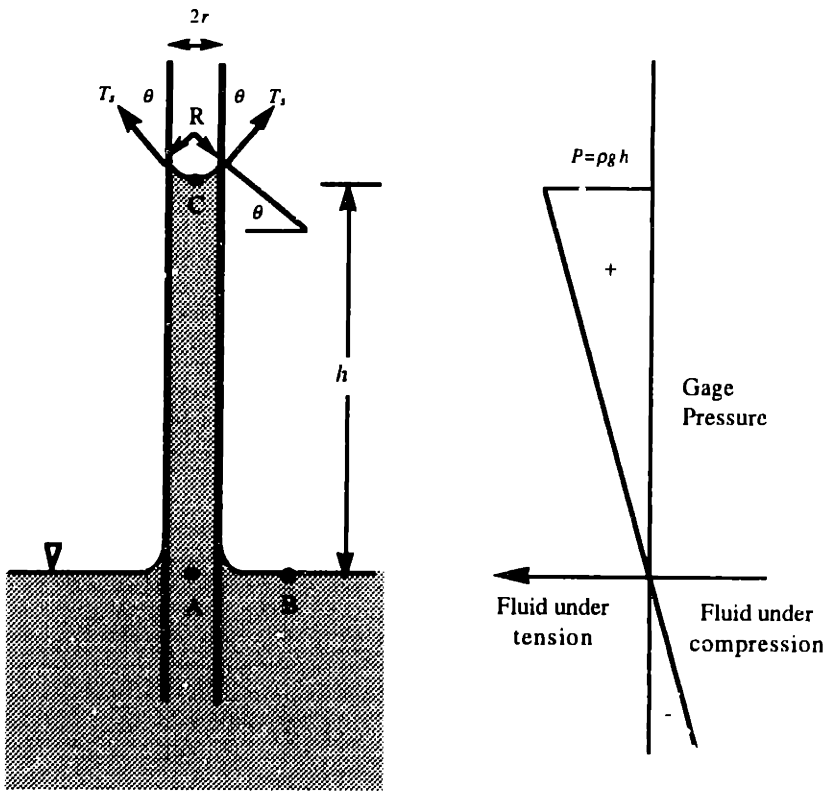

Figure 4.2 Physics of Capillarity in Small Tube

$$2\pi r T_s \cos\alpha = \pi r^2 \rho g h \tag{4.1}$$

where r is the radius of the capillary tube

T_s is the surface tension

θ is the contact angle

ρ is the density of the liquid

g is gravitation acceleration

and h is capillary height

The surface tension can be derived from Equation (4.1) as:

$$T_s = \frac{\rho g R h}{2} \tag{4.2}$$

and the capillary height, h, can be arranged as:

$$h = \frac{2T_s}{\rho g R} \tag{4.3}$$

where R is the meniscus radius of curvature, $R = \frac{r}{\cos\theta}$

Sometime the contact angle is taken as zero ($\theta = 0$) for simplicity. This gives the radius of curvature to be equal to the radius of the tube. So, the capillary height is found as:

$$h = \frac{2T_s}{\rho g r} \tag{4.4}$$

Equation 4.4 provides a good analogous point that the capillary height (or stress) depends inversely with the pore radius in gel bodies. The smaller the pores, the higher the height (or stress).

Figure 4.2 also plots the gage pressure of the liquid in the capillary column. At point B, the liquid is in equilibrium with atmospheric pressure. So, the pressure at this point is zero. At point A which has the same elevation as point B, the gage pressure must be equal to point B. The liquid inside the liquid column above point A is under tension. The magnitude of this tension increases linearly with the elevation and with its maximum at point C just under the surface of the meniscus. Therefore, the whole liquid column is under tension or suction (taken as positive in this thesis). The magnitude of hydrostatic tension in the liquid can be found as:

$$P = \rho g h = \frac{2T_s}{R} \tag{4.5}$$

So, the tension at point C depends inversely with the radius of curvature of the meniscus. In other words, the magnitude of the hydrostatic tension in the liquid is a inverse function of the pore radius.

4.2.1 Laplace's Equation of Capillary Pressure in Three-Dimensions

The surface tension causes the meniscus surface to behave like an elastic membrane similarly to the surface of a balloon with higher pressure inside. In two-dimensions, the meniscus surface assumes a concave curvature towards the larger pressure to balance off the pressure difference between both sides of the meniscus. The pressure difference between inside and outside of the meniscus surface can be calculated from the surface tension and the radius of curvature of the meniscus by force equilibrium across the membrane as Equation 4.1.

The gauge pressure difference across the meniscus surface in two-dimensions is presented in Equation 4.5. However, in absolute pressure basis, the pressure difference can be written as:

$$\Delta P = \frac{2T_s}{R} \tag{4.6}$$

In three-dimensional surface as in Figure 4.3, there can be two radii of curvature in two orthogonal principle planes as R_1 and R_2. The pressure difference of this three-dimensional concave surface can be derived with Laplace's equation as:

$$\Delta P = T_s\left[\frac{1}{R_1}+\frac{1}{R_2}\right] \tag{4.7}$$

where R_1 and R_2 are radii of curvature of a meniscus surface
in two orthogonal planes

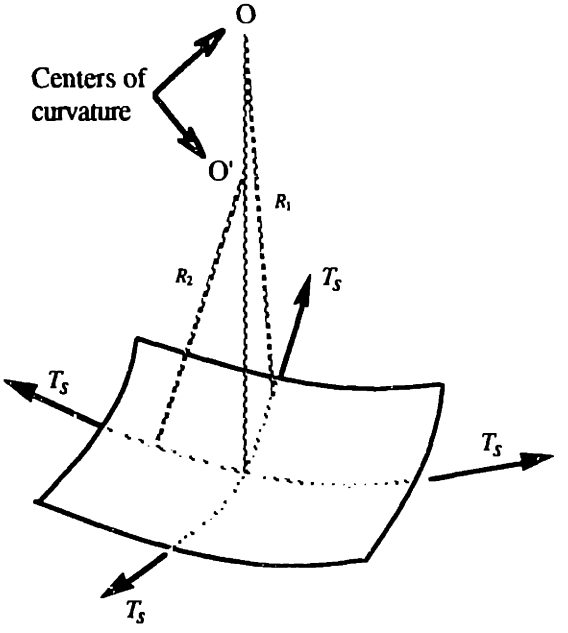

Figure 4.3 Radii of Curvature of a Meniscus in Three-Dimensions

In soil mechanics, the pressure difference in Equation 4.7 is generally known as matric suction. As the magnitude of matric suction increases, the radii of curvature decreases. On the other hands, when matric suction approaches zero, the surface flattens out.

4.3 CAPILLARY STRESS OF WATER

Water is a common solvent in most sols. Silica colloidal are dispersed in water because water molecules can nucleophilically attacked (or **hydrolysis**) the silicon atoms with its oxygen turning them into silicic acid (hydrolyzed). Silicic acid is a basic monomer which resides at the surface of a cluster of silica particles. These clusters can be dispersed and stabilized in water by several means such as charge stabilization or stearic barrier. When the stabilization is suppressed by reducing surface charges, obscuring the stearic barrier, or using of a coagulant; the silicic acid molecules are in a closer proximity and link together. The reaction is called **condensation** where a hydrogen atom group breaks off from a molecule of silicic acid and join with OH^- group in the water with a new molecule of water as a by product. Depronotated silicic acid atom then links up with a nearby silicic acid atom and form a dimer with Si-O-Si bond. The process continues from dimer to trimer and so on until a bigger cluster is formed. If the process continues, clusters will be linked into strands or chains, and then network that extent through out the liquid medium. When these gels are in the process of drying, the capillary of water has a critical effect on deforming the network bodies.

4.3.1 Surface Tension of Water

Surface tension is measured as the tensile force per unit length of liquid-solid surface. Surface tension force has a direction that is tangential to the surface of the liquid at the solid-liquid contact point. The magnitude of surface tension of water-air interface decreases as temperature increases as shown in Table 4.1

Surface tension of water-air can be lowered by surfactant agents such as aqueous silicone emulsions and liquid fatty alcohols (n-octyl alcohol or 2-ethyl hexyl alcohol). Only a small concentration of these agents is needed to lower water tension to about 30 mN/m.

Temperature [°C]	Surface tension [mN/m]
0	75.7
10	74.2
15	73.5
20	72.8
25	72.0
30	71.2
40	69.6
50	67.9
60	66.2
70	64..4
80	62.6
100	58.8

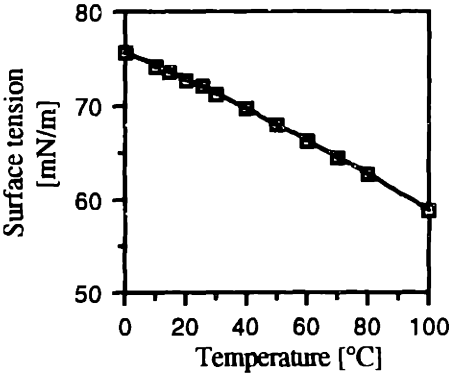

Table 4.1 Surface Tension of Water-Air [1]

4.3.2 Capillary Tension in Small Pores

In the drying process, liquid-vapor menisci form at the exterior of the gel body. Capillary curves the menisci and forces liquid under tension as shown in Figure 4.4. According to Laplace's equation in section 4.2.1, the magnitude of liquid tension is an inverse function of the pore radius (i.e. small pores create high liquid tension). The magnitude of liquid tension at point A can be approximated with Equation 4.7.

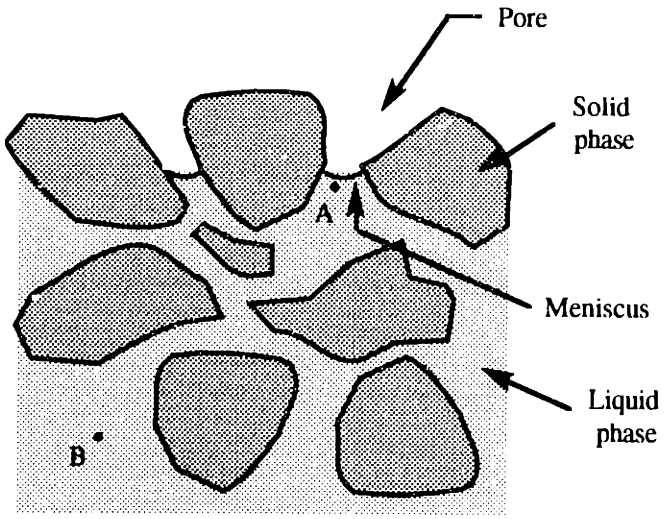

Figure 4.4 Small Menisci Form at the Exterior

Figure 4.5 shows a plot of approximated surface tension of water by assuming zero degree contact angle (perfect wetting) at 30°C. According to Figure 4.5, the surface tension at point A is in the order of 1 MPa for 10-100 nm pore radii. For smaller pore radius, the tension can be in the order of 100 MPa. How the liquid sustains this amount of tension without cavitation will be discussed in Section 4.3.3

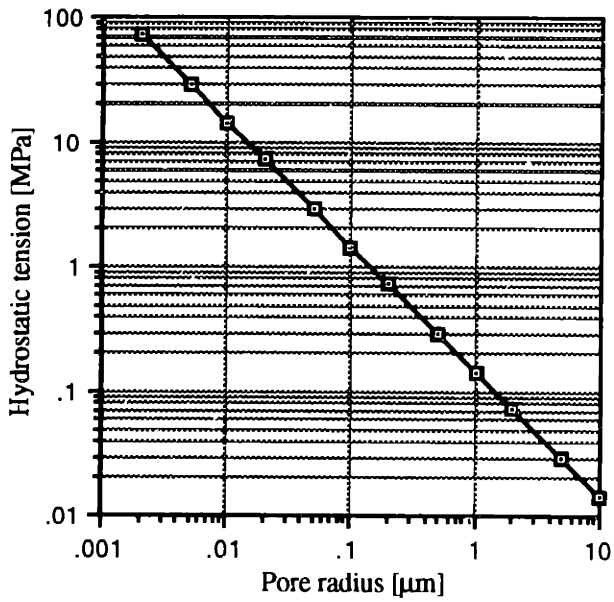

Figure 4.5 Estimated Magnitude of Surface Tension of Water as a Function of Pore Radii (assuming perfect wetting of water at 30°C)

The tension at point B is equal to point A if 1) the elevation difference at point A and B is negligible 2) there is no liquid flow from point B to point A. However, the latter case is not feasible if the network is deformable. Water flows from the interior to the exterior to feed the liquid-vapor evaporation at the interface. In the case of liquid transportation, the liquid tension at point B is not equal to the tension at point A. More detail of liquid tension distribution will be discussed in Section 4.4.

4.3.3 Water Cavitation Under High Liquid Tension

In most practical engineering cases the tensile strength of water is rather limited to a typical order of 1 bar (10^5 Pa). It is customary to assume that small vapor bubbles are responsible for cavitation inception beyond 1 bar. Maximum tensile strength in a liquid depends on the amount of dissolved gas and small particles content.

Greenspan and Tschiegg [2] found that when all particles of size larger than 0.2 μm are filtered, the tensile strength of water increases to about 200 bar and the influence of gas content vanishes. Filterization of particles below 0.2 μm will not improve the tensile strength. This is an important fact to indicate that bubbles are nucleated at the liquid-solid interface. Therefore, removing solid particles from the liquid by filterization improves the ultimate tensile strength in the liquid. Brigges [3] found that ultimate tensile strength in water is of the order of 200-300 bar.

This finding explains the fact that a number of trees can be taller than 10 meters (in fact, some trees are as tall as 100 meters). The membranes at the roots of these plants filter out small particles so that water could sustain high tensile stress. Water and minerals are lifted up from the root along the xylem to the menisci at the lip of their leaves for photosynthesis.

4.4 LIQUID TRANSPORT IN POROUS MEDIA

Liquid evaporates from the body at the liquid-vapor interface. The rate of liquid mass leaving the body is known as '**drying rate**'. Drying rate depends on several factors

such as relative humidity, vapor pressure, diffusibility of the liquid, level of energy of the systems, surface area of the pores, etc.

The liquid tension at point A at the liquid-vapor interface is governed by the radius of curvature at the meniscus. The tension in the interior (such as point B) is equal to that of point A if the network is rigid, or less than that of point A if the network is deformable. In the latter case, the liquid tension is maximum at the meniscus's surface and gradually reduces into the interior, Figure 4.6. The pressure gradient between the interior (point B) and the exterior (point A) drives the liquid out to the surface through narrow channels between strands of the network. Details of the pressure gradient and its relation with the network deformation due to liquid transport in porous media will be discussed in the next section.

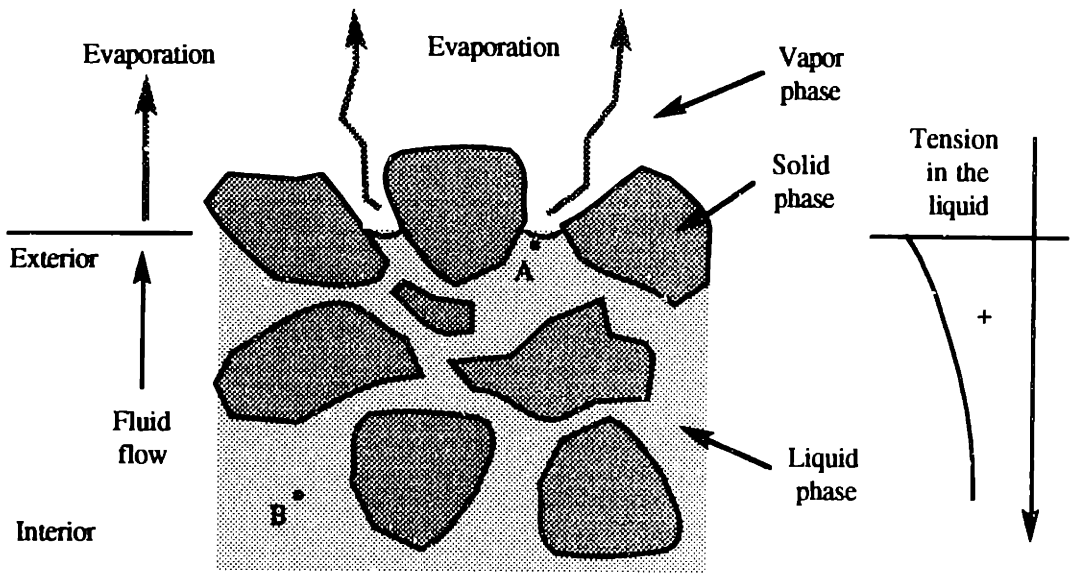

Figure 4.6 Flow of Liquid from the Interior to the Exterior by Pressure (tension) Gradient

4.4.1 Models of Porous Media and Pressure Gradient

A porous media can be represented by two models: 1) an assembly of several small channels, and 2) uniformly spaced spherical particles of equal size as shown in Figure 4.7. The channel model consists of a group of straight circular tubes running along the length of the media. Friction between the fluid and the channels causes a pressure gradient along the

flow direction. The channel model is only applicable to laminar flow where the Reynold's number, Re, is less than 2. On the other hand, the drag model is well applicable to turbulent flow where Reynold's number is greater than 2. This model consists of a series of rows of spaced spheres such that its pressure drop is calculated from fully developed drag of fluid through spheres [4].

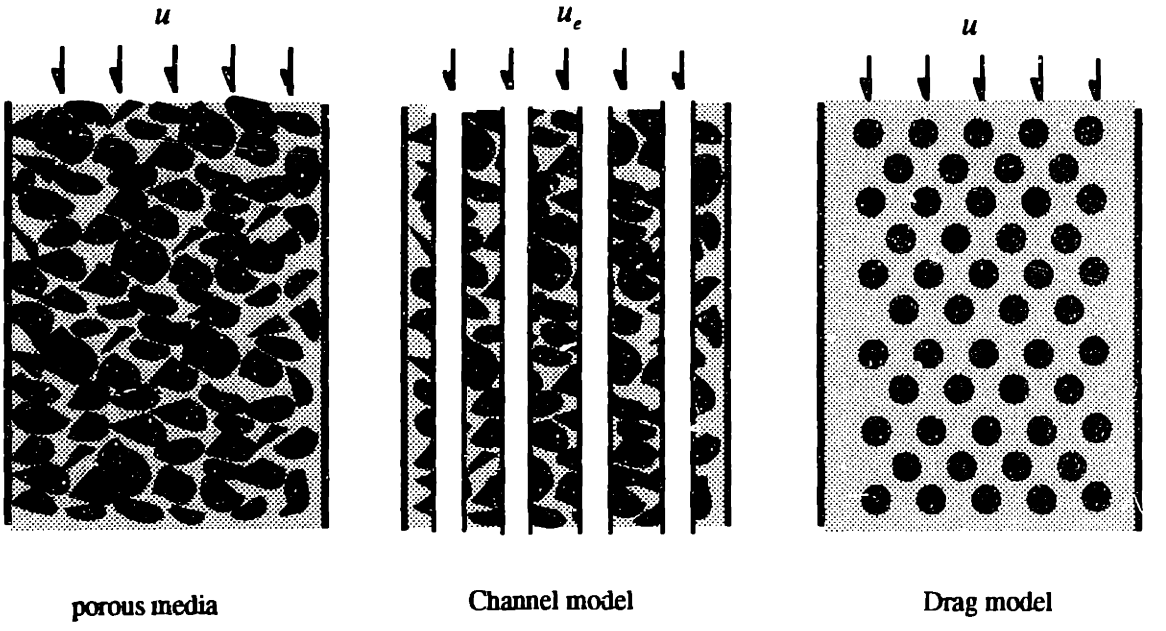

Figure 4.7 Channel and Drag Models of Porous Media

CHANNEL MODEL

Channel model is developed based on the theories of laminar flow in a circular tube. When a fluid with density ρ and viscosity μ flows, under laminar regime, through a straight circular tube with diameter D_p and length L, at an average flow speed u, the pressure drops, Δp_d, of this fully developed flow can be expressed according to Hagen-Poiseuille as:

$$\Delta p_d = \frac{32 L \mu u}{D_p^{\,2}} \tag{4.8}$$

The pressure drop can be rewritten to incorporate the concept of a friction factor by Fanning as:

$$\Delta p_d = 4f\frac{L}{D_p}\frac{\rho u^2}{2} \tag{4.9}$$

The friction factor is not only a function of Reynolds number, Re, but also of the surface roughness of the tube as:

$$f = 16\frac{\mu}{D_p u\rho} = \frac{16}{\mathrm{Re}} \tag{4.10}$$

Both Equation 4.8 and 4.9 are applicable only to circular tubes in laminar flow. For non-circular channels such as those in porous media, D_p will be replaced with an equivalent parameter called hydraulic radius, H_r. The hydraulic radius for porous media is defined as

$$\begin{aligned}
H_r &= \frac{\text{cross section area of a channel}}{\text{Wetted periphery}} \\
H_r &= \frac{\text{cross section area of a channel x tube length}}{\text{Wetted periphery x tube length}} \\
H_r &= \frac{\text{tube volume}}{\text{wetted area of the tube}} \\
H_r &= \frac{\text{total pore volume}}{\text{total surface area of particles in the porous medium}} \\
H_r &= \frac{\text{porosity}}{\text{specific surface area based on the volume of porous medium}} \\
H_r &= \frac{\varepsilon}{S_B} = \frac{\varepsilon}{S_v(1-\varepsilon)}
\end{aligned} \tag{4.11}$$

The hydraulic radius, H_r, is generally equal to one-quarter of the equivalent tube diameter for any cross section (including circular and others).

$$D \approx 4H_r \tag{4.12}$$

In this case S_B is the specific surface area of the powder bed which is also equals to specific area of a particle in the powder bed, S_v , multiplied by the packing fraction of the particle assembly, $1-\varepsilon$.

The flow speed in Hagen-Poiseuille has to be modified for porous media as well. Carman's tortuousity model [5] estimates fluid flow speed in a porous medium by comparing the resident time of a liquid molecule in the flow, Figure 4.8. The resident time required for the liquid molecule to travel through an equivalent channel is equal to that of the actual time required to pass through a real powder bed. Or, algebraically,

$$\frac{L_e}{u_e} = \frac{L}{u/\varepsilon} \tag{4.13}$$

where u is the bulk flow velocity of the liquid

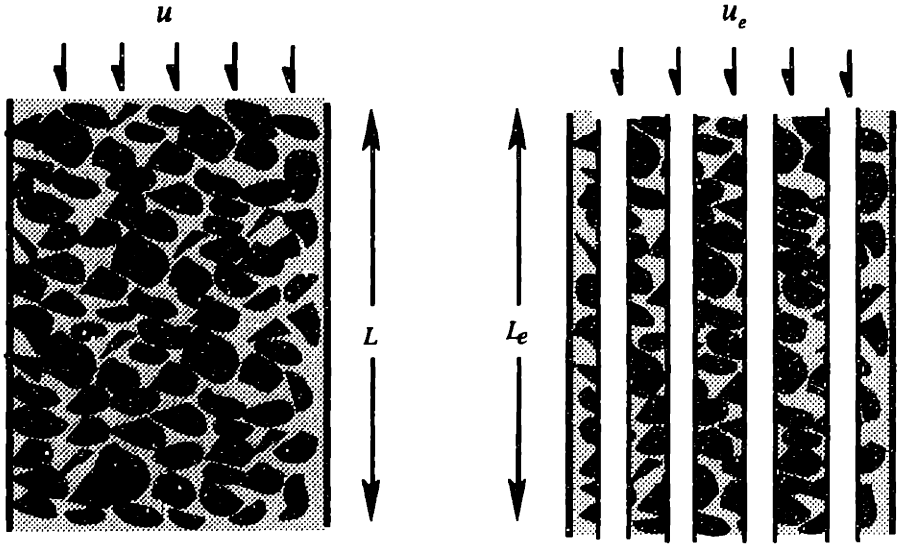

Figure 4.8 Equivalent Channel Length

Substituting the hydraulic radius and equivalent flow speed from Equation 4.11, 4.12, and 4.13 into Hagen-Poiseuille in Equation 4.8, gives

$$\Delta p_d = \frac{32 L_e \mu u_e}{(4H_r)^2} = 2\left(\frac{L_e}{L}\right)^2 \frac{S_v^{\,2}(1-\varepsilon)^2 L\mu u}{\varepsilon^3} \tag{4.14}$$

the term L_e/L is the ratio of equivalent channel length to the powder bed thickness, it is commonly known as tortuousity. For non-circular channels, the equation is corrected by a factor k_o to replace numerical constant 2.

$$\Delta p_d = k_o\left(\frac{L_e}{L}\right)^2 \frac{S_v^{\,2}(1-\varepsilon)^2 L\mu u}{\varepsilon^3} \tag{4.15}$$

Carman found the product of $k_o(L_e/L)^2$ depends on packing density and some other factors. Generally, this dimensionless term is close to 5. This finding is a very well known equation so called Kozeny-Carman equation [6]:

$$\Delta p_d = 5\frac{S_v^{\,2}(1-\varepsilon)^2 L_i \mu u}{\varepsilon^3} \tag{4.16}$$

where $k_o(L_e/L)$ is Kozeny constant and L_e/L is generally equivalent to $\sqrt{2}$.

In terms of Fanning's friction factor, Equation 4.16 can be written as

$$2f = \frac{\Delta P_d H_r}{L\rho(u/\varepsilon)^2} = \frac{5}{\mathrm{Re}} \tag{4.17}$$

The Reynold's number for flow in porous media is

$$\mathrm{Re} = \frac{\rho u_e H_r}{\mu} = \frac{\rho(u/\varepsilon)}{\mu}\left(\frac{\varepsilon}{S_B}\right) = \frac{\rho u}{\mu S_B} = \frac{\rho u}{\mu S_V(1-\varepsilon)} \tag{4.18}$$

Equation 4.17 and 4.18 are applicable for laminar flow when Re < 2. In the domain where Re > 2, pressure drop has to be found by the drag model which will be shown in the next section.

DRAG MODEL

The drag model is applicable to the turbulent flow regime where the Reynold's number is greater than 2. The model is based on a concept that the pressure drop across porous media has to be equal to the sum of fluid drag experienced by particles according to the conservation of momentum.

$$\Delta P_d = \frac{1}{A}\sum_{i=1}^{N} R_{mi} \tag{4.19}$$

where A is the cross section area of a porous medium
R_{mi} is the fluid drag experienced by ith particle
and N is total number of particles in the medium.

Drag theory assumes that the fluid flow pattern around any particle in the medium is identical. Thus, the fluid drag acting on any particle in the powder bed is alike.

However, the fluid flow approaching a particle is disturbed by its upstream neighbors. In other words, fluid drag experienced by ith particle has to be corrected for the signature of upstream spheres. The correction factor is a function of porosity $f(\varepsilon)$. If R is the fluid drag experienced by a particle in an undisturbed stream, then R_{mi} is:

$$R_{mi} = f(\varepsilon)R \tag{4.20}$$

According to the theory of drag of spheres, drag resistance is found by:

$$R = C_D \frac{\pi D_{sp}^{\ 2}}{4}\frac{\rho u^2}{2} \tag{4.21}$$

where C_D is the coefficient of drag of a single sphere

D_{sp} is the diameter of monosize spheres

The number of monosize spheres in a random pack powder bed is

$$N = \frac{6AL(1-\varepsilon)}{\pi D_{sp}^{\ 3}} \tag{4.22}$$

Substitute Equation 4.20, 4.21, 4.22 into 4.19 gives

$$\Delta P_d = \frac{3}{2} C_D (1-\varepsilon) f(\varepsilon) \frac{L}{D_{sp}} \frac{\rho u^2}{2} \tag{4.23}$$

The expression for $f(\varepsilon)$ is found by Steinour in 1944 as:

$$f(\varepsilon) = \frac{25(1-\varepsilon)}{3\varepsilon^3} \tag{4.24}$$

Therefore, equation (4.23) becomes,

$$\Delta P_d = \frac{25}{2} C_D \frac{(1-\varepsilon)}{3\varepsilon^3} \frac{L}{D_{sp}} \frac{\rho u^2}{2} \tag{4.25}$$

Burke and Plummer derived an empirical expression with dimensional analysis for the pressure drop [7]. The coefficient of drag C_D is replaced by their finding.

$$\Delta P_d = \frac{3.5}{4} \frac{(1-\varepsilon)}{\varepsilon^3} \frac{L}{D_{sp}} \frac{\rho u^2}{2} \tag{4.26}$$

Combining both channel and drag models gives a universal pressure drop in both laminar and turbulent regimes.

Ergun postulated an expression to summarize the data in both laminar and turbulent regimes as a sum of fluid drag consisting of two terms to the first and second order in fluid flow velocity [8].

$$\frac{\Delta P_d}{L} = 150\frac{(1-\varepsilon)^2}{\varepsilon^3}\frac{\mu u}{D_{sp}^{\ 2}} + 1.75\frac{(1-\varepsilon)}{\varepsilon^3}\frac{\rho u^2}{D_{sp}} \tag{4.27}$$

According to Fanning friction factor, Ergun's expression is equivalent to

$$2f = \frac{150(1-\varepsilon)}{\mathrm{Re}} + 1.75 \tag{4.28}$$

Ergun's work provides a bridge from the work of Kozeny-Carman in laminar domain to the Blake-Plummer theory in the turbulent domain as shown in Figure 4.9.

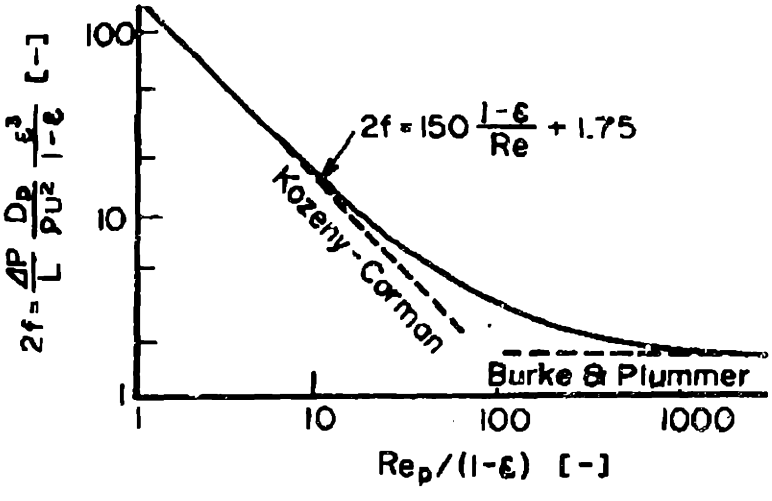

Figure 4.9 Comparison of Ergun's Correction to Kozeny-Carman and Blake-Plummer [4]

4.4.2 Darcy's Law

Drying of gel is a slow process. It takes a matter of hours, and probably days, to dry only a small piece of gel in air. A cylindrical gel made from of 100 nm at 50 weight percent silica binder with a volume of 0.5 μl was dried from the perimeter with an area of 1.263×10^{-6} square meters in 15 minutes. Estimated Reynold's number of liquid flow through the intergranular channels is

$$\mathrm{Re} = \frac{\rho u_e H_r}{\mu} = \frac{10^3 \dfrac{(0.66)(0.5x10^{-9})}{(1.263x10^{-6})(15x60)} \dfrac{100x10^{-9}}{3}}{10^{-3}}$$

$$\mathrm{Re} = 9.677x10^{-9} << 2$$

Therefore, the liquid transports from the interior to the exterior through intergranular channels in laminar flow and the pressure drop due to liquid transportation can be characterized with Kozeny-Carman's relation (Equation 4.16).

$$\Delta p_d = 5\frac{S_v^{\,2}(1-\varepsilon)^2 L\mu u}{\varepsilon^3}$$

Reshuffle Equation 4.16 to obtain flow speed:

$$u = \frac{\varepsilon^3}{5S_v^{\,2}(1-\varepsilon)^2}\left(\frac{1}{\mu}\right)\left(\frac{\Delta p_d}{L}\right) \tag{4.29}$$

Flow speed is equal to the volume flow rate per unit area perpendicular to the flow direction which is also defined as flux, J. In addition, the term $\Delta p_d / L$ in Equation 4.29 has a mathematical meaning of a pressure gradient. In one-dimensional flow in x-direction, the pressure gradient can be written as $\frac{\partial p_d}{\partial x}$. So Equation 4.29 can be rewritten as

$$J = -\frac{D}{\mu}\left(\frac{\partial p_d}{\partial x}\right) \tag{4.30}$$

where D is called specific permeability of the porous medium according to Kozeny and Carman, $D = \frac{\varepsilon^3}{5S_v^2(1-\varepsilon)^2}$

Darcy found the relationship in Equation 4.30 in 1856 as he was testing pressure drop across porous filters [9]. Therefore, Equation 4.30 is generally known as Darcy's law. The negative sign indicates that the flux has the opposite direction to the pressure gradient. Permeability has a unit of length square. Typically, physicists and chemists in most branches of applied sciences commonly use 'darcy' as the unit of measurement where 1 darcy is equal to $9.87 \times 10^{-9} cm^2$. In hydrology, permeability may have a unit in terms of seepage velocity of the percolating water per unit drop of hydraulic head. The validity of Darcy's law has been tested by many researchers [11-13]. It has been proven valid for a wide domain of fluid flows in laminar regime. Darcy's law becomes invalid for liquids at high velocities and for gases at any velocities.

In three-dimension, Darcy's law may be written with vector calculus as

$$J = -\frac{D}{\mu}\nabla P \tag{4.31}$$

This thesis takes liquid under tension as positive. So, the sign convention allows Darcy's law to be written as:

$$J = \frac{D}{\mu}\nabla P \tag{4.32}$$

According to Figure 4.8, , liquid transports from the interior to the surface by drying process. It has to pass through systems of small channels between the network of the solid phase. The friction causes liquid pressure to drop along the direction of flow or the liquid tension increases in the direction of flow. Liquid tension is maximum at the liquid-vapor interface, or at the menisci. It gradually reduces into the interior but never be under compression unless being squeezed by external forces. However, This is not the case in drying. The tension gradient depends on permeability of the porous body, flux density, and the fluid's viscosity as characterized by Darcy's law. The effect of liquid tension on the solid phase and deformation of gel body will be discussed in the following sections.

4.5 FORCE EQUILIBRIUM IN MULTIPHASE MEDIA

4.5.1 Effect of Tensioned Liquid on the Solid Phase

Multiphase bodies in static equilibrium must reach internal force balance between their phases. This law is true for gel bodies as well. When the liquid phase is under tension, the solid phase has to be under compression to balance off the force. This statement is proven by the diagram in Figure 4.9. A line is drawn to cut a gel body into two halves along line X-Y and the free body diagrams are drawn for each. At the cutting plane, the liquid is under tension (shown in black arrows). In fact, the liquid tensile force distributes over the cross section area occupied by the liquid. Each half is under static equilibrium, therefore, and the liquid tensile force must be balanced by compressive force in the solid phase (presented with white arrows). The sum of the liquid tensile force and the solid compression force is equal to zero within the free body. This is also true for the other half which carries the reaction forces of the first half.

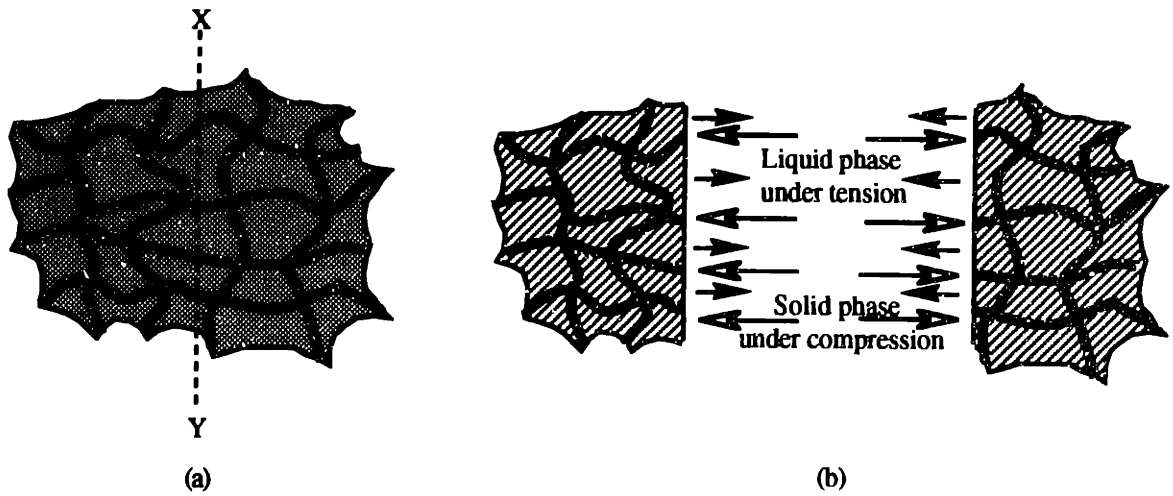

Figure 4.9 (a) A Gel is Cut Along Line X-Y (b) Free Body Diagrams of Both Halves Showing that Liquid Tension Puts the Solid Phase Under Compression

The response of the solid phase under liquid induced compressive stress is an interesting phenomena. In fact, the solid phase is squeezed by the liquid to consolidate.

Figure 4.10 may help to visualize the concept. In this figure, the solid phase is modeled as pure elastic by a network of springs. Suppose the body is small enough such that menisci form in the pores and the springs are not allowed to move freely at this point. The convex shape of the menisci causes the liquid to be under tensile stress. Consequently, the liquid tension, puts the spring network under compression. Once the springs are free, the network immediately consolidates to a length of L_1 from L_0 while the liquid volume remains unchanged at V_0.

Liquid can not be trapped in any of this cell, but must be allowed to transport out of the cells freely. Closed cells prevents the network from deforming and consolidating due to liquid incompressibility.

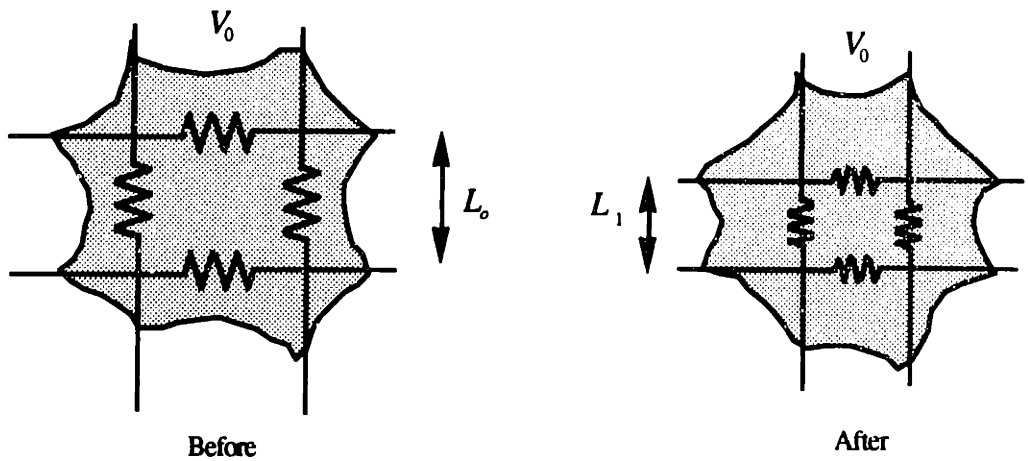

Figure 4.10 Spring Model of the Solid Phase under Liquid Tension

The spring model in Figure 4.10 is just a very simple illustration of the solid phase response to tensile stress in the liquid. In fact, the amount of deformation depends on mechanical properties of the solid phase.

4.5.2 Effective Stress for Saturated Gel and Soil

The phase relationship of gel has been defined at the beginning of this chapter as a network of solid strands enclosing continuous voids which contain liquid and/or air. Saturated gel refers to the condition when the voids are fully occupied with liquid.

Earth soils have some similarity to gels. Soils can be visualized as assemblies of solid particles surrounding continuous voids that contain water and/or air. Again, soils are under saturation if the voids contain only water. The mechanics of soils has long been developed by engineers and scientists in conjunction with human civilization. It is the science of soils under stress which has laid down fundamental rules and codes for various construction foundations along our history. Figure 4.11 illustrates a saturated soil and a gel with cross-section A under axial force F.

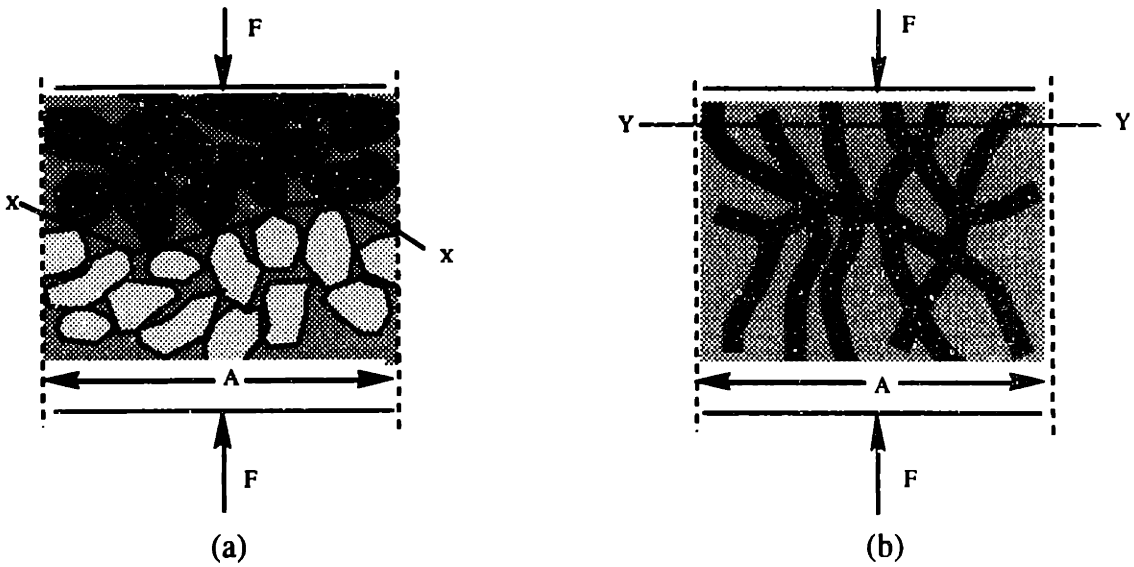

Figure 4.11 Saturated (a) Soil and (b) Gel under an External Stress

Water is incompressible. Therefore, a reduction of volume of saturated soil and gel are only possible if some of the water is allowed to escape from the voids. Normal stress is taken up by the solid phase through an increase in the interparticle force (or compression stress in the network strands) and an increase in liquid pressure. However, shear stress can be resisted only by the skeleton of the soil particles or the strands alone.

Consider plane XX in figure 4.11 passing through points of interparticle contact in the soil. The unevenness of plane XX is relatively small from a perfect flat surface due to small particle size. A normal force F applied over the area A is resisted partly by interparticle force and partly by the pressure (or tension) of the liquid, P. The direction and magnitude of these contact force, R, vary from point to point but can be separated into normal force, F_N, and shear force, F_T.

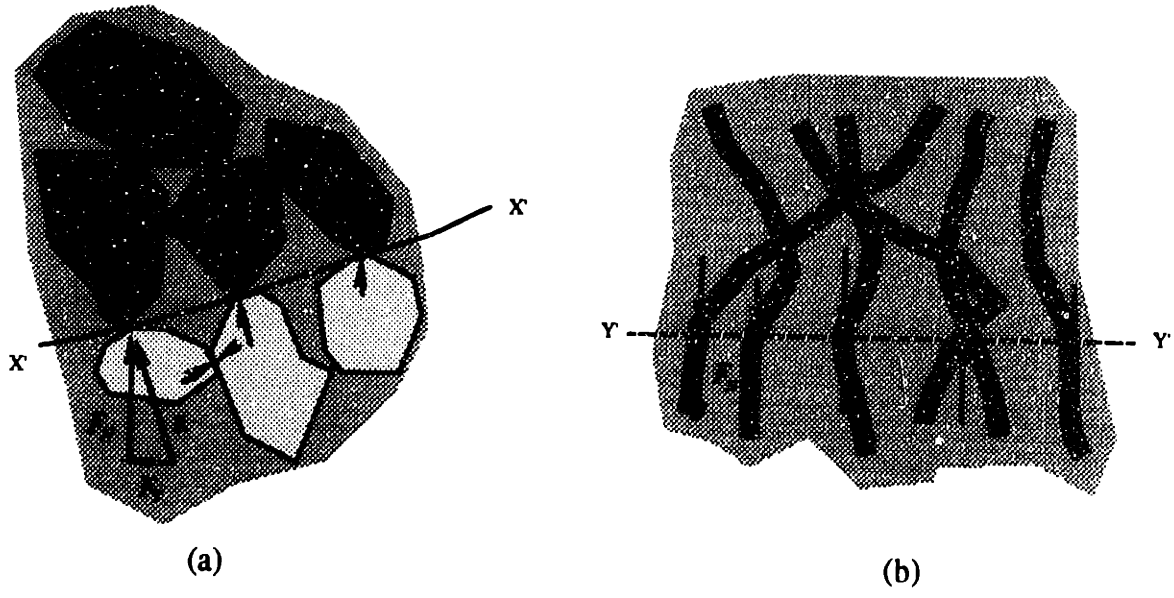

Figure 4.12 (a) Interparticle Force in Soil and (b) Compressive Force in Gel

The area of contact along plane XX is infinitesimal. So, the pore liquid acts on the entire area A. Balancing the forces in the vertical direction gives:

$$F = \sum F_N + PA \tag{4.33}$$

Note that the sign convention of P is negative for compression in the liquid. Divide Equation 4.33 by the total surface area of the soil, A

$$\frac{F}{A} = \sum \frac{F_N}{A} + P \tag{4.34}$$

$$\text{or} \qquad \sigma = \tilde{\sigma}_{soil} + P \tag{4.35}$$

where σ is the total normal stress on the plane of soil mass (positive means tensile stress)

$\tilde{\sigma}_{soil}$ is called effective normal stress (in soil mechanics)

P is the liquid pressure taken as positive for liquid under tensile stress

The error caused by assuming that the interparticle contact area of soil is negligible is typically 1 to 3 percent. It is very important to understand that the effective stress, $\tilde{\sigma}$, does not truly represent the contact stress between two particles (which would be much higher and random).

SATURATED GELS UNDER STRESS

For the case of gels, the surface area of network strands can not be disregarded. The cross section area of a gel consists of area of the solid phase, A_s , and the area of the liquid phase, A_L, i.e.,

$$A = A_s + A_L \tag{4.36}$$

A_s and A_L are related by the pore fraction ε such that

$$\varepsilon = \frac{A_L}{A_s + A_L} \tag{4.37}$$

$$\text{or} \qquad A_L = \frac{\varepsilon}{1-\varepsilon} A_s \tag{4.38}$$

The force balance in vertical direction for the gel is:

$$F = \sum F_N + PA_L \tag{4.39}$$

divided by the total surface area, A, gives:

$$\frac{F}{A} = \sum \frac{F_N}{A} + P\frac{A_L}{A} \tag{4.40}$$

or

$$\sigma = \tilde{\sigma} + \varepsilon P \tag{4.41}$$

Again, the effective stress is not truly representative of the actual stress in the network because it is not calculated from A_s. Using the effective stress will require a correction for the difference.

If the gel dries without being disturbed by an external stress, i.e., $\sigma = 0$ then,

$$\tilde{\sigma} = -\varepsilon P \tag{4.42}$$

According to Equation 4.36, 4.37, and 4.42. True compressive stress in the solid phase can be corrected from effective stress as:

$$\text{True compressive stress in the solid phase} = -\frac{\varepsilon}{1-\varepsilon} P \tag{4.43}$$

4.6 MECHANICS OF GEL

4.6.1 History and Assumption

Biot (1941) developed a theory to describe deformation of saturated and unsaturated Soil assuming that the skeleton was homogeneously elastic. In 1954 and 1962, Biot expanded his theory to cover anisotropy and visco-elasticity of homogeneous and heterogeneous bodies, respectively. It allows for compressibility of the solid and liquid phases and their relative movement to dissipate energy within both phases [14-17]. There

are numerous other researchers who have developed related models. Johnson and Chandler [18-19] have shown that the corrected model are special cases of Biot's theory.

This section is based on the work done by George Scherer from a very interesting series of papers called Drying gel [20-23] and his book called Sol-Gel Science with Brinker C. J. as the co-writer [24]. Scherer has developed an excellent concept of how liquid and solid phases interact in the process of drying and how to prevent cracking for gels in drying process.

Before proceeding to the physics and mathematics of stress and strain, there are a few important assumptions of the liquid-filled porous body as follow:

1) Properties of liquid and solid phases are independent. There is no chemical reaction between the two phases.

2) Both liquid and solid phases are incompressible.

3) The network is always at saturation (or supersaturation). There is no air in the body.

The second assumption may be quite difficult to understand. But, it is very important to the stress-strain relationship of a gel. Liquid and solid phases are incompressible meaning that the volume of liquid and the volume of the solid are conserved under stress. If the liquid is sealed inside the void, then the volume of the system is constant. But, if the liquid is allowed to drain out, then the network could be deformed under stress. And the volume of the liquid drained out must be equal to the volume change of the system. It is analogous to a plastic membrane filled with water in Figure 4.13. The solid phase is equivalent to the membrane. If the membrane is not ruptured, the liquid is trapped inside the bag. But, if the membrane leaks, the liquid could be drained out when the bag is subjected to stress. The volume of the bag is not conserved. But, the volume of the membrane and the liquid remains constant meaning that both the solid and the liquid phases are incompressible.

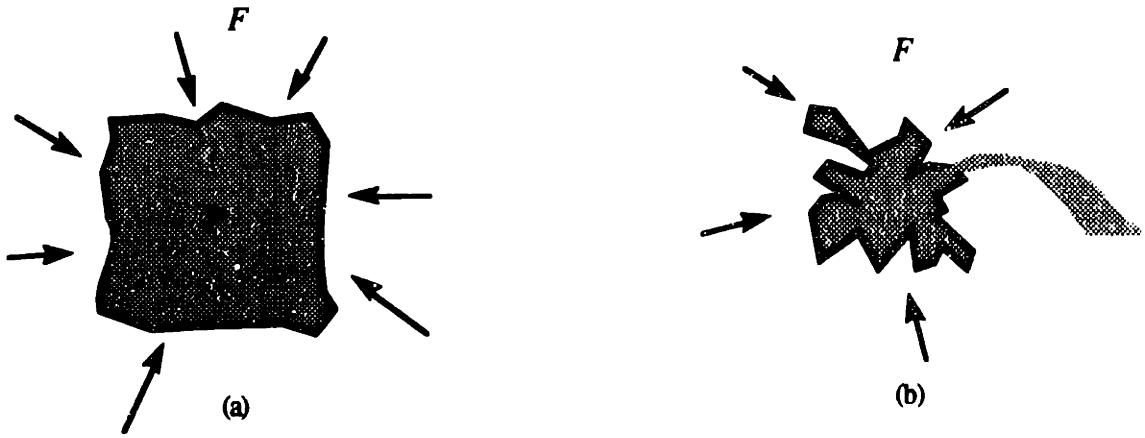

Figure 4.13 Plastic Membrane Filled with Water and Subjected to External Stress
(a) Sealed (b) Leaked Membrane Allows Water to Drain Out
(Both the membrane and the liquid are incompressible)

4.6.2 Elastic Model of Networks Without Liquid

Consider a drained unit cube that contains *no liquid* under external stresses as shown in Figure 4.14. Note that the figure shows the network with empty pores.

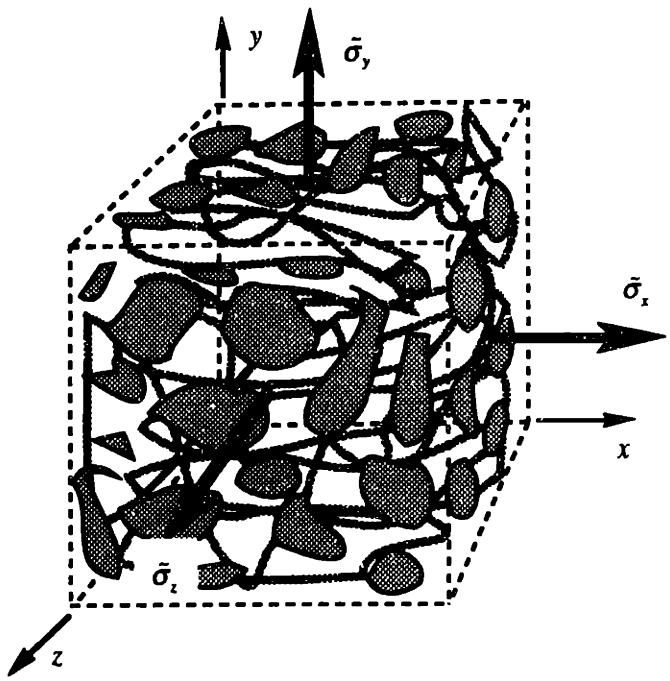

Figure 4.14 Unit Cube with Empty Pores Under Stress

Suppose that the solid phase is elastic where strain varies linearly with applied stress. The strain in x, y, and z-direction ($\varepsilon_x, \varepsilon_y, \varepsilon_z$) can be written as

$$\varepsilon_x = \frac{1}{E_p}\left[\tilde{\sigma}_x - \nu(\tilde{\sigma}_y + \tilde{\sigma}_z)\right] \tag{4.44a}$$

$$\varepsilon_y = \frac{1}{E_p}\left[\tilde{\sigma}_y - \nu(\tilde{\sigma}_x + \tilde{\sigma}_z)\right] \tag{4.44b}$$

$$\varepsilon_z = \frac{1}{E_p}\left[\tilde{\sigma}_z - \nu(\tilde{\sigma}_x + \tilde{\sigma}_y)\right] \tag{4.44c}$$

where E_p is the Young's modulus of the *porous body*. Note that E_p is approximately the product of Young's modulus of the solid phase to the packing fraction $\phi = (1-\varepsilon)$.

ν is the Poisson ratio of the *porous* body (not the solid phase)

$\tilde{\sigma}_x$, $\tilde{\sigma}_y$, $\tilde{\sigma}_z$ are effective stresses in x, y, and z-direction respectively.

Equation 4.44 can be combined using volumetric strain. Volumetric strain, ε_v, is defined as the ratio of the change in volume after the stress is applied to initial volume. ε_v is equal to the sum of linear strains in x, y, and z-directions

$$\varepsilon_v = \varepsilon_x + \varepsilon_y + \varepsilon_z \tag{4.45}$$

If only $\tilde{\sigma}_x$ is applied to the body ($\tilde{\sigma}_y = \tilde{\sigma}_z = 0$), then

$$\varepsilon_v = \varepsilon_x + \varepsilon_y + \varepsilon_x = \frac{(1-2\nu)}{E_p}\tilde{\sigma}_x = (1-2\nu)\varepsilon_x \tag{4.46}$$

The second equality indicates bulk modulus of the *porous* body, K_p, which is defined as the ratio of the stress to volume change of a porous body due to the stress. In elastic material, K_p and E_p are related as

$$K_p = \frac{E_p}{3(1-2\nu)} \tag{4.47}$$

Note that when the Poisson ratio, ν, is equal to 1/2, then the bulk modulus approaches infinity, or the porous body is incompressible.

On the other hand, if deformation of the porous body occurs without volume change such as when the body is incompressible or only pure shear is applied. It is more appropriate to categorize the deformation as under shear stress, not normal stress. In this case, shear modulus, G_p, should be used instead of Young modulus, E_p, (which only applies to normal stress deformation). The relation between shear and Young's modulus is

$$G_p = \frac{E_p}{2(1+\nu)} \tag{4.48}$$

4.6.3 Viscous Model of Networks Without Liquid

In the linear viscous model, **strain rate** varies linearly with applied stress. If a viscous body is subjected to a constant stress, the rate of change of stain is constant. In other words, the body continues to deform at a constant rate. The relation between strain rate and stress can be shown in Equation 4.49

$$\dot{\varepsilon}_x = \frac{1}{F}\left[\tilde{\sigma}_x - N(\tilde{\sigma}_y + \tilde{\sigma}_z)\right] \tag{4.49a}$$

$$\dot{\varepsilon}_y = \frac{1}{F}\left[\tilde{\sigma}_y - N(\tilde{\sigma}_x + \tilde{\sigma}_z)\right] \tag{4.49b}$$

$$\dot{\varepsilon}_z = \frac{1}{F}\left[\tilde{\sigma}_z - N(\tilde{\sigma}_x + \tilde{\sigma}_y)\right] \tag{4.49c}$$

where

$$\dot{\varepsilon}_x = \frac{\partial \varepsilon_x}{\partial t}, \dot{\varepsilon}_y = \frac{\partial \varepsilon_y}{\partial t}, \dot{\varepsilon}_z = \frac{\partial \varepsilon_z}{\partial t} \tag{4.50}$$

F is uniaxial viscosity of the viscous porous network

and N is Poisson ratio for the viscous porous network

In order to find total strain, Equation 4.50 shall be integrated with respect to time.

$$\varepsilon_x = \int \dot{\varepsilon}_x dt = \int \frac{1}{F}\left[\tilde{\sigma}_x - N(\tilde{\sigma}_y + \tilde{\sigma}_z)\right]dt \tag{4.51a}$$

$$\varepsilon_y = \int \dot{\varepsilon}_y dt = \int \frac{1}{F}\left[\tilde{\sigma}_y - N(\tilde{\sigma}_x + \tilde{\sigma}_z)\right]dt \tag{4.51b}$$

$$\varepsilon_z = \int \dot{\varepsilon}_z dt = \int \frac{1}{F}\left[\tilde{\sigma}_z - N(\tilde{\sigma}_x + \tilde{\sigma}_y)\right]dt \tag{4.51c}$$

With only $\tilde{\sigma}_x$ applied ($\tilde{\sigma}_y = \tilde{\sigma}_z = 0$), then

$$\dot{\varepsilon}_x = \frac{1}{F}\tilde{\sigma}_x = \frac{1}{3\eta}\tilde{\sigma}_x \tag{4.52}$$

where η is shear viscosity of the material and $F = 3\eta$

4.6.4. Visco-elastic Model of Networks Without Liquid

The linear visco-elastic model superimposes viscous and elastic responses in Equation 4.49 and 4.52. There are four important parameters in the linear visco-elastic model; F, N, E_p, and ν.

$$\dot{\varepsilon}_x = \frac{1}{F}\left[\tilde{\sigma}_x - N(\tilde{\sigma}_y + \tilde{\sigma}_z)\right] + \frac{1}{E_p}\frac{\partial}{\partial t}\left[\tilde{\sigma}_x - \nu(\tilde{\sigma}_y + \tilde{\sigma}_z)\right] \tag{4.53a}$$

$$\dot{\varepsilon}_y = \frac{1}{F}\left[\tilde{\sigma}_y - N(\tilde{\sigma}_x + \tilde{\sigma}_z)\right] + \frac{1}{E_p}\frac{\partial}{\partial t}\left[\tilde{\sigma}_y - \nu(\tilde{\sigma}_x + \tilde{\sigma}_z)\right] \tag{4.53b}$$

$$\dot{\varepsilon}_z = \frac{1}{F}\left[\tilde{\sigma}_z - N(\tilde{\sigma}_x + \tilde{\sigma}_y)\right] + \frac{1}{E_p}\frac{\partial}{\partial t}\left[\tilde{\sigma}_z - \nu(\tilde{\sigma}_x + \tilde{\sigma}_y)\right] \tag{4.53c}$$

The linear visco-elastic model contains sufficient information to describe the deformation of gels under stresses in most cases. However, its use is rather limited due to complicated mathematics and time-dependent components. The elastic model is not well suit to explain the deformation. Elastic model predicts that the gel shall return to its original shape as external stresses are removed which is impractical. The viscous model is not as mathematically complex and is well suited to capture the plastic deformation of gel bodies. Schrer has found that viscous models sufficiently well describe the deformation of most gels bodies without having to deal with the mathematics of visco-elasticity. Therefore, the viscous model was selected as a base model for this thesis work.

4.6.5. Effect of Liquid Phase in Networks

The presence of liquid phase in a network adds more complexity to the mechanics of a gel body. A simple example to describe hydrostatic effect is to compare the network cube to an imaginary balloon with an outer rubber skin and webs of rubber bridges connected the skin internally. When the balloon is filled with pressurized gas, it expands. And when the gas is evacuated, it flatens out. An important point here is that there must be fluid transport across the system to inflate or flatten the balloon. Were incompressible liquid is kept inside, the total volume of the balloon remains constant although it might be deformed under shear stress.

Similarly, hydrostatic pressure inside a network works like the liquid filled balloon - blowing up or contracting the gels. In this case, Equation 4.49 may be rewritten to incorporate an additional term to describe the presence of pressure in the liquid. By the sign convention of P that tension in liquid is positive, the hydrostatic terms are subtracted from elements in Equation 4.49. As the hydrostatic force is normal to all x, y, and z directions, the cartesian coordinates contains the signatures of hydrostatic pressure artifact as:

$$\dot{\varepsilon}_x = \tfrac{1}{F}\left[\tilde{\sigma}_x - N(\tilde{\sigma}_y + \tilde{\sigma}_z)\right] - cP \tag{4.54a}$$

$$\dot{\varepsilon}_y = \tfrac{1}{F}\left[\tilde{\sigma}_y - N(\tilde{\sigma}_x + \tilde{\sigma}_z)\right] - cP \tag{4.54b}$$

$$\dot{\varepsilon}_z = \tfrac{1}{F}\left[\tilde{\sigma}_z - N(\tilde{\sigma}_x + \tilde{\sigma}_y)\right] - cP \tag{4.54c}$$

c is a constant to be determined. It contains a unit of reversal of compliance. The product of cP represents the strain rate induced by the liquid pressure.

The volumetric strain rate in this case is $\dot{\varepsilon}_v = \dot{\varepsilon}_x + \dot{\varepsilon}_y + \dot{\varepsilon}_z$

$$\dot{\varepsilon}_v = \frac{(1-2N)}{F}\left[\tilde{\sigma}_x + \tilde{\sigma}_y + \tilde{\sigma}_z\right] - 3cP \tag{4.55}$$

$$\dot{\varepsilon}_v = \frac{1}{3\left(\dfrac{F}{3(1-2N)}\right)}\tilde{\sigma} - 3cP$$

$$\dot{\varepsilon}_v = \frac{\tilde{\sigma}}{3K_G} - 3cP \tag{4.56}$$

Here K_G is the bulk viscosity. In order to derive for c, we may impose a boundary condition that no fluid is allowed to escape from the body (no transportation). Therefore, the network is incompressible, thus, $\dot{\varepsilon}_v = 0$. Again, note that incompressible assumption does not mean that the body can not be deformed under shear stress. So, from Equation 4.56,

$$\tilde{\sigma} = 9K_G cP \tag{4.57}$$

From Equation 4.41, $\sigma_x = \tilde{\sigma}_x + \varepsilon P$

in three-dimensional

$$\sigma = \sigma_x + \sigma_y + \sigma_z \tag{4.58}$$

and $$\tilde{\sigma} = \tilde{\sigma}_x + \tilde{\sigma}_y + \tilde{\sigma}_z \tag{4.59}$$

and, Equation 4.41 in 3-Dimension is

$$\tilde{\sigma} = \sigma - 3\varepsilon P \tag{4.60}$$

From Equation 4.58, and 4.59

$$\tilde{\sigma} = \left(\frac{F_x + F_y + F_z}{A} \right) - 3\varepsilon P \tag{4.61}$$

But,

$$F_L = \varepsilon \left(\frac{F_x + F_y + F_z}{3} \right) \tag{4.62}$$

and

$$P = \frac{F_L}{A_L} = \frac{\varepsilon}{3} \left(\frac{F_x + F_y + F_z}{\varepsilon A} \right) = \left(\frac{F_x + F_y + F_z}{3A} \right) \tag{4.63}$$

From putting Equation 4.61 and 4.63 into Equation 4.60

$$\tilde{\sigma} = 3P - 3\varepsilon P = 3(1 - \varepsilon)P \tag{4.64}$$

take Equation 4.64 into Equation 4.57, then

$$3(1 - \varepsilon)P = 9K_G cP$$

or

$$c = \frac{\phi}{3K_G} \tag{4.65}$$

Therefore, the constitute Equation 4.54 become

$$\dot{\varepsilon}_x = \tfrac{1}{F}\left[\tilde{\sigma}_x - N(\tilde{\sigma}_y + \tilde{\sigma}_z)\right] - \frac{\phi}{3K_G}P \tag{4.66a}$$

$$\dot{\varepsilon}_y = \tfrac{1}{F}\left[\tilde{\sigma}_y - N(\tilde{\sigma}_x + \tilde{\sigma}_z)\right] - \frac{\phi}{3K_G}P \tag{4.66b}$$

$$\dot{\varepsilon}_z = \tfrac{1}{F}\left[\tilde{\sigma}_z - N(\tilde{\sigma}_x + \tilde{\sigma}_y)\right] - \frac{\phi}{3K_G}P \tag{4.66c}$$

From 4.57

$$\tilde{\sigma} = \phi\sigma \tag{4.67}$$

So, $\tilde{\sigma}$ varies as packing fraction, ϕ.

Equation 4.66 can be written in terms of total normal stress on the network, σ

$$\dot{\varepsilon}_x = \tfrac{1}{F}\left[\sigma_x - N(\sigma_y + \sigma_z)\right] - \frac{P}{3K_G} \tag{4.68a}$$

$$\dot{\varepsilon}_y = \tfrac{1}{F}\left[\sigma_y - N(\sigma_x + \sigma_z)\right] - \frac{P}{3K_G} \tag{4.68b}$$

$$\dot{\varepsilon}_z = \tfrac{1}{F}\left[\sigma_z - N(\sigma_x + \sigma_y)\right] - \frac{P}{3K_G} \tag{4.68c}$$

Effect of syneresis can be superimposed to Equation 4.68 which are shown by two components in Equation 4.69. The first term, $\dot{\varepsilon}_f$, represents internal driving forces which include syneresis, $\dot{\varepsilon}_s$, and the hydrostatic pressure, P. The second term stands for external stresses acting on the body.

$$\dot{\varepsilon}_x = \dot{\varepsilon}_f + \tfrac{1}{F}\left[\sigma_x - N(\sigma_y + \sigma_z)\right] \tag{4.69a}$$

$$\dot{\varepsilon}_y = \dot{\varepsilon}_f + \tfrac{1}{F}\left[\sigma_y - N(\sigma_x + \sigma_z)\right] \tag{4.69b}$$

$$\dot{\varepsilon}_z = \dot{\varepsilon}_f + \tfrac{1}{F}\left[\sigma_z - N(\sigma_x + \sigma_y)\right] \tag{4.69c}$$

where

$$\dot{\varepsilon}_f = \dot{\varepsilon}_s - \frac{P}{3K_G} \tag{4.70}$$

So, the volumetric strain rate $\varepsilon_v = \varepsilon_x + \varepsilon_y + \varepsilon_z$ is

$$\dot{\varepsilon}_v = 3\left(\dot{\varepsilon}_s - \frac{P}{3K_G}\right) + \frac{(1-2N)}{F}\sigma \tag{4.71}$$

Equation 4.69 are the constitute equation for viscous gels relating strain rate to external stress, syneresis, and internal liquid pressure.

4.7 CONTINUITY

4.7.1 Continuity in Cartesian Coordinate

The liquid tension P in Section 4.6 is not an independent parameter but a function of the meniscus curvature and liquid transport in the body according to Darcy's law. The theory of continuity in this section is only applicable to a saturated body with no presence of gas phase or bubbles.

Figure 4.15 illustrates an small cubic element of gel in a cartesian coordinate. The pore volume for this body are filled with liquid. In other words, the gel is saturated without air bubbles. The volume of the cube, $V = V_S + V_L$, consists of the volume of solid phase, V_s, and that of the liquid phase, V_L, where the bulk density is defined as $\phi = 1 - \varepsilon = \frac{V_s}{V}$ and the porosity as $1 - \phi = \varepsilon = \frac{V_L}{V}$. The cube has a cross section area of $A = A_s + A_L$ where A_s is the cross section area of the solid phase and A_L is that of the liquid phase.

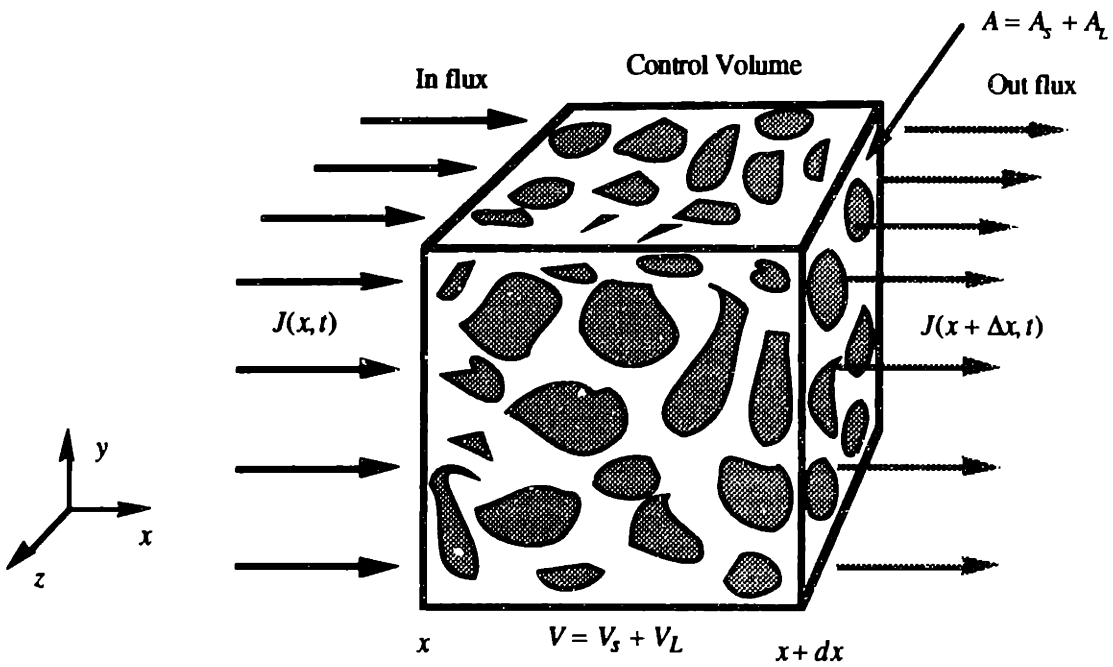

Figure 4.15 A Porous Cubic Control Volume with Liquid Transport

For simplicity, the liquid is allowed to transport in and out of the cube in the x-direction only, liquid mass flowing into the system at x net flowing out at $x+\Delta x$ for a time interval of t to $t+\Delta t$ must equal to mass increase in the system according to the law of mass conservation. For incompressible liquid, conservation of mass may reduce to volume since density is constant. Therefore,

$$V_L(t+\Delta t)-V_L(t)=J(x,t)A\Delta t-J(x+\Delta x,t)A\Delta t \tag{4.72}$$

J is the liquid flux which is defined as volume flow per unit area.

Rearranging Equation 4.72 to find rate of change of the volume per initial volume:

$$\frac{V_L(t+\Delta t)-V_L(t)}{V_L\Delta t}=\frac{J(x,t)A\Delta t-J(x+\Delta x,t)A\Delta t}{V_L\Delta t} \tag{4.73}$$

or

$$\frac{\dot{V}_L}{V_L}=-\frac{A_L}{\varepsilon A_L}\frac{\partial J(x,t)}{\partial x}$$

$$\frac{\dot{V}_L}{V_L}=-\frac{1}{\varepsilon}\frac{\partial J(x,t)}{\partial x} \tag{4.74}$$

Equation 4.74 can be generalized into three dimension as:

$$\frac{\dot{V}_L}{V_L}=-\frac{1}{\varepsilon}\left(\frac{\partial J}{\partial x}+\frac{\partial J}{\partial y}+\frac{\partial J}{\partial z}\right)$$

or, using vector calculus

$$\frac{\dot{V}_L}{V_L}=-\frac{1}{\varepsilon}\nabla\cdot J \tag{4.76}$$

Darcy's law with a sign convention for liquid tension to be positive is $J=\frac{D}{\mu}\nabla P$

$$\frac{\dot{V}_L}{V_L} = -\frac{1}{\varepsilon}\nabla \cdot J$$

$$\frac{\dot{V}_L}{V_L} = -\frac{1}{\varepsilon}\nabla \cdot \left(\frac{D}{\mu}\nabla P\right) \tag{4.77}$$

since volume of liquid must equal to volume of pore, $V_L = V_p$, so

$$\frac{\dot{V}_L}{V_L} = \frac{\dot{V}_p}{V_p} \tag{4.78}$$

and volumetric strain rate of the network is defined as

$$\dot{\varepsilon}_v = \frac{\dot{V}}{V} = \frac{\dot{V}_p}{V} = \frac{\dot{V}_L}{V} = \varepsilon\frac{\dot{V}_L}{V_L} \tag{4.80}$$

Therefore, volumetric strain rate is

$$\dot{\varepsilon}_v = -\nabla \cdot J = -\nabla \cdot \left(\frac{D}{\mu}\nabla P\right) \tag{4.81}$$

but,

$$\dot{\varepsilon}_v = \dot{\varepsilon}_x + \dot{\varepsilon}_y + \dot{\varepsilon}_z = 3\dot{\varepsilon}_f + \frac{1}{3\left(\frac{F}{3(1-2N)}\right)}\sigma = 3\dot{\varepsilon}_f + \frac{\sigma}{3K_G} \tag{4.82}$$

so

$$-\nabla \cdot \left(\frac{D}{\mu}\nabla P\right) = 3\dot{\varepsilon}_f + \frac{\sigma}{3K_G} \tag{4.83}$$

Equation 4.83 is one of Scherer's important findings. It describes the relation between internal pressure distribution in a gel body to external deformation and stresses. For example, the equation can describe the pressure distribution in the liquid phase inside the gel, if the body is squeezed by external stresses. On the other hand, it also explains the deformation behavior of the body where there is liquid transport.

4.7.2 Continuity in Cylindrical Coordinate

For a gel in a cylindrical coordinate with an inner radius r with width dr and thickness h as illustrates in Figure 4.16(a). If a section is taken from the cylindrical element with influx fluid transport of $J(r)$ and out flux $J(r+\Delta r)$ at the radius $r+\Delta r$. The initial volume of the pore in this control volume is $V_L(t)$ at time t and $V_L(t+\Delta t)$ at time $t+\Delta t$ respectively, Figure 4.16(b).

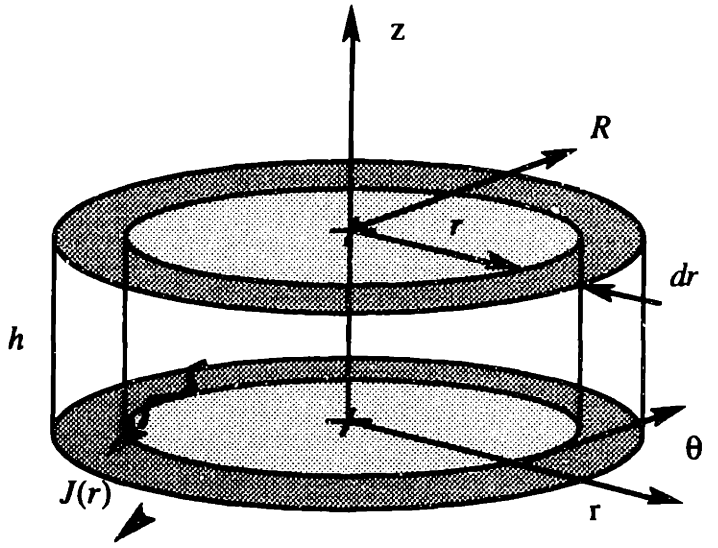

(a)

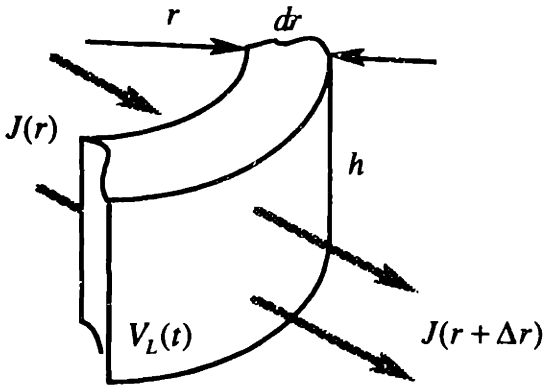

control volume

(b)

Figure 4.16 Fluid Transports in a Gel Body in a Cylindrical Coordinate

According to the law of mass conservation for a control volume with incompressible fluid, the conservation may be written with volume. The change in volume of pores in the cylindrical control volume is:

$$V_L(t+\Delta t) - V_L(t) = J(r,t)2\pi rh\Delta t - J(r+\Delta r,t)2\pi(r+\Delta r)h\Delta t \tag{4.84}$$

divided Equation 4.84 by initial volume $V_L(t)$ at time t

$$\frac{V_L(t+\Delta t) - V_L(t)}{V_L\Delta t} = \frac{J(r,t)2\pi rh\Delta t - J(r+\Delta r,t)2\pi(r+\Delta r)h\Delta t}{V_L\Delta t} \tag{4.85}$$

but, $V_L\Delta t = \varepsilon 2\pi rh\Delta r$, so

$$\frac{V_L(t+\Delta t) - V_L(t)}{V_L\Delta t} = \frac{J(r,t)r - J(r+\Delta r,t)(r+\Delta r)}{\varepsilon r\Delta r}$$

$$\frac{\dot{V}_L}{V_L} = \frac{-1}{\varepsilon r}\frac{\partial(rJ)}{\partial r} \tag{4.86}$$

substitute Darcy's law, $J = \frac{D}{\mu}\nabla P$, in Equation 4.86 gives

$$\frac{\dot{V}_L}{V_L} = \frac{-1}{\varepsilon r}\frac{D}{\mu}\nabla(r\nabla P) \tag{4.87}$$

Volumetric stain can be described as $\dot{\varepsilon}_v = \frac{\dot{V}}{V} = \frac{\dot{V}_p}{V} = \frac{\dot{V}_L}{V} = \varepsilon\frac{\dot{V}_L}{V_L}$, so the continuity equation for a cylindrical coordinate is:

$$\dot{\varepsilon}_v = \frac{-1}{r}\frac{D}{\mu}\nabla(r\nabla P) \tag{4.88}$$

Equation 4.88 relates the local volumetric strain rate to pressure distribution in the gel body. Note that cylindrical systems differs from the cartesian cases in that the radius r effects the distribution of fluid flux in the body.

Volumetric strain rate is the sum of the free strain rate and external stress, $\dot{\varepsilon}_v = 3\dot{\varepsilon}_f + \frac{\sigma}{3K_G}$.

So, continuity in cylindrical coordinate can be written as:

$$\frac{-D}{r\mu}\nabla(r\nabla P) = 3\dot{\varepsilon}_f + \frac{\sigma}{3K_G} \tag{4.89}$$

Liquid tension P is governed by liquid transport according to Darcy's law. The amount of liquid leaving the gel must be equal to the reduction of pore volume.

4.8 CHAPTER SUMMARY

Gel refers to a system of solid networks enclosing liquid between their interconnected pores. As gel dries, a liquid-vapor interface forms at the pore entrances. Due to the physics of wetting, the liquid-vapor interface is curved such that the radius of curvature is on the vapor side. This places the liquid under tensile stress. The liquid tension squeezes the network and causes the solid phase to be under compression. If the network is deformable, it will contract due the compressive stress and liquid will flow out to the exterior. In this case, maximum liquid tension takes places at the liquid-vapor interface and gradually lessens into the interior.

There are many ways to model network response under stresses. But the viscous model, where strain rate is a function of stress, seems to capture shrinkage phenomena without being too mathematically complicated. Constitutive equations for a viscous body under external stresses and internal liquid pressure are:

$$\dot{\varepsilon}_x = \frac{1}{F}\left[\sigma_x - N(\sigma_y + \sigma_z)\right] - \frac{P}{3K_G}$$

$$\dot{\varepsilon}_y = \frac{1}{F}\left[\sigma_y - N(\sigma_x + \sigma_z)\right] - \frac{P}{3K_G}$$

$$\dot{\varepsilon}_z = \frac{1}{F}\left[\sigma_z - N(\sigma_x + \sigma_y)\right] - \frac{P}{3K_G}$$

These constitutive equations can be expanded to capture the relationship between the liquid pressure and volumetric strain rate according to Darcy's law. Therefore, generalized constitute equations for liquid filled network system are:

$$-\nabla \cdot \left(\frac{D}{\mu}\nabla P\right) = 3\dot{\varepsilon}_f + \frac{\sigma}{3K_G} \qquad \text{for cartesian coordinates}$$

and

$$\frac{-D}{r\mu}\nabla(r\nabla P) = 3\dot{\varepsilon}_f + \frac{\sigma}{3K_G} \qquad \text{for cylindrical coordinates}$$

BIBLIOGRAPHY

[1] Kaye, G., Laby, T., *Tables of physical and Chemical Constants*, 14th ed., Longman, 1973, pp. 386.

[2] Greenspan, M., Tschiegg, C., *Radiation induced acoustic cavitation*, Jour. Res. Natl, Bureau of Standards -C. Engng. And Instument. 71 C, pp. 299-312, 1967

[3] Briggs, L., *Limiting negative pressure of water*, J. Appl. Phys., 21, pp. 721-722, 1950.

[4] Line K., Gotoh K., Higashitani K., *Powder Technology Handbook*, Marcel Dekker, New York, Chapter 2.7 (Fermeation) Flow Through Porous Media by Kanaoka C., Kanazawa University, Kanazawa, Japan, pp.139-149

[5] Carman P. C., Trans. Inst. Chem. Eng., 15:150, 1937

[6] Kozeny J., Ind. Eng. Chem., 22:67, 1927

[7] Burke S. P., Plummer W. B., Ind. Eng. Chem, 20:1196, 1928

[8] Ergun S., Chem. Eng. prog., 48:89, 1952

[9] Darcy J., *Les fontaines publiques de la ville de Dijon*, Dalmont, Paris, 1856.

[10] Vibert A., Genie Civil, 115, 84, 1939.

[11] Iwanami I., Trans Soc. Mech. Eng., Japan 6:24, 4., 1940.

[12] Le Rosen A.L., J. Amer. Chem. Soc., 64:1905, 1942.

[13] Emmerich A., Zucker 7, 309, 1954.

[14] Biot M. A., J. Appl. Phys., 12, p.155-164, 1941

[15] Biot M. A., J. Appl. Phys., 25 [11], p.1385-1391, 1954

[16] Biot M. A., Acoustical Soc. Am., 34 [9], p.1254-1264, 1962

[17] Biot M. A., J. Appl. Phys., 33 [4], p.1482-1498, 1962

[18] Johnson D. L., J. Chem. Phys., 77 [3], p.1531-1539, 1982

[19] Chandler R. N., Johnson D. L., J. Appl. Phys., 52 [5], p.3391-3395, 1981

[20] Scherer G.W., *Drying Gels I. General Theory*, Journal of Non-Crystalline Solids 87, p.199-225, North-Holland, Amsterdam, 1986

[21] Scherer G.W., *Drying Gels II. Film and Flat plate*, Journal of Non-Crystalline Solids 89, p.217-238, North-Holland, Amsterdam, 1987

[22] Scherer G.W., *Drying Gels III. Warping plate*, Journal of Non-Crystalline Solids 91, p.83-100, North-Holland, Amsterdam, 1987

[23] Scherer G.W., *Drying Gels IV. Cylinder and Sphere,* Journal of Non-Crystalline Solids 91, p.101-121, North-Holland, Amsterdam, 1987

[24] Brinker C. J., Scherer G. W., *Sol-Gel Science: the physics and chemistry of sol-gel processing*, Academic Presse, New York, 1990

Chapter 5.

Drying of Gels

5.0 INTRODUCTION

Chapter 4 provides the constitutive equations for gels in a cartesian and a cylindrical coordinates by relating the free strain rate to external stresses and internal liquid pressure (tension).

This chapter is a continuing work from Chapter 4 as an application of the constitutive equations to the physics of drying. There are several states in drying of gels. Different boundary conditions will be applied to the constitutive equations at each state to solve for internal liquid pressure, strain, and the network stress. The work in this chapter was originated by Scherer [1-4], but has been modified to provide more insight into the mechanics of drying gels.

Finally, three important parameters governing drying deformation are identified and discussed. These factors are key to a solution that may minimize shrinkage in drying.

5.1 CONSTRAINED FILMS

Consider a thin film of gel with thickness, L, of infinite size casted on a flat and rigid substrate defining x-y plane in Figure 1. There is no stress perpendicular to the free surface, z, so $\sigma_z = 0$. And stresses in x and y direction must be equal, $\sigma_x = \sigma_y$, since the film is under symmetry.

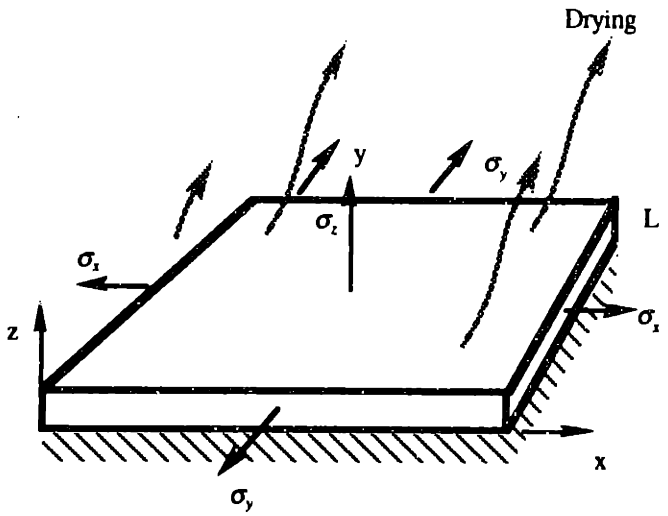

Figure 5.1 Section of Constrained film of Infinite Size on a Rigid Substrate

Strain rate in x-direction is

$$\dot{\varepsilon}_x = \dot{\varepsilon}_f + \tfrac{1}{F}\left[\sigma_x - N(\sigma_y + \sigma_z)\right] \tag{5.1}$$

since $\sigma_x = \sigma_y$, so Equation 5.1 reduces to

$$\dot{\varepsilon}_x = \dot{\varepsilon}_f + \frac{(1-N)}{F}\sigma_x \tag{5.2}$$

Integrate Equation 5.2 to obtain 'average' strain rate across the thickness, $\langle \dot{\varepsilon}_x \rangle$:

$$\int_0^L \dot{\varepsilon}_x dz = L\langle \dot{\varepsilon}_x \rangle = \int_0^L \dot{\varepsilon}_f dz + \tfrac{(1-N)}{F}\int_0^L \sigma_x dz \tag{5.3}$$

The last term on right hand side has to be zero since the body is in equilibrium. Thus, Equation 5.3 reduces to

$$\langle \dot{\varepsilon}_x \rangle = \frac{1}{L}\int_0^L \dot{\varepsilon}_f dz$$

but, $\dot{\varepsilon}_f = \dot{\varepsilon}_s - \dfrac{P}{3K_G}$, therefore,

$$\langle \dot{\varepsilon}_x \rangle = \frac{1}{L}\left[L\dot{\varepsilon}_s + \frac{1}{3K_G}\int_0^L P dz \right]$$

$$\langle \dot{\varepsilon}_x \rangle = \dot{\varepsilon}_s + \frac{\langle P \rangle}{3K_G} \tag{5.4}$$

Here, $\langle P \rangle = \frac{1}{L}\int_0^L P dz$ can be interpreted as 'average' liquid pressure along the thickness. Equation 5.4 relates the 'average' strain rate, $\langle \dot{\varepsilon}_x \rangle$, in x-direction across the thickness to the syneresis strain rate and the bulk effect of the 'average' liquid pressure, $\langle P \rangle$, across the thickness.

Local stress in the body arises with local strain difference, $\dot{\varepsilon}_x$, and the 'average' strain rate, $\langle \dot{\varepsilon}_x \rangle$. The local stress can be estimated from Equation 5.2 as

$$\sigma_x = \frac{F}{(1-N)}\left[\dot{\varepsilon}_x - \dot{\varepsilon}_f \right]$$

using 'average' strain rate as a representative of local strain rate, then

$$\sigma_x = \frac{F}{(1-N)}\left[\langle \dot{\varepsilon}_x \rangle - \dot{\varepsilon}_f \right]$$

$$\sigma_x = \frac{F}{(1-N)}\left[\left(\dot{\varepsilon}_s - \frac{\langle P \rangle}{3K_G} \right) - \left(\dot{\varepsilon}_s - \frac{P}{3K_G} \right) \right]$$

so,

$$\sigma_x = \frac{F}{3K_G(1-N)}\left(P - \langle P \rangle \right) \tag{5.5}$$

Therefore, local stress depends on the difference of the local tension and the 'average' liquid tension. If the local and the 'average' pressures are equal, then local stress approaches zero.

The volumetric strain rate is the sum of strain rate in all x, y, and z direction, $\dot{\varepsilon}_v = \dot{\varepsilon}_x + \dot{\varepsilon}_y + \dot{\varepsilon}_z$.

$$\dot{\varepsilon}_v = 3\dot{\varepsilon}_f + \frac{\sigma}{3K_G}$$

$$\dot{\varepsilon}_v = 3\left(\dot{\varepsilon}_s - \frac{P}{3K_G}\right) + \frac{\sigma}{3K_G} \tag{5.6}$$

in this case there is no stress in z-direction

$$\sigma = \sigma_x + \sigma_y + \sigma_z = 2\sigma_x$$

so,

$$\dot{\varepsilon}_v = 3\dot{\varepsilon}_s - \frac{1}{K_G}\left(P - \frac{2\sigma_x}{3}\right)$$

$$\dot{\varepsilon}_v = 3\dot{\varepsilon}_s - \frac{1}{K_G}\left(P - \frac{2(1-2N)}{3(1-N)}(P - \langle P\rangle)\right)$$

$$\dot{\varepsilon}_v = 3\dot{\varepsilon}_s - \frac{1}{K_G}[\beta P + (1-\beta)\langle P\rangle] \tag{5.7}$$

where $\beta = \frac{(1+N)}{3(1-N)}$. If N is small then, $\beta \to \frac{1}{3}$

Putting Equation 5.6 into $-\nabla\cdot\left(\frac{D}{\mu}\nabla P\right) = 3\dot{\varepsilon}_f + \frac{\sigma}{3K_G} = \dot{\varepsilon}_v$ gives:

$$3\dot{\varepsilon}_s - \frac{1}{K_G}[\beta P + (1-\beta)\langle P\rangle] = -\frac{D}{\mu}\frac{\partial^2 P}{\partial z^2}$$

so, pressure distribution in the liquid phase can be described with Equation 5.8 as:

$$\frac{D}{\mu}\frac{\partial^2 P}{\partial z^2} - \frac{[\beta P + (1-\beta)\langle P\rangle]}{K_G} = 3\dot{\varepsilon}_s \tag{5.8}$$

5.2 UNCONSTRAINED BODIES

5.2.1 Slabs

In this section, an unconstrained gel with infinite size in x and y-direction and thickness 2L is focused, Figure 5.2. The slab is drying from both top and bottom sides at an equal rate. The slab is free to deform and external stress at any cross section in zero ($\sigma = \sigma_x = \sigma_y = \sigma_z = 0$).

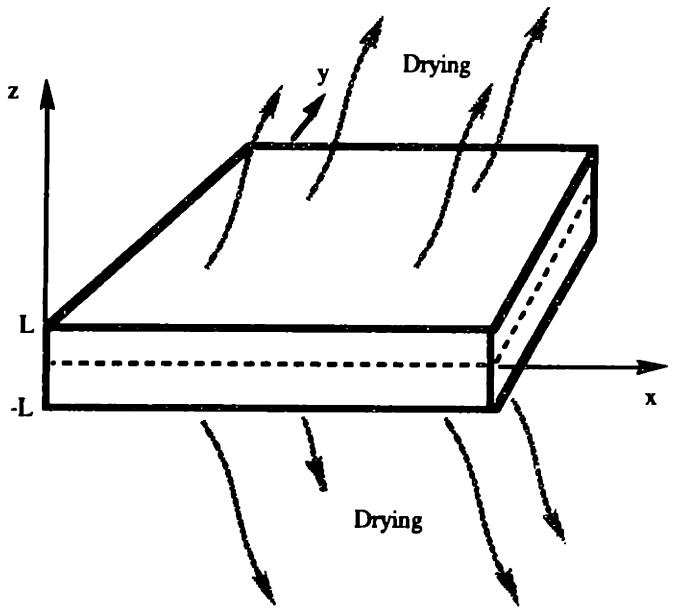

Figure 5.2 Drying of Unconstrained Slab from Both Sides

The fact that total external stress is zero reduces Equation 5.6 to

$$\dot{\varepsilon}_v = 3\left(\dot{\varepsilon}_s - \frac{P}{3K_G}\right)$$

So, $-\nabla\cdot\left(\frac{D}{\mu}\nabla P\right) = 3\dot{\varepsilon}_f + \frac{\sigma}{3K_G} = \dot{\varepsilon}_v$ can be written as

$$-\nabla\cdot\left(\frac{D}{\mu}\nabla P\right) = 3\left(\dot{\varepsilon}_s - \frac{P}{3K_G}\right) \tag{5.9}$$

Surfaces of drying are perpendicular to the z axis, so liquid pressure, P, is only a function of distance in the z-direction. In other words $\frac{\partial P}{\partial x} = \frac{\partial P}{\partial y} = 0$. So, Equation 5.9 may be rewritten as:

$$\frac{\partial^2 P}{\partial z^2} - \left(\frac{\mu}{DK_G}\right)P + \frac{3\mu}{D}\dot{\varepsilon}_s = 0 \tag{5.10}$$

which is a second order differential equation describing the pressure distribution in the liquid throughout the body. The generalized solution for Equation 5.10 is:

$$P(z) = 3K_G\dot{\varepsilon}_s + C_1 e^{z\sqrt{\beta}} + C_2 e^{-z\sqrt{\beta}} \tag{5.11}$$

where $\beta = \frac{\mu}{DK_G}$

Constant C_1 and C_2 will be solved with boundary conditions.

Step 1: Supersaturated Gel

Drying arises when gel is supersaturated meaning that the liquid-vapor interface does not yet reach the network boundary. So, the liquid tension at the network boundary of both top and bottom sides must be zeros or, mathematically $P(-L,t) = P(L,t) = 0$. It is very important to understand that drying starts with uncaptured liquid outside the network.

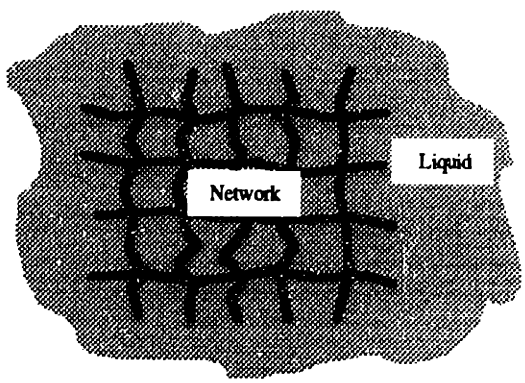

Figure 5.3 Supersaturated Gel

Applying $P(-L,t) = P(L,t) = 0$ to Equation 5.11 and solve for C_1 and C_2 gives:

$$P(z,t) = 3K_G\dot{\varepsilon}_s\left[1 - \frac{\cosh(z\sqrt{\beta})}{\cosh(L\sqrt{\beta})}\right] \tag{5.12}$$

Substitute the pressure distribution from Equation 5.12 into $\dot{\varepsilon}_v = 3\left(\dot{\varepsilon}_s - \frac{P}{3K_G}\right)$, yields local volumetric strain rate, $\dot{\varepsilon}_v(z)$ of

$$\dot{\varepsilon}_v(z) = 3\dot{\varepsilon}_s\left[\frac{\cosh\left(z\sqrt{\beta}\right)}{\cosh\left(L\sqrt{\beta}\right)}\right] \tag{5.14}$$

and the effective stress on the solid phase:

$$\tilde{\sigma}_x = \tilde{\sigma}_y = \tilde{\sigma}_z = -\varepsilon P$$

$$\tilde{\sigma}_x = \tilde{\sigma}_y = \tilde{\sigma}_z = -3\varepsilon K_G\dot{\varepsilon}_s\left[1 - \frac{\cosh(z\sqrt{\beta})}{\cosh(L\sqrt{\beta})}\right] \tag{5.15}$$

Plots of liquid pressure, local strain rate, and effective stress are shown in Figure 5.4.

It is clear from Figure 5.4 that the liquid pressure, local strain rate, and effective stress on the network depends strongly on syneresis rate, $\dot{\varepsilon}_s$. The liquid is under compression throughout the entire body. The pressure is zero at the network interface and maximum pressure is located at the center of the body. Local strain rate is maximum at the network surface and reduce exponentially to the center of the body. Effective stress is highest at the center plane of the body as liquid is squeezed out.

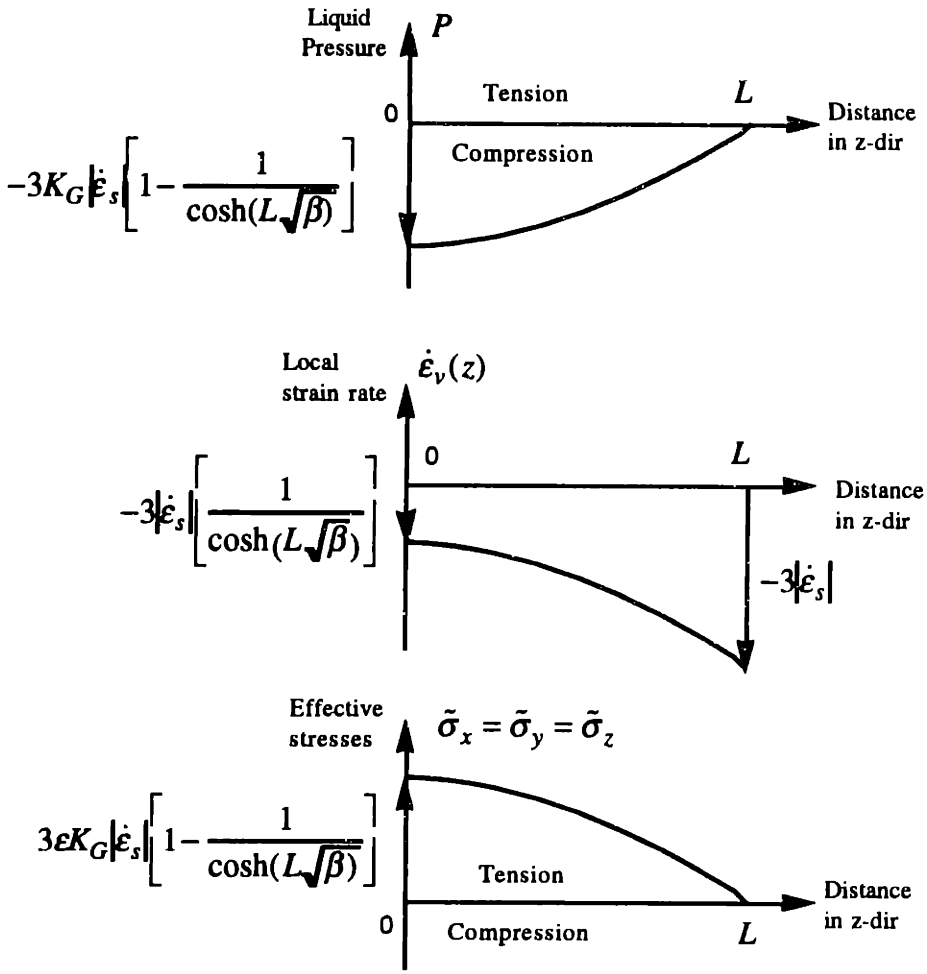

Figure 5.4 Distribution of Liquid Pressure, Local Strain Rate, and Effective Stress for Supersaturated Gel

Step 2: Saturated Gel

As drying progresses, the liquid-vapor interface eventually reaches to the network interim. At this point, the gel is at saturation meaning the volume of the liquid is equal to the volume of the pores. While drying continues, the liquid-vapor interface breaks up into menisci to cover individual pore entrances. Initially, the menisci have no curvature, thus develop neither tension nor compression on the liquid.

As drying continues, the liquid-vapor interfaces are about to recede into the pores placing the menisci in a curvature by the physics of wetting. The menisci are bent such that the radii of curvature are in the vapor phase. Such curvatures place the liquid under tension. The magnitude of liquid tension depends on the radius of curvature of the meniscus which is governed by the pore radius and the contact angle between the liquid and the solid according to Laplace's equation, Section 4.2.1.

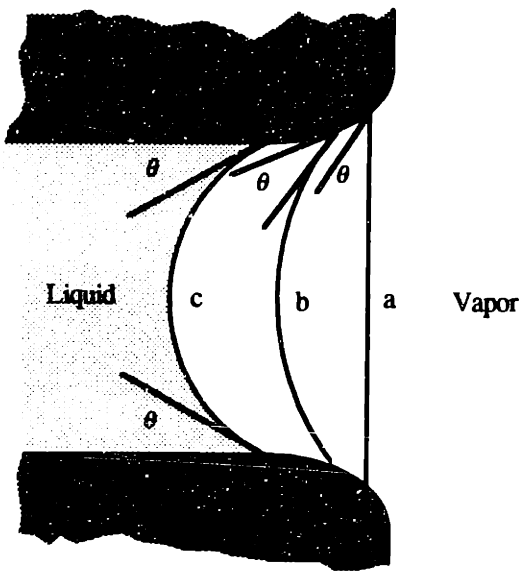

Figure 5.5 Liquid-vapor Interface is Curved Due to the Physics of Wetting as Receding into the Pore

Figure 5.5 illustrates the mechanism in which the liquid-vapor interface recedes into the pore. The pore entrance has a radius, r. Although the contact angle, θ, is rather fixed by the surface chemistry between the liquid and the solid phases, the radius of curvature of the liquid-vapor front depends on the location of the contact point. At first the liquid-vapor front has no curvature. So the liquid is neither under tension or compression. As drying continues and evaporates some of the liquid at the interface, the front is forced to move into the pore. This changes the radius of curvature of the liquid-vapor interface from infinite at point (a) to a finite value at point (b). As a consequence, the liquid starts to be under tensile stress. A pressure gradient now exists between the interior liquid and the exterior. If the solid phase is not deformable, there will be no liquid flow to the exterior and the tensile stress will be equally distributed throughout the liquid phase canceling the pressure

difference. However, if the network is deformable, liquid is allowed to transport from the interior to the exterior and feed the liquid-vapor interface at the pore entrance. In this case, there exists liquid pressure gradient according to Darcy's law, Figure 5.6. Drying continues at saturation condition until the network develops sufficient strength to bare the liquid tension load or the evaporation rate is excessive such that the network can not cope up with the drying rate. In such case, the liquid-vapor interfaces is curved to minimum, at point (c) and posts maximum tension on to the liquid before moving into the interior.

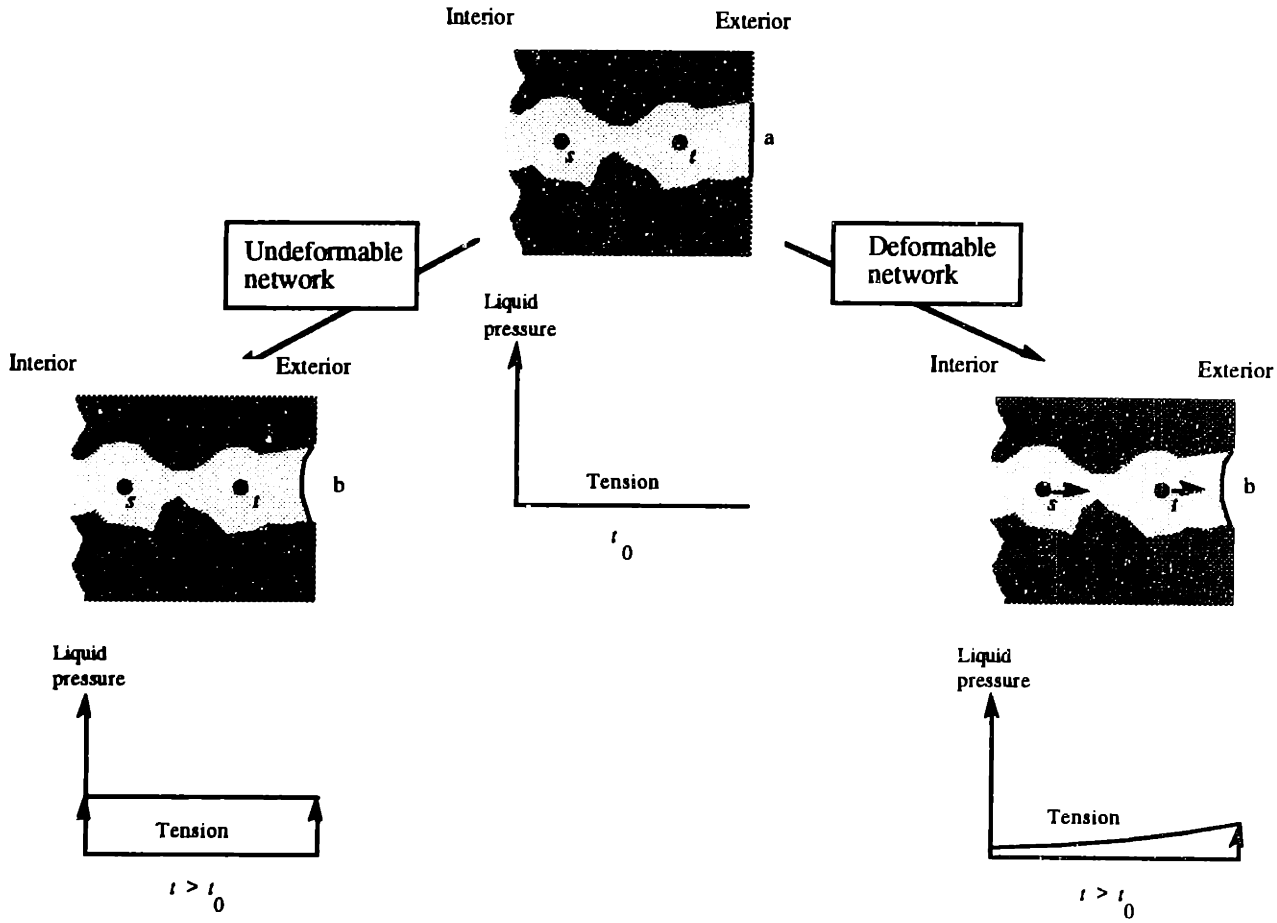

Figure 5.6 Liquid Pressure (tension) Distribution and Liquid Transportation for
1) undeformable network 2) deformable network

It is very important to realize that saturation drying requires that the network be *deformable* such that the volume of liquid flows out from the interior balances with the volumetric contraction of the gel body. During the whole course of drying, *deformation only takes place in sc uration drying*. Once the network stops contracting, there will be no further deformation although the liquid evaporation continues to empty the pores.

There are two important equilibrium mechanisms to be satisfied in saturation drying.

1) LIQUID TRANSPORT RATE AND LIQUID TENSION GRADIENT.

Generally drying rate depends on the vapor pressure and could be assume constant if the body is at saturation. Liquid flow rate from the interior must balance with the drying rate. Too much flow causes flood at the exterior (which is unlikely to happen). Too little flow forces the liquid-vapor to move into the network's interior. In saturated drying, liquid flow rate is regulated by the liquid tension at the pore entrance to match required drying rate. To obtain more liquid flow rate, the liquid-vapor interface protrudes into the pore and reduces its radius of curvature thus increases the liquid tension. And vice versa, it increases the radius of curvature to ease out the liquid flow. So, the radius of curvature of the meniscus is somewhere between point (a) and (c) according to Figure 5.5 .

In case the drying rate is excessive and although the radius of curvature has reached its minimum at c and still couldn't catch up with the required drying rate. At this point the liquid-vapor recedes into the network's interior and saturation ceases. Once the liquid phase is discontinuous, it can not place the solid phase under compression and shrinkage terminates. In other words, the shrinkage terminates when the liquid-vapor interface moves into the gel interior.

Mathematically, when the liquid-vapor front regulates the liquid flow rate, liquid tension at the gel boundary is P_E or $P(-L,t) = P(L,t) = P_E$. Solving Equation 5.11 gives liquid tension distribution

$$P(z,t) = 3K_G\dot{\varepsilon}_s + (P_E - 3K_G\dot{\varepsilon}_s)\left[\frac{\cosh(z\sqrt{\beta})}{\cosh(L\sqrt{\beta})}\right] \tag{5.16}$$

rearranging Equation 5.16 gives

$$P(z,t) = 3K_G\dot{\varepsilon}_s\left[1 - \frac{\cosh(z\sqrt{\beta})}{\cosh(L\sqrt{\beta})}\right] + P_E\left[\frac{\cosh(z\sqrt{\beta})}{\cosh(L\sqrt{\beta})}\right] \tag{5.17}$$

Equation 5.17 indicates that the liquid pressure distribution is influenced by two mechanisms 1) syneresis contraction, $\dot{\varepsilon}_s$, and 2) the capillary at the pore entrance, P_E. The first term on the right hand side is exactly the same as Equation 5.12. The second term refers to capillarity and the pressure gradient governed by Darcy's law.

2) LIQUID TRANSPORT RATE AND MAGNITUDE OF LIQUID TENSION

The second equilibrium in saturation drying is the balance of contracted volume of the network and the volume of liquid which has flowed to the exterior.

Liquid transportation results from the existence of a pressure gradient where the liquids is drained from the interior to feed into the evaporate zone at the exterior. As the liquid is under tensile stress and starts to leave the interior pores, the solid phase is placed under compression and starts to contract under a condition that the volume of liquid leaving the network must equal to the volumetric deformation of the solid phase. If not, air bubbles will be generated. Mathematical description of the volume balance is:

$$-2A\dot{V}_E = \int_{-L}^{L}\left(3\dot{\varepsilon}_s - \frac{\dot{P}}{K_G}\right)Adz \tag{5.18}$$

The left hand side of Equation 5.18 represents the rate of liquid leaving the network by evaporation on the top and bottom surfaces. The right hand side represents total volumetric change of the gel due to deformation.

substitute pressure distribution (Equation 5.16) into Equation 5.18

$$-2A\dot{V}_E = \int_{-L}^{L}\left\{3\dot{\varepsilon}_s - \frac{1}{K_G}\left(3K_G\dot{\varepsilon}_s + (P_E - 3K_G\dot{\varepsilon}_s)\left[\frac{\cosh(z\sqrt{\beta})}{\cosh(L\sqrt{\beta})}\right]\right)\right\}Adz$$

gives:

$$P_E = \frac{K_G\sqrt{\beta}\dot{V}_E}{\tanh(L\sqrt{\beta})} + 3K_G\dot{\varepsilon}_s \tag{5.19}$$

Equation 5.19 indicates that the magnitude of liquid tension at the pore entrance depends on drying rate. In other words, Equation 5.19 reviews the balance of liquid transport rate to magnitude of liquid tension according to Equation 5.16 and 5.19.

Putting P_E back to Equation 5.16 gives

$$P(z,t) = 3K_G\dot{\varepsilon}_S + K_G\sqrt{\beta}\dot{V}_E\frac{cosh(z\sqrt{\beta})}{sinh(L\sqrt{\beta})} \tag{5.20}$$

Equation 5.20 clearly indicates that liquid pressure distribution depends on the drying rate.

To calculate for volumetric strain rate, Equation 5.20 can be substituted into $\dot{\varepsilon}_v = 3\left(\dot{\varepsilon}_s - \frac{P}{3K_G}\right)$, so the local volumetric strain rate of the body, $\dot{\varepsilon}_v(z)$, is

$$\dot{\varepsilon}_v(z) = -\sqrt{\beta}\dot{V}_E\frac{\cosh(z\sqrt{\beta})}{\sinh(L\sqrt{\beta})} \tag{5.21}$$

Equation 5.21 indicates that volumetric strain rate of a network is generally a linear function of the drying rate. Additionally, the volumetric strain rate is a function of the z-direction where it maximizes at the exterior of the network. The volumetric strain rate reduces monotonically toward the center of the body.

Local stress in the solid phase is governed solely by the liquid pressure in the network, where

$$\tilde{\sigma}_x = \tilde{\sigma}_y = \tilde{\sigma}_z = -\varepsilon P = -\varepsilon\left(3K_G\dot{\varepsilon}_s + K_G\sqrt{\beta}\dot{V}_E\frac{\cosh(z\sqrt{\beta})}{\sinh(L\sqrt{\beta})}\right) \tag{5.22}$$

Equation 5.22 indicates that maximum local stress in the solid phase and the maximum liquid tension take place at the exterior of the network.

In summary, as long as the network contraction can cope with the liquid flow demand for drying, the system is always at saturation and the liquid-vapor interface remains at the pore opening. The rate of liquid flow is governed by the radius of curvature at the liquid-vapor interface. Radius of curvature reduces to obtain higher flow rate. Saturation can last for a long time in the case where the drying rate is slow and the network deforms plastically. This is the main shrinkage mechanism in gel drying. Saturation ceases when the network gains its strength and resists contraction.

Step 3: Subsaturated Drying

As the network gains its strength and resist contraction, the liquid-vapor front increases liquid tension by reducing the radius of curvature at the meniscus. But the minimum radius of curvature is limited by the pore radius and contact angle corresponding to the maximum liquid tension, P_R, at the liquid-vapor interface (point (c) in Figure 5.5). P_R is characterized by Laplace's equation as

$$P_R = \frac{2\gamma_{LV}\cos\theta}{R_{pore}} \tag{5.23}$$

where γ_{LV} is the liquid-vapor specific energy

R_{pore} is the pore radius

and θ is the contact angle between the solid and the liquid phase.

Suppose the liquid tension at the network boundary is $P(-L,t) = P(L,t) = P_R$. Equation 5.11 has a solution of

$$P(z,t) = 3K_G\dot{\epsilon}_S + (P_R - 3K_G\dot{\epsilon}_S)\left[\frac{\cosh(z\sqrt{\beta})}{\cosh(L\sqrt{\beta})}\right] \tag{5.24}$$

After the liquid tension reaches P_R, the liquid-vapor front moves into the network interior. The pore ahead of the liquid-vapor front is fully saturated with liquid at maximum tensile stress while the pore behind the front is empty. The difference in stress in front and behind the liquid-vapor interface is tremendous and could cause the body to crack. There may be several cracks at the same time but they all travel slowly with the liquid-vapor interface from the exterior to the interior of the body.

Shrinkage does not take place in subsaturation drying since the network has already developed sufficient strength to resist the contraction.

5.2.2 Cylinders

Drying of cylinders has some similarities to slabs but differs in coordinate system and boundary conditions.

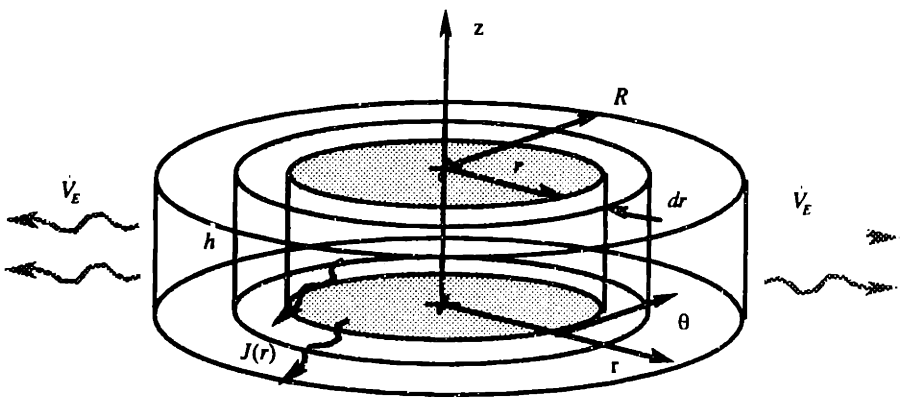

Figure 5.7 Drying of Cylindrical of Gel

Consider a unconstrained gel cylinder with thickness h and outer radius R drying only from the circumference area at the rate of $\dot{V}_E$ as in Figure 5.7. There is no stress perpendicular to free surface so, $\sigma_x = \sigma_y = \sigma_z = 0$. According to the constitute equation in the cylindrical coordinates in Equation 4.89

$$\frac{-D}{r\mu}\nabla(r\nabla P) = 3\dot{\varepsilon}_f + \frac{\sigma}{3K_G}$$

Liquid tension is only a function of the radius r, therefore $\frac{\partial P}{\partial \theta} = \frac{\partial P}{\partial z} = 0$. So, Equation 4.89 can be written as:

$$\frac{-D}{r\mu}\frac{\partial}{\partial r}\left(r\frac{\partial P}{\partial r}\right) = 3\dot{\varepsilon}_f + \frac{\sigma}{3K_G}$$

$$\frac{-D}{r\mu}\left(r\frac{\partial^2 P}{\partial r^2} + \frac{\partial P}{\partial r}\right) = 3\dot{\varepsilon}_f + \frac{\sigma}{3K_G} \qquad (5.25)$$

For the case of unconstrained gel, $\sigma_x = \sigma_y = \sigma_z = 0$, Equation 5.23 is simplified to

$$\frac{-D}{r\mu}\left(r\frac{\partial^2 P}{\partial r^2} + \frac{\partial P}{\partial r}\right) = 3\left(\dot{\varepsilon}_s - \frac{P}{3K_G}\right)$$

$$\frac{-D}{\mu}\left(\frac{\partial^2 P}{\partial r^2} + \frac{1}{r}\frac{\partial P}{\partial r}\right) = 3\dot{\varepsilon}_s - \frac{P}{K_G}$$

$$\frac{\partial^2 P}{\partial r^2} + \frac{1}{r}\frac{\partial P}{\partial r} - \frac{\mu}{DK_G}P = -3\frac{\mu}{D}\dot{\varepsilon}_s$$

$$\frac{\partial^2 P}{\partial r^2} + \frac{1}{r}\frac{\partial P}{\partial r} - \beta P = -3K_G\beta\dot{\varepsilon}_s \qquad \text{,where } \beta = \frac{\mu}{DK_G} \qquad (5.26)$$

Equation 5.26 is a modified Bessel function with a generalize solution of

$$\frac{d^2y}{dx^2}+\frac{1}{x}\frac{dy}{dx}-\left(\lambda^2+\frac{\eta^2}{x^2}\right)y=0 \tag{5.27}$$

The Bessel function has zeroth-order, $\eta=0$, with a general solution of

$$y=C_1I_0(x)$$

$$y=C_1\left[1+\frac{(\lambda x)^2}{2^2(1!)^2}+\frac{(\lambda x)^4}{2^4(2!)^4}+\frac{(\lambda x)^6}{2^6(3!)^6}+\ldots\right] \tag{5.28}$$

where C_1 is a constant to be determined

Therefore, the solution to Equation 5.28 is

$$P=3K_G\dot{\varepsilon}_s+C_1I_0\left(r\sqrt{\beta}\right)$$

$$P=3K_G\dot{\varepsilon}_s+C_1\left[1+\frac{\left(\sqrt{\beta}r\right)^2}{2^2(1!)^2}+\frac{\left(\sqrt{\beta}r\right)^4}{2^4(2!)^4}+\frac{\left(\sqrt{\beta}r\right)^6}{2^6(3!)^6}+\ldots\right]$$

$$P=3K_G\dot{\varepsilon}_s+C_1\left[1+\frac{\left(\sqrt{\beta}r\right)^2}{4}+\frac{\left(\sqrt{\beta}r\right)^4}{256}+\frac{\left(\sqrt{\beta}r\right)^6}{2985984}+\ldots\right]$$

Takes the first three terms in the series as an approximate solution

$$P=3K_G\dot{\varepsilon}_s+C_1\left[1+\frac{\beta r^2}{4}+\frac{\beta^2r^4}{256}\right] \tag{5.29}$$

where C_1 is to be determined by boundary condition

Step 1: Supersaturated Gel

In this case the liquid-vapor interface does not yet reach the network perimeter, therefore, the liquid pressure at the perimeter of the gel is zero, $P(r = R) = 0$. It is very important at this point to understand that drying starts with uncaptured liquid outside the gel body. Internal liquid transport in the network takes place by syneresis only.

For $P(r = R) = 0$, Equation 5.29 gives

$$0 = 3K_G\dot{\varepsilon}_s + C_1\left[1 + \frac{\beta R^2}{4} + \frac{\beta^2 R^4}{256}\right]$$

so,
$$C_1 = \frac{-3K_G\dot{\varepsilon}_s}{\left[1 + \frac{\beta R^2}{4} + \frac{\beta^2 R^4}{256}\right]}$$

and,
$$P = 3K_G\dot{\varepsilon}_s - \frac{3K_G\dot{\varepsilon}_s}{\left(1 + \frac{\beta R^2}{4} + \frac{\beta^2 R^4}{256}\right)}\left[1 + \frac{\beta r^2}{4} + \frac{\beta^2 r^4}{256}\right] \qquad (5.30)$$

Liquid pressure distribution is illustrated in Figure 5.8.

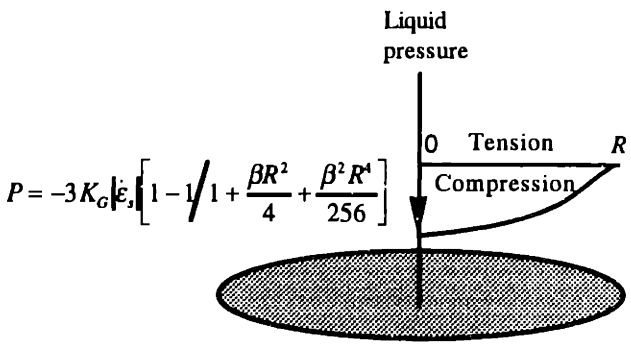

Figure 5.8 Pressure Distribution in Supersaturated Cylinder

So, volumetric stain rate for saturated cylindrical gel is

$$\dot{\varepsilon}_v = 3\dot{\varepsilon}_s - \frac{P}{K_G}$$

$$\dot{\varepsilon}_v = 3\dot{\varepsilon}_s \frac{\left[1 + \frac{\beta r^2}{4} + \frac{\beta^2 r^4}{256}\right]}{\left[1 + \frac{\beta R^2}{4} + \frac{\beta^2 R^4}{256}\right]} \tag{5.31}$$

Strain rate distribution is depicted in Figure 5.9. Maximum strain rate takes place at the interim of the network due to highest liquid pressure.

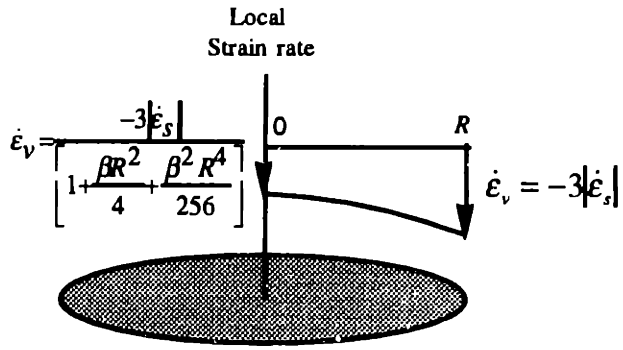

Figure 5.9 Distribution of strain rate

For saturated cylindrical gel, local volumetric strain rate depends on $\beta = \frac{\mu}{DK_G}$ and syneresis. If there is no syneresis, the volumetric strain rate is zero everywhere in the body.

Effective stress born by solid phase in the network is a strong function of syneresis as well as the porosity and fluid viscosity. The stress distribution is shown in Figure 5.10.

$$\tilde{\sigma}_x = \tilde{\sigma}_y = \tilde{\sigma}_z = -3\varepsilon\dot{\varepsilon}_s \frac{\left[1 + \frac{\beta r^2}{4} + \frac{\beta^2 r^4}{256}\right]}{\left[1 + \frac{\beta R^2}{4} + \frac{\beta^2 R^4}{256}\right]} \tag{5.32}$$

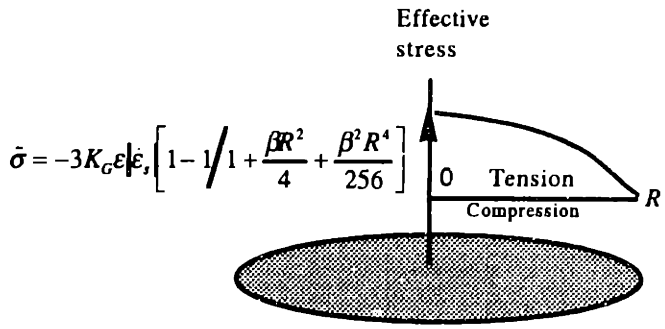

Figure 5.10 Distribution of Effective Stress in a Supersaturated Cylinder

Case 2: Saturated Gel

Saturation takes place as the liquid-vapor interface reaches the network exterior. All the pores in saturated gel are covered with curved liquid-vapor menisci so the liquid is under tension.

Assume that the network is deformable and able to respond to the contraction driven by drying rate. In this case, the liquid-vapor interface is able to regulate the liquid flow from the interior with the radius of curvature. If the liquid tension at the liquid-vapor interface is P_E or $P(r = R) = P_E$, then Equation 5.29 can be written as:

$$P_E = 3K_G\dot{\varepsilon}_s + C_1\left[1 + \frac{\beta r^2}{4} + \frac{\beta^2 r^4}{256}\right]$$

or

$$C_1 = \frac{P_E - 3K_G\dot{\varepsilon}_s}{\left[1 + \frac{\beta R^2}{4} + \frac{\beta^2 R^4}{256}\right]}$$

solving for C_1 in Equation 5.26

$$P(r) = 3K_G\dot{\varepsilon}_s + \left(P_E - 3K_G\dot{\varepsilon}_s\right)\frac{\left[1+\frac{\beta r^2}{4}+\frac{\beta^2 r^4}{256}\right]}{\left[1+\frac{\beta R^2}{4}+\frac{\beta^2 R^4}{256}\right]} \tag{5.33}$$

Rearranging Equation 5.33

$$P(r) = 3K_G\dot{\varepsilon}_s\left\{1-\frac{\left[1+\frac{\beta r^2}{4}+\frac{\beta^2 r^4}{256}\right]}{\left[1+\frac{\beta R^2}{4}+\frac{\beta^2 R^4}{256}\right]}\right\} + P_E\frac{\left[1+\frac{\beta r^2}{4}+\frac{\beta^2 r^4}{256}\right]}{\left[1+\frac{\beta R^2}{4}+\frac{\beta^2 R^4}{256}\right]} \tag{5.34}$$

Equation 5.34 illustrates that liquid tension distribution is superimposed from two mechanisms; syneresis, $\dot{\varepsilon}_s$, and capillarity which shows up in liquid tension at the liquid-vapor interface, P_E. The terms containing β account for pressure loss due to liquid transportation according to Darcy's law.

Saturation requires that the network is able to cope with the contraction driven by drying rate at the liquid-vapor interface. Therefore, the liquid flow rate out to the exterior must be equal to the contraction rate of the network and also equal to evaporation rate at the liquid-vapor interface. Mathematically, the conservation of mass (or volume for incompressible liquid) can be described as:

$$-2\pi RhV_E = \int_0^R \left(3\dot{\varepsilon}_s - \frac{P}{K_G}\right)2\pi rhdr \tag{5.35}$$

The term on the left hand side of Equation 5.35 represents the rate of evaporation. The right hand term indicated rate of volumetric contraction of the network from syneresis and liquid pressure. This volume change is equal to the volume of liquid flow from the interior to the exterior.

Substitute Equation 5.34 into 5.35 gives

$$-2\pi RhV_E = \int_0^R \left\{ 3\dot{\varepsilon}_s - \frac{1}{K_G}\left(3K_G\dot{\varepsilon}_s + \left(P_E - 3K_G\dot{\varepsilon}_s\right)\frac{\left[1+\frac{\beta r^2}{4}+\frac{\beta^2 r^4}{256}\right]}{\left[1+\frac{\beta R^2}{4}+\frac{\beta^2 R^4}{256}\right]} \right) \right\} 2\pi rhdr$$

solving for P_E

$$P_E = 3K_G\dot{\varepsilon}_s + K_G\dot{V}_E \frac{\left[1+\frac{\beta R^2}{4}+\frac{\beta^2 R^4}{256}\right]}{\left[\frac{R}{2}+\frac{\beta R^3}{16}+\frac{\beta^2 R^5}{1536}\right]} \tag{5.36}$$

substitute P_E back to Equation 5.34 to obtain $P(r)$

$$P(r) = 3K_G\dot{\varepsilon}_s + K_G\dot{V}_E \frac{\left[1+\frac{\beta r^2}{4}+\frac{\beta^2 r^4}{256}\right]}{\left[\frac{R}{2}+\frac{\beta R^3}{16}+\frac{\beta^2 R^5}{1536}\right]} \tag{5.37}$$

Equation 5.37 indicates a few important points. Liquid tension distribution depends on drying rate or evaporation rate. Higher drying rate means that more liquid has to flow out to the exterior per unit time resulting in more pressure gradient. The tension is highest at the exterior of the network and decreases quadratically in radial direction to a minimum point at the centerline of the cylinder.

In terms of the volumetric strain rate of the network, $\dot{\varepsilon}_v = 3\dot{\varepsilon}_s - \frac{P}{K_G}$, so

$$\dot{\varepsilon}_v = -\dot{V}_E \frac{\left[1+\frac{\beta r^2}{4}+\frac{\beta^2 r^4}{256}\right]}{\left[\frac{R}{2}+\frac{\beta R^3}{16}+\frac{\beta^2 R^5}{1536}\right]} \tag{5.38}$$

The volumetric strain rate of the network varies linearly with the drying rate. However, the strain rate is a function of the radial distance from the centerline. The volumetric strain rate is highest at the exterior of the network and monotonically decreases to the lowest point on the centerline of the cylindrical. In average the volumetric strain rate of the body is

$$\bar{\dot{\varepsilon}}_v = \frac{1}{R}\int_0^R \dot{\varepsilon}_v(r)dr$$

$$\bar{\dot{\varepsilon}}_v = \frac{-\dot{V}_E}{\left[\frac{R^2}{2}+\frac{\beta R^4}{16}+\frac{\beta^2 R^6}{1536}\right]}\int_0^R\left(1+\frac{\beta r^2}{4}+\frac{\beta^2 r^4}{256}\right)dr$$

$$\bar{\dot{\varepsilon}}_v = -\dot{V}_E \frac{\left[1+\frac{\beta R^2}{12}+\frac{\beta^2 R^4}{1280}\right]}{\left[\frac{R}{2}+\frac{\beta R^3}{16}+\frac{\beta^2 R^5}{1536}\right]} \tag{5.39}$$

Effective stress is a function of pressure distribution. At any single point in the network the stress is $\tilde{\sigma}_r = \tilde{\sigma}_\theta = \tilde{\sigma}_z = -\varepsilon P(r)$ or

$$\tilde{\sigma}_r = \tilde{\sigma}_\theta = \tilde{\sigma}_z = -\varepsilon\left\{3K_G\dot{\varepsilon}_s + K_G\dot{V}_E \frac{\left[1+\frac{\beta r^2}{4}+\frac{\beta^2 r^4}{256}\right]}{\left[\frac{R}{2}+\frac{\beta R^3}{16}+\frac{\beta^2 R^5}{1536}\right]}\right\} \tag{5.40}$$

Effective stress is maximum at the network interim and gradually reduces to the center of the cylinder.

Step 3: Subsaturated Gel

The network develops strength and finally resists the contraction. When the contraction ceases, the liquid-vapor front reaches its smallest radius curvature resulting in highest liquid tension, P_R as described by Laplace's equation as $P_R = \frac{2\gamma_{LV}\cos\theta}{R}$. The boundary condition is now $P(r = R) = P_R$. Equation 5.33 is replaced by

$$P(r) = 3K_G\dot{\varepsilon}_s + \left(P_R - 3K_G\dot{\varepsilon}_s\right)\frac{\left[1+\frac{\beta r^2}{4}+\frac{\beta^2 r^4}{256}\right]}{\left[1+\frac{\beta R^2}{4}+\frac{\beta^2 R^4}{256}\right]} \tag{5.41}$$

with corresponding effective stress

$$\tilde{\sigma}_r = \tilde{\sigma}_\theta = \tilde{\sigma}_z = -\varepsilon\left\{3K_G\dot{\varepsilon}_s + \left(P_R - 3K_G\dot{\varepsilon}_s\right)\frac{\left[1+\frac{\beta r^2}{4}+\frac{\beta^2 r^4}{256}\right]}{\left[1+\frac{\beta R^2}{4}+\frac{\beta^2 R^4}{256}\right]}\right\} \tag{5.42}$$

After this, the liquid-vapor interface moves into the network interior and drying is governed by diffusion process. No major shrinkage shall take place beyond saturation drying since the network can no longer contract. Again, the network may crack due to tremendous compressive stress difference in front and behind of the liquid-vapor interface as it moves into the network interior toward the centerline.

5.3 SHRINKAGE IN DRYING

5.3.1 Drying Shrinkage Controlling Factors

There are three important features that control the magnitude of shrinkage in saturated drying:

1) LIQUID CONTENT AT GEL POINT

Amount of liquid content defines maximum shrinkage potential, which is the shrinkage capacity. Systems with lower liquid content have less ability to shrink than those with higher liquid content. Mathematically, volumetric shrinkage, Sh_v, depends on the volume of liquid that evaporates from the system:

Sh_v = Volume of liquid evaporates

$$Sh_v = V_L\big|_{\text{point of gel}} - V_L\big|_{\text{end of sat.}}$$

$$Sh_v = \frac{\varepsilon_i}{(1-\varepsilon_i)}V_s - \frac{\varepsilon_f}{(1-\varepsilon_f)}V_s$$

$$Sh_v = \left[\frac{\varepsilon_i}{(1-\varepsilon_i)} - \frac{\varepsilon_f}{(1-\varepsilon_f)}\right]V_S$$

$$\frac{Sh_v}{V_S} = \left[\frac{\varepsilon_i}{(1-\varepsilon_i)} - \frac{\varepsilon_f}{(1-\varepsilon_f)}\right]$$

$$\frac{Sh_v}{(1-\varepsilon_i)V} = \left[\frac{\varepsilon_i}{(1-\varepsilon_i)} - \frac{\varepsilon_f}{(1-\varepsilon_f)}\right]$$

$$\frac{Sh_v}{V} = \varepsilon_v = \left[\varepsilon_i - \frac{(1-\varepsilon_i)}{(1-\varepsilon_f)}\varepsilon_f\right] \qquad (5.43)$$

where ε_v is the volumetric strain

ε_i is the pore fraction at point of gel

ε_f is the pore fraction at the end of saturation. $\varepsilon_f < \varepsilon_i$

V_L is the volume of liquid phase, $V_L = \varepsilon V$

V_S is the volume of solid phase, $V_S = (1-\varepsilon)V$

V is the total volume of the system, $V = V_S + V_L$

According to Equation 5.43, volumetric strain depends on pore fraction difference at gel point and at the end of saturation. If the system has a small pore fraction at gel point, ε_i, it has less shrinkage potential. The concept of shrinkage minimization by reducing the liquid content at the point of gellation is illustrated in Chapter 6.

2) STRENGTH OF THE NETWORK

Strength of the network in the saturation state increases with time and depends mostly on chemical processes known to ceramists as 'dissolution-redeposition' reaction. The processes involves with the degree of dissolution of the solid phase into the liquid and the degree of redeposition of the solid back to the neck area where solid particles join. Increasing the neck area results in augmenting the strength of the network. Details of dissolution-redeposition will be discussed in the Chapter 6.

According to the mechanics of viscous gel, volumetric strain rate, $\dot{\varepsilon}_v$, is a function of syneresis, pressure, network strength, and external stress according to Equation 4.71

$$\dot{\varepsilon}_v = 3\left(\dot{\varepsilon}_s - \frac{P}{3K_G}\right) + \frac{(1-2N)}{F}\sigma$$

for system without external stress, Equation 4.71 reduces to.

$$\dot{\varepsilon}_v = 3\left(\dot{\varepsilon}_s - \frac{P}{3K_G}\right) \tag{5.44}$$

Integrate Equation 5.44 to obtain total strain:

$$\int_{t_i}^{t_f} \dot{\varepsilon}_v dt = 3\int_{t_i}^{t_f}\left(\dot{\varepsilon}_s - \frac{P}{3K_G}\right)dt$$

$$\varepsilon_v = 3\varepsilon_s - \int_{t_i}^{t_f} \frac{P}{K_G}dt \tag{5.45}$$

$$\varepsilon_v = 3\varepsilon_s - \int_{t_i}^{t_f} \frac{F}{3(1-2N)}Pdt \tag{5.46}$$

Approximate Equation 5.46 by assuming $P = P_R$ according to Equation 5.23. And N is not a function of time.

$$\varepsilon_v = 3\varepsilon_s - \frac{P_R}{3(1-2N)}\int_{t_i}^{t_f} Fdt \tag{5.47}$$

Therefore, total strain depends on $\int_{t_i}^{t_f} Fdt$ which is equivalent to the time dependent bulk modulus of the network.

3) LIQUID TENSION

Capillarity forces liquid to go under tensile stress as the liquid-vapor reaches the network interim. Liquid tension then places the solid network under compression causing it to squeeze the liquid out to the exterior. Therefore, drying shrinkage can be reduced if the magnitude of liquid tension is attenuated. Equation 5.47 shows how total strain relates to liquid under tension.

$$\varepsilon_v = 3\varepsilon_s - \frac{P_R}{3(1-2N)}\int_{t_i}^{t_f} F dt$$

Liquid tension can be lowered by several means. Reducing surface tension of the liquid chemically is a possibility. Increase of pore radius is another option. And supercritical drying is also proven successful in sol-gel research.

These features are shown in schematic in Figure 5.11. The tank is analogy to the network which captures liquid internally between its strands. The wall of this tank is deformable with varying strength presented by set of time dependent dashpots (for viscous response). The volume of liquid enclosed in the pores is analogous to the liquid content which defines maximum shrinkage possibility. And the meniscus at the entrance stands for liquid tension by capillarity. This is the driving force to consolidate the tank, or the network.

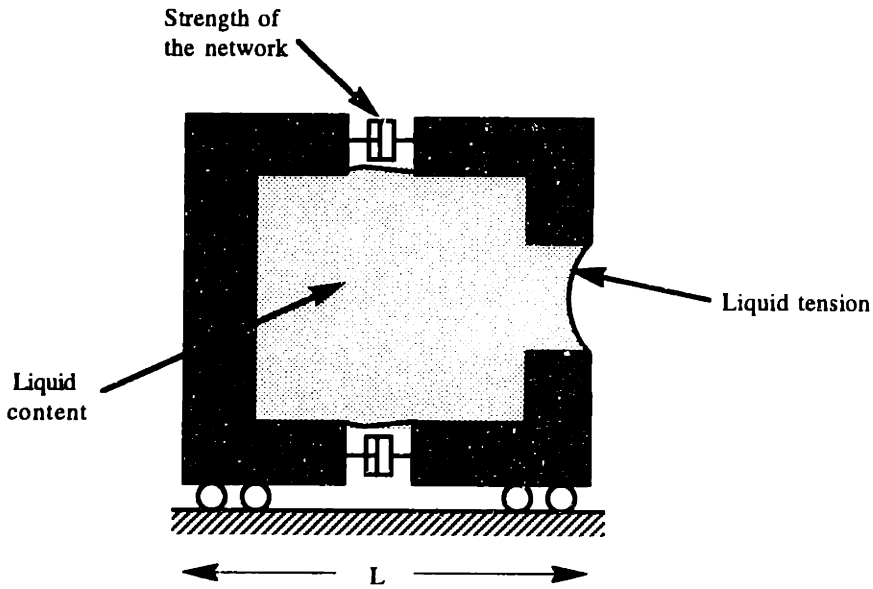

Figure 5.11 Three features that control drying shrinkage

5.4 CHAPTER SUMMARY

The physics and mathematics of the drying of gels are shown in this Chapter by solving the constitutive equations from Chapter 4 with various boundary conditions.

Liquid is placed under tensile stress because of capillarity. The geometry of pore entrances and wetting bend the liquid-vapor interface into a meniscus and force the liquid to be under tension (suction). In case the network is rigid, the liquid tension will be equalized through the entire liquid phase and there will be no liquid transport. Further drying mandates that the liquid-vapor interface recede into the interior of the gel. On the other hand, if the network is deformable, the liquid starts to flow from the interior to the exterior with a pressure gradient as described by Darcy. The liquid flow rate to the exterior must be equal to the evaporation rate at the liquid-vapor interface. And at the same time, the flow rate must be equal to the rate at which the network contracts so that the network remains at saturation with no presence of vapor phase. It is the evaporation rate that regulates the rate at which liquid flows from the interior through the radius of curvature of the menisci at the pore entrances. In case the drying rate is so high such that the network can not cope with the rate of contraction, then the liquid-vapor interface will move into the interior.

Network contraction (shrinkage) continues as the network builds up its strength. When the network strength is sufficient to resist the compressive stress induced by the liquid tension, the contraction ceases marked the end of saturation. At this point, the liquid-vapor interface reaches its smallest radius and the network is at its maximum compression. As drying continues, the liquid-vapor interface moves into the network interior after which drying is governed by a diffusion process. There is no shrinkage at this subsaturation state. The compressive stress in front and behind the liquid-vapor interface is so drastic that cracks may be initiated.

A large fraction of shrinkage deformation of drying gels takes place during saturation drying (if neglecting the slow process of syneresis). Therefore, the magnitude of drying shrinkage depends strongly on the difference in the amount of the liquid (or pore fraction) in the pore at the point of gel and at the termination point of saturation. So, there are three strategies that help minimizing drying shrinkage.

1) Minimize the liquid content at gel point

Level of liquid content at gel point determines the shrinkage potential of the gel. Reducing the liquid content at the gel point directly lowers the shrinkage capacity.

2) Increase the strength of the network

The strength of the network governs the difference between the pore fraction at the gel point and the saturation termination point. The network strength shall be maximized.

3) Lower the liquid tension

The magnitude of liquid tension is the only the network deformation driving force. Liquid tension is governed by the surface physics of the pore liquid and the network solid as well as the method of drying (natural or supercritical drying).

BIBLIOGRAPHY

[1] Scherer G.W., *Drying Gels I. General Theory*, Journal of Non-Crystalline Solids 87, p.199-225, North-Holland, Amsterdam, 1986

[2] Scherer G.W., *Drying Gels II. Film and Flat plate*, Journal of Non-Crystalline Solids 89, p.217-238, North-Holland, Amsterdam, 1987

[3] Scherer G.W., *Drying Gels III. Warping plate*, Journal of Non-Crystalline Solids 91, p.83-100, North-Holland, Amsterdam, 1987

[4] Scherer G.W., *Drying Gels IV. Cylinder and Sphere,* Journal of Non-Crystalline Solids 91, p.101-121, North-Holland, Amsterdam, 1987

Chapter 6.

Stress-Strain Relationship of Drying Gels

6.0 INTRODUCTION

The mechanics of drying gel and the theory of drying shrinkage were discussed in Chapters 4 and 5 with mathematical models. Although these mathematical descriptions wonderfully provide 'perceptive' on shrinkage mechanism, the theories always disregard practical difficulties of parameter measurement and estimation in reality. For example, the mathematical description of the total shrinkage of drying gel can be presented as:

$$\varepsilon_v = 3\varepsilon_s - \frac{P_R}{3(1-2N)}\int_{t_i}^{t_f} F dt$$

The problem is that not a single parameter on the right hand side of the equation has been quantified because actual properties of viscous gel are extremely difficult to measure. One can never fully isolate the coupling effects of the liquid and the solid phase nor capture the time-dependent properties of gel accurately. There is a gap between the theory development and the actuality such that the theory can be used predictively but not definitely.

In this chapter, actual shrinkage of drying gels is quantified experimentally. Since shrinkage is a function of boundary stress, the shrinkage stress-strain relation between binder and its boundaries is explored. But this stress-strain connection is quite different from that of general material testing where samples are tension loaded in order to track their stress and strain. Instead, binder is placed between a set of flexible parallel boundaries and is allowed to dry. The boundaries maintain the consolidation characteristic of the powder bed. Their elastic response places the binders under tensile stress known in this thesis as **shrinkage stress**. Strain is defined as the normalized movement of the boundaries. In this case, the stress-strain are registered with various boundary stiffness and binder

materials. Finally, a map of stress-strain with shrinkage loci is created to illustrate their relationship. This chapter begins with the shrinkage data collected from Three-Dimensional Printing parts. Then the shrinkage minimization strategies suggested in Chapter 5 are put to test on binders. And finally, the experimental work to identify the binder stress-strain relation is reviewed.

6.1 DRYING SHRINKAGE CHARACTERS IN THREE-DIMENSIONAL PRINTING

6.1.1 Test Protocol

Prior to June 1994, shrinkage was quite a mysterious phenomena at Three-dimensional Printing. During that time, shrinkage was quantified with a contact measurement technique using a super micrometer. Since the external surfaces of tested parts were not flat, the measurements were not precise and inconclusive. Christopher Harris reported in his thesis that there was no shrinkage during drying and a negligible amount (0.01%) after heat treatment to 1000°C. Khalil Sardouk later discovered that shrinkage was, in fact, 0.5% after 900°C heat treatment. Khalil's measurement also lacked precision and repeatability. Although several experiments were initiated, true shrinkage origins were not found.

A new measurement procedure was developed by this thesis work after January 1995 with non-contact techniques. A microscope CCD camera was mounted on the tip of a coordinate measuring machine (CMM). The accuracy, resolution, and repeatability were greatly improved. This new non-contact and non-invasive technique allowed for measurement of shrinkage in green in addition to dried and heat-treated parts. Samples were modified to have fiduciary marks on their top surfaces by skipping portion of print lines as shown in Figure 6.1.

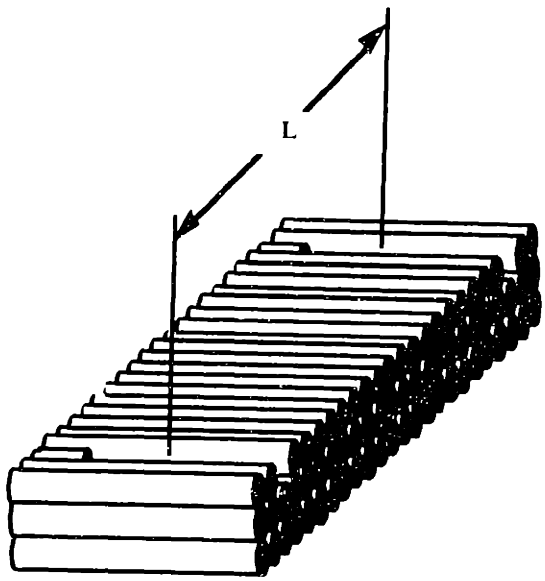

Figure 6.1 Fiduciary Marks are Made by Skipping Portion of Print Lines on the Top Surface

Five different sample lengths with cross section of 0.375" x 0.210" (width x height) were printed with incorporated fiduciary marks. The marks were placed to obtain part length of 0.1309, 0.3720, 0.7441, 1.9980, and 3.9961 inches. Five sets of shrinkage bars were built along the slow axis at the same time on top of an 5"x6" alumina substrate. Figure 6.2 illustrates the sample layout from a top view.

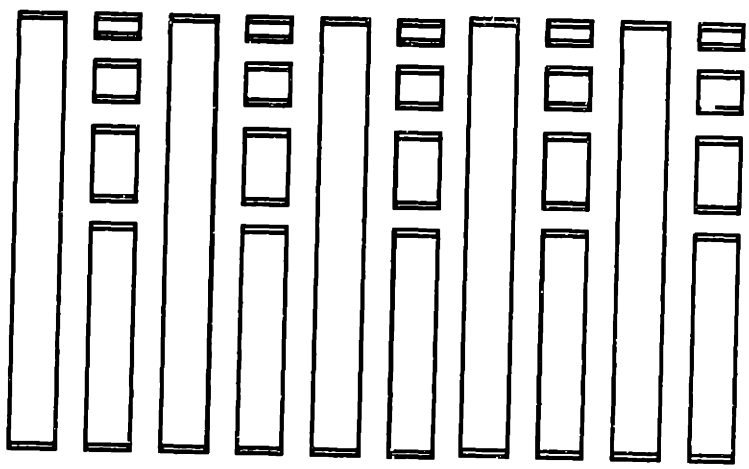

Figure 6.2 Layout of Samples on the Powder Bed

A CCD microscope camera with a magnification of 8X was lined up with the fiduciary marks to read their coordinates with the CMM's display. Measurement were made at these following sequences respectively:

1. Green (within 5-10 minutes after printing completion)
2. Dried (left in an oven or air for at least 10 hours)
3. Fired (fired to 900°C for 1 hour and cooled to ambient temperature)

The printing pattern used in these experiment was 'normal raster' where binder was printed onto the powder bed in straight line rasterization. The line and layer spacings were both set at 175 μm with a Diconix printhead running at about 1.2 cc/min. The fast axis speed was 1.5 m/sec. Resulted ratio of the volume of the binder to the volume of the pores, or **printing saturation level**, was approximately 75 percent.

Shrinkage on postdipped bars were sometime quantified as well. The bars were dipped into a solution of Nyacol 830 and water at 1:4 by volume and refired to 900°C for another hour. Typical shrinkage measurement using the fiduciary mark technique is shown in Figure 6.3

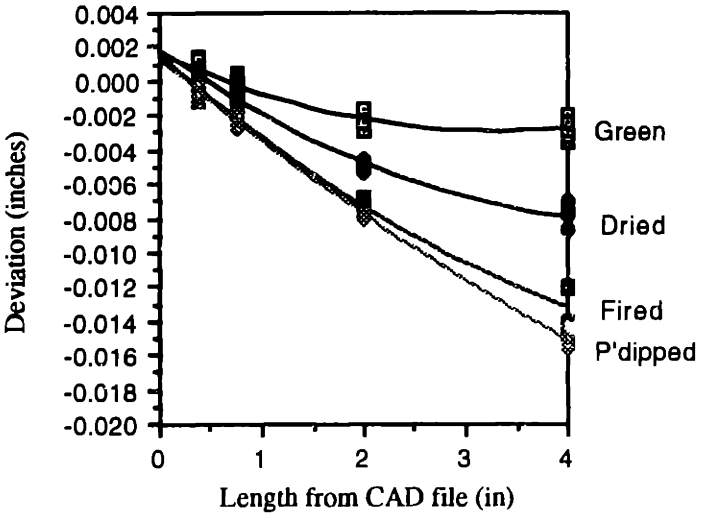

Figure 6.3 Typical Shrinkage from Fidutual Mark Technique

The horizontal axis represents the designed part length in CAD model where the fidutual marks were made (0.3720, 0.7441, 1.9980, and 3.9961 inches respectively). The vertical axis represents deviation of the part length from the designed values. Negative values on the vertical axis indicate that the part is shorter than its expected value. This data is not normalized to give an absolute sense of part shrinkage.

6.1.2 Hypothesis and Evidence of Shrinkage Controlling Factors

At the beginning of this thesis work, shrinkage phenomena was very mysterious. The very first set of data from new optical technique, although proven accurate, perplexed us even more due to lots of process parameters involved in shrinkage. In order to distinguish important parameters from irrelevant ones, this thesis work set up a hypothesis of shrinkage origins according to the preliminary data obtained. The presumption was that shrinkage depends on 1) Types of binder, 2) Types of Powder, and 3) Citric acid content in the powder. The idea is shown schematically in Figure 6.3. The purpose of this experimental work in this chapter has been to prove the above hypothesis and to assess the relative impact of its component parts.

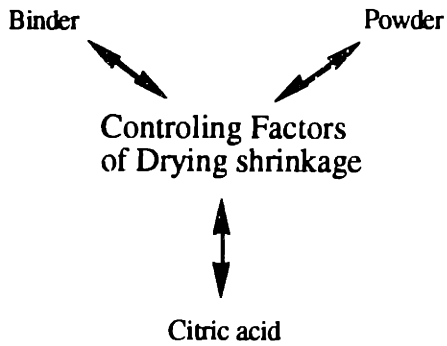

Figure 6.3 Controlling Factors of Drying Shrinkage

• BINDER

In order to prove that the cohesive force induced by the liquid bridges of water residency in the powder bed was insufficient to cause shrinkage, de-ionizzed water was printed at 80 percent saturation onto Norton 7920 packed to approximately 40 percent with 0.5 weight percent citric acid content. It was found that the shrinkage was undetectable both when the samples were wet and dried, Figure 6.4 (a). Therefore, the fact that the water is captured in the network pores of gelled binder and subsequently evaporates from the network causes shrinkage.

Were the liquid bridge between powder particles be a source of shrinkage, the water printing experiment should have revealed the shrinkage artifact. As a matter of fact, the magnitude of capillary stress induced by the liquid bridges between powder particles is

unable to produce particle rearrangement, hence no shrinkage was observed (Estimated capillary stress of the water can be interpolated from Figure 4.5 at approximately 4000 Pa at full saturation). But in the case of drying binders (printed at equivalent conditions, Figure 6.4 (b)), the enclosed liquid in gelled network is under much higher tensile stress than the former case due to smaller pore radii of the gel. The network is placed under tremendous compressive stress which causes the network to contract and shrinkage.

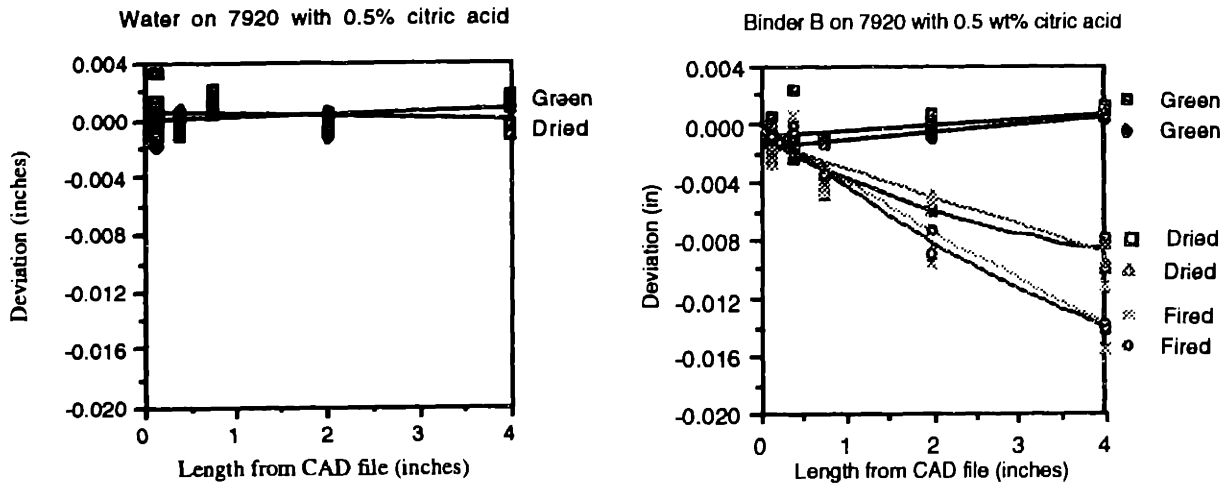

Printing condition:	
Line spacing:	170 μm
Layer spacing:	170 μm
Printing saturation:	80 %
Printhead:	Diconix - single jet
Rasterization:	Straight line
Drying:	Oven dried at 80°C for >12 hours
Heat treatment:	900°C for 1 hour

Figure 6.4 Shrinkage as Printing With (a) Water (b) Binder B Acid Gelled[1]

• POWDER PACKING DENSITY

Although powder does not produce shrinkage, it controls the magnitude of shrinkage through packing density. A highly packed powder always sustains less shrinkage than that a powder of lower packing density.

---

[1] Obtained from two separate sets of samples

According to Chapter 2, ultrasound misting could lower the packing density by about 16 percent (From low 40's to mid 30's packing fraction) with just a small amount of moisture. As a result, powder with lower densities always shrinks substantially more than highly packed ones. Figure 6.5 compares the shrinkage in low packed (misted) and normal (unmisted) Norton 7920 powder printed at 80 percent saturation. The powder has 0.5 weight percent citric acid.

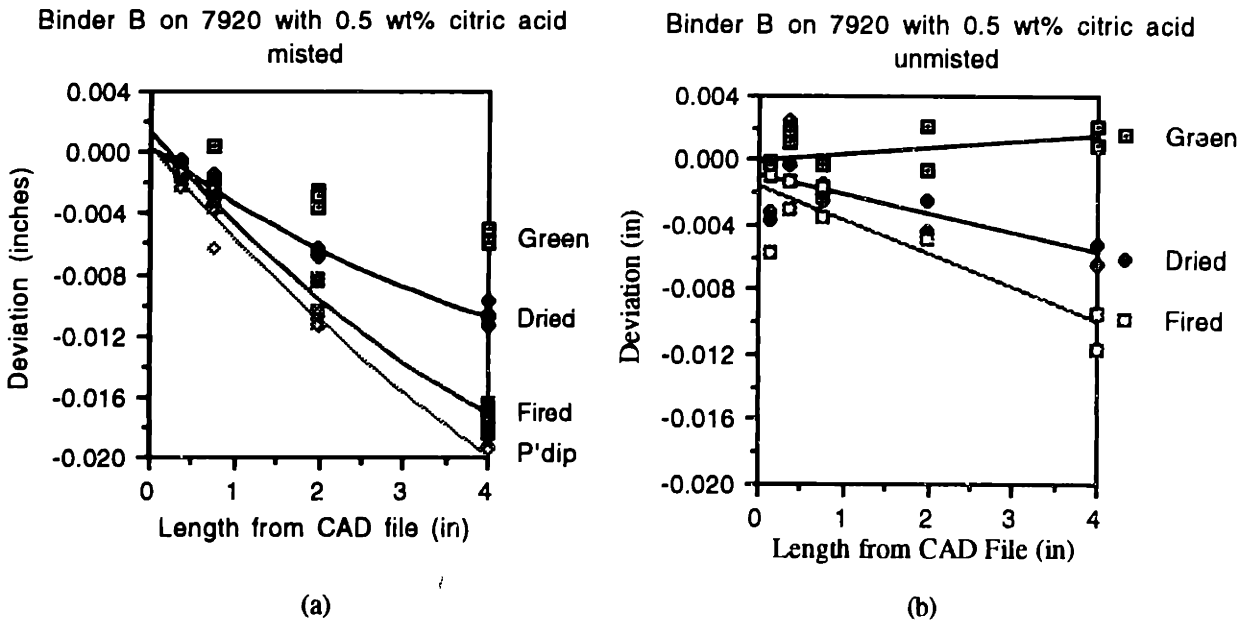

Figure 6.5 Effect of Powder Packing Density on Shrinkage[2]
a) Low Packing Density by Misting b) Normal Packing Density

In addition to the packing density, the morphological effect is shown in Figure 6.6 with CB-A30S spherical powder. Shrinkage of CB-A30S is less than Norton 7920 (lamella) because of the considerably higher packing density and deformation characteristic to isostatic shrinkage stress. Details of morphological impact on powder deformation under stress will be elaborated in Chapter 7.

[2] Printing condition as same as Figure 6.4

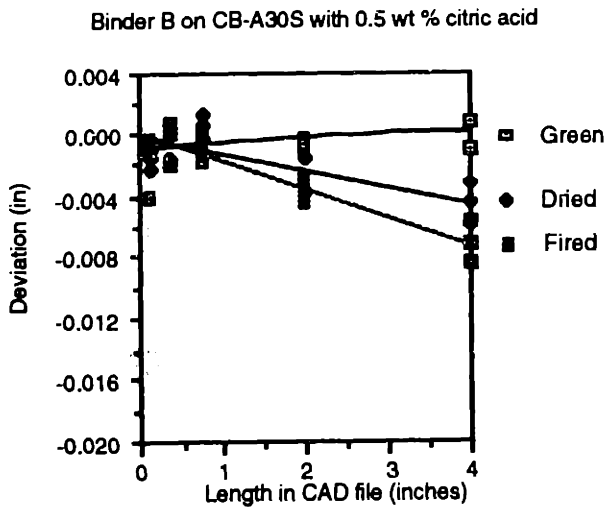

Figure 6.6 Shrinkage of CB-A30S Spherical Powder[3]

• CITRIC ACID CONTENT

There is significant evidence that the citric acid contents in the powder bed governs the shrinkage magnitude. Powder with higher citric acid content always has more shrinkage. This occurs on both Norton 7920 and CB-A30S powder, Figure 6.7 and 6.8. Citric acid content has a critical role in the rate and the degree of gelation of silica binder [1].

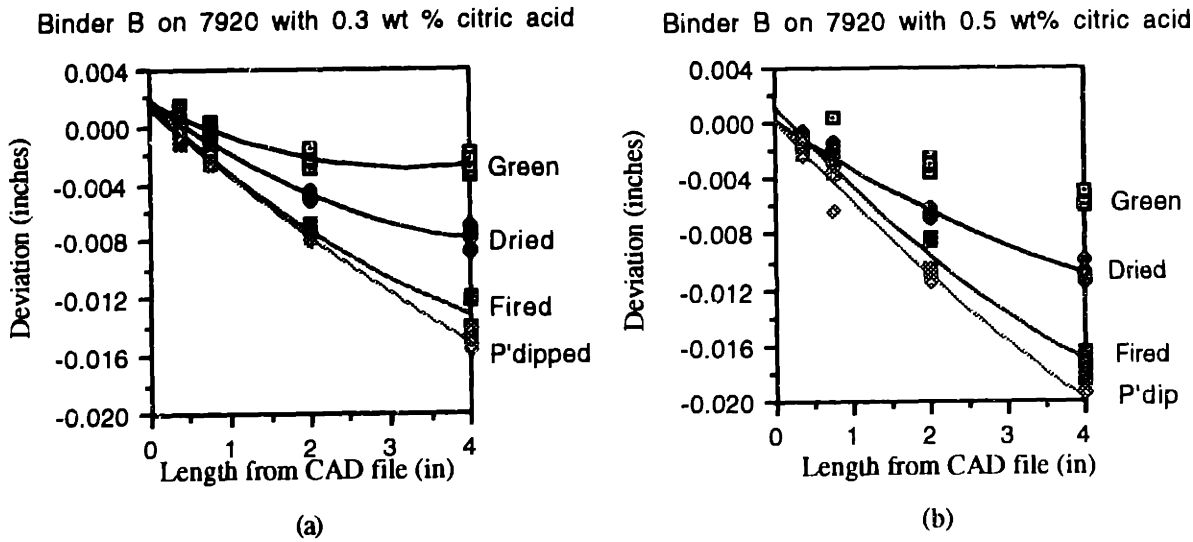

Figure 6.7 Shrinkage of Norton 7920 Powder[3] with a) 0.3 wt % and b) 0.5 wt % Citric Acid Content

[3] Printing condition as same as Figure 6.4

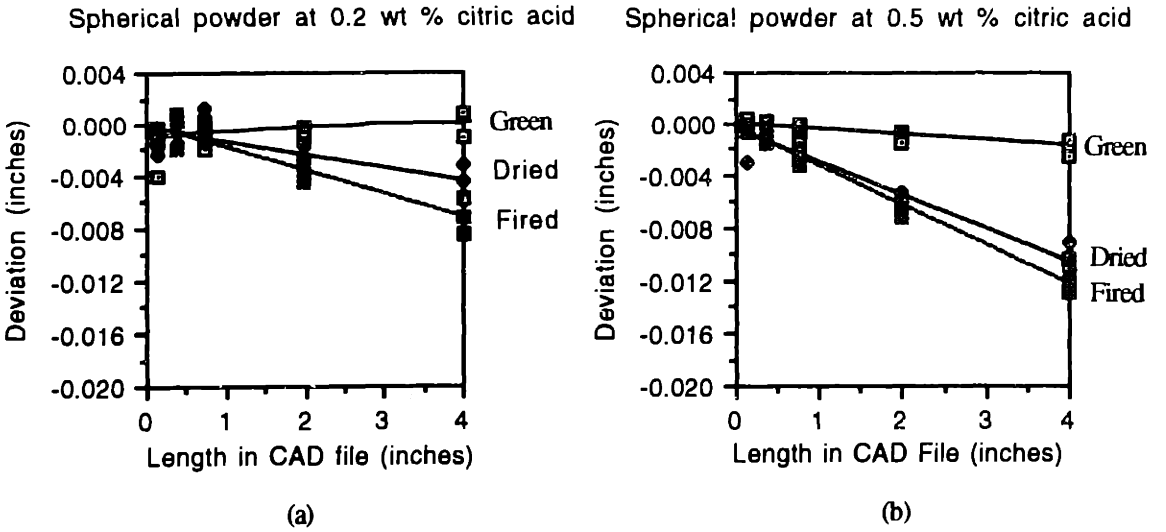

Figure 6.8 Shrinkage of Spherical Powder with Different Citric Acid Content[4]

There are two possibilities concerning the relation of shrinkage and citric acid content in the powder bed. First, since citric acid is very hydroscopic, it may dissolve and cause shrinkage after the powder bed is printed. Second, citric acid content increases the degree of gelation of Binder B. Therefore, more shrinkage may take place with the higher level of gelation.

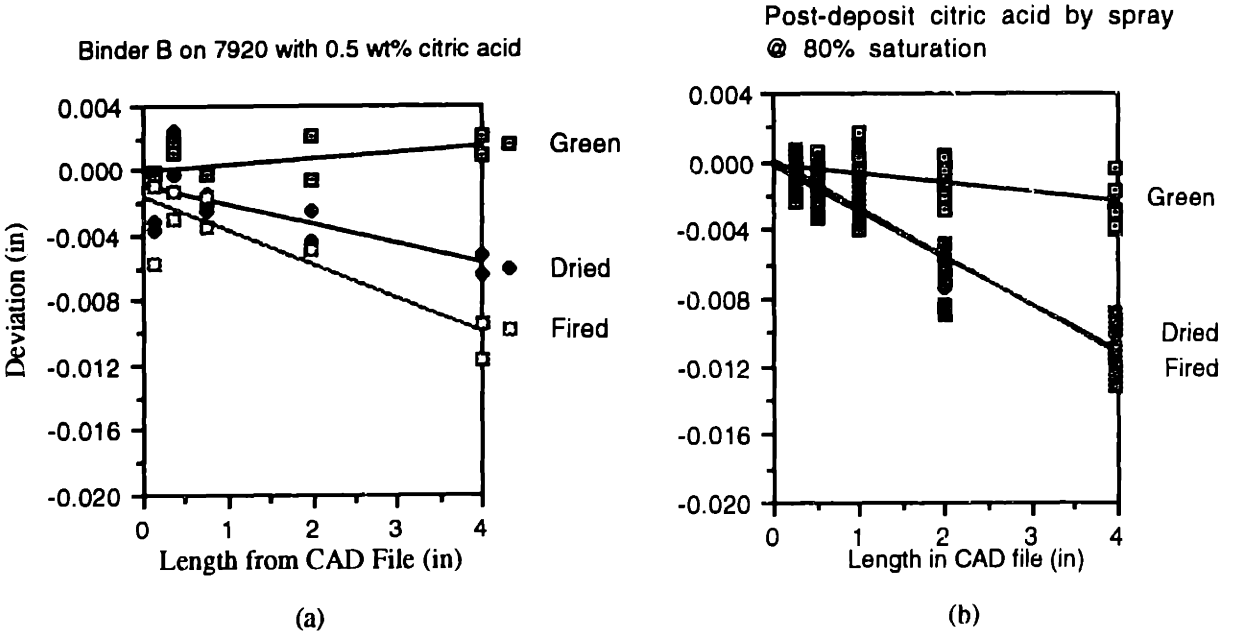

Figure 6.9 Shrinkage Comparison of (a) Powdered Acid[4] (b) Sprayed Acid Solution

[4] Printing condition as same as Figure 6.4

A special experiment was designed to prove that citric acid dissolution does not cause shrinkage. Instead of mixing citric acid into alumina powder, the acid was made into a solution and sprayed on the powder after spreading but prior to printing. If shrinkage is conceived by powdered acid dissolution, then there should not be any shrinkage with the sprayed acid case. The result of this test is shown in Figure 6.9 (a) and (b). The amount of shrinkage in the sprayed acid setup is equivalent to that where powdered citric acid is mixed into the powder bed. Therefore, acid dissolution does not produce shrinkage but rather the acid involvement with binder gelation.

• SHRINKAGE COMPARISON AMONG FAST AND SLOW AXES

Shrinkage samples on both fast and slow axis were printed simultaneously at 80% saturation onto Norton 7920 and compared, Figure. 6.10. It was found that there was no conclusive shrinkage difference between the fast and slow axes in either dried or after fired (heat treatment) state.

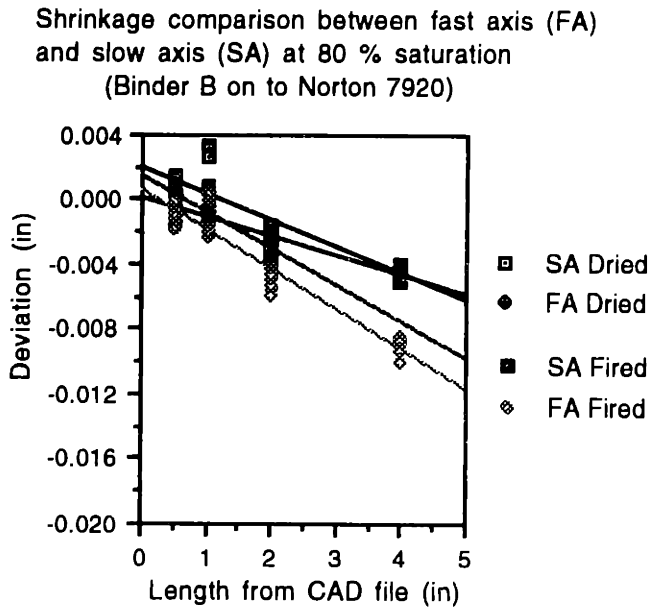

Figure 6.10 Shrinkage Comparison Between Samples built with Fast and Slow Axis[5]

[5] Printing condition as same as Figure 6.4

In summary, water trapped binder network after gellation originates drying shrinkage in Three-Dimensional Printing. The magnitude of drying shrinkage correlates well with the degree of binder gelation which involves with the citric acid content in the powder. Although the acid dissolutes in water, this does not directly contribute to shrinkage. Powder is also not a shrinkage source but it contributes to the magnitude of shrinkage through its packing densities and morphology.

6.2 STRATEGIES FOR SHRINKAGE REDUCTION

According to the gel deformation theory in Chapter 5, drying shrinkage takes place only after gelation was initiated. The shrinkage continues while under saturation drying until the network strength is capable of taking up the compressive stress induced by capillary. Beyond this point, saturation and shrinkage terminate and the liquid-vapor interface recedes into the gel's interior. There can be no further shrinkage after the end of saturation. Equation 5.43 indicates some important factors that control the amount of drying shrinkage of a gel.

$$\frac{Sh_v}{V} = \left[\varepsilon_i - \frac{(1-\varepsilon_i)}{(1-\varepsilon_f)} \varepsilon_f \right] \tag{5.43}$$

where $\frac{Sh_v}{V}$ can be viewed as volumetric strain or shrinkage

ε_i is the pore fraction at point of gel

ε_f is the pore fraction at the end of saturation. $\varepsilon_f < \varepsilon_i$

V is the total volume of the system, $V = V_S + V_L$

There are a few interesting points in Equation 5.43. First, the pore fraction at point of gel, ε_i, can be viewed as maximum drying *shrinkage potential.* Suppose the gel network develops no strength, so the shrinkage continues until the water is depleted or $\varepsilon_f = 0$. In this case, the volumetric strain is equal to

$$Sh_v = \varepsilon_i V \tag{6.1}$$

Therefore, the pore fraction at the point of gel dictates the shrinkage potential of the body. In other words, minimizing the pore fraction, ε_i, should result in lowering shrinkage potential.

Binder B was designed to gel rapidly when the pH is below 7.5. As silica particles polymerize, water is enclosed inside the interconnected pore between the network strands. This produces a high pore fraction at the gel point and results in a high shrinkage potential. On the other hand, Binder B can be gelled by drying. Initially, drying allows water to leave the binder freely without being under tensile stress. By the time the system reaches the point of instability and the network is formed, water is almost depleted from the system. Therefore, the shrinkage potential in this latter case is less.

Second, the amount of shrinkage depends on the reduction in pore fraction between the point of gel and the end of saturation (ε_i and ε_f). The reduction indicates a balance between gel strength and capillary stress. For example, in the case of a strong network, ε_f is not too different from ε_i and shrinkage will be minimal. When the network is weak, there will be more shrinkage, vice versa. Strength of the network depends mostly on chemical reactions during and after gelation known among researchers in sol-gel science as 'resolution and redeposition processes' which will be discussed in Section 6.2.2.

Third, Capillarity places liquid under tension. It is the only shrinkage driving force. Capillary stress in the liquid depends on 1) contact angle, 2) pore radius, and 3) liquid surface tension. Contact angle depends on surface chemistry between the solid and the liquid. Although it is possible to replace pore liquid with another liquid with lower surface tension in sol-gel technique, it is beyond the possibility for Three-Dimensional Printing to do so. Pore radius is governed by the silica particle size. Bigger particle assembly usually produces larger pores, thus with lesser capillary stress. The surface tension of water can be adjusted chemically with liquid fatty alcohol such as n-octyl alcohol and 2-ethyl hexyl alcohol. It only takes a small concentration (a few ppm) of these alcohols to lower water surface tension.

6.2.1 Shrinkage Reduction by Lowering Liquid Content at Point of Gellation

The liquid content determines shrinkage potential. Binder B gelled rapidly with chemicals resulting in an instantaneous formation of the network. The network captures liquid in its interconnected pores as shown in Figure 6.11. According to Chapter 4 and 5, liquid leaving the pores causes the network to deform. Total volumetric deformation of a gel is always equal to the volume of liquid leaving the body from the beginning to the end of saturation drying. Therefore, shrinkage potential depends directly on the level of liquid content in the binder at the point of gel. Gels that capture more internal liquid at the point of gel contain more shrinkage potential.

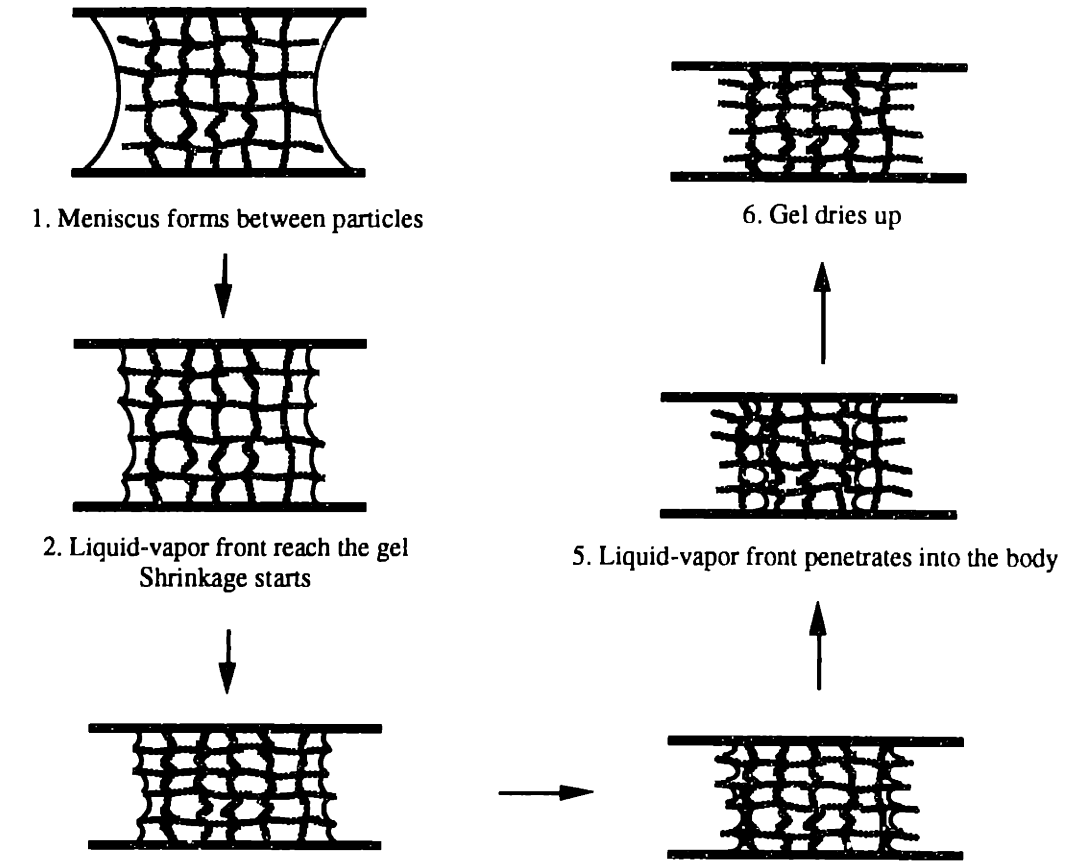

Figure 6.11 High Shrinkage Potential of Acid Gelled Colloidal Silica
Due to High Liquid Content at the Point of Gellation

In order to lower the liquid content at point of gel, some other gelation techniques may be employed. One simple technique is to gel colloidal silica by drying. This technique

decreases shrinkage potential by reducing the liquid content at the gel point. During early stages of drying, large portions of water in colloidal silica are initially allowed to leave the system by evaporation prior to gelation. Since there is no presence of solid network prior to gelation, the liquid is not under tensile stress and there is no shrinkage driving force at this state.

By the time the colloid reaches the critical concentration and gelation occurs, more than half of the water content has been liberated allowing the network to form with low liquid content and low shrinkage potential. The concept can be visualized in Figure 6.12 where drying shrinkage takes place during state 3 and 4.

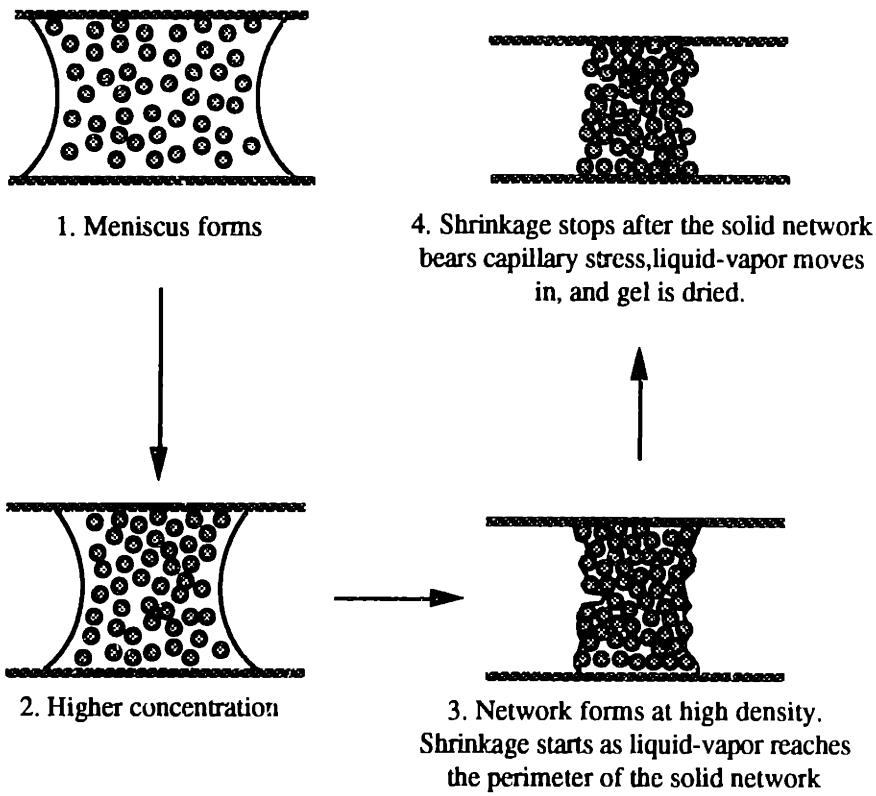

Figure 6.12 Low Shrinkage Potential by Drying of Colloidal Silica

Silica gel produced by drying of Binder B has slightly less pore fraction than acid gel as shown in mercury intrusion data in Figure 6.13. Both siiica gels have similar pore size distribution between 10 nm to 80 nm but the acid gel has slightly more pore volume under 10 nm.. Drying induced gel appears to be stronger because of higher density.

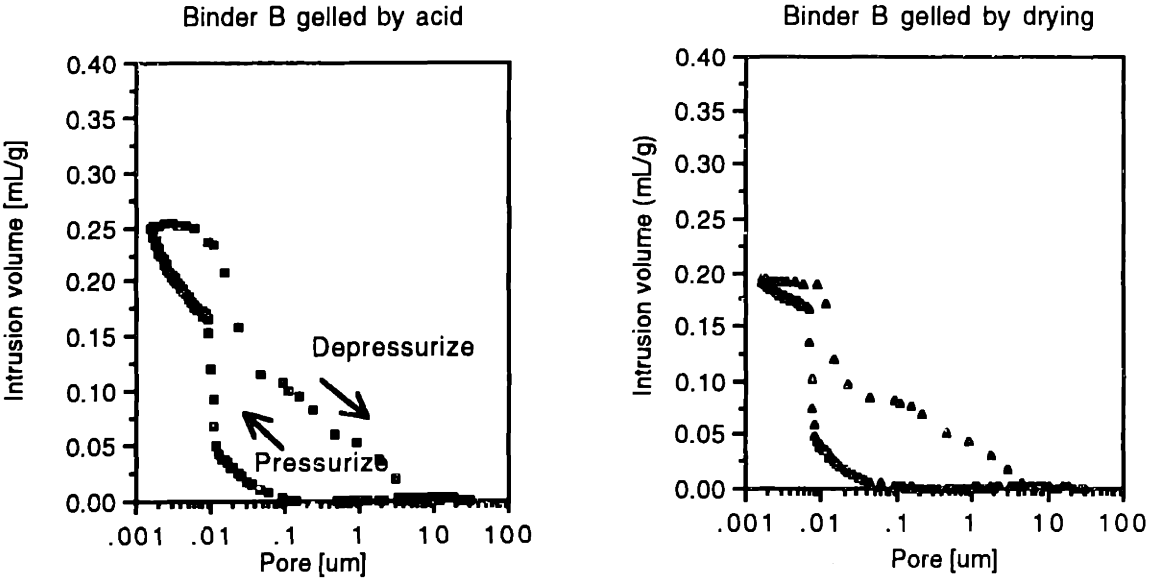

Figure 6.13 Mercury Intrusion of Gels Derived from Binder B by Acid and by Drying. Gel Derived by Drying Packs to Higher Density with Less Pore Volume under 10 nm.

Silica gels derived from Nyacol 9950 by drying and by aluminum nitrate exhibit the similar pore distribution where most of the pore volume concentrate at approximately 0.01 μm. However, the gels have less densities than that of Binder B with a total pore volume of 0.3 mL/g due to no presence of plasticizing agent (PEG).

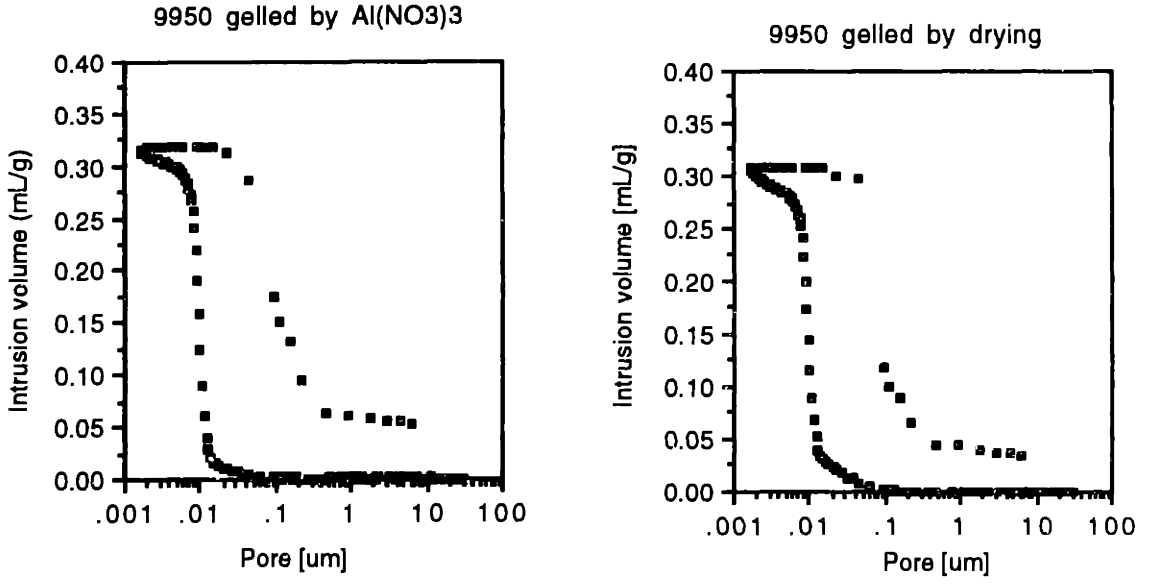

Figure 6.14 Mercury Intrusion of Gels Derived from Nyacol 9950 With a Salt and Drying

The concept of lowering liquid content at the gel point was tested using Binder B and Norton 7920 powder. One set of alumina powder was mixed with powdered citric acid at 0.5 weight percent while the other was free of acid. Both powders were packed to approximately 40 percent packing fraction and were printed with Binder B at approximately 80 percent saturation. Drying shrinkage is reduced, when gelled with drying, and found to be about half of that of Binder B acid gelled, Figure 6.15.

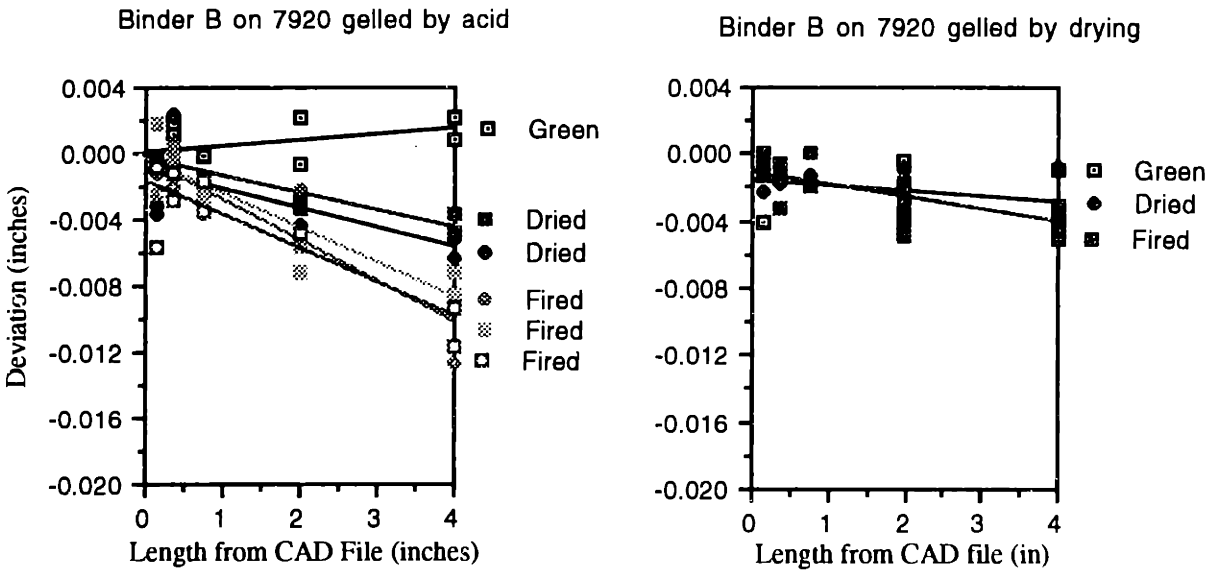

(a) Acid Gelled (b) Gelled by Drying

Figure 6.15 Effect of Acid and Drying Gelation on Three-Dimensional Printing of Ceramic Process with Binder B onto Norton 7920 powder

6.2.2 Increase Network Strength

A second alternative to minimize shrinkage during drying is to increase the network strength chemically. This process is known among researchers in sol-gel science as 'aging of gel'. Strength increase in gel aging involves two chemical processes referred to as 'solubility and redeposition'.

Solubility is the ability of particles to dissolve into a solution. Solubility of a surface depends on its radius of curvature, r. Positive surface radii such as those of particles ($r > 0$) yields higher solubility than flat ($r \rightarrow \infty$) or negative radii. Crevices and

necks between particles have negative radii so their solubility is low. Solubility of particles depends inversely with particle radii hence smaller particles yield greater solubility. Solubility and redeposition causes material to dissolve from area with positive radii and redeposit in areas of negative radii. In other words, the net curvature of the solid phase and the interfacial area is reduced [2].

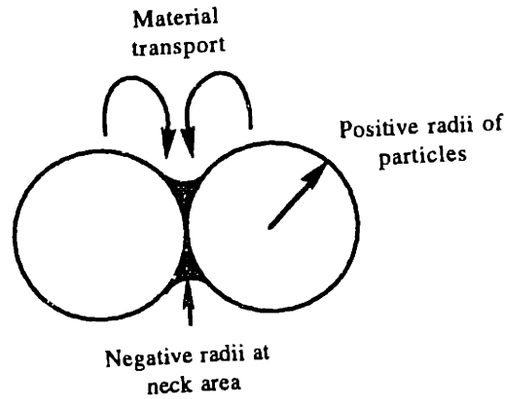

Figure 6.16 Material Transport from Area with Positive Radii to Negative Radii.
The Growth of Neck Area Strengthen the Network

Growth of interfacial area augment the strength and stiffness of the networks allowing them to withstand capillary stress without much shrinkage [3]. The concept is shown in Figure 6.16. Solubility and redeposition depends on temperature, pH, concentration, and type of solvent.

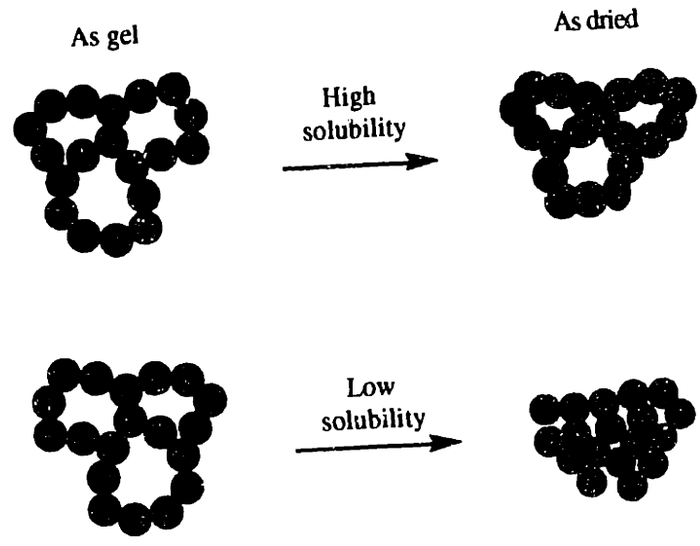

Figure 6.17 Strong Network Withstands Capillary Stress with Less Shrinkage

Iler has discussed the solubility and redeposition of silica at length in his book [4]. Solubility of silica in water was studied by Struckman in 1855 [5]. It was concluded that amorphous silica dissolved in water at 100-150 ppm at room temperature. The curves of silica solubility are illustrated in Figure 6.18.

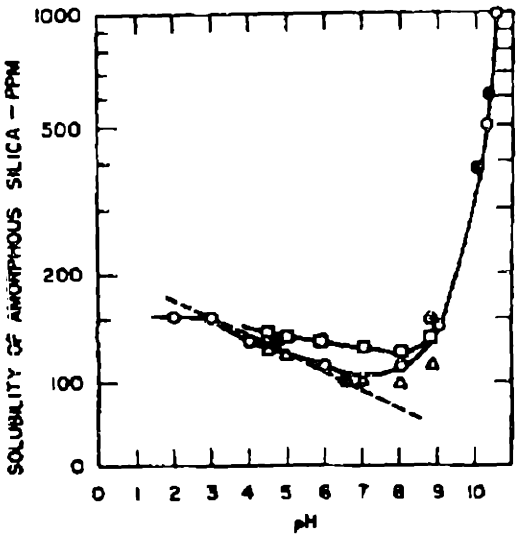

Figure 6.18 Solubility of Amorphous Silica with pH.
From many sources included Cherkinskii, Knyaz'kova, and Baumann

Not only is the solubility depends on pH and temperature, but also the rate of dissolution. Baumann [6] has shown that between pH 3 to 6, the dissolution rate increases proportionally with the amount of hydroxyl ion concentration. Dissolution rate is less sensitive to the ion outside of this pH range, Figure 6.19.

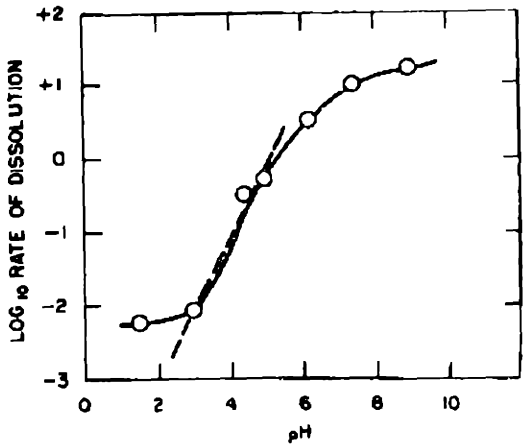

Figure 6.19 Dissolution Rate of Amorphous Silica with pH [6]

As indicated by Figure 6.18 and 6.19, the solubility and dissolution rate of amorphous silica rapidly increases at high pH. At pH 10, amorphous silica exhibits 5 times the solubility and 3 orders of magnitude of dissolution rate than at pH 5.

Binder B was designed to gel with PEG bridging when the pH is lower than 7.5. But it was not designed to age at high pH since PEG linkages will be destroyed, thus, dispersed silica particles again. Therefore, the concept of solubility and redeposition was tested with Nyacol 9950 at 50 weight percent. Nyacol 9950 is known to gel with the presence of positive charges. Aluminum nitrate was selected as the coagulant for its high positive charge and acidic solution. Nyacol 9950 was mixed with aluminum nitrate until the pH was about 3. The mixture was stirred until gelation took place. Then one set of the mixture is mixed with ammonium hydroxide (1 M) solution until the pH returned to about 10. Both samples were dried in air for 24 hours at room temperature. Gel aged with higher pH appeared to have much higher stiffness because of extra solubility and redeposition. Figure 6.20 shows mercury intrusion of both gels after drying

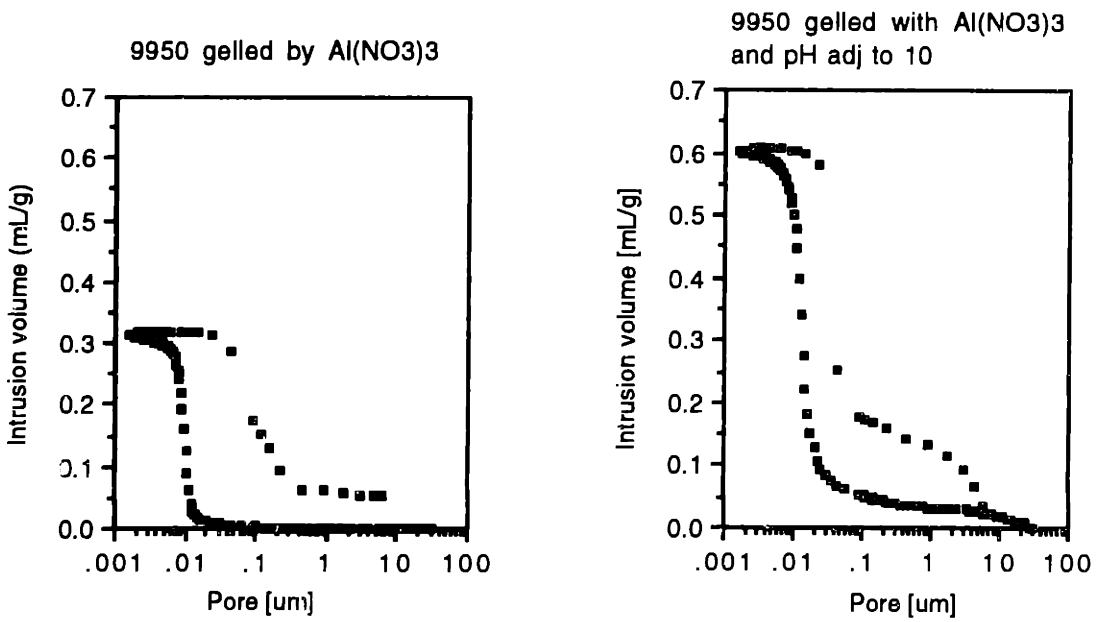

Figure 6.20 Mercury Intrusion of Nyacol 9950 aged at (a) pH 5 (b) pH 10

Gel aged with high pH exhibits pore distribution between 0.1 to 30 μm which is not the case for that aged at low pH. Although both gels maintain an average pore diameter of about 10 nm, gel aged at high pH possesses about twice the pore volume. This is

because the network has developed more strength and stiffness to prevent pores from being collapsed and closed down by capillary stress. Density of dried gel is another indicator of network strength and stiffness. Dried gels with low density must have superior network strength to withstand tremendous capillary stress. Figure 6.21 illustrates densities of the Nyacol 9950 aged at low and high pH in Figure 6.20 measured by the porosimeter.

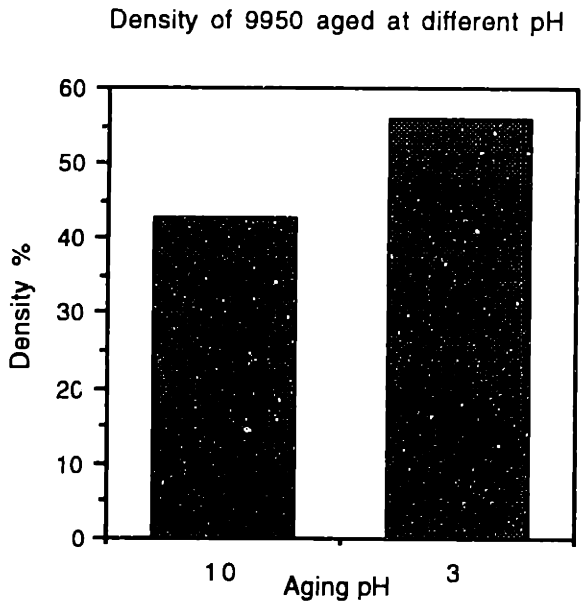

Figure 6.21 Density of Nyacol 9950 Gelled by Aluminum Nitrate and Aged at different pH.

Although the gelation mechanism is not the same as colloidal silica, alkoxide silica gels derived from tetraethoxysilane (TEOS) and tetramethoxysilane (TMOS) exhibit higher network stiffness and pore fraction with lower shrinkage after being catalyzed and aged in basic environment. Kawaguchi [7,8], Brinker [9], and many other researchers found that alkoxide gels aged in high pH produced less shrinkage and less density than at low pH similarly to colloidal silica.

In summary, drying shrinkage can be lowered by increasing of the network strength and stiffness. It is achievable by augmenting silica dissolution from particle surface and depositing them onto interfacial areas. The result is high strength and high stiffness network that is capable of withstanding capillary stress without much shrinkage. These findings suggest a direction for further research in the chemistry of silica to reduce shrinkage.

6.2.3 Reducing Capillary Stress

Shrinkage can be lowered by reducing the magnitude of liquid tension induced by capillarity. A few of the current techniques in sol-gel research are discussed below with their limitation to Three-Dimensional Printing.

• REPLACING WATER WITH A LIQUID OF LOWER SURFACE TENSION

Liquids of lower surface tension are sometime deployed. Behrman [10] dehydrated alkoxide silica gel from ammonia. Silica-alumina gels were washed with methanol and dried in an autoclave. Kearby [11] produced low density gel from water-miscible organic liquids such as alcohol or ketones and subsequently dried at atmospheric pressure. Popular solvents include alcohol, water miscible solvents, acetone, and hexane. These liquids have much less surface tension than water and therefore place significantly less capillary stress on the network.

However, all of these techniques have the luxury of post-gelation processing such as washing, adding, and replacing pore water with other liquid while Three-Dimensional Printing doesn't. The fact that silica gelation in Three-Dimensional Printing takes place inside the powder bed limits most of these post-gelation techniques.

• SUPERCRITICAL DRYING

Shrinkage is driven by liquid tension caused by capillarity at the liquid-vapor interface. However, the liquid and vapor coexist without an interface in supercritical state and no liquid tension is generated. In this way supercritical drying gels can be made with minimal shrinkage by conducting the evaporation above the critical temperature and pressure. Prassas et al. [12] and Van Lierop [13] have proven that supercritical drying prevents uncontrolled shrinkage and cracking during drying.

Supercritical drying can be achieved with autoclaves. The pressure and the temperature are increased in such a way that the phase boundaries are not crossed (path A or B) [13]. Once the pressure and the temperature are above the critical value, the liquid is

vented out while keeping the temperature constant above the critical temperature (path C) shown in Figure 6.22.

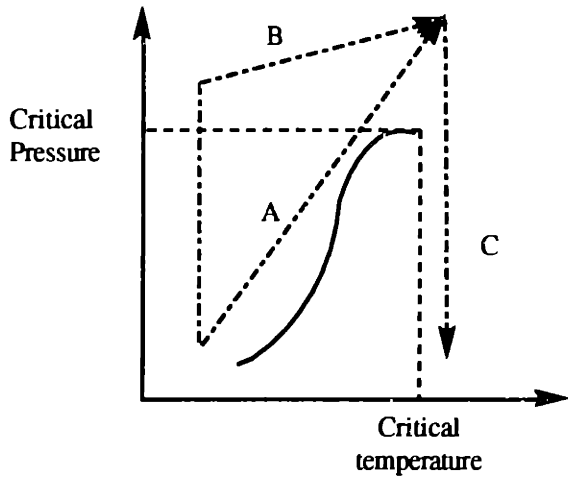

Figure 6.22 Supercritical Drying

The shortcoming of supercritical drying to Three-Dimensional Printing was reported by Kistler [14]. He found that silica gel with water solvent dissolved if subjected to supercritical conditions but not with ethanol solvent. This restriction confines the use of supercritical drying to unpractical alcohol solvents for Three-Dimensional Printing. Another shortcoming of supercritical drying is the high pressure and temperature requirement (220.0 bars at 374°C for water) as well as time required. The autoclave must be made of special materials to avoid the danger of extreme pressure and temperature.

6.3 SPECIFIC VOLUME OF BINDERS

Shrinkage can be viewed with the change of specific volume. Comparing the volumetric change of bodies of different sizes could well be done by taking volume per unit weight or specific volume which is the inverse of density. The change in specific volume equals volumetric shrinkage per unit mass as described by Equation 6.1.

$$Sh_{spec.v} = \frac{1}{\rho_i} - \frac{1}{\rho_f} \tag{6.1}$$

where $Sh_{spec.v}$ is volumetric shrinkage in drying per unit mass between state i and state j

ρ_i is the density of the network at the point of gel

ρ_f is the density of the network at the end of saturation

Both $\frac{1}{\rho_i}$ and $\frac{1}{\rho_f}$ are the specific volume or volume per unit mass. So, $Sh_{spec.v}$ has a unit of volume change per unit mass. Volumetric strain or volume change per unit volume of the system is described by Equation 6.2

$$\varepsilon_v = \rho_i Sh_{spec.v} = \left(1 - \frac{\rho_i}{\rho_f}\right) \tag{6.2}$$

There are a couples of ways to measure the volume of irregular shaped rigid bodies. A direct way is to calculate it from outside dimensions which may require some approximation. An alternative to direct method is to displace the volume with some kind of liquid of a known density. In this way, the volume can be calculated from the weight of displaced liquid.

The displacement technique is applicable to estimate the volume of porous bodies provided that the liquid does not wet the surface. Mercury is a very good candidate for the job. It is known for high surface tension and a non-wet property to most surfaces. In addition, the high density of mercury makes the weight measurement sensitive to small changes of volume. Figure 6.23 illustrates displacement technique with mercury. First, the sample is weighed (a). Then it is put into a chamber of known weight and density (b). The weight is recorded. Next, mercury is filled into the chamber (c) and the total weight is recorded again.

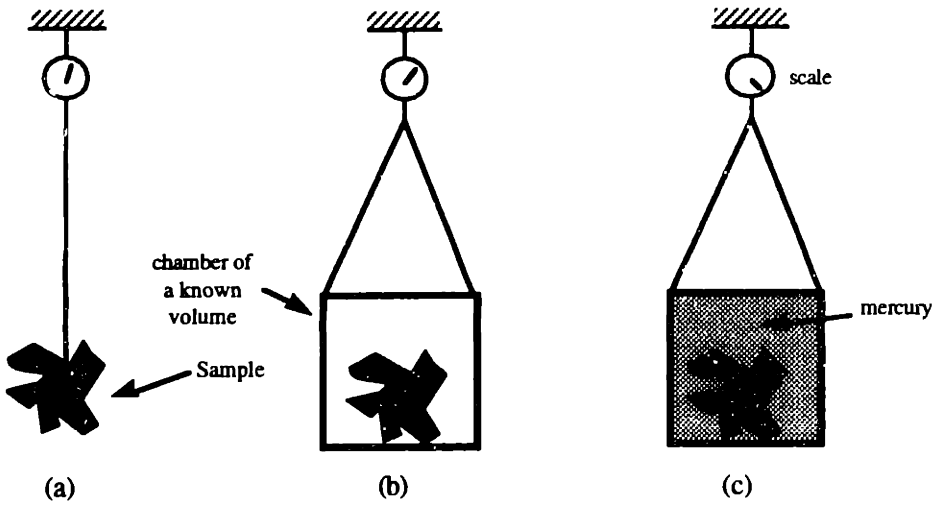

Figure 6.23 Measurement of Volume by Mercury Displacement Principle
(a) Sample weight (b) Sample in a chamber of known volume (c) Mercury filled the chamber

The volume of the sample can be calculated from weight difference between point (b) and (c). Dividing the volume by the sample's weight at point (a) gives specific volume. Practically, densities and specific volumes are obtainable from a porosimeter in a matter of minutes. Furthermore, the technique also provides pore volume distribution when mercury is forced to go into the pores at pressure.

Specific volume of Three-Dimensional Printing Binders in dry and after heat treatment to 900°C are plotted in Figure 6.24. The specific volumes at the gel point were taken by excluding the mass of the liquid phase which is equal to weight lost between gel and dried state. The specific volume of dried and heat treated gels were taken from samples with approximately 0.5 cc of volume after being dried in an oven at 80°C for 12 hours and after being heat treated to 900°C for 1 hour at 5°C per minute heat rate up ramp, respectively.

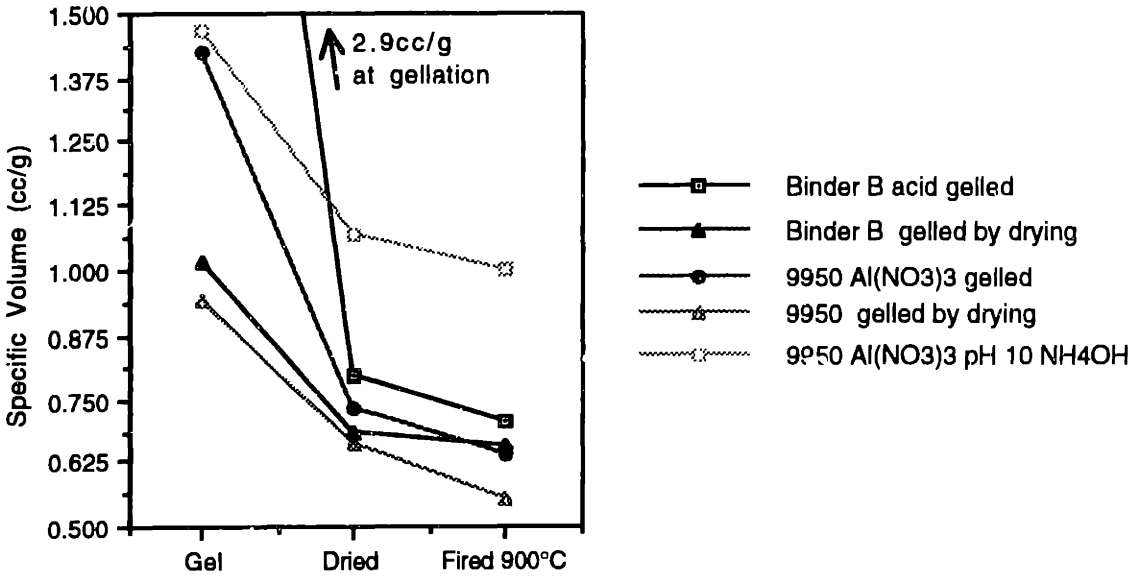

Figure 6.24 Specific Volume of Binders

The specific volumes reduce when binders dry and are heat treated. The reduction in specific volume between each process step indicates shrinkage. According to Figure 6.24, it is obvious that acid gelled Binder B has dramatic change of specific volume between the point of gellation and after being dried. It, therefore, predicts that the drying shrinkage of acid gelled Binder B with will be much more if gelled by the drying method or if straight Nyacol 9950 were used as a binder. The reduction of specific volume of current and prospect binders from point of gellation is illustrated in Figure 6.25.

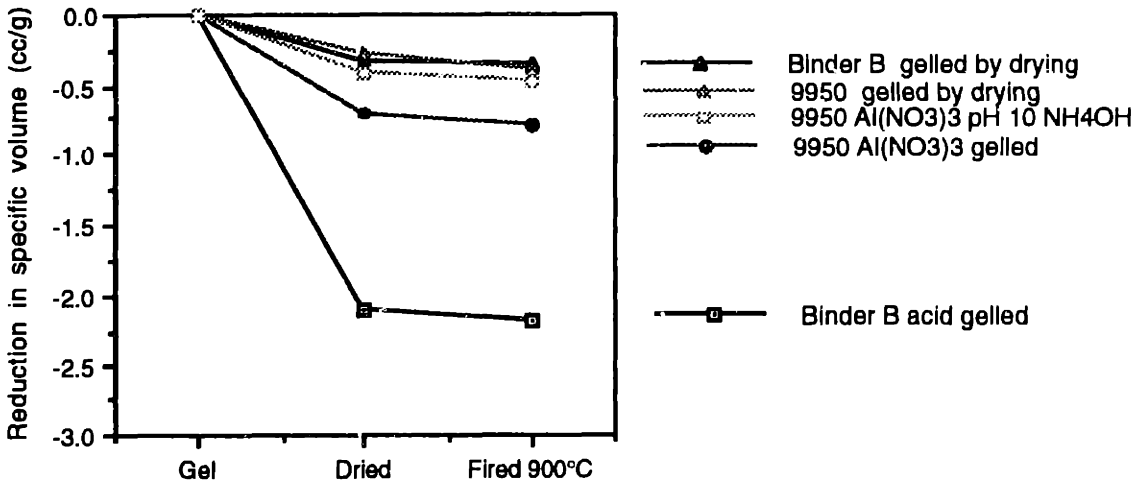

Figure 6.25 Reduction in Specific Volume of Binders

The smallest reduction in specific volume is found in several binders gelled by drying where the solid particles slowly polymerize into networks without liquid tension development. The largest reduction in specific volume takes place with rapid gelation which extends networks to capture a large amount of liquid in the pores. Such is the case for acid gelled Binder B and salt gelled Nyacol 9950. This confirms the shrinkage minimizing theory with low liquid content in Section 6.2.1.

It is very important to understand that it is not only the reduction in specific volume of the binder alone that controls shrinkage in Three-Dimensional Printing, but the interaction between the binder that the powder. Binders join two adjacent powder particles by bridging them at the neck or at their closest point. While the binder exerts pulling, the powder is places under compression and serves as detainment boundaries for binder. Therefore, the shrinkage of binder alone does not truly constitute the shrinkage of this composite structure. If the powder exhibits no relative movement between particles under tensile stress of the binder, then there will be no shrinkage no matter how much binder deformation there is. This fact seeds the idea for binder stress-strain experiment described in the next section. Here the boundary conditions and the binder deformation combine to produce part shrinkage.

6.4 STRESS-STRAIN MAP OF DRYING BINDERS

6.4.1 Principle of Powder-Binder Shrinkage Interaction

Shrinkage of Three-dimensional Printing parts are not constituted by binder deformation alone, but together with the response of powder under binder shrinkage stress. The concept of powder-binder shrinkage interaction was shown in schematic in Figure 6.26 which illustrates a model of powder 'resistance' to the shrinkage stress of liquid bridge binder. In the case of high powder resistance, there will be minimal shrinkage with the binder deformation. On the other hand, where the powder resistance is low, the shrinkage will be substantial. This emphasizes the need to investigate both powder, binder, and their interaction for a full understanding of shrinkage.

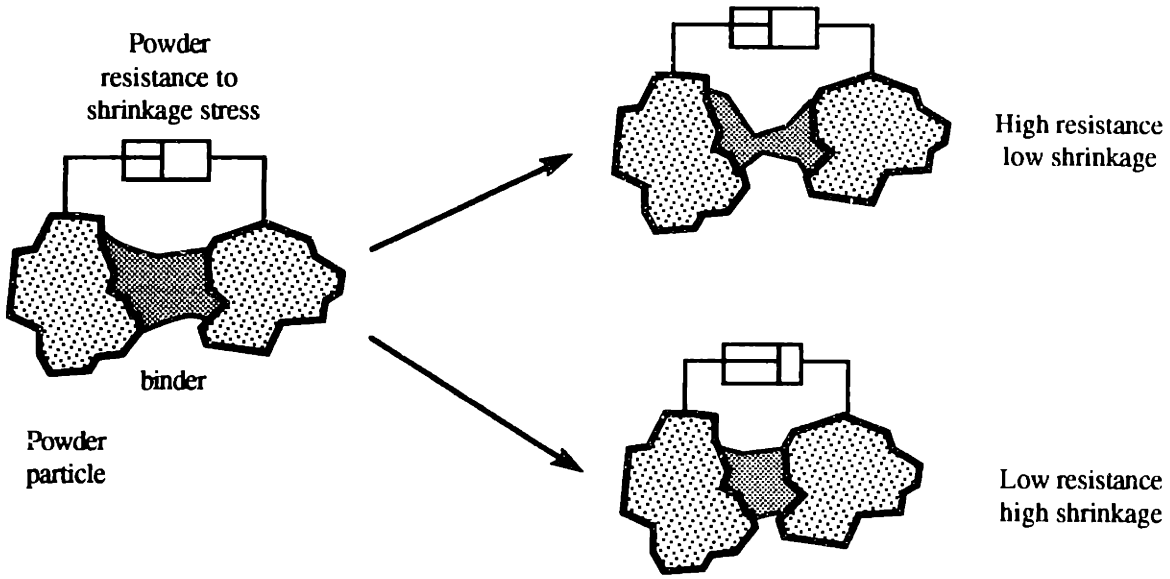

Figure 6.26 Powder-Binder Shrinkage Interaction Showing Low Shrinkage for High Powder Resistance to Shrinkage Stress and High Shrinkage for Low Resistance, Vice Versa.

Powder resistance to shrinkage stress can be simply modeled by a special elastic member that only compresses without springing back (or one-way spring). A schematic of the special spring is shown in Figure 6.27 (a) with a compression spring and a ratchet in compound. The spring takes up the compression load from shrinkage consolidation. However, it is not allowed to return to its initial free length. The concept can be visualized by the ratchet mechanism that governs one way motion.. In the case where there is no unloading, the ratchet mechanism may be eliminated, Figure 6.27 (b).

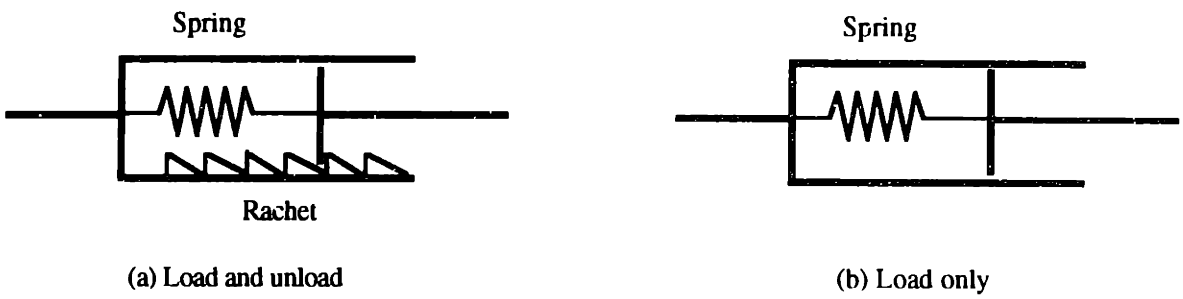

Figure 6.27 Model of Shrinkage Resistance

In reality, powder consolidation under shrinkage stress is constituted by the sliding and restacking of particles in the powder bed into a greater density. The shrinkage force is balanced by interparticle friction which depends on the packing fraction and the shape of the powder. The response within the range observed in Three-Dimensional Printing is linear plastic such that the stress varies with the strain and when the shrinkage force is removed, powder will not return to its original volume due to the irreversible process of sliding and restacking. The 'virtual' spring stiffness, k, in the powder resistance model is a function of initial pore fraction at virgin state, ε_i, and morphology of the powder, ψ, or:

$$k = k(\varepsilon_i, \psi) \tag{6.3}$$

Details of powder response to shrinkage stress will be discussed further in Chapter 7. As of this point, the resistance is to be modeled as an adjustable elastic spring

The concept of powder-binder shrinkage interaction can be tested with a setup shown in Figure 6.28. Here a drop of binder is detained between a set of parallel flat plates made out of dense alumina. One side of the plate is grounded to the frame while the other is mounted on an elastic leaf spring. As the binder consolidates, it pulls on the movable plate and exerts tension force to the spring. The movement can be monitored by an optical sensor system. Stress is calculated from the ratio of the tension force in the spring and the cross-section of the *initial* neck area of the binder. It is very important to point out that this is not a true stress on the binder's neck due to reduction in the cross-section area, but more as an engineering stress. Strain is calculated from the ratio of the boundary movement to initial binder height.

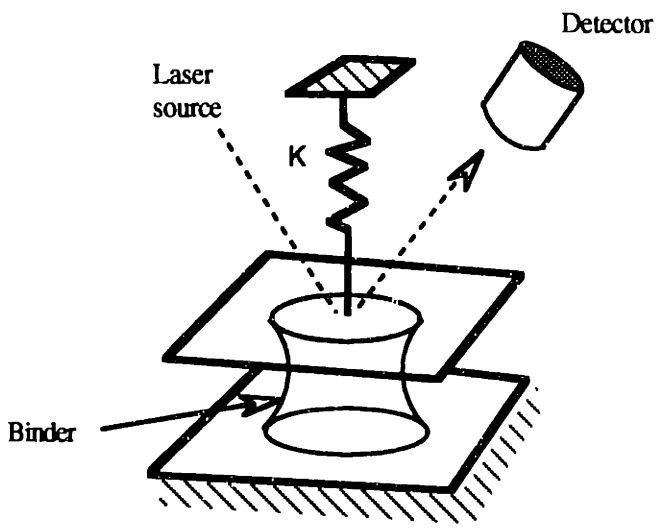

Figure 6.28 Schematic of Binder Stress-Strain Experiment

6.4.2 Design of Binder Stress-Strain Experiment

Since stress and strain are both functions of the boundary movement, they linearly vary upon one another. The plot of stress versus strain is a straight line with a constant slope depending on the boundary stiffness, k, initial binder height, and the neck area. The conceptual setup design in Figure 6.28 was further iterated to the final design in Figure 6.29. Springs are made from hardened ground steel feeler stock with two simple supports at both ends to maintain the parallel. The boundaries are made of dense electronic grade alumina substrates. Alumina was selected to maintain powder-binder wetting characteristic. One of the boundaries was glued on the spring beam while the other was mounted on a set screw which controls initial binder height.

Due to the high liquid tension in drying (about 3 MPa), binders are known to crack as saturation ceases and the liquid-vapor interface recedes into the interior. Cracks propagate into the interior behind the liquid-vapor front because of the tremendous stress different in front of and behind the liquid-vapor interface. Whether a body will crack in drying depends on the stress level, its strength, and size. Small bodies may survive drying crack free because of less stress gradient. The dimension threshold for crack free is known as the critical thickness. Our binders have a critical thickness in the order of 10-30 μm. Anything above this dimension is subject to crack.

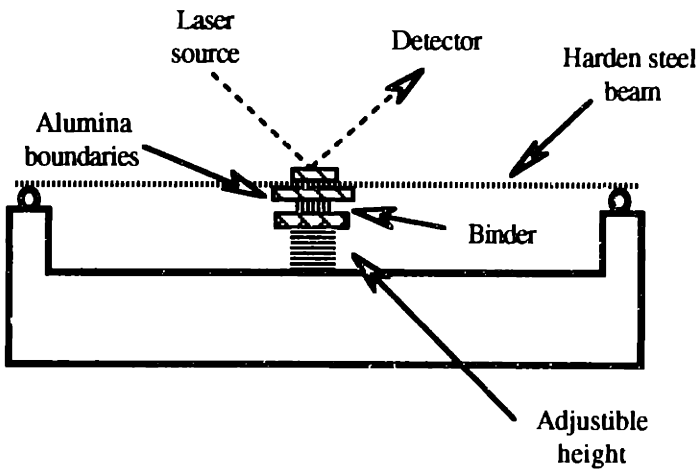

Figure 6.29 Design of Powder-Binder Shrinkage Interaction Machine

However, 10-30 μm is impractical fort the binder stress-strain experiment. The strain associated with this small sample will be almost undetectable. In fact, a practical

sample size probably needs to be approximately 1000 μm or 1mm. As a consequence, cracking at the end of saturation is inevitable. According to the theory of drying deformation in Chapter 4 and 5, most of drying shrinkage takes place when the body is under saturation. Shrinkage terminates as the saturation ceases. Therefore, technically, cracking which appears after the end of saturation should not effect the magnitude of drying shrinkage. This is a very important assumption for the binder stress-strain experiment.

Selected binder volume for the setup was 5 μl due to good accuracy and repeatability of the volume measurement. Initial binder height was set to be about 250 μm. This left the binder radius to be approximately 800 μm. The spring beams are made of 1095 high carbon steel with 48/62 Rockwell scale C hardness and a Young's modulus of 107 GPa. They are made with 0.5 inches width. The stiffness at the middle of the beam is governed with Equation 6.4

$$\frac{y_d}{W} = \frac{l^3}{48EI} \tag{6.4}$$

where y_d is the deflection at the center of the beam
W is the load at the center of the beam
l is the beam span which is 2.0 inches in this case
E is the Young's modulus of the beam = 107 GPa
I is the moment of area of the cross-section

Properties and stiffness of the beams used in this experiment are shown in Table 6.1

Beam Thickness mils	Boundary compliance mm/g	Boundary compliance mils/g	Average initial binder height mils
4	0.25	8.88	11.15
7	0.041	1.6	10.73
10	0.0144	0.568	9.08
17	0.0029	0.116	11.40

Table 6.1 Properties and Compliance of the Beams Used in Powder-Binder Shrinkage Interaction Experiment

Shrinkage strain of the binder was monitored by the deflection at the center of the beam with a PRS-15 Point Range Sensor by CyberOptics. The sensor makes use of laser triangulation technology to detect the position of the target. PRS-15 has 0.38 μm resolution with measurement range of 0.15 mm, Figure 6.30. The extreme resolution of PRS-15 makes it very useful for detecting tiny shrinkage in situ.

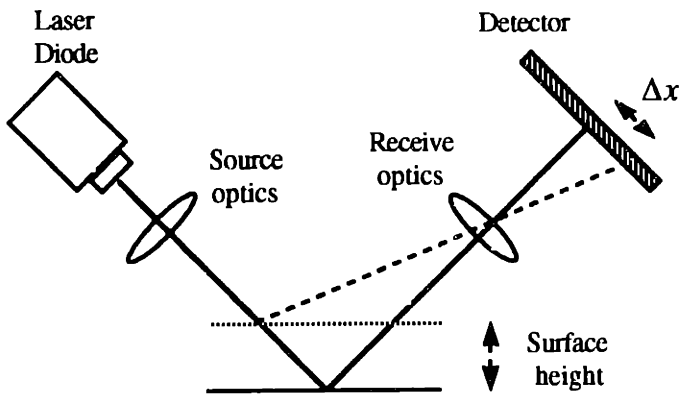

Figure 6.30 Laser Triangulation Principle

Stress on the binder results from shrinkage deformation against the spring beam. The stress equals the product of the spring stiffness and the deflection over the *initial* cross section area of the binder.

$$\sigma_b = \frac{\text{Force}}{\text{area}} = \left(\frac{kl_o}{A_b}\right)\delta \tag{6.5}$$

where σ_b is the binder shrinkage stress

k is the stiffness of the boundary (or the beam)

l_o is the initial binder height

A_b is the cross section area of the binder

δ is the strain of the binder

According to Equation 6.5, stress linearly varies with strain by $\frac{kl_o}{A_b}$ ratio. A map of stress versus strain of binders is shown as a straight lines with a slope of $\frac{kl_o}{A_b}$ depending on boundary stiffness, k, as shown in Figure 6.31 (a)

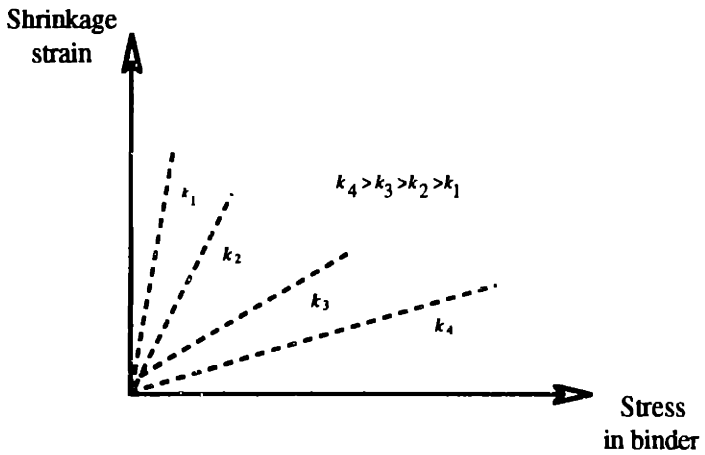

(a)

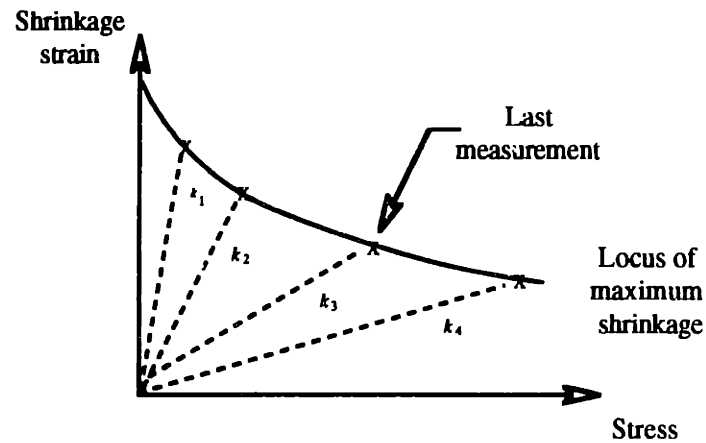

(b)

Figure 6.31 (a) Stress Varies Linearly With Strain per Boundary Compliance
(b) Locus of Maximum Shrinkage

More important than the stress-strain relation is the loci of maximum shrinkage of the binders. These are the loci of last shrinkage values prior to binder cracking for a range of boundary stiffness. The concept of shrinkage locus is shown in Figure 6.31 (b). Shrinkage locus relates maximum shrinkage strain to boundary compliance for an individual binder. In reality, the boundary stiffness is determined by powder characteristics. Therefore, the locus represents shrinkage equilibrium between the powder and the binder. For example, maximum strain for the case of stiff boundary (or stiff powder), k_4, is lower than for that of less boundary stiffness, k_1.

Shrinkage loci were measured with three binder systems; 1) Binder B gelled by acid 2) Binder B gelled by drying, and 3) Nyacol 9950 at 50 weight percent gelled by drying. Acid gelled Binder B represents the case where network is formed with high liquid content. Drying gelled Binder B stands for the system with less liquid content at the point of gel. And, lastly, drying gelled Nyacol 9950 at 50 weight percent represents systems with high silica loading gelled at low liquid content without organic additives similar to investment casting.

6.4.3 Experimental Result

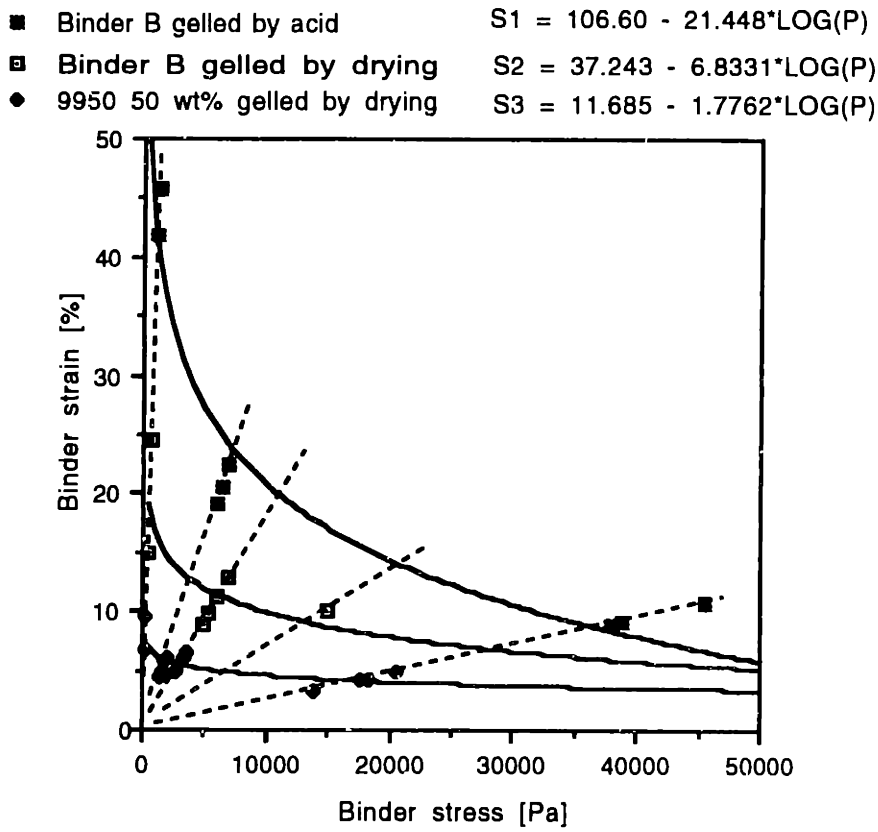

Figure 6.32 Shrinkage Strain Loci of Tested Binders

The shrinkage strain locus for acid gelled Binder B is the highest while drying gelled Binder B has approximately 50 percent less strain. Nyacol 9950 gelled by drying maintains the least strain, Figure 6.32. Between acid and drying gelled Binder B, the result is consistent with the theory in Chapter 5 that liquid content at gel point determines

shrinkage potential. When network strength is unable to withstand the compression load induced by capillary, more liquid content means more shrinkage.

Binder B and Nyacol 9950 are different by organic additives and silica content. Shrinkage of Binder B gelled by drying is more than that of Nyacol 9950. This is an indication that the organic additives in Binder B prohibit silica particles from building strong interparticle bonds. PEG is suspected in this case. Above pH 7.5, PEG attaches one end of its chain to a silica particle and entends the other end outward creating a barrier that repels one another particles. The barrier serves as a plasticizer and prohibits particles to polymerize and to form a strong silica network

6.4.4 Model Development and Discussion

The lines and slopes of the loci in Figure 6.32 must have some underlying meanings. Let's look at the a simple case of a composite consisting of two *elastic* materials bounded by rigid frames. Material p has the Young's modulus of E_p with a cross section area A_p. while material b has the Young's modulus of E_b with a cross section area A_b as shown in Figure 6.33 (a). Material b is known to shrink during drying with a shrinkage strain potential of α. The shrinkage strain potential, α, is defined as maximum free strain of material b with no boundary constraint. The magnitude of strain potential depends on drying which can be categorized by the pore fraction. The term $\frac{\varepsilon_i - \varepsilon(t)}{\varepsilon_i - \varepsilon_f}$ is normalized ratio of pore fraction where ε_i is the pore fraction at point of gel, ε_f is the pore fraction when saturation terminates, and $\varepsilon(t)$ is current pore fraction of drying body at time t ($\varepsilon_i > \varepsilon(t) > \varepsilon_f$). Suppose there is no constrain from material p, material b would shrink by $\alpha l_o\left(\frac{\varepsilon_i - \varepsilon(t)}{\varepsilon_i - \varepsilon_f}\right)$ as shown in Figure 6.33 (b). But, since material b is constrained by material p, they will reach a new equilibrium where material b is under tension and material p is under compression. Material b elongates to a distance of $\delta_b l_o$ with a force of P_b and material p is shorten by $\delta_p l_o$ with a force of P_p, Figure 6.33 (c).

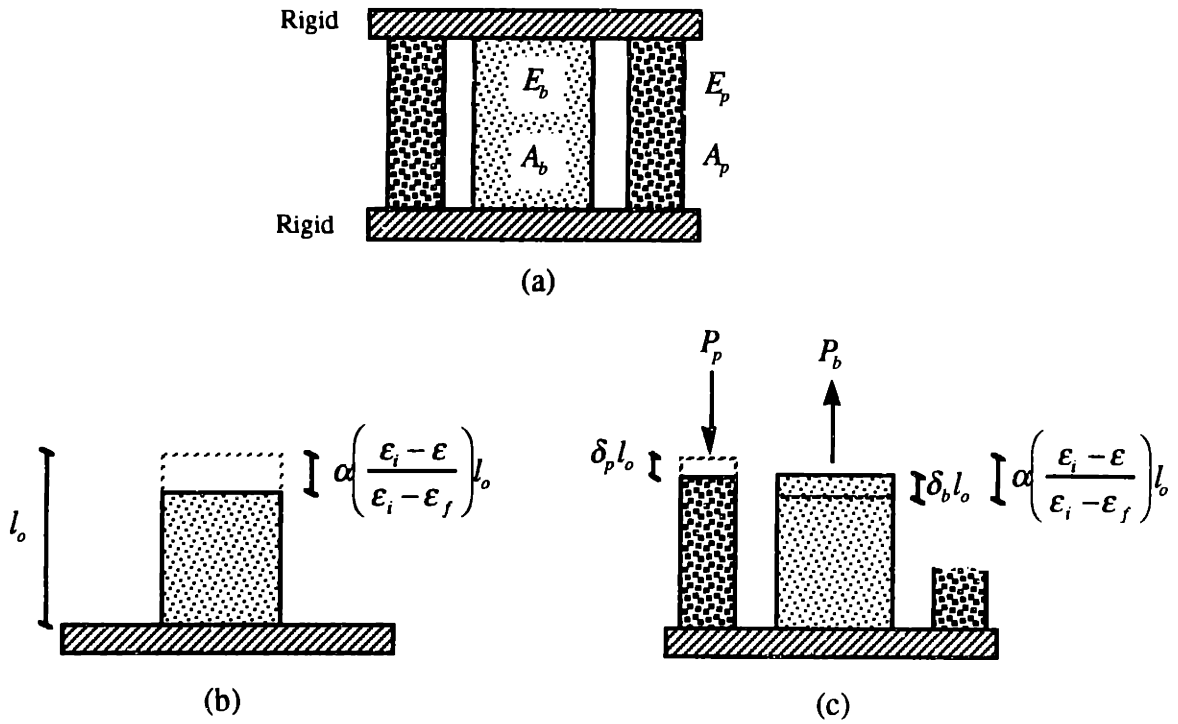

Figure 6.33 Shrinkage of Elastic Composite Materials

The composite is, at all time, under static equilibrium, therefore, P_p is always equals to P_b. Displacement $\delta_b l_o$ and $\delta_p l_o$ always add up to $\alpha l_o\left(\frac{\varepsilon_i-\varepsilon(t)}{\varepsilon_i-\varepsilon_f}\right)$ or:

$$\alpha\left(\frac{\varepsilon_i-\varepsilon(t)}{\varepsilon_i-\varepsilon_f}\right)l_o=\delta_b l_o+\delta_p l_o \tag{6.6.a}$$

or

$$\alpha\left(\frac{\varepsilon_i-\varepsilon(t)}{\varepsilon_i-\varepsilon_f}\right)=\delta_b+\delta_p \tag{6.6.b}$$

But, from stress-strain relationship, $\delta_b=\frac{P_b}{E_b A_b}$ and $\delta_p=\frac{P_p}{E_p A_p}$

so Equation 6.6.b is

$$\alpha\left(\frac{\varepsilon_i-\varepsilon(t)}{\varepsilon_i-\varepsilon_f}\right)=\frac{P_b}{E_b A_b}+\frac{P_p}{E_p A_p}$$

$$\alpha\left(\frac{\varepsilon_i - \varepsilon(t)}{\varepsilon_i - \varepsilon_f}\right) = P\left(\frac{1}{E_b A_b} + \frac{1}{E_p A_p}\right)$$

$$P = \frac{\alpha\left(\frac{\varepsilon_i - \varepsilon(t)}{\varepsilon_i - \varepsilon_f}\right)}{\left(\frac{1}{E_b A_b} + \frac{1}{E_p A_p}\right)} \tag{6.7}$$

where $P = P_p = P_b$

Total shrinkage strain of the composite is

$$\delta_p = \frac{P}{E_p A_p}$$

substitute into Equation 6.7

$$\delta_p = \frac{\alpha\left(\frac{\varepsilon_i - \varepsilon(t)}{\varepsilon_i - \varepsilon_f}\right)}{\left(\frac{E_p A_p}{E_b A_b} + 1\right)} \tag{6.8}$$

In case material p is replaced by pure elastic springs with a constant, k, the term $E_p A_p$ is replaced by kl_o where l_o is the initial length of the composite, Figure 6.34.

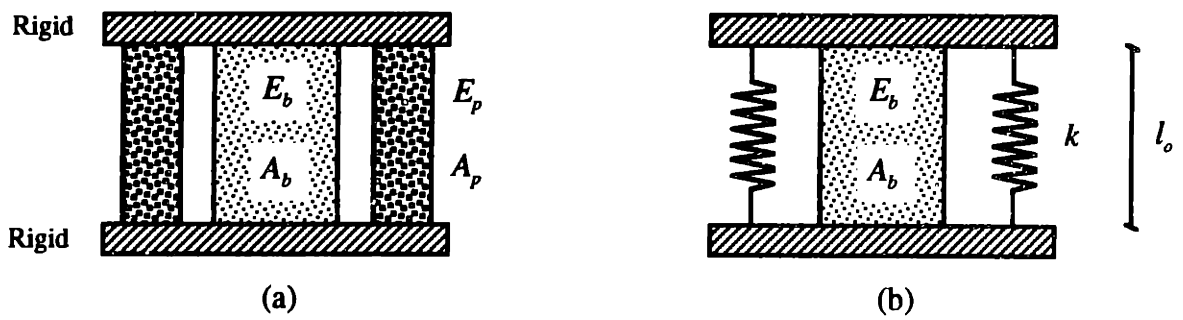

Figure 6.34 Replacing Elastic Member p by a Pure Spring

So, Equation 6.8 can be written as

$$\delta_p = \frac{\alpha\left(\frac{\varepsilon_i - \varepsilon(t)}{\varepsilon_i - \varepsilon_f}\right)}{\left(\frac{kl_o}{E_b A_b} + 1\right)} \tag{6.9}$$

Stress on material b is

$$\sigma = \frac{kl_o \delta_p}{A_b} \tag{6.10}$$

so Equation 6.10 may be restated in terms of stress and strain as

$$\delta_p = \frac{\alpha\left(\frac{\varepsilon_i - \varepsilon(t)}{\varepsilon_i - \varepsilon_f}\right)}{\left(\frac{\sigma}{E_b \delta_p} + 1\right)}$$

or

$$\delta_p = \alpha\left(\frac{\varepsilon_i - \varepsilon(t)}{\varepsilon_i - \varepsilon_f}\right) - \frac{\sigma}{E_b} \tag{6.11}$$

However, δ_p and σ are not truly independent but being constrained by Equation 6.10 where $\delta_p = \left(\frac{A_b}{kl_o}\right)\sigma$. So, the relationship of stress and strain can be plotted as Figure 6.35.

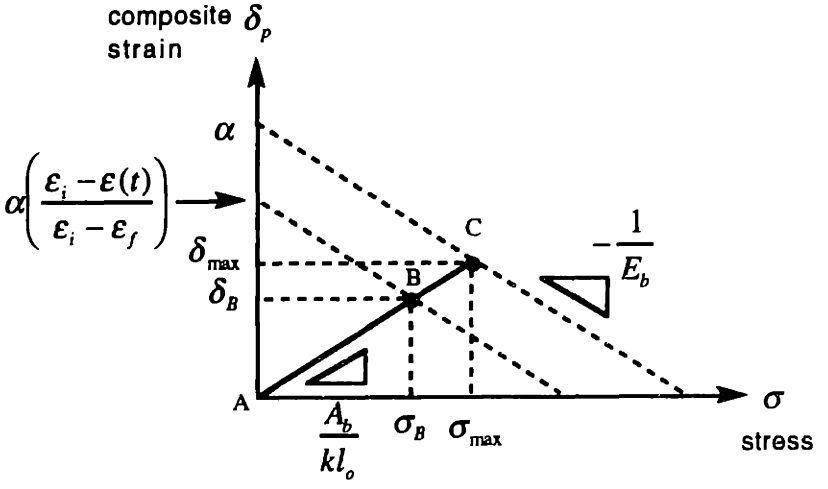

Figure 6.35 Model of Shrinkage Strain Locus and Stress-Strain Map

According to Equation 6.11, the negative slope of shrinkage locus represents the Young's modulus of the binder. The shrinkage stress-strain relation follows a straight line (AC) with a slope of $\frac{A_b}{kl_o}$ starting at point A. At any arbitrary point B along line AC, stress and strain of the composite at this point are σ_B and δ_B respectively while shrinkage strain potential reaches $\alpha\left(\frac{\epsilon_i-\epsilon_B}{\epsilon_i-\epsilon_f}\right)$ as illustrated in Figure 6.35. When the shrinkage strain potential reaches its maximum at α at point C, the stress and strain in the composite are at their utmost at σ_{max} and δ_{max} respectively. There is no further shrinkage beyond this point and the liquid-vapor front starts to move into the interior.

Nevertheless, the model in Figure 6.35 is unable to capture the full picture of shrinkage stress-strain. It is obvious that the shrinkage locus is not a straight line as shown in Figure 6.32 but rather curved. This could be explained by:

1) The model was developed from elastic properties of both composite materials. In fact, the behavior of drying binder is time-varying viscoelastic which makes it much harder to model.
2) The model simplifies the problem into one dimension whereas real drying deformation takes place in three-dimension. The relation between radial and axial deformation in three-dimensional shrinkage is much more complex. For stiff boundaries, it is easier for the gel to deform radially than axially. So, the shrinkage strain potential is lower in this case. For loose boundaries, the strain potential increases. This is shown in Figure 6.36 and 6.37.

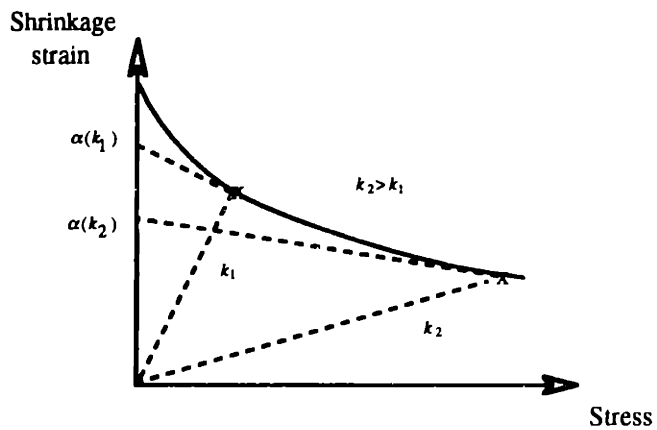

Figure 6.36 Shrinkage Strain Potential Depends on Boundary Resistance

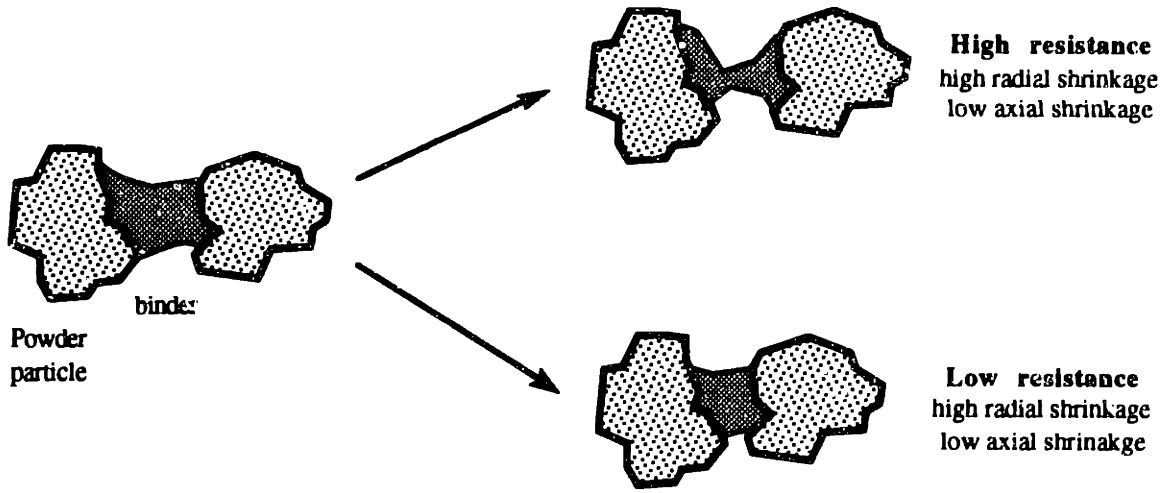

Figure 6.37 Radial and Axial Shrinkage as a Function of Boundary Resistance

However, the model is able to capture powder-binder shrinkage interaction such that the binder drying deformation places the powder under compression. As the shrinkage strain potential continues to increase upon drying, both phases are further exposed to more stress, but at all time maintain their quasi-static equilibrium which defines the level of shrinkage of the composite. The shrinkage strain potential peaks at the end of saturation, at the same time, the total shrinkage of the composite reaches its maximum.

Binder B gelled by acid maintains high liquid content at the point of gel. As a direct consequence, it has a high shrinkage potential (high α) resulting in high shrinkage strain. When Binder B is gelled by drying, a portion of water escapes from the system during early state of drying without placing the network under tensile stress. By the time the network is formed only a fraction of water is enclosed, thus, the shrinkage potential is low. Despite reduced shrinkage potential, the network is unable to develop high strength due to several organic additives which prohibits silica dissolution and redeposition. Therefore, the shrinkage is approximately half of the acid gelled case, but is still substantial. When the binder is free of the organic additives with high silica content such as Nyacol 9950 at 50 weight percent, the network is stronger and, therefore, has significantly less drying shrinkage.

6.5 SHRINKAGE DURING HEAT TREATMENT

Another source of shrinkage in Three-Dimensional Printing of ceramic process is from the heat treatment. Silica particles sinter and viscously flow to deposit in the interfacial areas and strengthen the printed parts. However, the particles are also brought closer resulting in shrinkage. The rate of sintering depends on temperature, particle shape and size, and surface energy.

The shrinkage strain during heat treatment of binders can be tested with a dilatometer. Samples were push against a rigid wall with a spring loaded alumina rod that measures minute displacement while the samples are being heated in the furnace. Tested binders include: 1) Binder B gelled with acid, 2) Binder B gelled by drying, 3) Nyacol 9950 at 50 weight percent, and 4) Bimodal colloidal silica at 43.5 weight percent made from Nyacol 9950 (100nm) and Nyacol 830 (10nm) at 70:30 solid volume ratio. All binder samples were casted in flat dishes at room temperature. A small piece were cut from each binder disk and tested for heat treatment shrinkage in the dilatometer, Figure 6.38

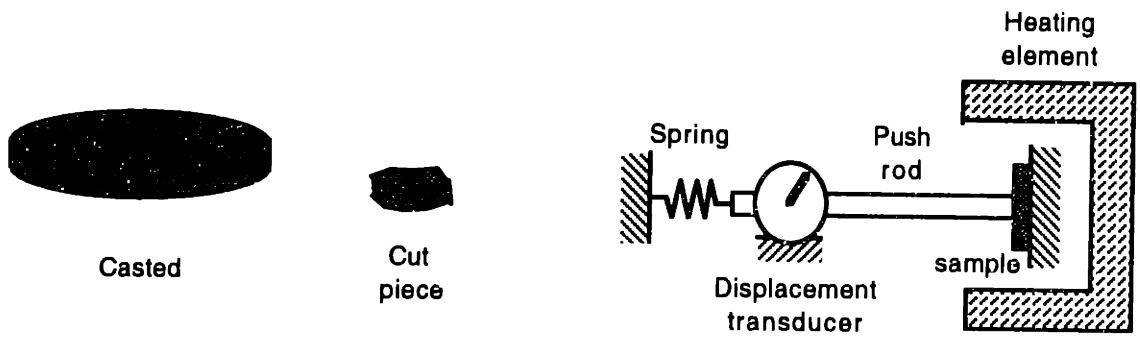

Figure 6.38 Prepared Sample and Dilatometer

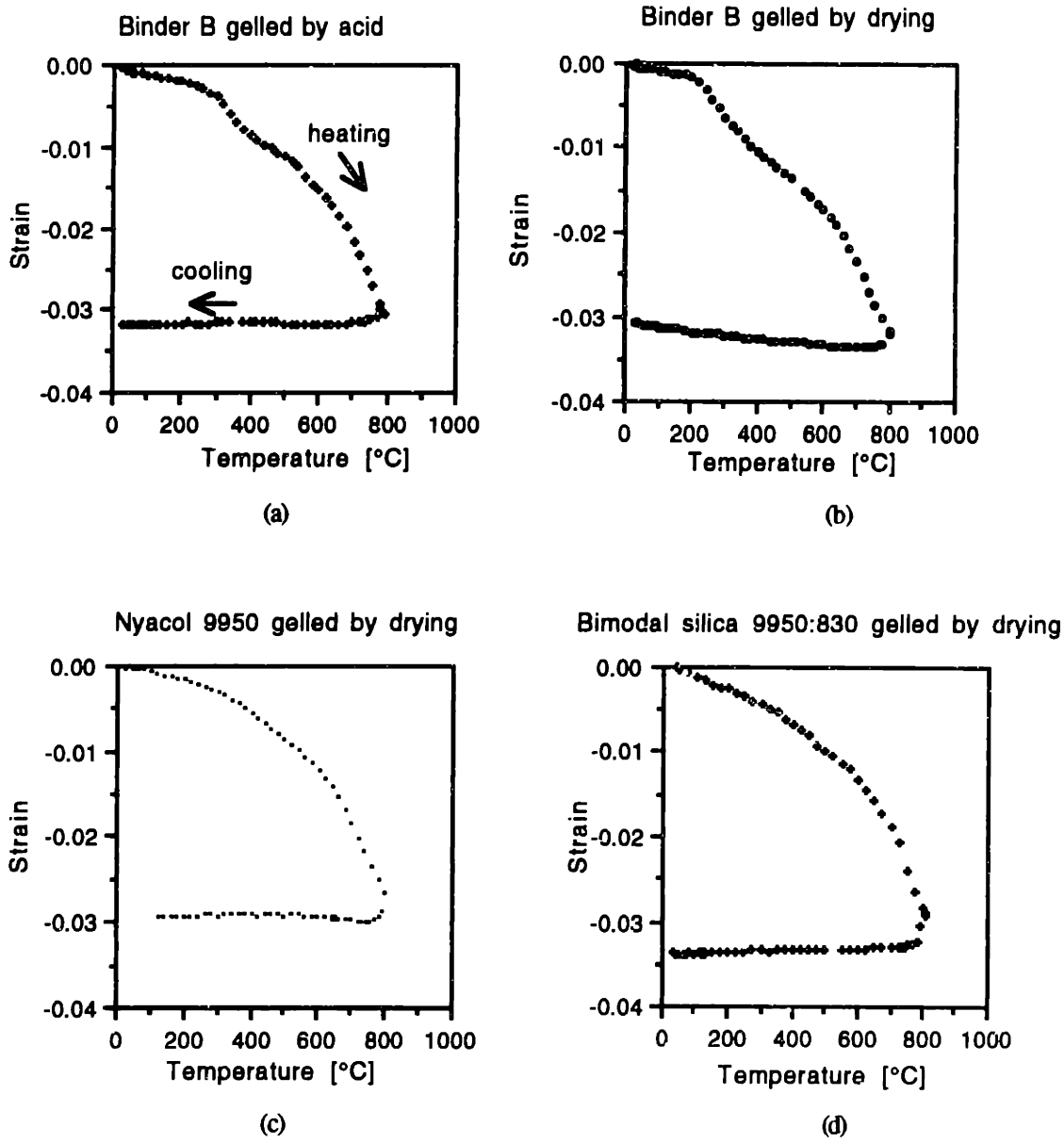

Figure 6.39 Heat Treatment Shrinkage Strain of Binders
(a) Binder B Gelled with Acid (b) Binder B Gelled by Drying
(c) Nyacol 9950 at 50 wt % gelled by drying (d) Bimodal Colloidal Silica

Heat treatment shrinkage strain for the binders are shown in Figure 6.39. Binder B both gelled by acid and drying have shrinkage strain of 3.2 percent when heat treated to 900°C. While bimodal silica has slightly more heat treatment strain of 3.5 percent because of higher degree of sintering of small silica particles (10nm). The shrinkage of Nyacol 9950 at 40 weight percent is least among tested binders at slightly less than 3 percent.

Heat treatment shrinkage starts slowly below 300°C and rapidly increases with temperature. The strain sharply increases above 600°C due to the fact that a large fraction of the silica particles sinter above the temperature. During drying, capillary stress is so high such that both Binder B and Nyacol 9950 are packed to comparable densities, Figure 6.24. The fact that Binder B contains some organic additives contributes to an additional shrinkage of 0.3 to 0.5 percent when burned out at 300-400°C. This is a primary cause for extra shrinkage strain for Binder B as compared to Nyacol 9950. The bimodal silica binder contains 30 percent of solid volume of fine silica particles (10 nm) which sinter at a lower temperature and the effect of small particle has shown up from the beginning. As a consequence, bimodal silica binder has more heat treatment shrinkage than Binder B and Nyacol 9950.

6.6 CHAPTER SUMMARY

A new optical measurement technique was developed to provide accurate and repeatable shrinkage information for Three-Dimensional Printing of ceramics. The technique has revealed that drying shrinkage is originated and controlled by three important process materials:

1) BINDER
2) POWDER
3) CITRIC ACID

Binder and citric acid content involve in the gelation mechanism which defines the amount of liquid being enclosed inside the network at the point of gel. The liquid volume defines maximum possible deformation known as shrinkage strain potential. There will be less shrinkage with low liquid content at the gel point. Not only does the strain potential define the amount of drying shrinkage, but also with the ability of gel network to withstand the compressive stress induced by the liquid capillarity. The network strength and stiffness are governed by 'dissolution and redeposition' processes. To achieve high network strength, silica has to dissolve into the solvent and redeposit back to interfacial areas where particles join. Network of silica gel can be strengthen when aged at high pH ($\approx$10).

In Three-Dimensional Printing, gelation is initiated inside the powder bed. Therefore, powder serves as bridging points for tiny pieces of gel to hang on. As the binder shrinks, powder is placed under compressive stress. It is the powder characteristic under compressive stress that partly governs the shrinkage limit of the composite (powder+binder).

The amount of shrinkage of the composite depends on three factors:

1) Shrinkage strain potential
2) Properties and Strength of the gel under tensile stress
3) Character of the powder under compressive stress

A one-dimension shrinkage model was derived assuming gel and powder shrinkage and deformation characters are elastic. It was found that the amount of the composite in the model, δ_p, is governed by the level of boundary stress, σ, and other properties of both gel and powder as described by Equation 6.10 and 6.11

Along with the theoretical work, this chapter presents experimental result of powder/binder shrinkage interaction in Figure 6.32 for Binder B gelled with acid and drying as well as Nyacol 9950 gelled by drying. Although there are some discrepancies between the model and the real phenomena due to the assumption, the model captures the underlying concept of powder/binder shrinkage interaction.

Lastly, heat treatment shrinkage were measured with a dilatometer on Binder B, Nyacol 9950 at 50 weight percent, and a bimodal silica binder. After firing to 900°C, it was found that Nyacol 9950 has the least shrinkage strain of less than 3 percent. Binder B gelled with acid and drying have comparable shrinkage strain of 3.3 percent. Organic burnout is accounted for extra shrinkage strain in Binder B as compared to Nyacol 9950. The bimodal silica binder has the most shrinkage strain of about 3.5 percent because of the presence of small silica particles.

BIBLIOGRAPHY

[1] Bredt J., *Binder Stability and Powder\Binder Interaction in Three Dimensional Printing*, MIT PhD Thesis, Dept. of Mechanical Engineering, Supervised by E. M. Sachs, 1995.

[2] Brinker, C., Scherer, G., *Sol-Gel Science: The Physics and Chemistry of Sol-Gel Processing*, Academic Press, 1990.

[3] Brinker, C., Scherer, G., *J. Non-Cryst. Solids*, 70 (1985), 301-322

[4] Iler, R., *The Chemistry of Silica*, Wiley, New York, pp. 222-230 and 519-523, 1979

[5] Struckman, *Ann. Chem.*, 94, pp.341, 1855

[6] Baumann, *Beitr. Silokose-Forsch.*, 37, pp. 47, 1955

[7] Kawaguchi, T., et al., *J. Non-Cryst. Solids*, 87, pp.199, 1986

[8] Kawaguchi, T., Hishikura, H., Iura, J., Shrinkage Behaviour of Silica Gels During Drying, J. *Non-Cryst. Solids*, 100, pp. 220-225, 1988

[9] Brinker, C., Scherer, G., *Sol -> Gel -> Glass: I Gelation and Gel Structure*, J. Non-Cryst. Solids, 70, pp. 301-322, 1985

[10] Behrman, A., U.S. Pat. 2,400,907, 1946

[11] Kearby , K., U.S. Pat. 3.438,379 (Shell Development Co.), 1947

[12] Prassas, M., Phalippou, J., Zarzycki., J., *J. Mater. Sci.* 19 (1984) 1656

[13] Van Lierop, J., Huizing A., Meerman, W., and Mulder, C., *J. Non-Cryst. Solids* 82 (1986) 265

[14] Cravalho, E., Smith, J., *Engineering Thermodynamics*, MIT, 1981

[15] Kistler, S., J. Phys. Chem., 36 (1932) 52-64

[16] Schuber, H., *Chem Ing. Techn.*, 51, pp. 277-282, 1979

Chapter 7.

Powder Deformation Response to Shrinkage Stress

7.0 INTRODUCTION

Binder penetrates the powder bed from the printhead at a speed of approximately 10 meters per second. The droplets flatten out at the impact point. But due to the soft nature of the powder bed, they do not immediately stop or bounce off at the impact point but gradually slow down while indenting the powder. During the course of deceleration, binder coalesces the powder particles along its trajectory with its surface tension. The coalescence slows down as the mass increases and as kinetic energy dissipates into the powder bed. Finally, they all come to rest after a few milliseconds and a few thousandth of an inch below the impact surface.

But, this is not the end of the mechanism, due to the surface tension of liquid under contact with small pores, binder is pulled to fill the voids immediately, and the phenomena ceases as soon as the matric suction equilibrates throughout the liquid body. At this point, the liquid already bridges out to several particles, knitting them into a network. A few seconds later, gelation starts and solid network appears in the binder. Water is captured and enclosed in the interconnected pores of the network.

The binder takes a few more hours to dry the liquid off. As the liquid-vapor interface reaches the pore entrances and about to move into the pore, the interface is curved by the physics of wetting. This places the liquid under tension. As a result, the binder network is under compression. Unless the network develops sufficient strength to withstand the compressive stress, it is forced to consolidate and squeeze out interior liquid to the exterior. However, binder can not deform freely because of its attachment to the powder. Binder deformation tugs along the particles and increases both the contact stress and the coordination number causing the powder to undergo compression. It is the balance between binder shrinkage force and powder resistance force that defines the degree of deformation in Three-Dimensional Printing parts.

7.1 POWDER UNDER STRESS

7.1.1 Mohr's Stress Diagram

It is very important for Three-Dimensional Printing to understand the yield characteristics of powder under external stresses as well as how interparticle friction and cohesive forces increase the immobility of the powder. Related theories for stability of powders and bulk solids went back to the work of Coulomb [1], Rankine [2], as well as several others. It has since developed into the theory of soil mechanics. The theory was used to design vessels storing powders and bulk solids, Ketchum [3] and Reimbert and Reimbert [4]. In recent years, more numerical methods have been used to obtain explicit solutions, Johanson and Jenike [5] and Garder [6-9].

If compressive stress is taken as positive, the coordinates of equivalent tangential and normal stresses for a small element at any point and any orientation in the powder bed can be fully described by Mohr's stress diagram. For an element with compressive stresses in horizontal and vertical directions, σ_1 and σ_2, equivalent stress for the element at orientation θ is described by Mohr's stress diagram (circle) in Figure 7.1

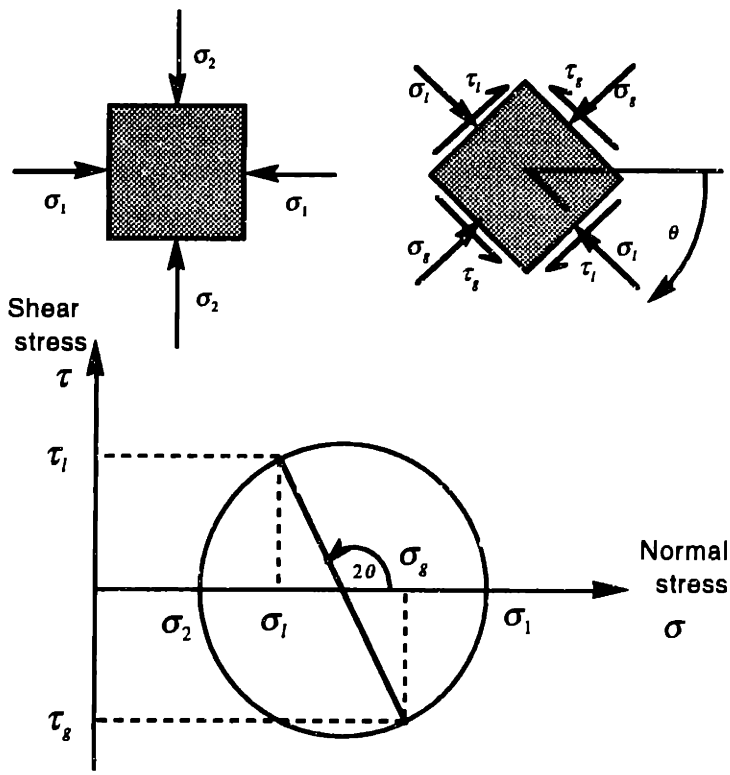

Figure 7.1 Mohr's Stress Diagram

There are a couple points to be noted. First, the orientation θ on the element becomes 2θ on the circle but in the opposite direction. Second, shear stress τ_l and τ_g are always equal in magnitude but in the opposite directions.

The coordinates of normal and shear stress of the element at any orientation can be mathematically described as:

Normal stress $$\sigma_l = \frac{1}{2}(\sigma_1 + \sigma_2) + \frac{1}{2}(\sigma_1 - \sigma_2)\cos 2\theta \tag{7.1}$$

Shear stress $$\tau_l = \frac{1}{2}(\sigma_1 - \sigma_2)\sin 2\theta \tag{7.2}$$

where the radius of Mohr's circle is $\frac{1}{2}(\sigma_1 - \sigma_2)$ with the center at $\frac{1}{2}(\sigma_1 + \sigma_2)$

7.1.2 Coulomb Failure Criteria

Coulomb [1] developed a theory which identified a condition where powder loses its static stability and starts to yield or flow under shear stress. The failure takes place when shear stress is equal to shear strength of the powder. Coulomb expressed shear strength, τ_f, of powder on a plane of failure as a linear function of normal stress, σ_f, on the plane at the same point. :

$$\tau_f = (\sigma_s + \sigma_f)\tan\phi$$

$\tan\phi$ is the slope of yield locus where ϕ is called angle of internal friction. σ_s can be viewed as apparent tensile stress. Graphically, σ_s is the intercept of the yield locus to the normal stress axis, Figure 7.2.

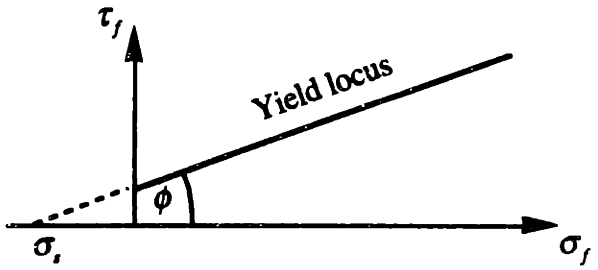

Figure 7.2 Yield Locus as Described by Coulomb

Physical interpretation of Coulomb's yield locus is shown in Figure 7.3. The locus defines the boundary for the stress state at any point in the powder which can be represented by a Mohr's stress diagram. If the Mohr's diagram is contained within the Coulomb yield locus (like circle A, for example), then the external stress acting upon the powder at this point is distributed to the neighbor particles and equalized. In this case, the powder remains under static equilibrium with no mobilization. On the other hand, if the stress state at any point in the powder has its associate Mohr's diagram tangent with the yield locus such as circle B, then the powder is in a state of incipient failure. In this case, the interparticle frictional forces are fully mobilized and the powder is in a state of plastic equilibrium. If sliding starts at this point, the powder will continue to yield indefinitely until the stress state changes and, once again, be contained within the envelope of the locus as circle A.

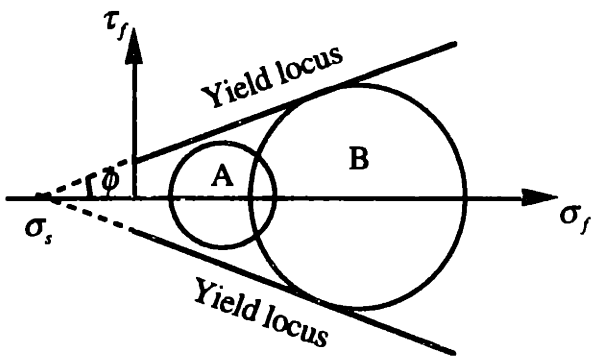

Figure 7.3 Physical Interpretation of Yield Locus

There cannot be anywhere in the powder that Mohr stress diagram intersects or exceeds the yield locus because plastic sliding will set forth before such a condition could develop.

In addition to shear stress, the yield loci are bounded by normal stress as well. The reason is that powder could be deformed with isostatic compressive or tensile stress. It is found that the compressive limit on the right of yield loci is a sector of the Mohr circle that contains the last point of compressive termination on the yield locus (point F). Similarly, tensile limit is a sector of the Mohr diagram that contains the tensile termination point on the yield locus (point G), Figure 7.4

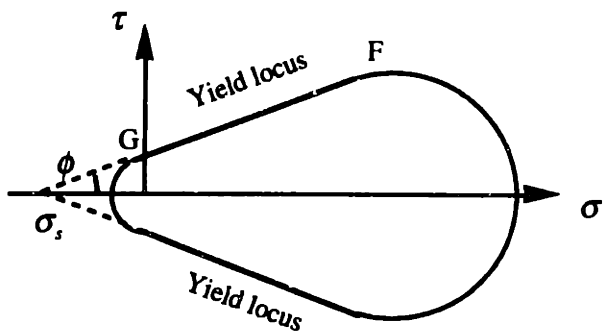

Figure 7.4 Yield Locus with Tensile and Compressive Limits

Mohr-Coulomb yield criterion is widely used in practice because of its simplicity although it is not the only means to quantify failure criterion for powder. The yield locus exhibits slight curvature when the powder is cohesive, Figure 7.5. But, in general, a straight line approximation is quite appropriate for most applications.

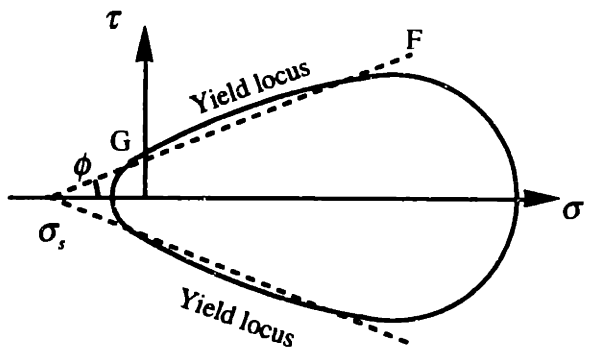

Figure 7.5 Slightly Curved Yield Locus Due to Powder Cohesion

7.1.3 Yield Loci and Pore Fraction

The yield loci in previous sections are plotted at a particular pore fraction. In fact, the magnitude of yield loci depends on the pore fraction of the powder bed. The higher the packing (low pore fraction), the larger the yield loci. In other words, the stability of the powder increases with the packing fraction. Figure 7.6 illustrates yield loci in 3-dimensional with normal stress, shear stress, and pore fraction axes. Details of how the yield loci progress as a function of pore fraction were investigated by Hvorslev [10] and Roscoe [11] which will be discussed in the next section. Note that the loci are shown with only the upper envelope and the normal stress axis is positive to the upper left corner for simplicity of presenting a complex surface.

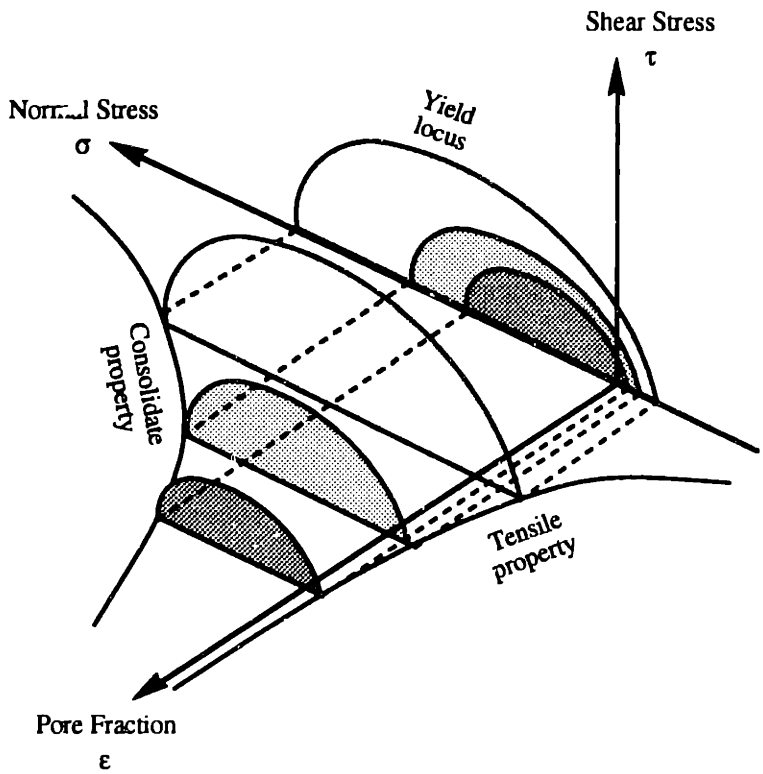

Figure 7.6 Yield Loci as Function of Stress State and Pore Fraction

7.2 POWDER RESPONSE TO SHEAR STRESS

7.2.1 Hvorslev's Surface

Hvorslev [10] in 1937 worked to identify stability failure of powder as a function of normal stress, shear stress, and pore fraction. His work is illustrated in a three-dimensional diagram in Figure 7.7. Hvorslev controlled the powder at a constant compressive stress, σ_D, at point D with pore fraction ε_D and started to apply shear stress. As the shear stress increased, the stress state climbed vertically along line DE. When the shear stress reached τ_E at point E, the powder failed and dilated plastically along curved EF where pore fraction increased from ε_D to ε_F. During the dilation, maximum shear strength dropped exponentially from τ_E to τ_F. Hvorslev tested for the failure shear strength by varying the compressive stress and pore fraction and concluded that the peak shear strength varied linearly with the compressive stress, but exponentially with the pore fraction as:

$$\tau_f = K_1\sigma_f + K_2 e^{(-K_3\epsilon)} \tag{7.3}$$

where K_1, K_2, and K_3 are constants for powder.

Hvorslev neglected the powder response to tensile stress so his finding only applies for compression cases. Figure 7.7 illustrates slightly curved yield loci due to powder cohesion.

7.2.2 Roscoe's Surface and Critical State Line

Roscoe et. al. [11] studied the stability of isostatically prepared powder to shear stress. Isostatic press means that powder is compressed with equal amount of compressive pressure in any direction with no shear present. The isostatic response is shown as a curvature containing point A on $\tau = 0$ plane with pore fraction ε_A in Figure 7.7.

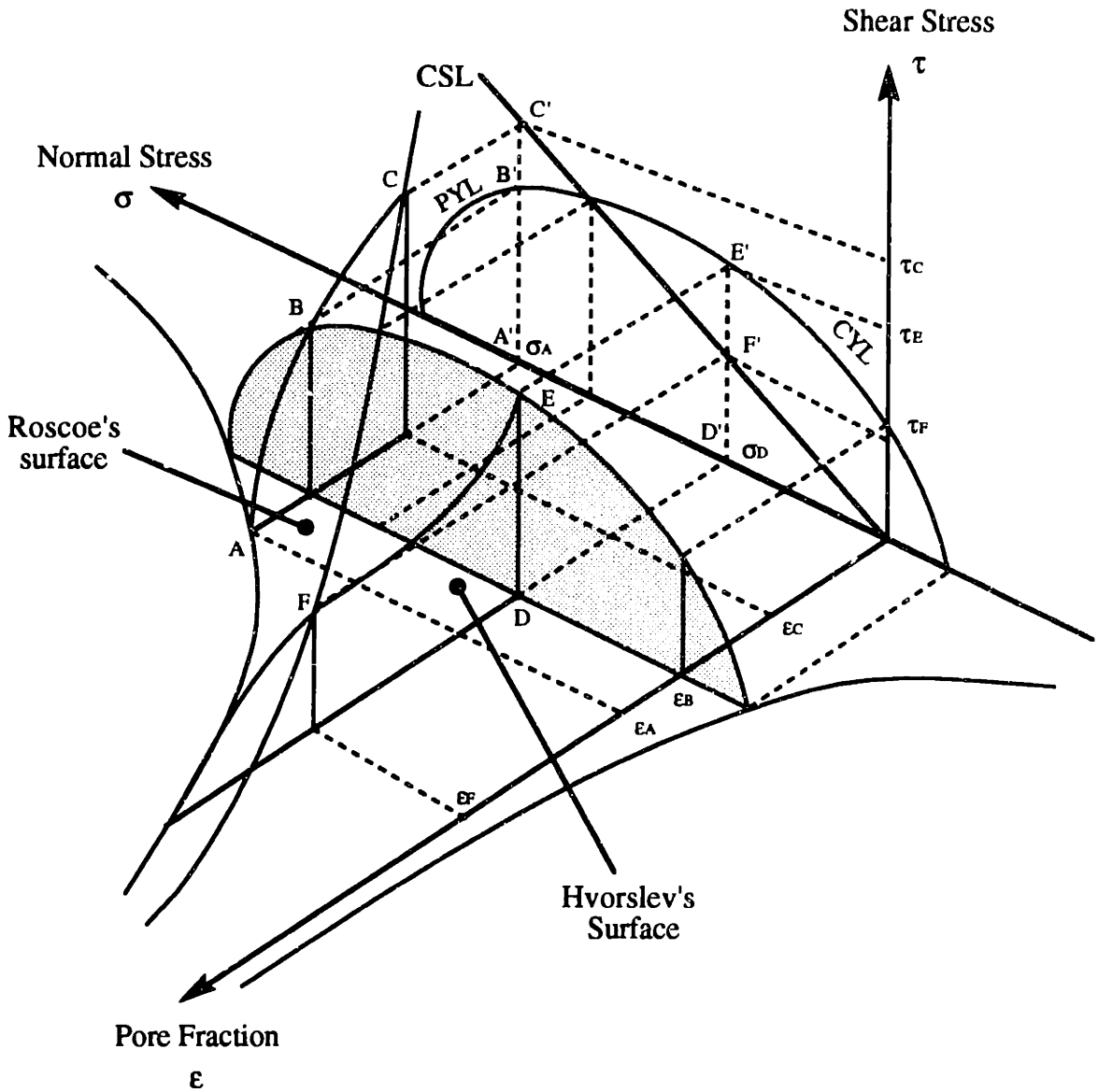

Figure 7.7 Roscoe and Hvorslev's Surfaces and How Powder Consolidate/Dilate Under Compressive and Shear Stress

Then shear stress was applied to the sample in such a way that compressive stress remained undisturbed. Therefore, the powder response must be on $\sigma = \sigma_A$ plane. As the shear stress increased, the powder started to yield and consolidate (having lower pore fraction) and left point A along curve ABC. The consolidation continued until the stress state reached point C and stopped there with shear stress expressed as τ_C and pore fraction ε_c.

Point C and F lie along an interesting line called Critical State Line (CSL). It is where both dilation and consolidation responses of the powder direct to and reach equilibrium. Therefore, CSL serves as the division boundary between the two regimes. The projection of CSL onto $\sigma - \tau$ surface appears to be a straight line passing through the origin. Part of the yield locus in the region that powder dilates to shear stress is called Powder Yield Locus (PYL) and the surface in this regime is called Hvorslev's surface. On the other hand, the yield locus where powder consolidates under shear stress is called Consolidate Yield Locus (CYL). CYL's of various pore fraction form a surface known as Roscoe's surface.

7.3 POWDER RESPONSE TO ISOSTATIC STRESS

7.3.1 Shrinkage and Isostatic Stresses

Upon knowing the yield criterion for powder due to external stresses in previous sections, the goal of this section is focused on the topic of shrinkage caused by binder deformation.

The volume of binder per the volume of voids in the powder bed, or saturation, is one of the important process parameters in Three-Dimensional Printing. Saturation can be varied by either adjusting binder flow rate through the nozzle, raster speed of the fast axis, or line and layer spacing. Insufficient saturation results in low part strength, disintegration, and delamination. Therefore, Three-Dimensional Printing usually keeps the printing saturation level at about 80 percent. Binder resides at the area where powder particles join forming network of liquid-bridge particles. The liquid is not continuous throughout the network, but rather as clusters with air pores in between. Since the liquid bridges are not directly connected, liquid pressure in a cluster does not need to equilibrate with its neighbors.

Capillary stress in drying causes binder to deform. In this case, the binder pulls the along the particles where it anchors to. The particle movement increases the coordination number as well as the interparticle contact force. As a consequence, the powder is under

compressive stress. However, there is no shear stress developed, so the particles are under omni-directional compression, or isostatic stress.

Powder under compression resists further binder deformation. The point where the resistance force from the powder equilibrates with the shrinkage force from the binder defines the shrinkage of the composite. This concept is the main focus of powder-binder shrinkage interaction which will be elaborated in the next Chapter.

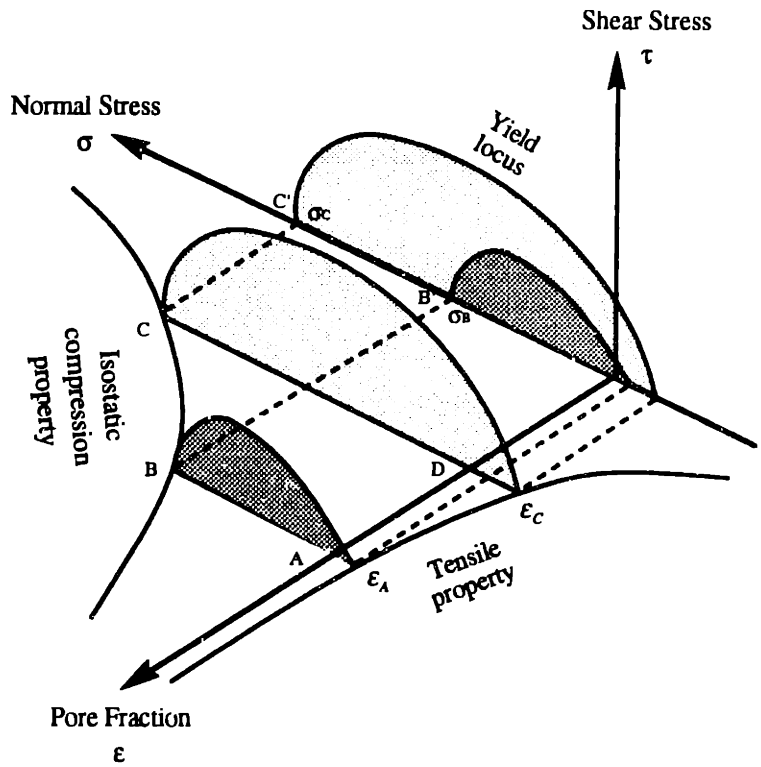

Figure 7.8 Isostatic Compression Property

Figure 7.8 illustrates the process of isostatic compression of the powder bed. At all times, there is no shear stress so the isostatic consolidation takes place only in the $\sigma - \varepsilon$ plane. First, the powder bed is at point A with pore fraction ε_A and with no stress applied. Stress state of the powder starts to move along line AB when isostatic pressure is applied. When the isostatic stress reaches point B, σ_B, the powder begins to consolidate along line BC. The result of powder consolidation increases the coordination number and the packing density thus extend the powder resistance to the stress. More and more isostatic pressure is

required to consolidate the powder further on. When the stress state reaches point C and is unloaded, the powder is packed to ε_c and travels along line CD to point D.

Binder applies compressive stress on the powder internally. In other words, the driving force of shrinkage is contained in the printed parts. To study the phenomena, an external isostatic stress may be applied to dry particles to imitate the shrinkage stress of the binder under these assumption:

1) Binder only exerts isostatic compressive stress on the powder.
2) The presence of binder doesn't change the mobility of the particles. Therefore, dry or binder filled powders behave similarly to isostatic compressive stress.

Although these assumption may not provide perfect similarities between the two loading stresses, they should sufficiently give a close approximation of how particles respond to shrinkage stress. Figure 7.9(a) shows binder shrinkage stress and Figure 7.9(b) illustrates proposed plan to study the phenomena with external isostatic stress on dry powder

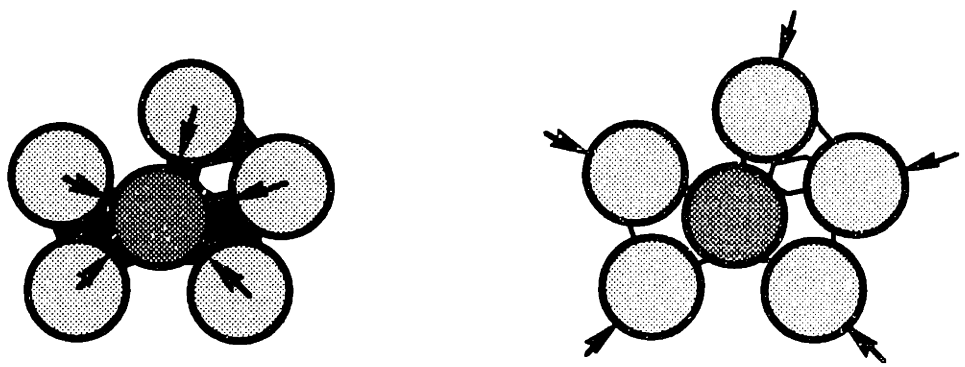

(a) (b)

Figure 7.9 Equivalent of Shrinkage Stress and External Isostatic Stress

A simple way to apply isostatic stress to powder is to use liquid as a medium. Static fluid is known to be free of shear stress and thus provides a perfect environment for isostatic compression. Liquids are superior to gases for their incompressibility. This way, the change of powder volume due to isostatic stress is detectable by measuring the change of combined volume of the powder and the liquid. However, the powder must be prevented from being wetted by the liquid. This allows the isostatic stress to be externally applied to the powder as a lump - not by individual grain.

7.3.2 Experiment Protocol

A instrument available to test for powder deformation to isostatic test is the porosimeter. However, the sample preparation for this test has to be different from standard practice. The porosimeter used in this experiment is made by Porometric model 9220. Powder was prepared in a pouch made from plastic sticker to prevent mercury to wet to the powder under compression. Approximately 0.5 cc of powder was poured on top of the sticker film and wrapped around. Air was bled out from the pouch before it was sealed and cut. The thickness of the film was about 0.003 inches and therefore its mass and volume were negligible. The method of powder preparation is shown with completed sketch of a pouch in Figure 7.10

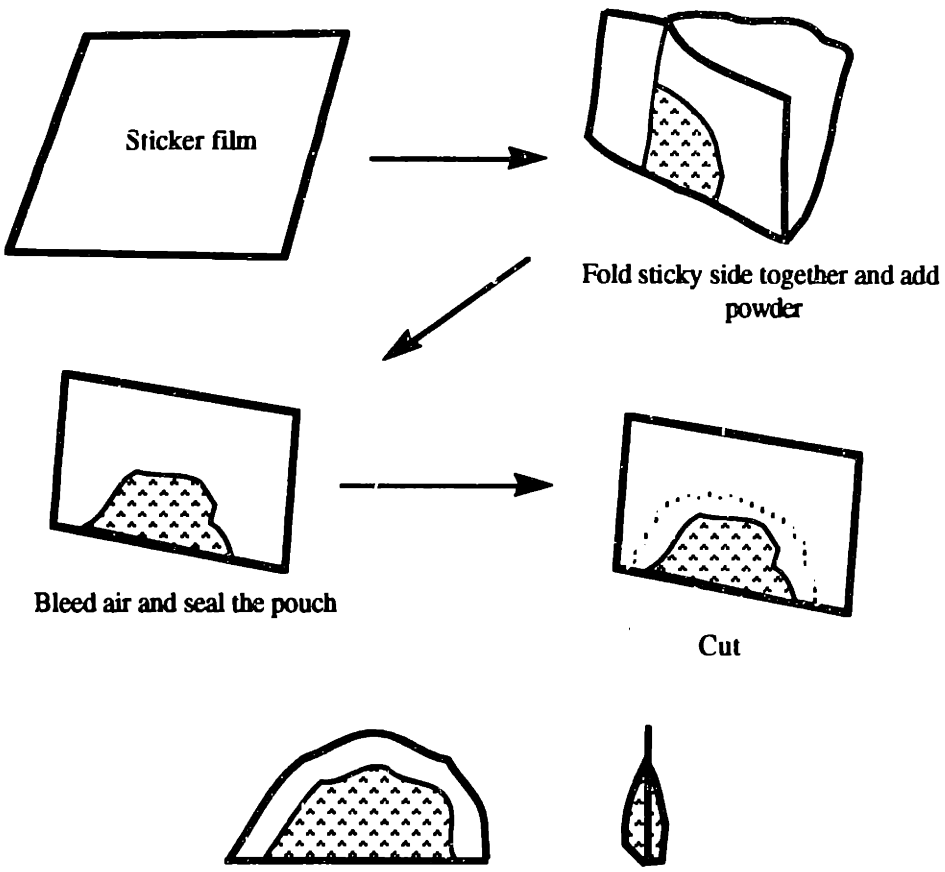

Figure 7.10 Powder Preparation into a Pouch

7.3.3 EXPERIMENT RESULT

NORTON 7920

Each sample was weighed and then put into a penetrometer with known weight and volume (about 3.2 ml) and sealed. Air was taken out from the penetrometer and mercury was allowed to fill into the chamber. Knowing the weight of the penetrometer at this point, one should be able to figure out the volume of the sample. Then the setup is compressed, in steps with equilibrate time of 5 seconds, to a pressure of 28 psi and once again to 60,000 psi. The volume change of the sample due to isostatic test was recorded with associated pressure.

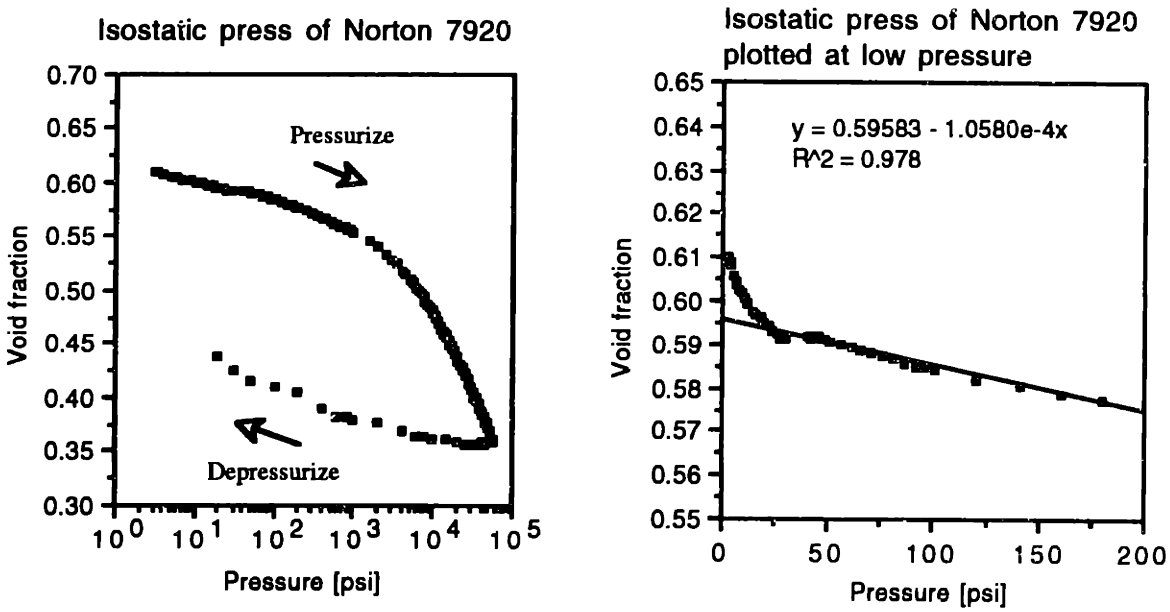

(a) (b)

Figure 7.11 Isostatic Compression of Norton 7920 (a) Reduction of Void Fraction at Full Pressure Cycle (b) Reduction of Void Fraction at Low Pressure

According to Figure 7.11 (a), the powder response to isostatic compression during pressurization represents the isostatic compression property in Figure 7.8. The Pore (or void) fraction reduces as a function of isostatic pressure. The figure clearly indicates that the powder strain to isostatic stress has plastic response for it does not spring back to original volume during depressurization. Figure 7.11 (b) shows the powder response to

stress at low isostatic pressure. The initial reaction of the powder is not linear but rather a rapid drop in the void (or pore) fraction. This also corresponds to a large degree of powder strain. Finally, when the pressure is about 25 psi, the consolidation slows down and varies linearly with pressure up to about 3,000 psi.

Powder linear strain can be calculated from reduction of pore fraction of the sample as:

$$\varepsilon_{powder} = 1 - \left[\frac{1-\varepsilon_i}{1-\varepsilon}\right]^{1/3} \tag{7.4}$$

where ε_{powder} is the linear powder strain

ε_i is the initial pore fraction of the powder prior to isostatic compression

ε is current pore fraction of the powder

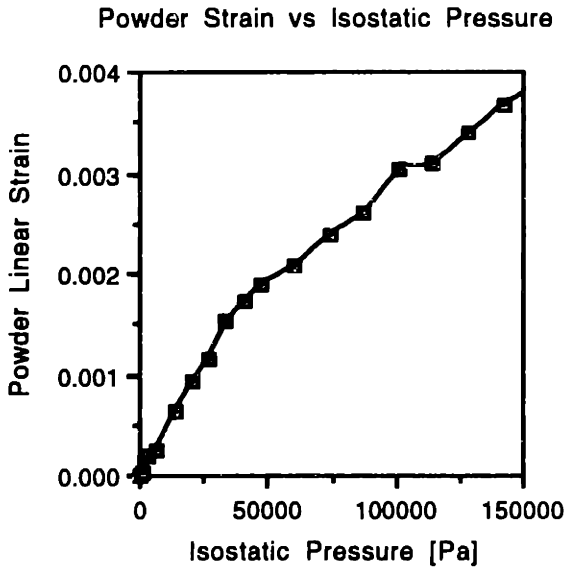

Figure 7.12 Powder Strain as a Function of Isostatic Pressure

Figure 7.12 illustrates an interesting plot of powder strain as a function of isostatic pressure. Shrinkage in Three-Dimensional Printing of ceramics is in the order of 0.2 to 0.35 percent which corresponds to isostatic pressure of around 50,000 to 100,000 Pascal.

It is found that the amount of powder strain is a strong function of initial packing fraction and isostatic pressure as shown in Figure 7.13. It is obvious that powder with

lower initial packing fraction deforms at a higher strain rate than that of higher packing fraction for the same pressure increment.

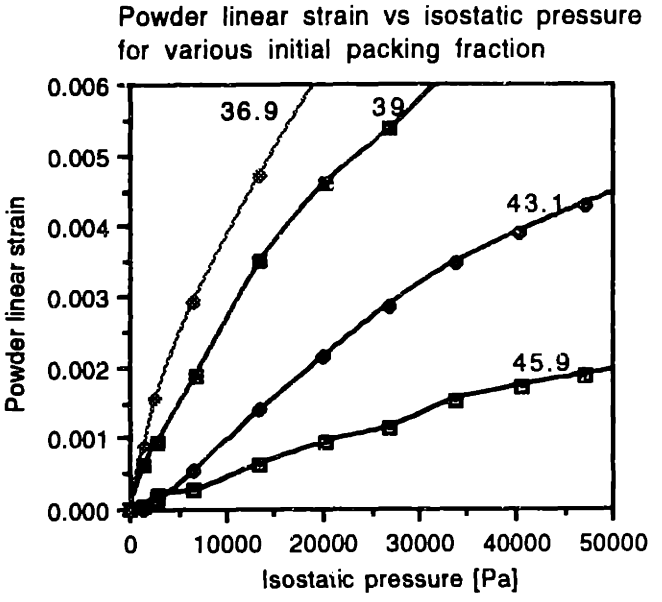

Figure 7.13 Powder Strain of Norton 7920 is a Function of Initial Packing Fraction and Isostatic Pressure (Numbers Indicate Initial Packing Fraction in Percent)

CB-A30S SPHERICAL ALUMINA

Similar to Norton 7920, the strain response of spherical alumina CB-A30S to isostatic stress can be shown in Figure 7.14. Initial strain increases rapidly with the stress up to about 20,000 Pa. Beyond that pressure, the strain varies linearly with isostatic stress to about 0.4 GPa. Figure 7.14 (b) clearly indicates the strain at low isostatic pressure (<1MPa) showing two distinct regimes of linearity and non-linearity.

When the powder strain is plotted as a function of initial packing fraction, the result is very similarly to that of Norton 7920 powder. CB-A30S has higher apparent packing density than Norton 7920 due to less interparticle friction. According to Figure 7.15, the spherical powder with packing fraction of to 46 percent has a comparable strain response as Norton 7920 at packing fraction of 37 percent. When the packing fraction increases, the powder gains more resistance and therefore has less strain for the same isostatic stress.

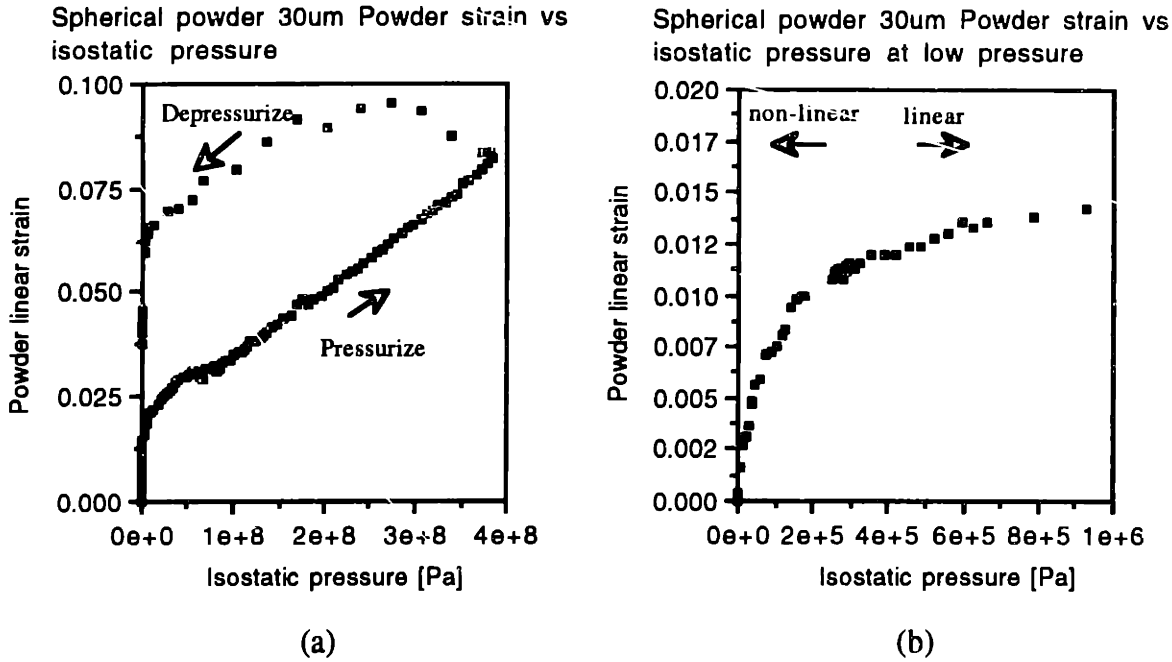

Figure 7.14 Powder Strain as a Function of Isostatic Pressure (a) Full Pressure Cycle (b) Low Pressure

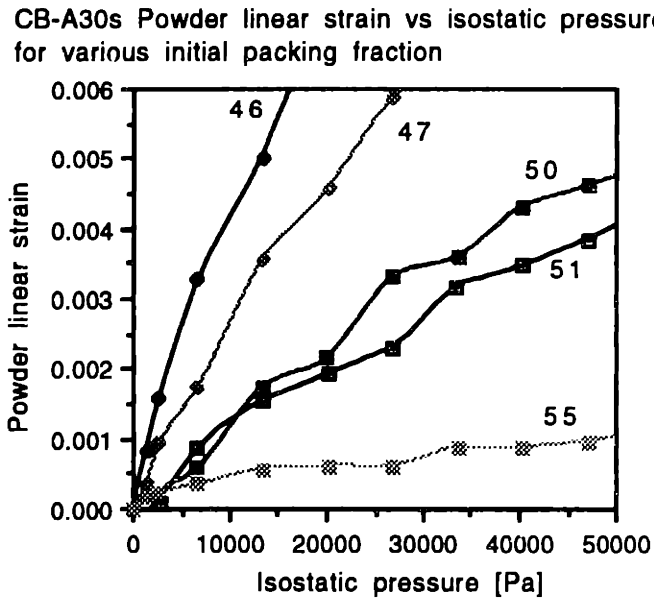

Figure 7.15 Powder Strain as a Function of Initial Packing Fraction and Isostatic Pressure (Numbers Indicate Initial Packing Fraction in Percent)

7.4 DISCUSSION

There are two major mechanisms involved in isostatic deformation of powder: rearrangement - restacking, and elastic-plastic deformation. Particle rearrangement and restacking takes place at very low pressure when particles slide relative to one another and reorder into a tighter packing formation. The deformation behavior of the powder at this level is strongly dependent on powder morphology, in other words, interparticle friction and correspondent packing density, particle size and shape, surface area, and surface coatings [12,13,14]. After the particles are brought together at a close proximity, elastic-plastic deformation occurs at interparticle contact areas where the inherent material properties become the dominant factors controlling densification. Figure 7.16 illustrates powder deformation under both mechanisms.

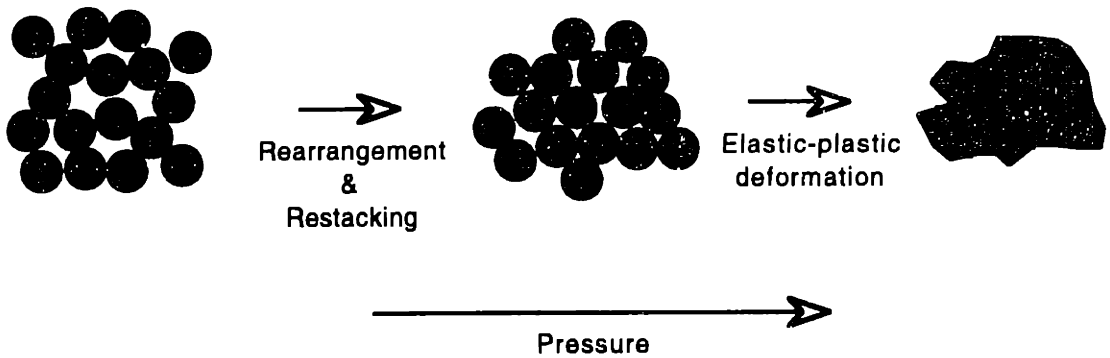

Figure 7.16 Mechanisms of Powder Deformation Under Isostatic Pressure Starts with Particle Rearrangement and Restacking. Elastic-plastic Deformation of the Particles Takes Place at Higher Isostatic Pressure After the Particle Assembly Reaches Tight Formation.

Shapiro and Kolthoff [15], Konopicky [16], and Heckel [17] arrived at the same differential equation to characterize powder deformation at elastic-plastic regime. The rate of change of densification per isostatic pressure(P_{iso}) is a function of associated pore fraction or

$$\frac{d\phi}{dP_{iso}} = k\varepsilon$$

but $\varepsilon = 1 - \phi$, so

$$\frac{d\phi}{dP_{iso}} = k(1-\phi) \tag{7.5}$$

where ϕ is packing fraction of the powder assembly

ε is pore fraction of the powder assembly, $\varepsilon = 1-\phi$

k is a constant

Rearrange Equation 7.5 gives

$$\frac{1}{1-\phi}d\phi = kdP_{iso}$$

and integrate

$$\int_{\phi_i}^{\phi} \frac{1}{1-\phi}d\phi = k\int_{0}^{P_{iso}} dP_{iso}$$

where ϕ_i is the initial packing fraction

$$-\ln(1-\phi)+\ln(1-\phi_i) = kP_{iso}$$

$$\ln\left(\frac{1}{1-\phi}\right) = kP_{iso} + \ln\left(\frac{1}{1-\phi_i}\right) \tag{7.6}$$

Plot of Equation 7.6 is shown in Figure 7.17

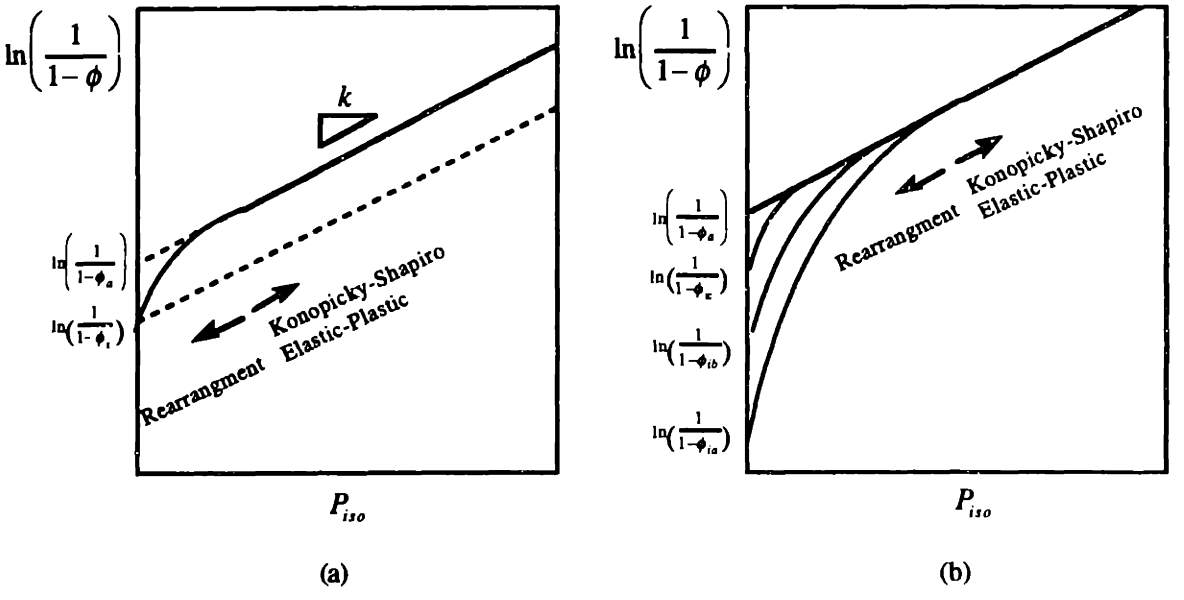

Figure 7.17 Powder Deformation of Konopicky-Shapiro (a) Wide Pressure Range (b) Low Pressure

The Konopicky-Shapiro relationship is applicable over a wide range of pressure (linear portion), but does not extend to very low pressure where deformation is governed by particle restacking and rearrangement (non-linear portion). In practice, extrapolation of the Konopicky-Shapiro relation gives a displaced intercept value of $\ln(\frac{1}{1-\phi_a})$ instead of $\ln(\frac{1}{1-\phi_i})$, Figure 7.17. Packing fraction ϕ_a is found to be even greater than tapping densities [18] and strongly depends on particle geometry and morphology. At very low isostatic pressure where powder deformation is governed by particle rearrangement and restacking, the relationship between $\ln(\frac{1}{1-\phi})$ and P are represented by curvatures associated with their initial packing fraction as shown in Figure 7.17 (b) where $\phi_{ic} > \phi_{ib} > \phi_{ia}$. These curvatures end up in a straight line which marks the beginning of Konopicky-Shapiro's elastic-plastic deformation. Figure 7.18 illustrates the measured deformation of Norton 7920 powder with initial packing fraction of 0.38.

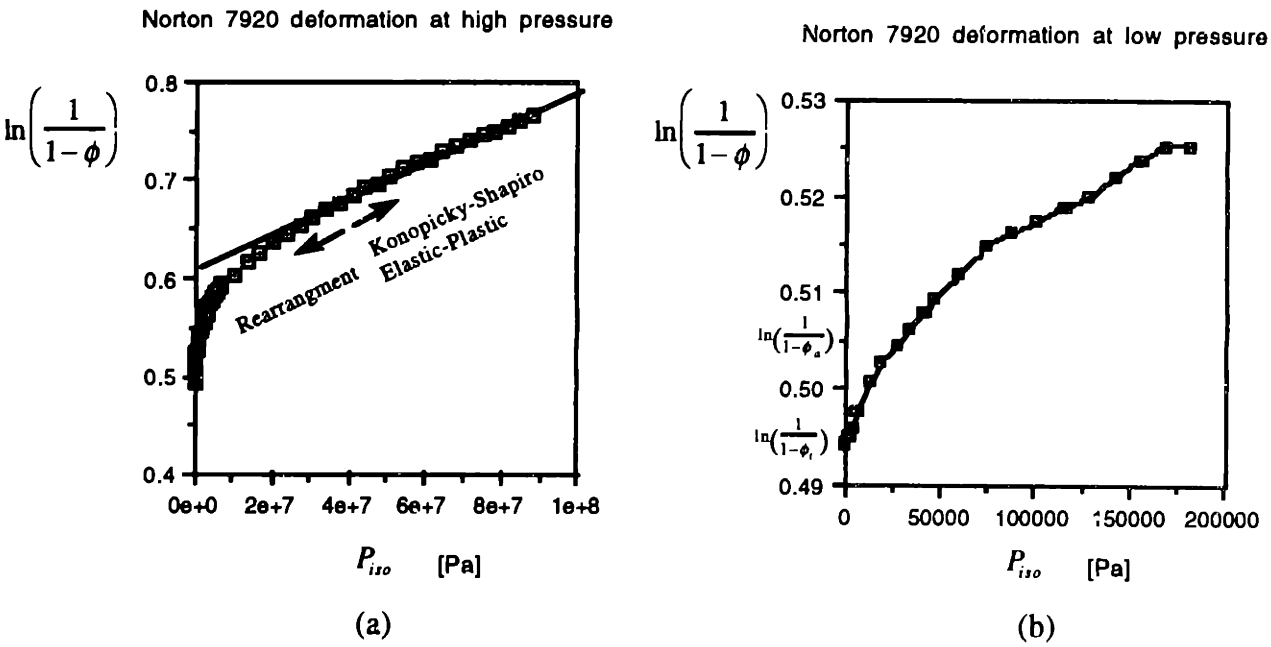

Figure 7.18 Deformation of Norton 7920 at (a) High Pressure (b) Low Pressure Plotted with Konopicky-Shapiro Theory Clearly Shows Two Distinct Deformation Regimes

Powder deformation during drying and heat treatment in Three-Dimensional Printing occurs at very low pressure (less than 6 psi or 40688 Pa). Therefore, shrinkage of Three-Dimensional Printing of ceramics is strictly governed by particle rearrangement and

restacking where morphology, initial packing density, and isostatic pressure have very important roles. Unfortunately, powder deformation due to rearrangement and restacking is not well documented due to the complex nature of morphological quantification of particles.

7.4.1 Norton 7920.

The powder strain of Norton 7920 in Figure 7.13 can be approximated with linear regression shown in Figure 7.19. Although there are some non-linearity, the linear approximation could sufficiently capture most essential information.

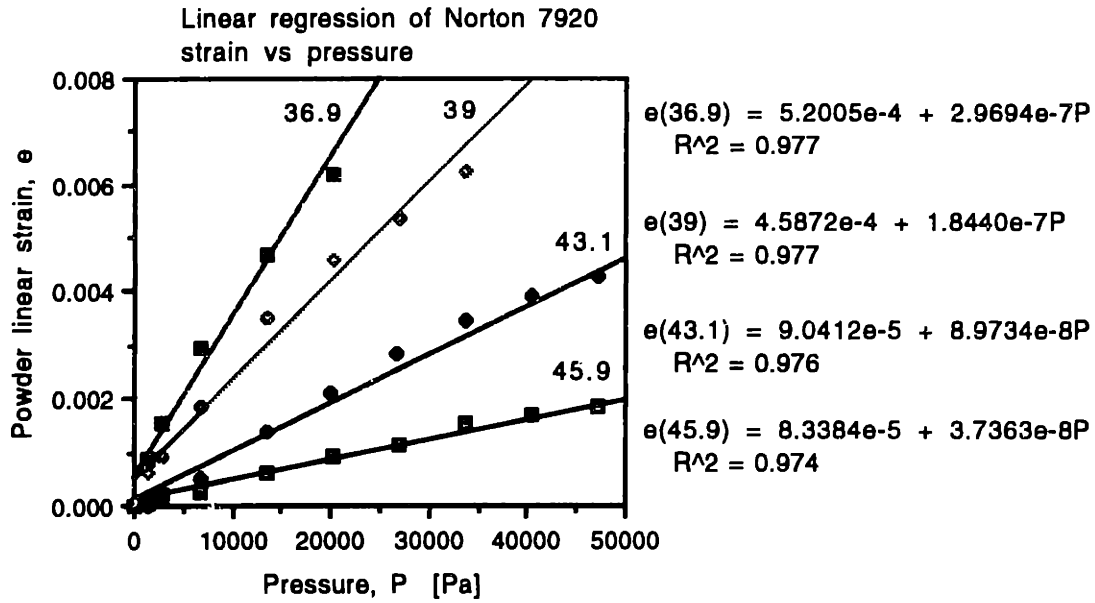

Figure 7.19 Linear Regression of Norton 7920 Strain vs Isostatic Pressure
(the numbers are initial packing fraction in percent)

The slope of each line in Figure 7.19 is clearly a function of initial packing fraction, ϕ_i. Thus, the objective of this section is to create a mathematics model that describes powder deformation strain as a function of initial packing fraction.

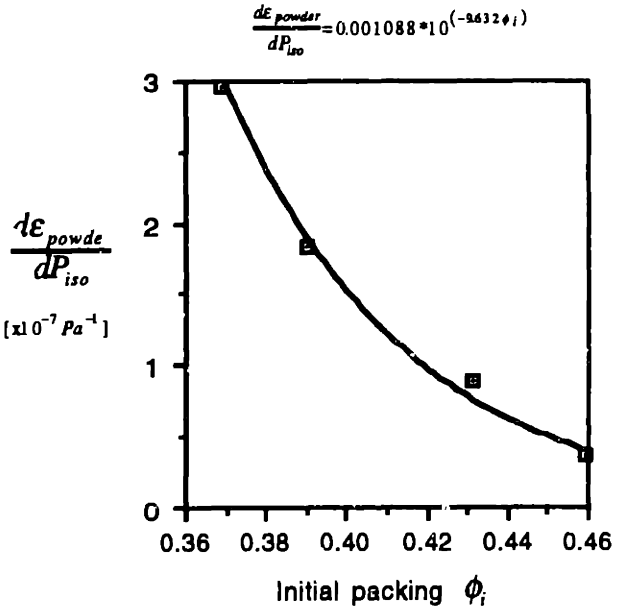

Figure 7.20 Slope of Powder Strain and Isostatic Pressure as a Function of Initial Packing Fraction

The slopes in Figure 7.19, $\frac{d\varepsilon_{powder}}{dP_{iso}}$, are plotted against initial packing fraction, ϕ_i, in Figure 7.20 with a resultant exponential fit of

$$\frac{d\varepsilon_{powder}}{dP_{iso}} = 0.0010884 * 10^{(-9.6321\phi_i)} \qquad [Pa^{-1}] \qquad (7.7)$$

integrate Equation 7.7 gives

$$\int_0^{\varepsilon_{powder}} d\varepsilon_{powder} = 0.0010884 * 10^{(-9.6321\phi_i)} \int_0^{P_{iso}} dP_{iso}$$

So, powder strain response to isostatic pressure for $0.36 < \phi_i < 0.46$ is

$$\varepsilon_{powder} = \left[0.0010884 * 10^{(-9.6321\phi_i)}\right] P_{iso} \qquad (7.8)$$

where P_{iso} is in Pascal

Therefore, Equation 7.8 can be used to describe the slope in Figure 7.19 for any initial packing density and isostatic pressure for Norton 7920 powder.

7.4.2 CB-A30S Spherical Powder

The relation of powder linear strain, ε_{powder}, and isostatic pressure, P_{iso}, per initial packing fraction of CB-A30S in Figure 7.15 can be approximated by linear regression as shown in Figure 7.21.

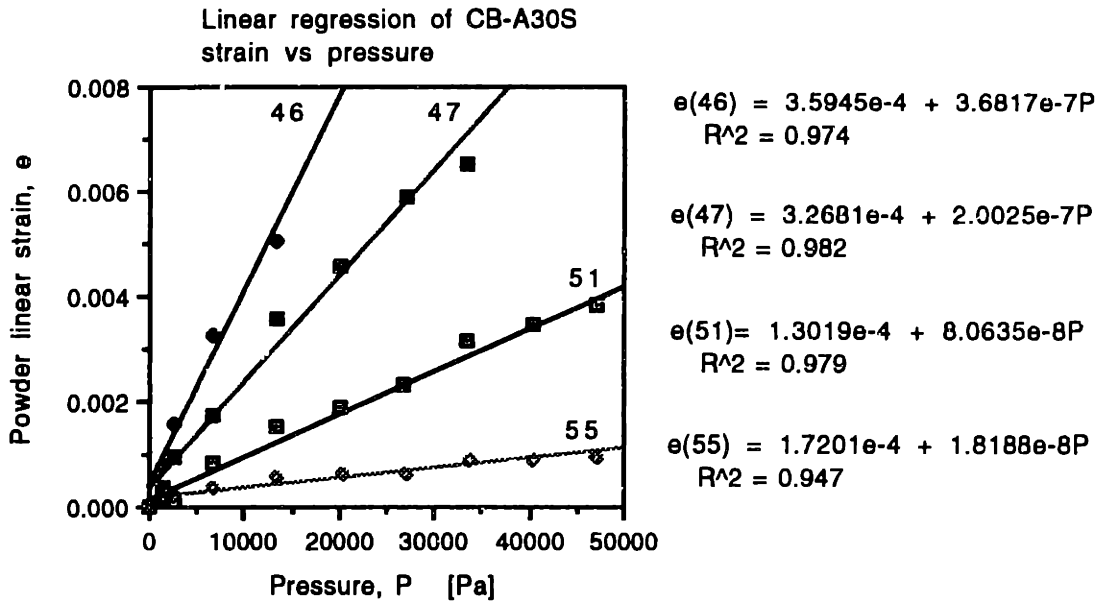

Figure 7.21 Linear Regression of CB-A30S Strain vs Isostatic Pressure
(the numbers are initial packing fraction in percent)

The slope of each linear regression approximation in Figure 7.21, $\frac{d\varepsilon_{powder}}{dP_{iso}}$, is plotted in Figure 7.22 against its initial packing density, ϕ_i. The slope decreases with initial packing fraction as expected.

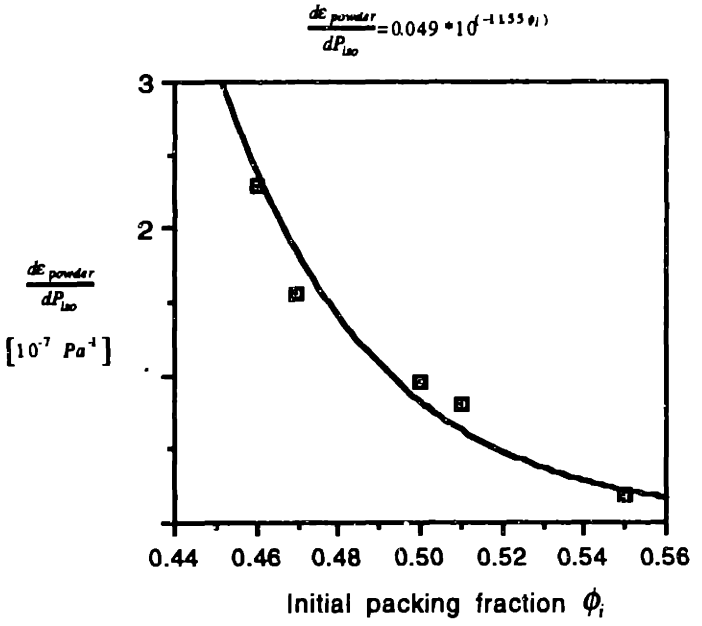

Figure 7.22 Slope of powder linear strain and isostatic pressure as a function of initial packing fraction for CB-A30S spherical alumina

From regression analysis, it was found that

$$\frac{d\varepsilon_{powder}}{dP_{iso}} = 0.0495 * 10^{(-11.558\phi_i)} \qquad [Pa^{-1}] \quad (7.9)$$

integrate Equation 7.9

$$\int_0^{\varepsilon_{powder}} d\varepsilon_{\text{powder}} = 0.00495 * 10^{(-11.558\phi_i)} \int_0^{P_{iso}} dP_{iso}$$

So, linear strain response of CB-A30S to isostatic stress, P_{iso}, is:

$$\varepsilon_{\text{powder}} = \left[0.0495 * 10^{(-11.558\phi_i)}\right] P_{iso} \qquad (7.10)$$

where $\varepsilon_{\text{powder}}$ is linear strain in the powder

ϕ_i is the initial packing fraction of the powder bed, $0.44 < \phi_i < 0.56$

P_{iso} is the isostatic pressure in Pascal

7.5 CHAPTER SUMMARY

This chapter was dedicated to powder response under stress. Similar to general solid mechanics, the stress state of powder can be represented with Mohr's stress diagram (circle). It was Coulomb who first described the theory of powder yield criteria using Mohr's circle as the fundamental basis for powder yield locus. Mohr's circle representing the stress state of the powder must be contained inside Coulomb's yield locus in order for the powder to remain in static equilibrium with no mobilization. On the other hand, if the Mohr's diagram is tangent to the yield locus, then the powder is in a state of incipient failure and the powder is in a state of plastic deformation. Once mobilization starts, the powder will continue until the stress state can once again be contained within Coulomb's yield locus. The size of the yield locus envelope depends on the pore fraction. Therefore the highly packed system has higher stability.

In Three-Dimensional Printing, binder goes into the powder bed and resides in areas where particles are in close contact. The capillary stress in drying causes binder to deform and to pull along attached particles. As a consequence of the relative movement, the number of contacts and the contact forces among the particles increase causing the particles to be under pure compression in omni-direction without shear stress, or isostatic compression. Powder under compression resists shrinkage stress from the binder. The point where shrinkage and resistance force equilibrate defines the shrinkage of the composite

A simple way to test powder with isostatic stress is to use a liquid, which is free of shear stress, as a compressive medium. Powder samples were wrapped and prepared in pouches made of a thin membrane. The samples were then compressed with mercury in a porosimeter where the volume change as a function of isostatic pressure was recorded. At the same time, powder linear strain was calculated from reduction of the pore fraction.

It was found that the amount of powder strain is a strong function of initial packing fraction and isostatic pressure. Powder with lower initial packing fraction deforms at a higher strain than that with higher packing fraction for the same isostatic pressure increment. At the low pressure regime, the strain increases nonlinearly with the pressure.

The deformation at this initial phase is governed by particle rearrangement and restacking and is strongly dependent on initial packing and powder morphology. After the particles are brought together to a certain proximity by the stress, elastic-plastic deformation sets forth at interparticle contact areas.

Powder deformation during drying and heat treatment in Three-Dimensional Printing occurs at very low shrinkage pressure (less than 6 psi or 40688 Pa). Therefore, it is strictly governed by particle rearrangement and restacking where morphology and initial packing density have very important roles. Due to this very small pressure window, the nature of strain and isostatic pressure can be approximated with linear regression. The slopes of the approximation lines varies exponentially with initial packing fraction. Therefore, the powder strain can be described mathematically as

For Norton 7920 $$\varepsilon_{powder} = \left[0.0010884 * 10^{(-9.6321\phi_i)}\right] P_{iso} \quad , \; 0.36 < \phi_i < 0.46$$

For CB-A30S $$\varepsilon_{powder} = \left[0.0495 * 10^{(-11.558\phi_i)}\right] P_{iso} \quad 0.44 < \phi_i < 0.56$$

where ε_{powder} is the linear powder strain

ϕ_i is the initial packing fraction

P_{iso} is the isostatic pressure in Pascal

Both Norton 7920 and CB-A30S spherical powder behave similarly to isostatic stress. But, CB-A30S has higher apparent packing densities due to its morphological superiority.

Bibliography

[1] Coulomb, C., *Essai sur an Application des Règles des Masimes et Minimus à Quelques Problèmes de Statique Relatifs à l'Architecture*. Mémoires de Savants Étrangers de l'Académic des Sciences de Paris, 1776.

[2] Rankine, W. J., *On the Stability of Loose Earth*, Phil. Trans. Roy. Soc, London, 147, 9-127, 1857.

[3] Ketchum, M. S., *The design of Walls, Bins and Grain Elevators*, New York, McGraw Hill, 1919.

[4] Reimbert , M., Reimbert, A., *Silos: Traité Théorique et Pratique*, 3rd ed.,Paris, Editions Eyrolles, 1961.

[5] Johanson, J. R. and Jenike A. W.,*Stress and Velocity Fields in Gravity Flow of Bulk Solids*, Bull. 116, Utah Engng. Expt. Stn., Bull. Univ. Itah 53, 21, 1962

[6] Gardner, G. C., *Limiting Conditions for Flow of a Cohesive Granular Material down an Inclined Plane (Chute) or between Parallel Inclined Walls (Bin or Channel)* , Chem. Eng. Sci. 17, 1079-1086, 1962.

[7] Gardner, G. C., *The "Best" Hopper Profile for Cohesive Materials*, Chem. Eng. Sci. 18, 35-39, 1963.

[8] Gardner, G. C., *The Axisymmetric "Best" Hopper, its Relevance to the Plane "Best" Hopper and "Best" Hoppers Integrated with Bins*, Chem. Eng. Sci. 19, 283-288, 1964

[9] Gardner, G. C., *The Region of Flow when Discharging Granular Materials form Bin-hopper Systems*, Chem. Eng. Sci. 21, 261-273, 1966.

[10] Hvorslev, M. J., *On the Physical Properties of Disturbed Cohesive Soils*, Ingeniorvidenskabelige Skrifter A, 45, (March), 9, 1937

[11] Roscoe, K. H., Schofield, A. N., Wroth C. P., *On the Yielding of Soils*, Geotechnique 8, 22-53, 1958.

[12] Bockstiegel, G., *Probability aspects in powder compaction*, Prod. First Int. Conf. On the Compaction and Consolidation of Particulate Matter, ed. A.S. Goldberg, Powder Advisory Centre, London, 1972

[13] Hausner, J., *The role of interparticle friction in powder technology*, Proc. First Int. Conf. On the Compaction and Consolidation of Particulate Matter, ed. A. S. Goldberg, Powder Advisory Centre, London, 1972

[14] Beddow, J., *Int. J. Powder Metallurgy*, 9, 127, 1973

[15] Shapiro, I., *Kolthoff, I., J. Phys. And Colloid Chem*, 51, 483, 1947

[16] Konopicky, K., *Radex Rundschau*, 3, 141, 1948

[17] Heckel, R., *Trans Met. Soc*, AIME, 221, 1001, 1961

[18] James, P., *PhD Thesis*, Loughborough University of Technology, 1976

Chapter 8.

Powder-Binder Shrinkage Interaction

8.0 INTRODUCTION

Shrinkage in Three-Dimensional Printing is originated in binder deformation during drying and sintering. Drying shrinkage depends on the physics of capillarity where the liquid phase under tensile stress deforms the network that encapsulates the liquid body. Sintering shrinkage takes place during heat treatment where binder material softens and viscously flows to deposit at the interfacial area. Details of drying and heat treatment shrinkage were discussed Chapter 4 to 6.

In Three-Dimensional Printing process, binder is jetted and absorbed into interparticle voids of the powder bed by matric suction. Binder transportation in the powder bed is governed by capillary potential which ceases after the liquid body is under equilibrium. The binder finally resides in the region where powder particles make contact to minimize its surface to result in minimal surface energy. In other words, the binder bridges powder particles and knits them into a composite network.

As binder shrinks, it pulls along attached powder particles which are, however, mechanically locked with their neighbors. The movement places the powder under compressive stress while the binder undergoes tensile stress. This is a very interesting and very important interaction in Three-Dimensional Printing which will be referred to as 'Powder-Binder Shrinkage Interaction'. This chapter is intended to focus on the concept of powder/binder shrinkage interaction as well as shrinkage prediction. Although the concept was originated and tested with silica and alumina, the notion of this powder-binder shrinkage interaction may well be applied to other pairs of materials.

This Chapter is organized into four main sections. The first section is an introduction of the concept of powder-binder shrinkage interaction. The second section is a

review of theoretical development that describes particulate assemblies. The next two sections are on experimental protocol, result, and discussion. The findings are summarized and proposed for a new powder-binder system for Three-Dimensional Printing in Section 8.5. Finally the chapter ends with a summary in Section 8.6

8.1 EQUILIBRIUM OF BINDER SHRINKAGE AND POWDER RESISTANCE

8.1.1 Equilibrium of Shrinkage and Resistant Stresses

Binder consolidates during drying and sintering and pulls attached particles along. However, the particles are not free to move in the powder bed since they are mechanically constrained with their adjacent neighbors in the assembly. Relative movement of the particles in the powder bed shall only take place when the binder exerts shrinkage force that sufficiently overcomes powder's resistance. According to the result in Chapter 7, required stress to rearrange the particles is only in the order of 1-3 psi. The stress developed by the binder is isostatic and will be referred to, in this thesis, as **shrinkage stress**. By nature, binder only consolidates, therefore, shrinkage stress is always tensile stress. On the other hand, the network of particles in the region of the binder are under isostatic compression which will be referred to as **resistant stress**.

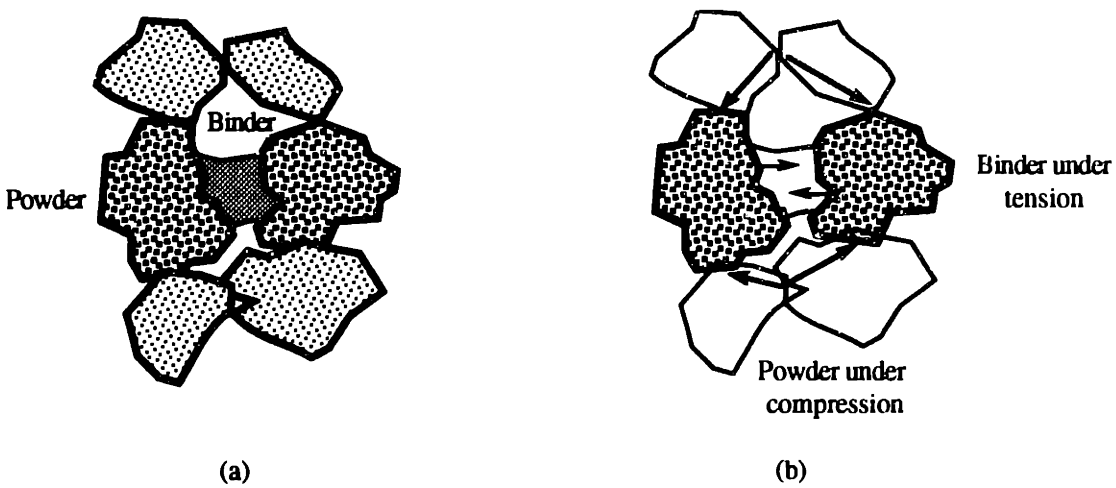

Figure 8.1 Binder Shrinkage and Powder Resistant Stress
(a) Powder and Binder in Assembly (b) Force Balance Between Powder and Binder

At all times, the associated *force* (not the stress) from both shrinkage and resistant stresses are at balance so the powder-binder assembly always remains at quasi-static equilibrium. Figure 8.1 illustrates how binder deformation induces shrinkage and resistant stresses. The only case where stress can be used to identify the equilibrium is when the binder fills up the void at the cross-section, $A_S = A_L$, such as in Figure 8.2 (a). At a lower saturation, the cross-section area at the binder's necks are always smaller than that of the powder. Therefore, the resistant stress in the powder is less than the shrinkage stress in the binder, Figure 8.2 (b). Note that line X-Y is approximately a straight line if the particles are small.

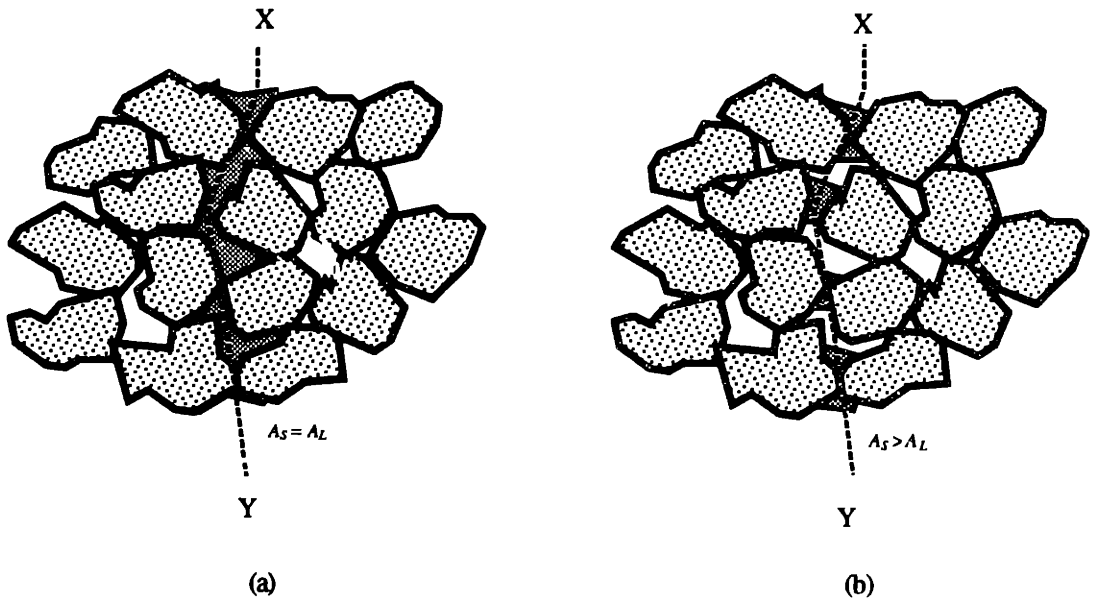

Figure 8.2 (a) Force and Stress Balance are Equivalent When Binder completely fills the Voids (b) When the Saturation is Lowered, Shrinkage Stress is Higher than Resistant Stress due to Smaller Cross-Section Area at the Necks of the Binder. At All Times, the Powder and Binder Remain Under Force Balance.

A portion of the binder stays on the surface of the powder outside the neck as in Figure 8.3 (b). This makes it really difficult to predict the cross-section area of the neck as a function of saturation. In fact, the reduction in the cross-section area is governed by initial saturation level, solid content in the binder, wetting physics of the binder onto the powder, size and shape of the powder particles and their distribution, and packing fraction.

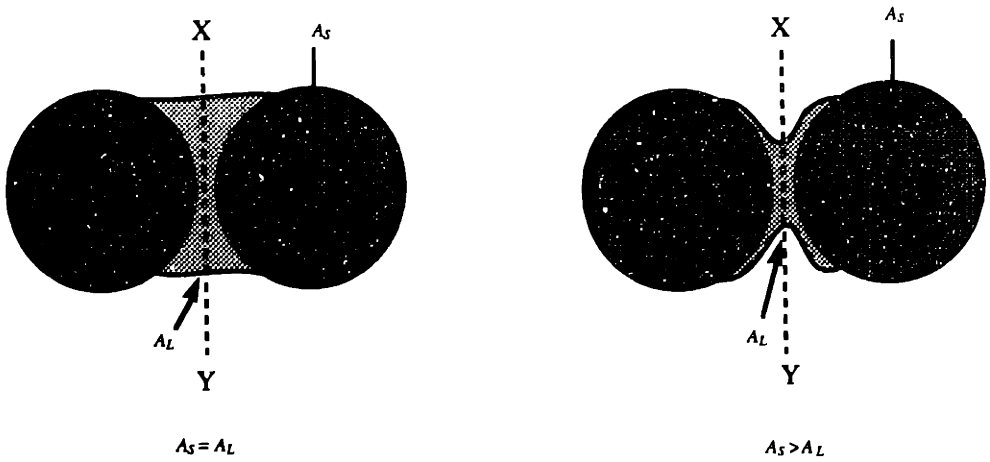

(a) Binder Neck at High Saturation (b) Reduction of Neck Area at Low Saturation

Figure 8.3 Reduction of A_L/A_S at a Lower Saturation

8.1.2 Relation of Binder and Composite Strain

Binder strain of Three-Dimensional Printing's ceramic binders were recorded and discussed in Chapter 6 while powder strain due to isostatic stress were documented in Chapter 7. In this section, the interaction between powder and binder regarding shrinkage deformation will be focused when both materials are combined into a **composite**.

Binder wicks into intergranular pores immediately after contacting with small pores. During the course of binder movement, air may enter into the binder and break up the liquid phase. The liquid transportation ceases when the matric suction is equilibrated through out the liquid body. At this point, binder already bridges out to several particles and intertwines them into networks. Binder occupancy of the pore volume at this point must be at saturation or very close to saturation. Water slowly leaves the system by evaporation. Finally, the liquid-vapor interface enters the pore volume and empties the pore volume. Remaining binder stays as films on the surface of the particles and the areas where particles come into contact. These binder films gel after reaching a critical concentration or by surfactant and remain coated on the surfaces of the particles. Further drying of the gel produces deformation. Gels at the neck region consolidate and bring particles into a tighter

formation causing shrinkage. The portion of gel that stays coated on the surface of the particles remains as a thin film (about 5 μm thick) for both acid and drying gellation. Figure 8.4 (a) and (b) illustrates surface coated films of Binder B on CB-A30S and Norton 7920 powder respectively.

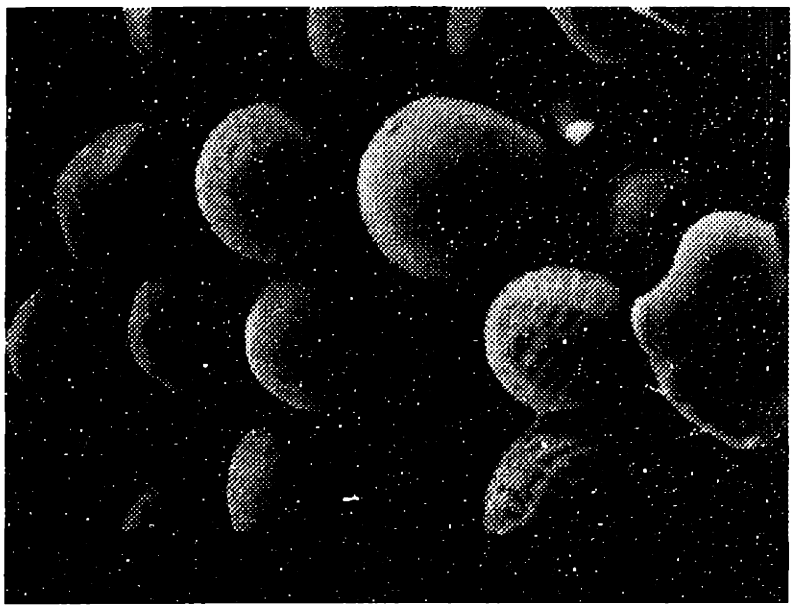

(a)

(b)

Figure 8.4 Dried Gel Remains as Thin Film On Particles' Surfaces
(a) on CB-A30S Spherical Powder and (b) on Norton 7920 Platelet Powder

Although there is a portion of binder coated on the surface of the particles, it does not affect the shrinkage of the composite as does the binder in the neck areas. Therefore, a shrinkage model can be constructed by ignoring the surface coated portion of the binder.

The particle shape of Norton 7920 is typically angular and irregular while that of the spherical powder is smooth and almost a perfect sphere. But for simplicity, they can be approximated as polygons of average size R from the center of the body to the surface, Figure 8.5 (a). Consider two particles with a mean particle separation of kR (where k is a constant to be found), joined by binder in Figure 8.5 (b),. As binder deforms with a strain of ε_{binder} (resulting in total deformation of $\varepsilon_{binder}kR$), the composite strain , ε_{comp}, which includes the particles and the binder is:

$$\varepsilon_{comp} = \frac{\varepsilon_{binder}kR}{2R + kR}$$

or

$$\varepsilon_{comp} = \frac{\varepsilon_{binder}}{1 + \frac{2}{k}} \tag{8.1}$$

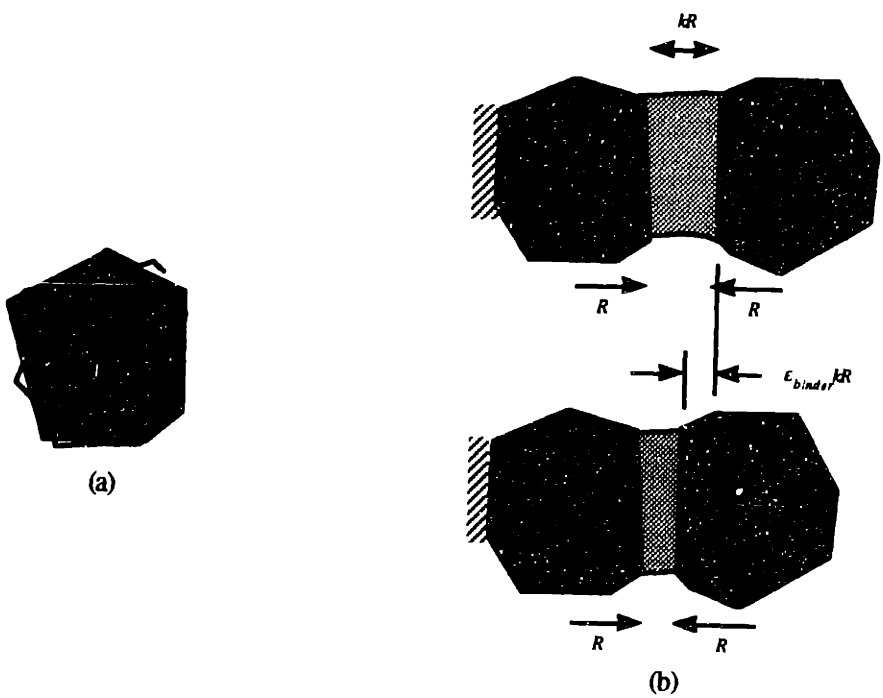

(a)

(b)

Figure 8.5 Geometrical Relationship Between Strain of Binder and the Composite

Therefore, strain of the composite, ε_{comp}, varies linearly with binder strain, ε_{binder}, with an attenuation factor of $1+\frac{2}{k}$. In other words, the closer the particles are ($k \rightarrow 0$), the less strain the composite has for a given binder deformation.

The model in Figure 8.5 can be simply expanded from one-dimension into a cellular structure to capture the shrinkage in three-dimensions. The cellular model is shown in Figure 8.6 consisting of several polygons bonded orthogonally by binder. Each polygon is connected to six adjacent neighbors (unless for those at the surface or the edge) with an average particle separation of kR and a particle size of R from the center to the particle surface.

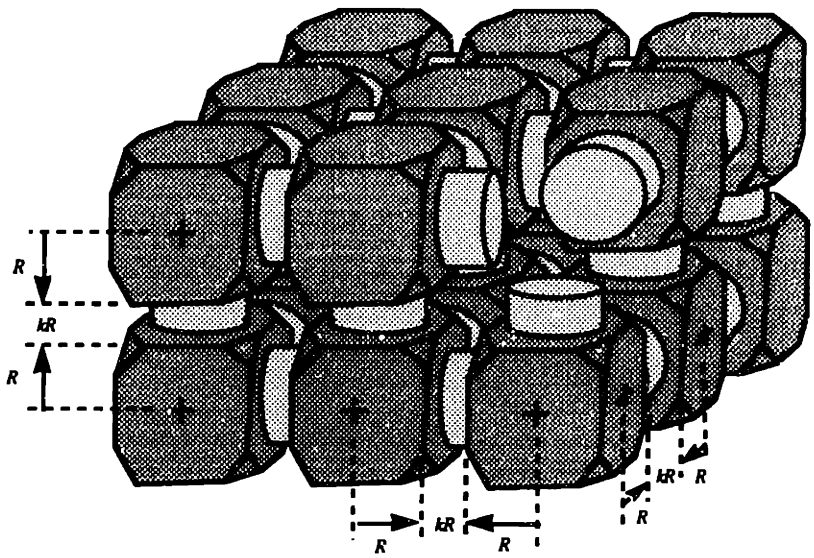

Figure 8.6 Cellular Structure of Powder and Binder Composite with Mean Particle Separation of kR

According to Equation 8.1, the magnitude of mean particle separation, k, significantly governs the amount of shrinkage of the composite. From the binder strain measurement in Chapter 6, the magnitude of binder strain during drying ranges from 0.04 to 0.45 depending on binder materials and the boundary compliance. However, typical composite strain of Three-Dimensional Printing ceramic process during drying falls between 0.0025 to 0.0150. Based on these measurements, the mean particle separation in Three-Dimensional Printing, according to Equation 8.1, should be approximately $0.02R$

to $0.07R$. Figure 8.7 illustrates relationship between binder strain, mean particle separation, and composite strain according to Equation 8.1. Theoretical findings on mean particle separation will be discussed in the following sections.

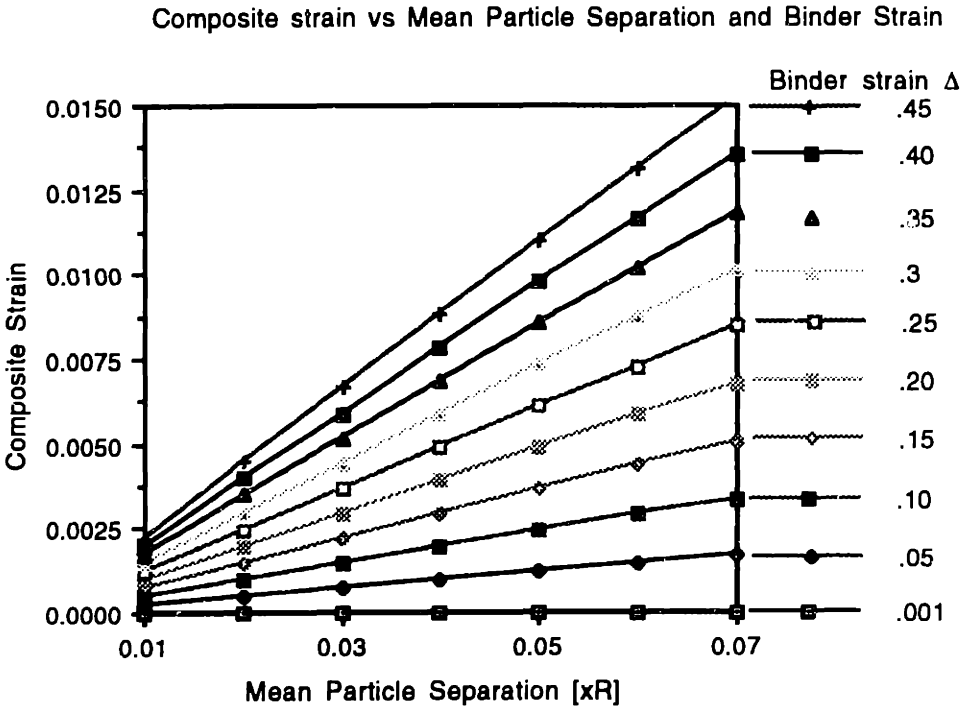

Figure 8.7 Composite Strain, ε_{comp}, and Binder Strain, ε_{binder}, are Related by the Mean Particle Separation, k

8.2 SPATIAL STRUCTURE OF PARTICULATE ASSEMBLIES

Knowledge of the spatial structure of particles in random assembly such as the radial distribution function, the first-layer neighbors, and the mean particle separation is very important when dealing with powder deformation. The work shown in the previous section clearly emphasizes how important the mean particle separation is to the strain magnitude of the composite.

8.2.1 Radial Distribution Function

Radial Distribution Function, $g(r)$, is defined as the local density of particles, normalized by its bulk-mean value, at a radial distance r from a central reference sphere [1]. The topic has been studied by a number of researchers including simulation and experiments [2-5]. Scott [3] determined radial distribution function for random packed monosize spheres by pouring 4,000 - 1/8 in steel balls in dimpled wall basket to reduce the wall effect. The assembly was fixed by pouring hot parafin wax and allowing it to cool. Positions of innermost 1,000 balls were measured in three-dimensional and the data was processed by a computer. Similarly, a computational simulation can be well applied to the task by numerically generating a particulate assembly.

The local density of the powder as a function of radius from a center reference can be calculated with computer. The methodology for a particulate system is shown in Figure 8.8. Figure 8.8 (a) illustrates a particle assembly consisting of monosize spheres in 2 dimension with first and second layer neighbors from a center reference. Figure 8.8 (b) shows how radial distribution function of the **first-layer neighbors** are calculated.

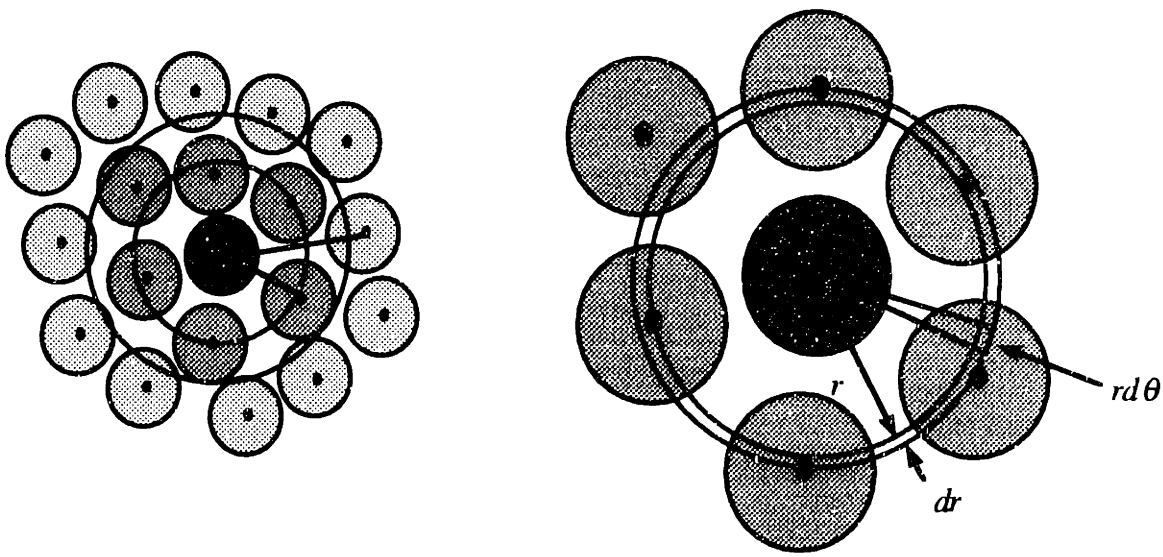

Figure 8.8 Radial Distribution Function in Two-Dimension
(a) Particulate Assembly Showing First and Second Layers (b) Local Density Inside the Ring

According to Figure 8.8 (b), for a small ring with radius r and width dr from the center reference, the local radial density is the portion of the ring that is occupied by particles divided by the total area of the ring. In other words, it is the ratio of the shaded portion to the total area of the ring. Mathematically, local radial density equals

$$\frac{\int_0^{2\pi} i(r,\theta) r dr d\theta}{2\pi r dr}$$

where $i(r,\theta)$ is a toggle variable representing particles or pores where

$i(r,\theta) = 0$ over the area represented by the pores (unshaded area)

$= 1$ over the area represented by the particles (shaded area)

Therefore, the radial distribution function of a particulate assembly in two-dimension is

$$g(r) = \frac{\frac{\int_0^{2\pi} i(r,\theta) r dr d\theta}{2\pi r dr}}{\frac{\int_0^R \int_0^{2\pi} i(r,\theta) r dr d\theta}{\int_0^R 2\pi r dr}}$$

or

$$g(r) = \frac{R^2 \int_0^{2\pi} i(r,\theta) d\theta}{2\int_0^R \int_0^{2\pi} i(r,\theta) r dr d\theta} \tag{8.2}$$

The concept can be applied to identify the radial distribution function of a particulate assembly in three-dimensions as:

$$g(r) = \frac{\frac{\int_0^{2\pi}\int_0^{2\pi} i(r,\theta,\alpha) r d\theta r d\alpha dr}{\int_0^{2\pi}\int_0^{2\pi} r d\theta r d\alpha dr}}{\frac{\int_0^R \int_0^{2\pi}\int_0^{2\pi} i(r,\theta,\alpha) r d\theta r d\alpha dr}{\int_0^R \int_0^{2\pi}\int_0^{2\pi} r d\theta r d\alpha dr}} \tag{8.3}$$

where α represents azimuth angle of the spherical coordinate.

Note that the toggle variable $i(r,\theta,\alpha)$ is a function of three coordinates

Most of the research generally used either monosize or multisize spheres to described the particulate assemblies due to the fact that the description of a sphere in space only requires three position coordinates in spatial and a radius information. However, for angular particles, three rotational coordinates as well as a set of shape description parameters are required additionally to the position coordinates. As a consequence, it is extremely complex to describe angular particles in assemblies especially when the shape of each particle is different and irregular.

The radial distribution function for monosize spheres is plotted in Figure 8.9. The damped oscillation implies short range order in the particle arrangement with a shell like pattern of surrounding particles about the center sphere.

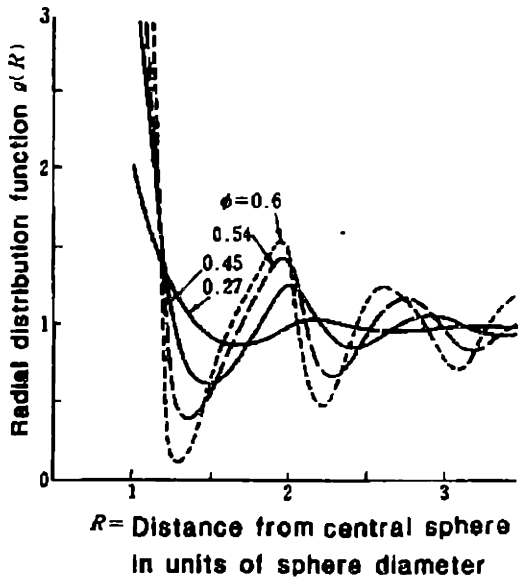

Figure 8.9 Radial Distribution Function
where ϕ is the Mean Packing Fraction of the Assembly [6]

8.2.2 MEAN PARTICLE SEPARATION

According to Figure 8.8 (a) and (b), the inner most shell of particles surrounding the center sphere is referred to as first-layer neighbor. Structural characteristics of the first-layer neighbor were captured by Gotoh [7] and Suzuki [8]. While Chandrasekhar [9], Bansal and Ardel [10], and Gotoh et. al. [6] discussed average center-to-center distance between a central sphere and its first-layer neighbor, Figure 8.10.

In microscale, mean particle separation refers to an average distance between the center sphere to the first-layer neighbor. On the other hand, in macroscale, the mean particle separation stands for an average free spacing between adjacent particles in the powder bed. This is the area where binder resides and knits particles into a composite. Therefore, the separation dictates the ratio of average binder span and the particle radius which was early described as k in Equation 8.1. So, particulate systems with wide particle separation must have higher composite strain than systems with narrow separation.

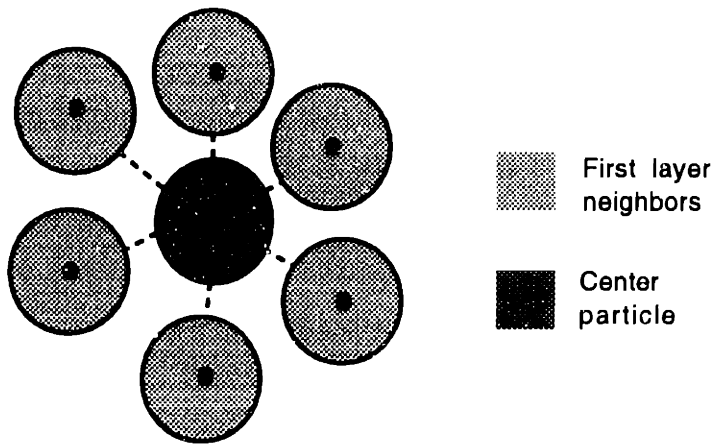

Figure 8.10 Concept of Mean Particle Separation in the First-Layer Neighbors (Dashed lines)

Mean particle separation for monosize sphere particulate systems was studied by Gotoh [6]. He found that the separation was a strong function of packing fraction, ϕ. Figure 8.11 illustrates the relationship between particle separation from a central sphere to its first-layer neighbors in units of the sphere radius and the packing fraction where R_l is for the outer edge, R_m is the average separation, and R_n is for the nearest neighbor.

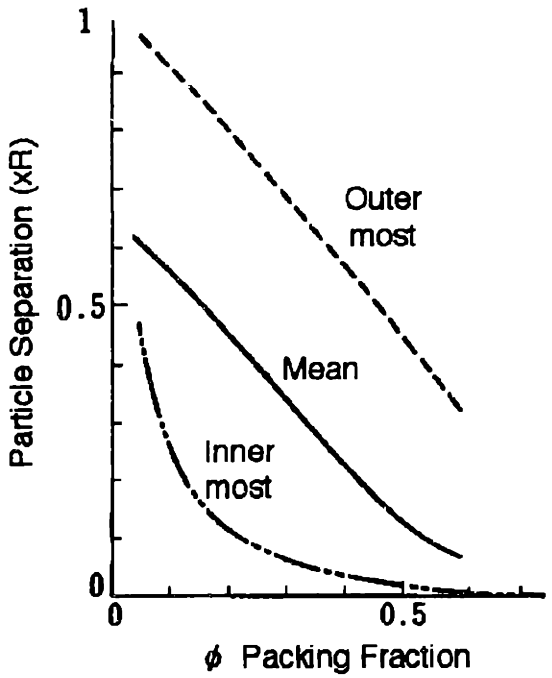

Figure 8.11 Relationship Between Packing Fraction and Particle Separation of Monosize Spheres [Modified from 6]

This thesis work is mostly interested in the value of the mean particle separation. The particulate assemblies remain in a stable state when the inner most approaches zero or the particles make physical contact with their neighbors. For monosize spheres, particles initiate contact when the packing fraction is approximately 55 percent. At this point, it is found that the mean particle separation is approximately 8 percent of the particle radius.

In case of angular and irregular particle assemblies, the mean separation is much harder to estimate because of the complexity of the system description in spatial coordinates and the fact that the mean separation depends on the shape and the orientation of each individual grain. It is envisioned that the difference between the separation of inner most particle and the outer most will be wider than that of spherical assemblies. According to this presumption, it may be fair to expect that the mean separation of angular and irregular particles will be more than that of spherical powder for the same particle size as well.

When particle assemblies are modeled as cellular structures as in Figure 8.12, the mean particle separation is defined differently from random packed monosize spheres. In the cellular structure, the powder bed can be viewed as an assembly of monosize polygons in cubic order while the spacing between each polygon is equal to the mean particle separation.

This research work is more interested in quantifying the mean particle separation for the cellular structure. Although cellular structure may not best represent actual random packing of particulate systems in three-dimensions, it is reasonable and simple to capture the fundamental mechanism of shrinkage of the composite at this point. Once the shrinkage knowledge has been captured, powder-binder assemblies may well be modeled at a more complex level such as in triangular or hexagonal formation.

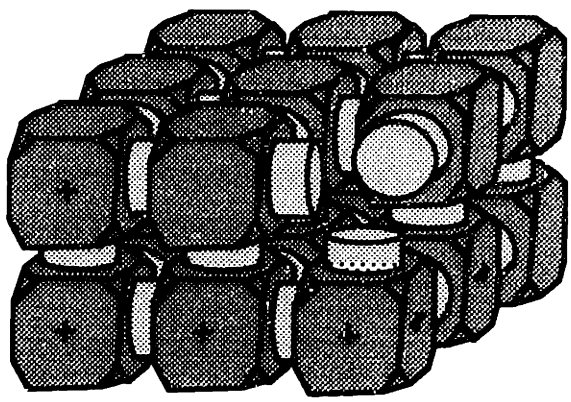

Figure 8.12 Cellular Structure Model of Particles in Assembly

In the next section, the mean particle separation of Norton 7920 and CB-A30S will be identified experimentally based on the concept of cellular structure.

8.3 Experiment Protocol

The motivation behind this experiment is to combine the result of binder deformation in Chapter 6, Figure 8.13 (a and b), with the experimental findings of powder deformation due to isostatic or resistant stress in Chapter 7, into a shrinkage model based on the cellular structure in Figure 8.12. This thesis work assumes each unit cell experiences a similar environment and, therefore, evolves through the shrinkage process at the same pace and condition. Shrinkage anisotropy within and between layers which leads to warpage or curling will not be assessed at this point.

Deformation of powder with empty pores was referred to as powder strain. But when the pores are filled with binder, the deformation will be referred to as **composite strain** in this thesis work. Therefore, powder and composite strain describe the same phenomena depending whether there is binder presenting in the pores or not. Similarly, in saturated printing, shrinkage and resistant stresses must be at equilibrium to remain static so both stresses may be used interchangeably for their equality. However, the relationship between binder and powder strains can be described only if the mean particle separation is realized. If so, both binder and powder strain characteristics can be used to identify the equilibrium of powder-binder shrinkage interaction which is a highlight of this thesis.

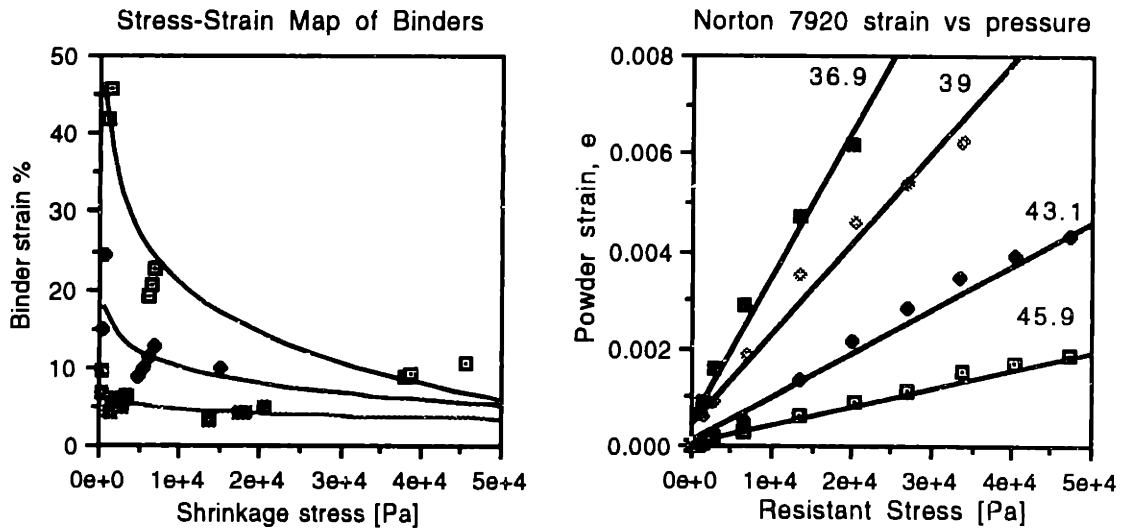

(a) (b)

Figure 8.13 (a) Binder Strain as a Function of Shrinkage Stress

(b) Powder Strain as a Function of Resistant Stress

Therefore, the goal was to describe the mean particle separation according to the cellular structure of Norton 7920 and CB-A30S powders such that the geometrical ratios between binder and powder strain of both powder are identified. This allows for superimposition of binder and powder strain in Figure 8.13 to determine powder-binder shrinkage equilibrium conditions.

Powder was tap densified into a set of four quartz combustion boats (with known volumes) at various packing densities. Then binder was dropped onto the powder bed from a dropper. Each droplet size was approximately 2 to 3 millimeters. Upon contact with the powder bed, binder was absorbed into the pores in about a second. The droplets overlapped and formed a line approximately 1 inch long. Once first binder deposition was completed, binder was redeposited on the wetted area of the line to guarantee that saturation was reached. Finally, two 100 μm OD silicon with 33 μm carbide fibers core at 1/8 inches in length were vertically pinned into each end of the line as markers. Lines created by this technique were about 5 millimeter wide and 4 millimeter thick, Figure 8.14

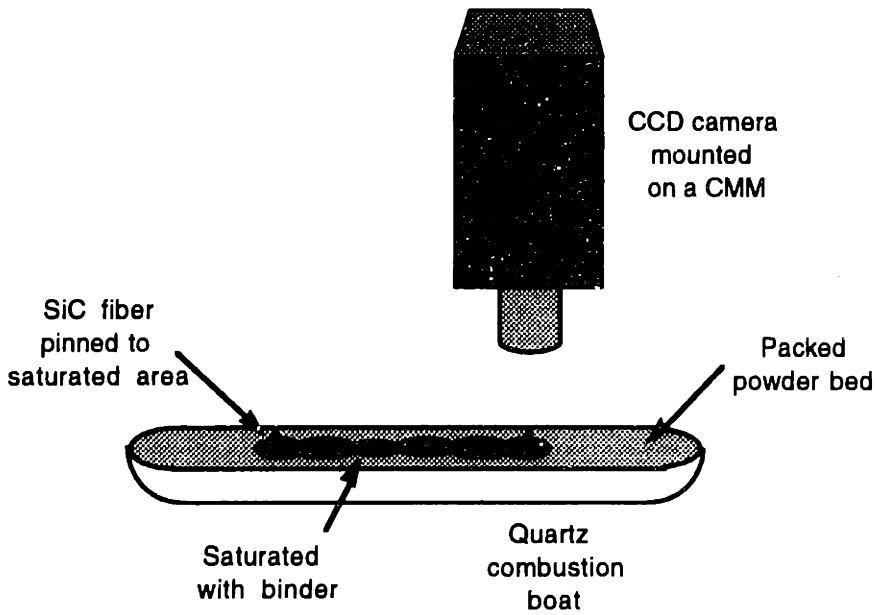

Figure 8.14 Shrinkage Measurement to Identify Mean Particle Separation

The coordinates of the tips of the markers were recorded by a microscope CCD camera mounted on the tip of a Coordinate Measuring Machine (CMM) at three different states : wet, dried, and after 900°C heat treatment. There was no shrinkage on wet

samples according to the experimental findings in Section 6.1.2. Therefore, drying and heat treatment shrinkage strains were calculated using the distances between the pins at wet condition as references. Tested binders included 1) Binder B with acid gelled, 2) Binder B gelled by drying, 3) Nyacol 9950 at various silica contents as well as organic derivatives, and 4) Sodium Silicate. On the powder side, Norton 7920 at 28 μm and CB-A30S spherical alumina powder were selected for their extreme particle morphology.

8.4 RESULT AND DISCUSSION

8.4.1 Result

NORTON 7920

Binder B acid gelled (0.5 wt%)			Binder B gelled by drying			Nyacol 9950 @ 50 wt % drying		
Packing fraction %	Drying shrinkage strain	Drying + heat treated strain	Packing fraction %	Drying shrinkag estrain	Drying + heat treated strain	Packing fraction %	Drying shrinkag estrain	Drying + heat treated strain
32.6	0.0066	0.0088	35.9	0.0053	0.0072	32.6	0.0050	n/a
40.6	0.0041	0.0052	40.1	0.0035	0.0053	37.9	0.0024	0.0044
42.0	0.0029	0.0042	42.5	0.0027	0.0045	40.2	0.0019	0.0034
43.5	0.0042	0.0056	44.7	0.0027	0.0045	43.5	0.0019	0.0034

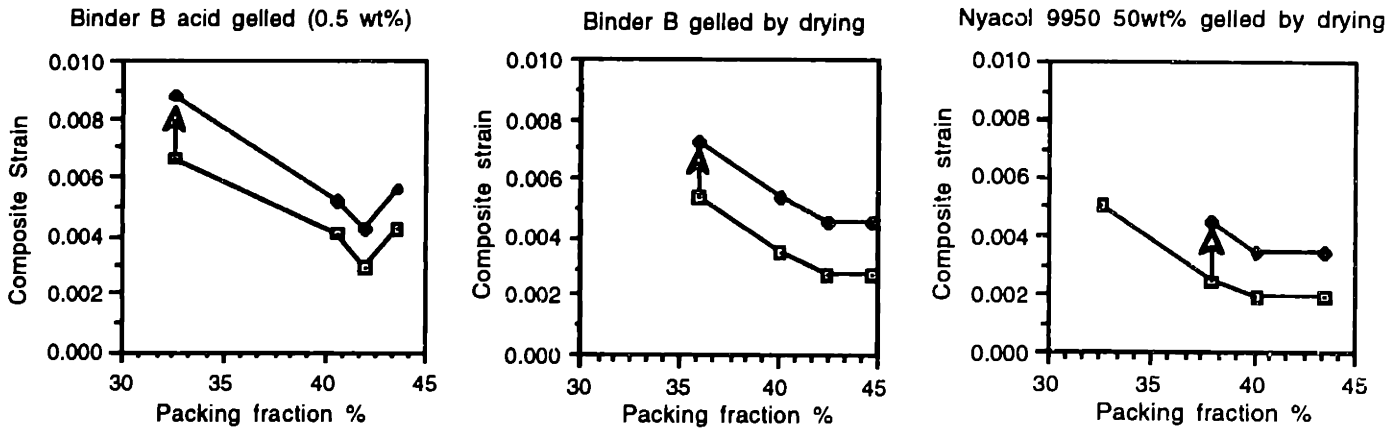

Table 8.1 and Figure 8.15 Measured Composite Strain of Norton 7920 with Various Binders. Arrows Indicate Heat Treated Strain Increment From Drying Strain For the Same Sample.

(a) Binder B acid gelled (b) Binder B gelled by drying (c) Nyacol 9950 @50wt% gelled by drying

Bimodal Nyacol 9950:830 @ 7:3 vol 43.5 wt %			Nyacol 9950 @ 43.5 wt %			Nyacol 9950 @ 30 wt %		
Packing fraction %	Drying shrinkage strain	Drying + heat treated strain	Packing fraction %	Drying shrinkag estrain	Drying + heat treated strain	Packing fraction %	Drying shrinkag estrain	Drying + heat treated strain
35.9	0.0042	0.0064	36.1	n/a	n/a	36.0	0.0038	0.0057
38.7	0.0037	0.0060	38.3	0.0033	0.0054	40.1	0.0022	0.0032
44.3	n/a	n/a	41.7	0.0022	0.0041	43.0	0.0016	0.0027
45.6	0.0023	0.0051	44.8	0.0019	0.0036	46.1	0.0022	0.0035
Nyacol 9950 @ 17.5 wt %			Sodium Silicate: water @ 1:1			Nyacol 9950 @ 30 wt%+0.3wt% PEG (matched Binder B)		
Packing fraction %	Drying shrinkage strain	Drying + heat treated strain	Packing fraction %	Drying shrinkag estrain	Drying + heat treated strain	Packing fraction %	Drying shrinkag estrain	Drying + heat treated strain
35.5	n/a	n/a	35.9	0.0064	0.0108	38.5	0.0031	0.0043
38.3	0.0016	0.0022	40.2	0.0079	0.0105	40.7	n/a	n/a
41.6	0.0019	0.0031	42.1	n/a	0.0084	41.5	0.0023	0.0038
42.8	0.0016	0.0018	44.9	0.0072	0.0074	46.9	0.0024	0.0037

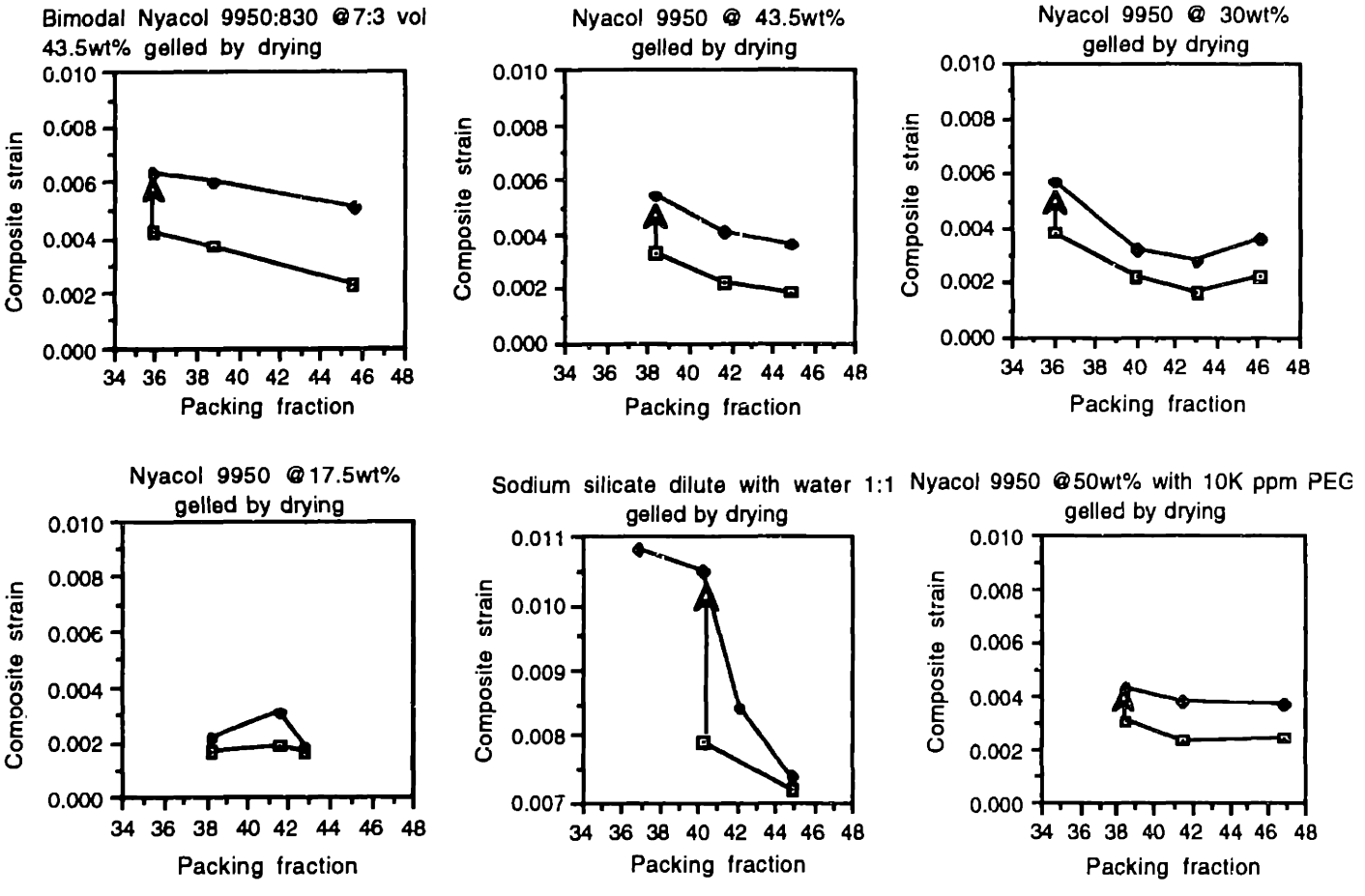

Table 8.2 and Figure 8.16 Measured Composite Strain with Other Concentration and Binders

CB-A30S

Binder B acid gelled (0.5 wt%)			Binder B gelled by drying			Nyacol 9950 @ 50 wt %		
Packing fraction %	Drying shrinkage strain	Drying + heat treated strain	Packing fraction %	Drying shrinkag estrain	Drying + heat treated strain	Packing fraction %	Drying shrinkag estrain	Drying + heat treated strain
42.2	0.0040	0.0048	51.1	0.0016	0.0018	49.6	n/a	n/a
51.6	0.0018	0.0031	53.4	0.0015	0.0016	53.5	0.0009	0.0014
53.9	0.0016	0.0031	54.7	n/a	n/a	54.6	0.0003	0.0010
57.9	0.0016	0.0028	59.4	0.0012	0.0016	58.0	0.0006	0.0011

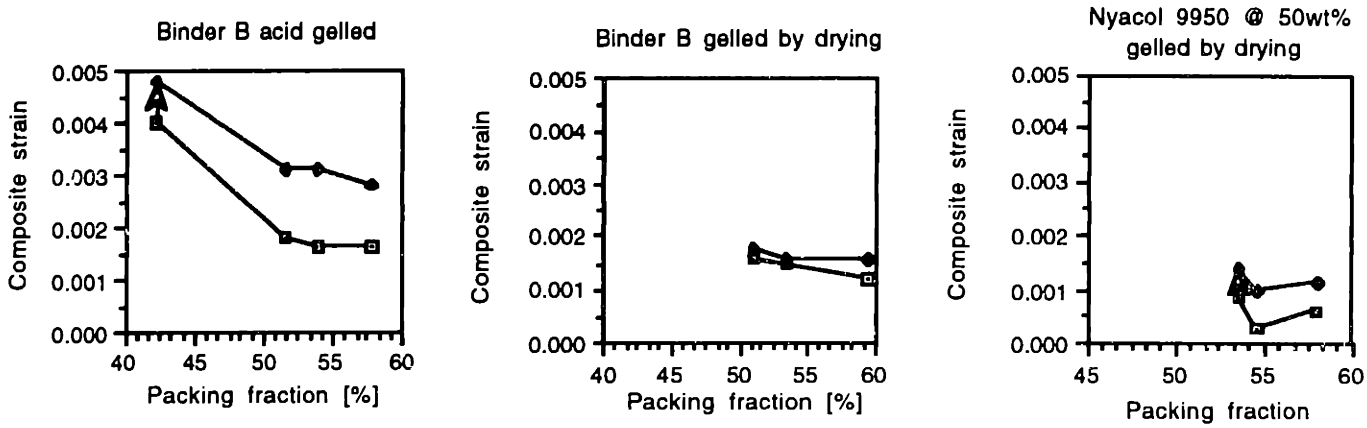

Table 8.3 and Figure 8.17 Measured Composite Strain of CB-A30S with Various Binders

Arrows Indicate Heat Treated Strain Increment From Drying Strain For the Same Sample

Drying and heat treatment strain of Norton 7920 and CB-A30S are shown in Table 8.1, 8.2, and 8.3 with associated plots in Figure 8.15, 8.16, and 8.17 as a function of packing densities. The arrows indicate additional heat treatment strain (900°C) to drying strain for the same sample. The result clearly indicates that strain of the composite gradually reduces as a function of packing density for all binders.

Among the three binders, Nyacol 9950 provides the least composite strain while acid gelled Binder B offers the most shrinkage strain consistent with the result in Chapter 6. This is true for both powder types but with different strain magnitudes. CB-A30S spherical powder provides much less composite strain than Norton 7920 for its higher apparent packing densities due to tighter particle formation.

Drying shrinkage strain from **bimodal** colloidal silica consisting of Nyacol 9950 (100 nm) and Nyacol 830 (10nm) at 70:30 solid volume ratio at 43.5 weight percent are not different from that of Nyacol 9950 at the same concentration (0.5 - 0.6 percent strain).

However, there is a clear indication that heat treatment strain of the bimodal binder is higher.

Drying and heat treatment shrinkage strain reduces accordingly with silica content in the binders. Figure 8.16 illustrates the tendency on curve 2, 3, and 4 (both A and B). The shrinkage at 17.5 weight percent silica content is approximately 60 percent of the case when the silica content is 43.5 weight percent. Sodium silicate provides higher drying and heat treatment strain (in which maximum strain exceeds 1 percent) than any other binders in the experiment.

8.4.2 Discussion

QUANTIFYING OF THE MEAN PARTICLE SEPARATION OF CELLULAR STRUCTURE

The drying shrinkage data from Figure 8.15 and 8.17 can be replotted on stress-strain map of Norton 7920 (Figure 7.19) and CB-A30S powder (Figure 7.22) with Binder B acid gelled, Binder gelled by drying, and Nyacol 9950 gelled by drying as in Figure 8.18 (a) and (b).

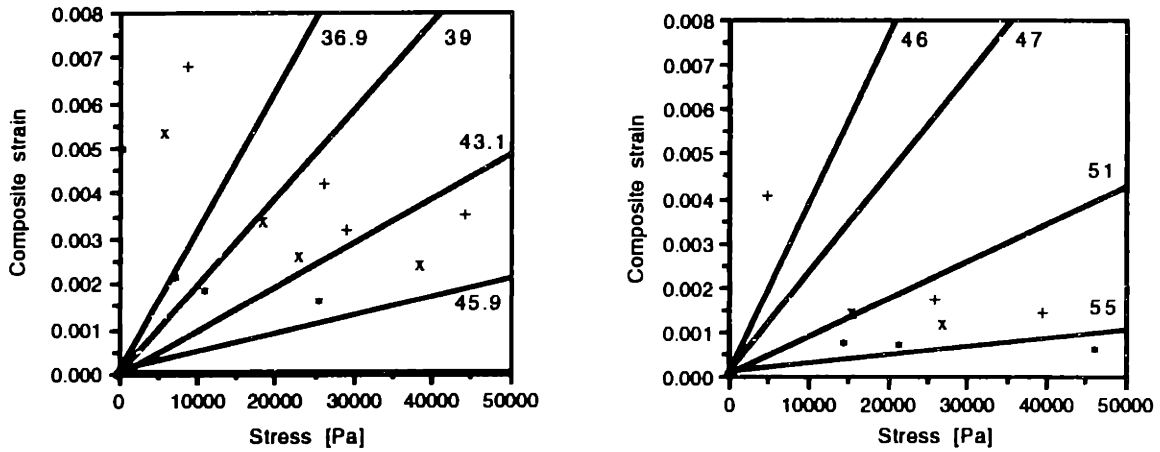

(a) (b)

Figure 8.18 Drying Strain Plotted on Powder Stress-Strain Map of (a) Norton 7920 (b) CB-A30S

+ Binder B acid gelled x Binder gelled by drying * Nyacol 9950 @ 50 wt % gelled by drying.

Then the stress-strain map of the binders in Figure 6.32 was rescaled and superimposed to fit the strain patterns in Figure 8.18. Such scales represent the ratio between composite and binder strain, $\frac{\varepsilon_{comp}}{\varepsilon_{binder}}$, which can be directly computed to give mean particle separation, k, for both powder as

$$\frac{\varepsilon_{comp}}{\varepsilon_{binder}} = \frac{k}{2+k}$$

or

$$k = \frac{2\frac{\varepsilon_{comp}}{\varepsilon_{binder}}}{1-\frac{\varepsilon_{comp}}{\varepsilon_{binder}}} \qquad (8.4)$$

Rescaling and fitting binder strain into Figure 8.18 results in the plots in Figure 8.19 (a) and (b).

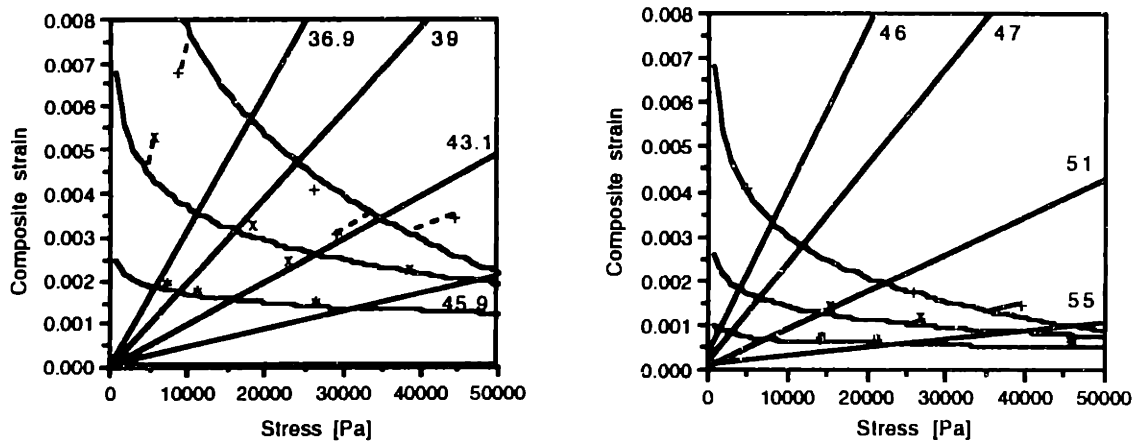

(a) (b)

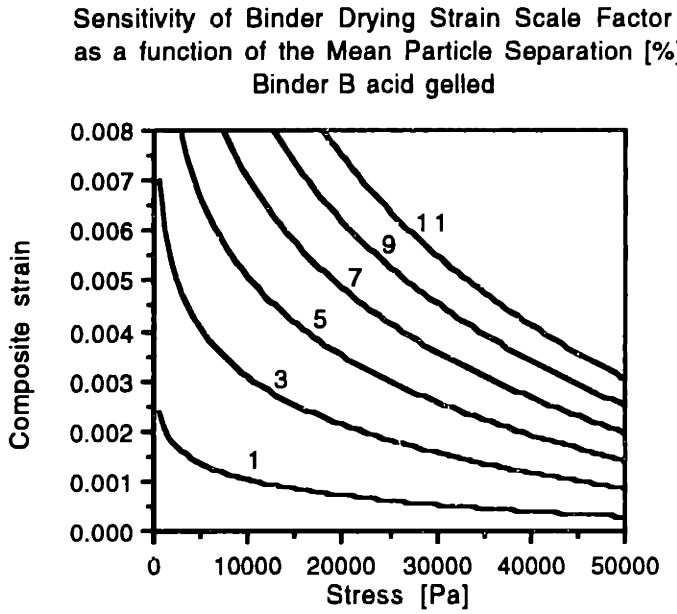

(c)

Figure 8.19 Fitted Drying Strain with the Stress-Strain Map of the Binders to Estimate Mean Particle Separation for Cellular Structure of (a) Norton 7920 (b) CB-A30S

+ Binder B acid gelled x Binder gelled by drying * Nyacol 9950 @ 50 wt % gelled by drying

(c) Sensitivity of Binder Drying Strain Scale factor as a function of the Mean Particle Separation [k, %] (shown with Binder B acid gelled)

Therefore the mean particle separation for the cellular structure, k, can be computed from the ratio of $\frac{\varepsilon_{comp}}{\varepsilon_{binder}}$ as in Table 8.4. Note that the mean particle separation is very close to Gotoh [6] which is illustrated in Figure 8.11

Norton 7920 % of particle radius, R	CB-A30S % of particle radius, R
7.69	2.90

Table 8.4 Computed Mean Particle Separation for Cellular Structure

Obtained mean particle separation for the spherical powder were slightly below Gotoh's prediction [6]. The discrepancy may be explained by two factors: first, Gotoh's work was based on monosize spheres where as CB-A30 has some size distribution. Second, particle formations in any particulate network are mix of serial and parallel elements. The composite strain in parallel formation is sensitive to the distribution of the particle separation where close spacing prohibits the strain movement of the formation, Figure 8.20.

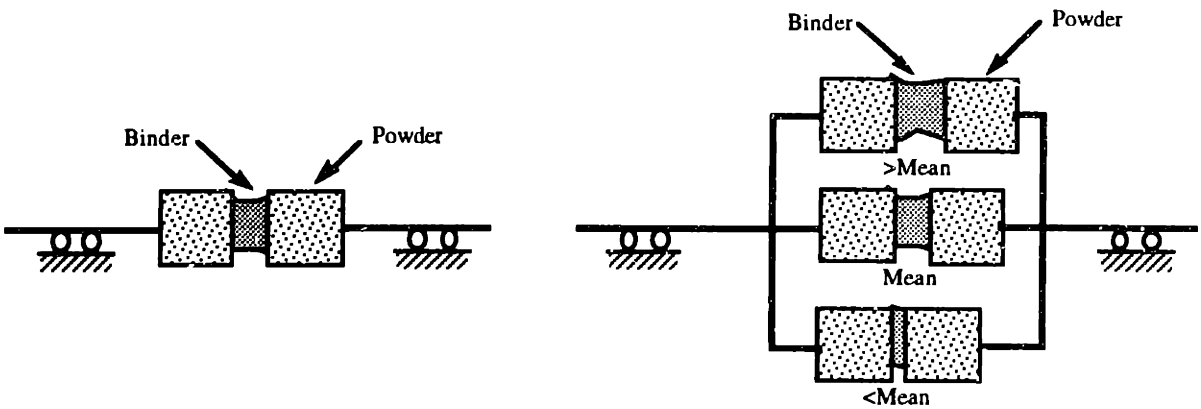

Figure 8.20 (a) Serial Particle Formation (b) Parallel Particle Formation

Figure 8.19 (a) and (b) are one of the highlights of this thesis work. There are four straight lines in each figure representing the powder strain response to shrinkage stress for different initial packing fraction. In addition, there are three curves depicting the binder strain loci of three binder types (2 types of Binder B and Nyacol 9950). The fact that

shrinkage and resistant stress are equalized when binder saturates the pores allows for the lines and the curves to be superimposed. The locations where these lines and curvatures cross identify the shrinkage equilibrium point of the powder and the binder. For example, Norton 7920 at 39 percent packing fraction printed with Binder B to saturation and gelled with equivalent 0.5 weight percent citric acid in powder is predicted to have drying shrinkage strain of 0.47 percent with associated shrinkage and resistant stress of 22,500 Pascal. Similarly, CB-A30S spherical powder packed to 51 percent and printed with the same binder to saturation should result in 0.2 percent drying shrinkage strain with resistant stress of 22,500 Pascal.

Heat treatment shrinkage to 900°C can further confirm the ratio of $\frac{\varepsilon_{comp}}{\varepsilon_{binder}}$ for Norton 7920 and Binder B. Binder strain during heat treatment to 900°C was found to be approximately 3 to 3.5 percent for Binder B and Nyacol 9950 at 50 weight percent. Therefore, with the mean particle separation, expected additional heat treatment strain of the composite from dried state are:

$$\varepsilon_{comp} = \frac{\varepsilon_{binder}}{1+\frac{2}{k}} = \frac{0.035}{1+\frac{2}{k}}$$

Item	Norton 7920	CB-A30S
Mean Particle Separation, k [% of particle radius]	7.69	2.90
Predicted additional Heat Treatment Composite Strain from Dried State [%]	0.13	0.05

Table 8.5 Predicted Heat Treatment Strain of the Composite Based on Computed Mean Particle Separation

Figure 8.21 reveals measured heat treatment shrinkage strain of the composite plotted in the stress-strain map while the dotted lines represent drying shrinkage strain. It is clear that the prediction and measurement of shrinkage during heat treatment are quite accurate for both Norton 7920 and CB-A30S powder.

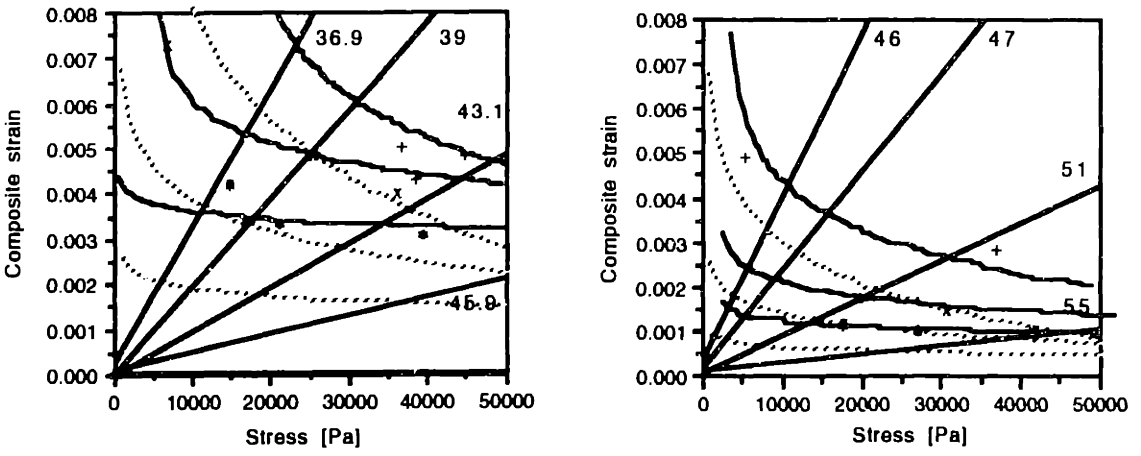

Figure 8.21 Drying + Heat Treatment Strain of (a) Norton 7920 (b) CB-A30S

\+ Binder B acid gelled x Binder gelled by drying * Nyacol 9950 @ 50 wt % gelled by drying.

Composite strain during drying and associated shrinkage or resistant stress can be described mathematically by combining regression data of the binders in Figure 6.32; powder strain responses in Equation 7.8, 7.12, 8.1; and ratio of $\frac{\varepsilon_{comp}}{\varepsilon_{binder}}$ from Table 8.4 and 8.5.

Mathematically, drying shrinkage for Norton 7920 with packing fraction $0.36 < \phi_i < 0.46$ as described by Equation 7.8 can be rewritten to Equation 8.5 as:

$$\varepsilon_{composite} = \left[0.0010884 * 10^{(-9.6321\phi_i)}\right]P \tag{8.5}$$

where P is shrinkage or resistant stress in Pascal obtained from solving Equation 8.6

$$ALog(P) + 0.0294 * 10^{(-9.6321\phi_i)}P = B \tag{8.6}$$

where A and B are given in Table 8.6

P is shrinkage or resistant stress in Pascal

ϕ_i is initial packing fraction, $0.36 < \phi_i < 0.46$

Similarly, drying shrinkage strain for CB-A30S with packing fraction $0.44 < \phi_i < 0.56$ described with Equation 7.12 can be rewritten as:

$$\varepsilon_{composite} = \left[0.0495 * 10^{(-11.558\phi_i)}\right] P \tag{8.7}$$

where P is shrinkage or resistant stress in Pascal obtained from solving Equation 8.8

$$ALog(P) + 3.4632 * 10^{(-11.558\phi_i)} P = B \tag{8.8}$$

where A and B are given in Table 8.6

P is shrinkage or resistant stress in Pascal

ϕ_i is initial packing fraction, $0.44 < \phi_i < 0.56$

Binder Types	A	B
Binder B acid gelled	0.2145	1.0660
Binder B gelled by drying	0.0683	0.3724
Nyacol 9950 @ 50 wt % gelled by drying	0.0178	0.1169

Table 8.6 Constants for Equation 8.5 and 8.7

Additional heat treatment strain of 0.13 and 0.05 can be added to drying shrinkage strain from Equation 8.6 and 8.8 for Norton 7920 and CB-A30S powder respectively.

SHRINKAGE OF BIMODAL COLLOIDAL SILICA AND SODIUM SILICATE

Drying shrinkage strain of bimodal colloidal silica consisting of Nyacol 9950 (100nm) and Nyacol 830 (10nm) at 70:30 solid volume with overall solid concentration of 43.5 weight percent is not different from monosize Nyacol 9950 at the same solid loading. It is probably because small particles are more reactive to gel at a higher liquid content thus

eliminating the advantage of bimodal packing. In addition, heat treatment shrinkage of bimodal silica is more than that of monosize Nyacol 9950 colloidal silica. It is because small particles sinter at a lower temperature and cause more shrinkage due to higher material flow toward the neck area.

Sodium silicate is generally used as a low cost binder for investment casting. But, the sodium presence in the binder lowers sintering temperature of silica glass resulting in more silica transport to deposit at the neck area. As a consequence, heat treatment shrinkage of sodium silicate binder is exceptionally higher that other binders.

8.4.3 Printing Shrinkage

Three-Dimensional Printing process may never deposit binder to full saturation due to bleeding where binder is squeezed out from the printed area by the roller during compaction and attaches some particles to the surface in an uneven manner. As a consequence, Three-Dimensional Printing generally keeps the saturation level at approximately 80 to 85 percent which is below the range in which powder-binder shrinkage interaction theory was based.

Figure 8.22 (a) and (b) reveal the composite strain of parts printed with Nyacol 9950 at 50 weight percent with various printing saturation and gelled by drying on Norton 7920 and CB-A30S respectively. Fully saturated data were taken from the experiment in Section 8.3 while printing saturation of 65 and 80 percent were made with triangular-distribution pattern with a base width of ± 175 μm[1]. Powder packing fraction for Norton 7920 and CB-A30S is approximately 42 and 55 percent, respectively. It was found that overall drying plus heat treatment shrinkage drops drastically as a function of printing saturation level. For Norton 7920, printing saturation levels of 65 and 80 percent provide factors of 3.5 and 2 less shrinkage than when printing at saturation, respectively. However, the reduction in shrinkage does not come free. Part strength is lower at low printing saturation.

CB-A30S provides substantially less amount of shrinkage than Norton 7920 due to lower mean particle separation, Figure 8.21 (b). However, the shrinkage seems to be more sensitive to printing saturation on Norton 7920 than on CB-A30S.

---

[1] Detail in Section 8.5

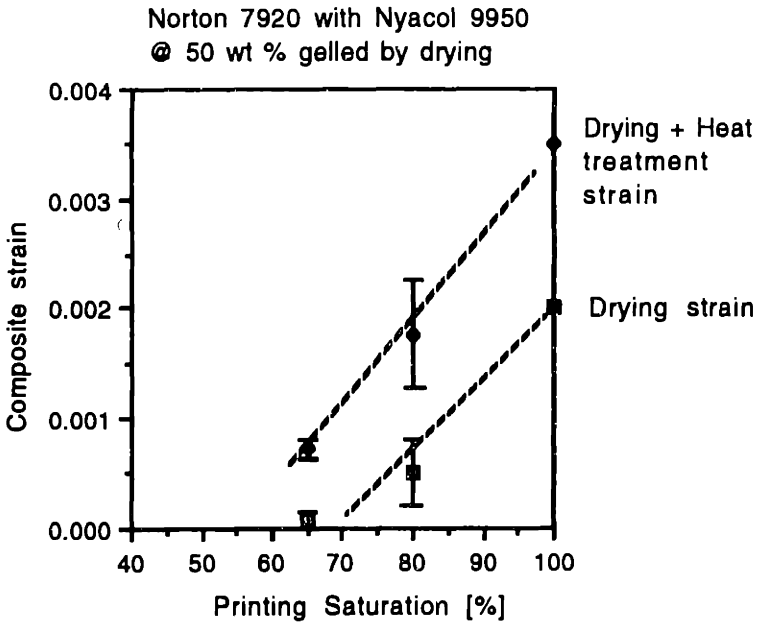

(a)

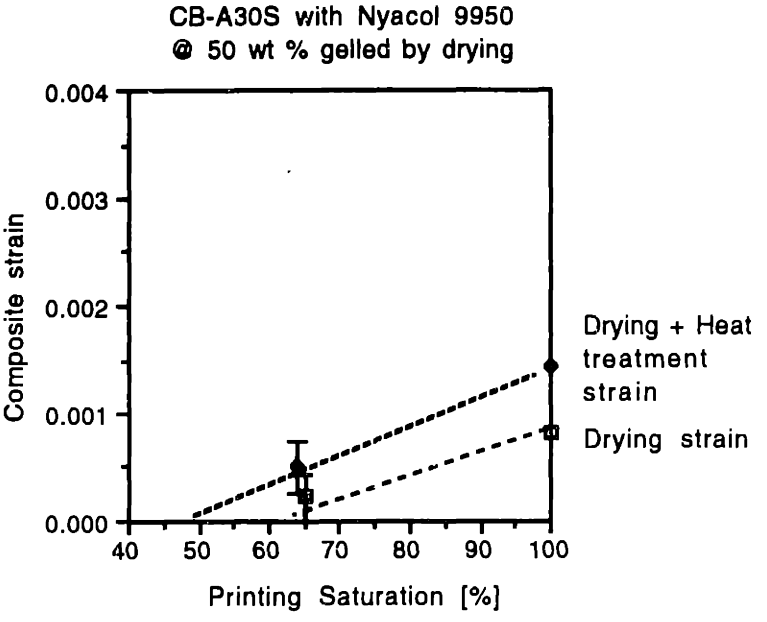

(b)

Figure 8.22 Reduction in Shrinkage Strain as a Function of Printing Saturation Level with triangular proportional deflection (see Section 8.5) (a) Norton 7920 (n=3 and 5 for printing saturation of 80 and 60 percent respectively) (b) CB-A30S Spherical Powder (n=3)

There are two hypotheses which may explain the reduction of shrinkage as a function of printing saturation:

1) Non-uniform Binder Distribution in the Powder at Low Saturation

In some cases, the level of saturation can not be practically treated as uniformly distributed. The co-existing nature of powder-binder reaches a saturation level that equilibrates the matric suction of the liquid phase. In other words, when binder is absorbed into the pores, it travels outward from the point of deposition into dried pores while lowering local saturation of the wetted area from 100 percent down to its nature equilibrium saturation level which will be referred to as Sat_{eq}. At Sat_{eq}, liquid transportation ceases.

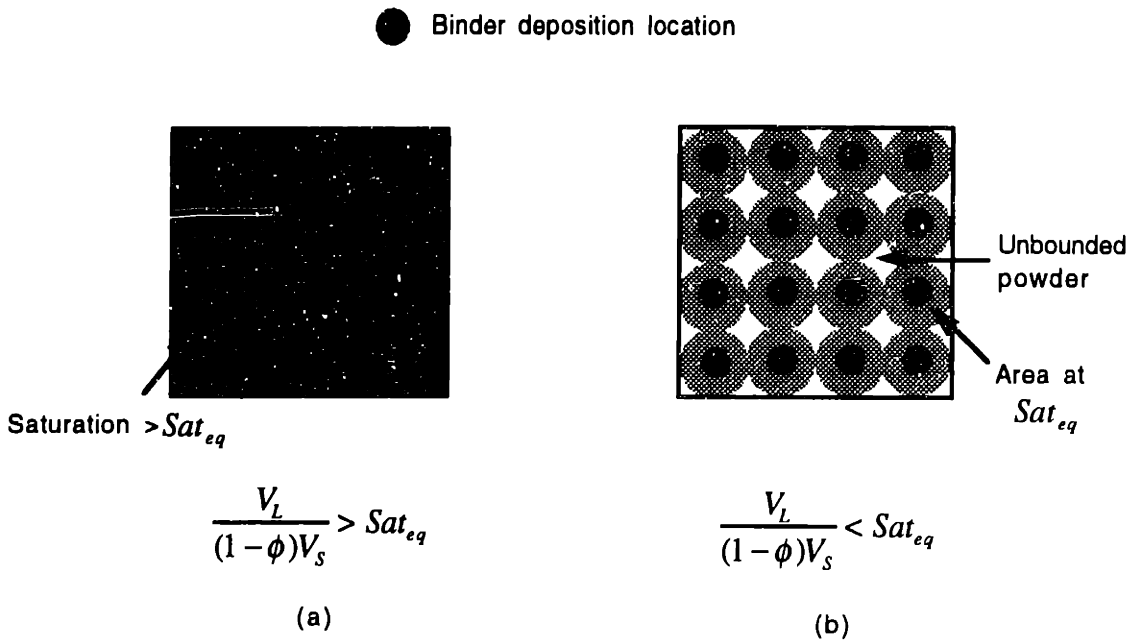

Figure 8.23 Level of Printing Saturation (a) High (b) Low

Suppose one deposits binder with total volume of V_L into a powder which has a total volume of V_S and with a packing fraction of ϕ. For the case where **printing saturation level**, $\frac{V_L}{(1-\phi)V_S}$, is greater than Sat_{eq} (or $\frac{V_L}{(1-\phi)V_S} > Sat_{eq}$), it is likely that the binder will be uniformly distributed over the entire powder volume since there is excess binder to be spread around. In this way, local saturation level at any point in the powder

will be higher than Sat_{eq}, Figure 8.23 (a). On the other hand, in the case where the printing saturation level is less than Sat_{eq}, $\frac{V_L}{(1-\phi)V_S} < Sat_{eq}$, the binder only occupies a portion of the powder volume with a local saturation level of Sat_{eq} but leaves some unbounded powder in the unwetted region. Therefore, in micro scale, saturation will not be uniform through out the powder but high around the spots where binder was initially deposited, Figure 8.22 (b).

In this case the print patterns affect mechanical properties as well as shrinkage characteristics of the parts. When binder is not well distributed throughout the volume of the powder at low saturation, printed parts internally contain some unbound particles and may even fall apart if the binder is not well connected. On the other extreme, if the same amount of binder concentrates only at a portion of the powder, then printed parts may be intact. According to Bredt [11], the level of Sat_{eq} for Norton 7920 printed with Binder B is approximately 85 percent with the packing fraction, ϕ, of 0.4. It may not be too far off to assume that Sat_{eq} for Nyacol 9950 is approximately the same.

Evidences that support the theory of non-uniform binder distribution at low saturation were obtained. Norton 7920 was printed with Nyacol 9950 at different concentrations and saturation levels according to Table 8.7 All of the tested binders were gelled naturally by drying.

According to Table 8.7, Run A was printed with concentrated Nyacol 9950 at 50 weight percent but at low saturation while Run B was printed with diluted Nyacol 9950 at full saturation. Although Run A and B were prepared at different binder concentration and printing saturation level, both of them contained approximately the same amount of silica per unit volume of the powder. However, both drying and heat treatment strain of Run A was significantly less than that of Run B. Comparing Run A to Run C in which an even lesser amount of silica was deposited onto the powder by printing to saturation of a more diluted Nyacol 9950, shrinkage strain of Run A is still much less than Run C by a factor of two.

Assuming that Nyacol 9950 gels at the same critical concentration, the only explanation to account for the shrinkage strain difference between Run A, B, and C in

Table 8.7 is the **binder distribution** in the powder bed. High concentration binder printed at low saturation can not disperse throughout the pore media such that uniform binder distribution is achieved. As a consequence, there will be 'clusters' of highly concentrated binder around the deposition points. These clusters do not adhere well to one another due to limited amount of silica content at their boundaries, therefore the shrinkage strain and the part strength are affected at low printing saturation levels. On the other hand, in the case where binder was diluted but deposited into the powder at high saturation, binder dispersed and was well distributed into the pores bridging out to almost every particles in the powder bed. Therefore, although there is more shrinkage, part strength increases substantially.

	Run A	Run B	Run C
Nyacol 9950 Concentration			
[weight %]	50	30	17.5
[volume %]	33	20	12
Printing Saturation level [%]	65 (note 1)	100 (note 2)	100 (note 2)
Silica content in the pores [% pore volume occupied]	21.5	20	12
Shrinkage strain at powder packing fraction of 0.4 [%]			
Drying [%]	<0.05	0.22	0.17
Drying + Heat treatment [%]	0.09	0.32	0.27

Table 8.7 Binder Distribution Affects Shrinkage Strain at Low Saturation

Note 1. Machine deposits with Δ-distribution at ± 175 μm, Layer and Line Spacing are 175 μm

Note 2. Manual deposits with a dropper

Therefore, when the printing saturation level is below the natural saturation, Sat_{eq}, one ought to be cautious about the binder deposition pattern as well as its distribution in the powder bed. Print patterns that allow isotropic binder dispersion would be better for high part strength requirement, but may result in higher shrinkage.

2) Reduction in Binder Neck Volume and the Effect of Tri-axial Stress

In this case, binder is assumed uniformly distributed and saturation is homogeneous over that entire powder volume. In this regard, a lowering printing saturation level affects the ratio of binder neck area, A_L, to that of the powder, A_S, thus altering the equilibrium point in powder-binder shrinkage interaction. Binder's shrinkage stress will have to be greater than powder's resistant stress to remain in force balance, Figure 8.24.

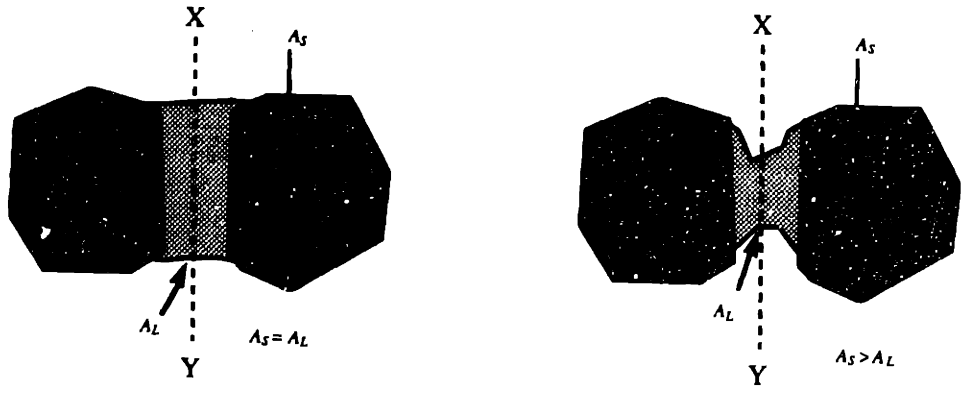

Figure 8.24 Reduction in Printing Saturation Reduces Binder's Neck Area

With regard to the powder-binder interaction diagrams in Figure 8.19 and 8.21, Changes in $\frac{A_L}{A_S}$ ratio can be illustrated in Figure 8.25. At any point of time, forces developed by shrinkage and resistant stress must be equal.

$$F_L = F_S$$

or

$$(\text{Shrinkage Stress})A_L = (\text{Resistant Stress})A_S$$

$$\frac{A_L}{A_S} = \frac{\text{Resistant Stress}}{\text{Shrinkage Stress}} \tag{8.9}$$

At saturation, $\frac{A_L}{A_S}$ is always unity such that shrinkage and resistant stresses are equal and the composite is at point B. However, when the binder's neck area is reduced or

$Sat_{eq} < \frac{A_L}{A_S} < 1$, then shrinkage stress must be greater than resistant stress. The composite will reach a new equilibrium at point A and A' instead with a lower composite strain, Figure 8.25.

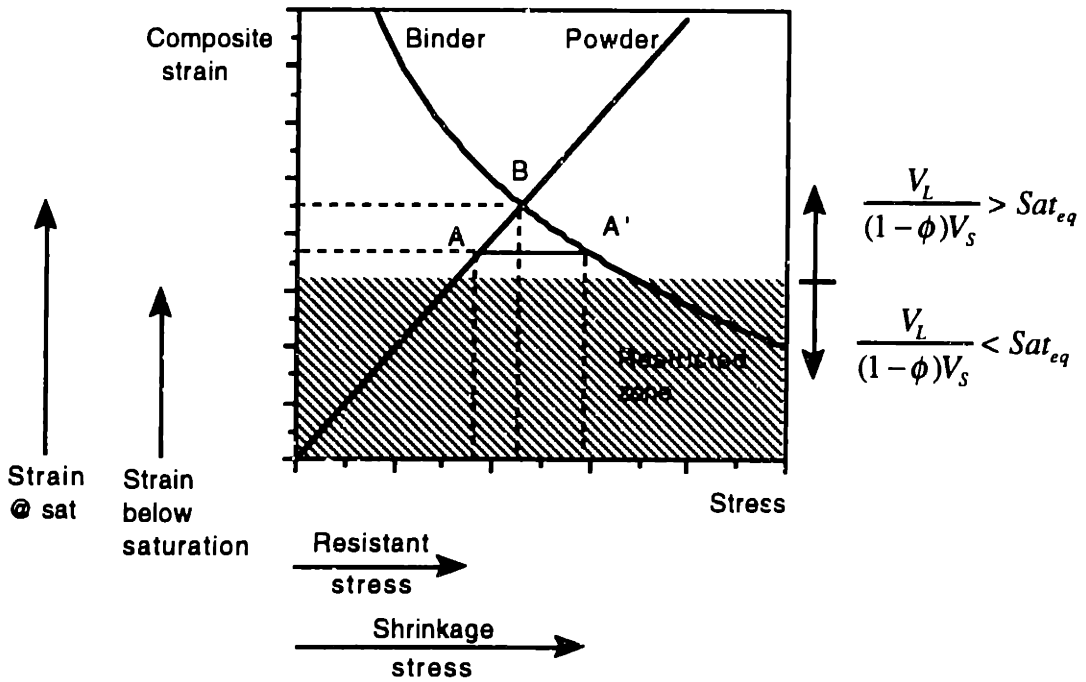

Figure 8.25 Concept of Reduction of Composite Strain by Lowering Printing Saturation

In addition, the reduction of the neck volume may enhance the tri-axial stress in the binder neck and reduce the shrinkage, Figure 8.26.

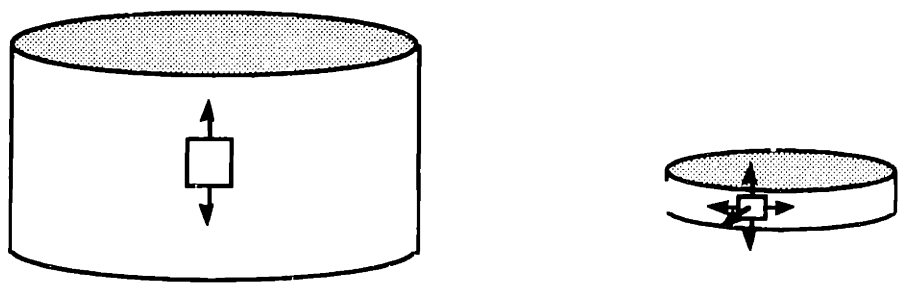

Uniaxial Stress

Tri-axial Stress

Figure 8.26 Tri-axial Stress in the Binder Neck at Low Saturation

8.5 CB-A30S AND NYACOL 9950: A NEW POWDER-BINDER SYSTEM

Upon knowing that CB-A30S can reduce shrinkage by about 50 percent that of convention powder-binder system[2] by reducing the mean particle separation (or higher packing fraction), and that Nyacol 9950 which cuts down shrinkage with low liquid content at gellation and higher solid content, this last experiment was proposed as a cap stone to the thesis work to take the best of both powder and binder into application.

Jetting Nyacol 9950 at 50 weight percent through a small orifice of 40 μm is proven difficult. Time before clogging (with Jim Serdy's BOA jet) was approximately 2-3 hours which was just enough to build small parts. A more serious problem with Nyacol 9950 was high drying rate and material deposit rate on the catcher. Regular catcher cleaning was mandatory every 5-10 minutes. Nyacol 9950 is very viscous (12 centipoise) and therefore requires high pressure to drive it through a 40 μm orifice. The achieved flow rate was 0.8 cc per minute at a line pressure of about 40-42 psi while CB-A30S spherical alumina powder was packed to 55 percent.

The printing pattern was incorporated with a triangular-distribution droplet placement scheme such that droplets were proportionally diverted (or sprayed) from the centerline with a triangular density function, Figure 8.27. Each line was overlapped by 50 percent of the line width, therefore, binder density of two adjacent lines (such as ABG and HCF) were combined into a uniform distribution (ABCF). Triangular-distribution droplet placement minimizes anisotropy between Fast Axis (FA) and Slow Axis (SA). The experiment selected equal line and layer spacing of 175 μm with a printing saturation level of 65 percent.

Shrinkage samples were made with the same dimension as described in Section 6.1.1. There were 30 layers in which the 3 top layers was made to incorporate the fidutial marks at each end. Distance between the fidutial marks were recorded after drying and heat treatment to 900°C and compared to the original length in the CAD file.

---

[2] Norton 7920 packing to about 40 percent with Binder B gelled by citric acid.

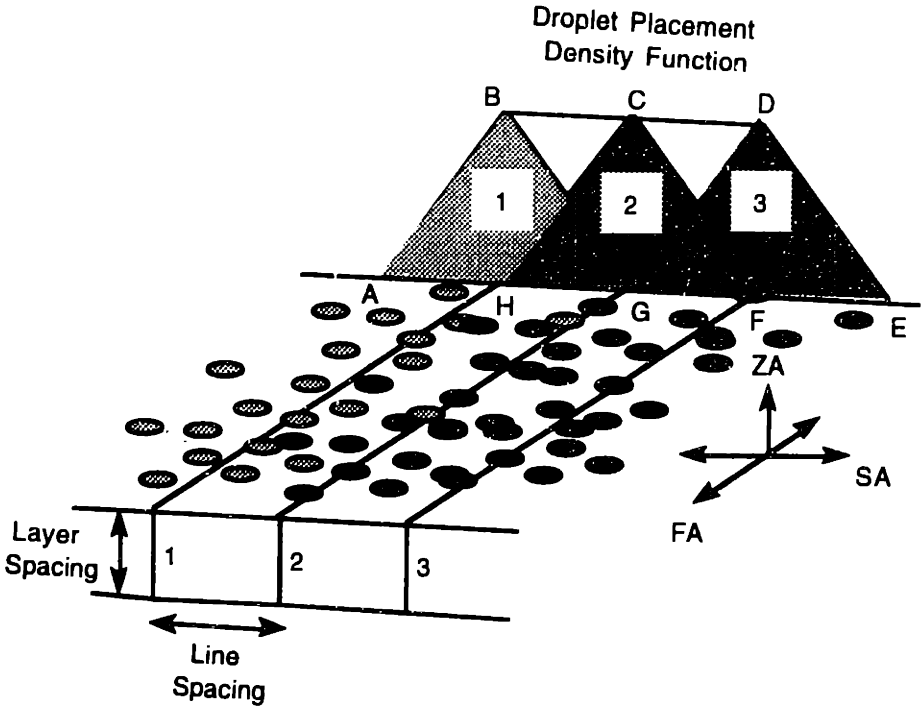

Figure 8.27 Triangular-Distribution Droplet Placement Scheme

Nyacol 9950 printed nicely on to the powder without ejection. The binder was absorbed immediately into the pores after impact. However, Nyacol 9950 dried off too rapidly causing shrinkage anisotropy between layers. After the third layer was completed, warping was a problem. Stability of 9950 was augmented by the addition of 100 ppm of polyethylene glycol at a molecular weight of 20,000. PEG stabilized the binder and slowed down the gelation so as to eliminate the warping problem. It was found that PEG increased shrinkage slightly. Therefore the amount of PEG was limited to only 100 ppm (while Binder B contains 1,000 ppm PEG).

There was no serious bleeding found on the samples. Surface quality of the proposed material system is slightly rougher than that of the standard system. Unbound powder can be cleaned and separated from the printing region very easily even at the fidutial mark where only a single line was skipped.

	Standard System		New System
Powder:	Norton 7920 - Platelet		CB-A30S - Spherical
Apparent packing fraction [%]	43-45		52-57
Binder	Binder B		Nyacol 9950 at 50 wt % +100ppm PEG at 20K MW
Printing Saturation Level	80	90	65
Gellation Mechanism	Citric acid at 0.5 wt % of powder		Natural Drying
Rasterization	Straight line	Δ-Dist ±200μm	Δ-Distribution ± 175 μm
Line Spacing [μm]	175	175	175
Layer Spacing [μm]	175	175	175
Shrinkage strain [%]			
Drying	0.25	N/A	<<0.005 (undetectable)
Drying+Heat treatment to 900°C	0.40	N/A	≈0.05
Modulus of Rupture on Slow axis bars [MPa]	0.99	4.54	1.46
STD [MPa]	0.05	0.11	0.24

Table 8.8 Standard and New Material Systems

It was found that shrinkage of proposed spherical alumina CB-A30S with Nyacol 9950 gelled by drying is significantly lower than current standard practice of Norton 7920 with Binder B by a factor of 6-8. The measurement revealed that overall shrinkage strain including drying and heat treatment of proposed material system is in the order of 0.05 percent, Table 8.8

However, part strength of the proposed material system seems to be lower than expected although it was well beyond that of the standard system. In fact, one may consider raising the printing saturation level of the proposed system to about 75 percent to gain part strength and tolerate only slightly more part shrinkage. Good shell strength shall be about 3 MPa of modulus of rupture. Another technical problem of using Nyacol 9950 as a binder is the ability to jet it through a small orifice. In fact, if Nyacol 9950 can be deposited onto a powder bed with an alternate method such as spraying, it will be a marvelous binder for the future of the Three-Dimensional Printing of ceramics.

8.6 CHAPTER SUMMARY

Binder consolidates during drying and sintering and pulls attached particles along with its shrinkage stress. The particles are, however, mechanically constrained with their neighbors, thus their movement induced compressive stress in the powder known as resistant stress. At all time, the *forces* developed from both shrinkage and resistance stress must be equal such that the powder and the binder always remain under static equilibrium.

In case where relative movement of particles (shrinkage) exists, the relation of binder strain to powder (or composite) strain is governed by the magnitude of mean particle separation which is the average free distance from one particle to others in the first-layer neighbor. Researchers [6] have estimated that the mean particle separation for monosize spheres in random packing is approximately 3 to 8 percent of the particle radius at apparent packing fraction. For angular particles, especially with irregular shapes, the mean particle separation tends to be higher for the same packing fraction.

For simplicity, this thesis work tries to model particle assemblies with a cellular structure consisting of polygon particles. The distance between each polygon particles in a unit cell is equal to the mean particle separation of that particular powder. However, it is assumed each unit cell experiences similar environment and, therefore, evolves through shrinkage process at the same pace and condition. Shrinkage anisotropy within and between layers which leads to warpage or curling is not a focus of this work.

In order to understand the shrinkage characteristics of Norton 7920 and CB-A30S, the mean particle separation of these powders shall be found. An experiment was conducted by depositing binders with known shrinkage behaviors to saturate powder which was packed at various densities. It was found that the mean particle separation of Norton 7920 and CB-A30S were 0.0769 and 0.0290 of the particle radius, respectively. The numbers were reconfirmed with heat treatment shrinkage information as well. However, the mean particle separation obtained from the measurement is slightly lower than previously predicted by Gotoh [6] due the fact that shrinkage is not only governed by the mean value of particle separation but also by its distribution. Since CB-A30S spherical powder naturally packs to a tighter formation than Norton 7920, its shrinkage level is approximately half of the platelet powder. And with the extremely low shrinkage strain of

Nyacol 9950 at 50 weight percent gelled by drying, this powder-binder system was proposed as a new material system for the Three-Dimensional Printing of ceramic process.

Shrinkage strain of the composite (powder and binder) was found to reduce drastically with printing saturation level. Although this has proven positive to minimize shrinkage, one has to optimize the shrinkage level to part strength which is also effected by saturation. An experiment was performed by printing Nyacol 9950 at 50 weight percent with 100 ppm PEG onto CB-A30S at 65 percent saturation. Overall heat treatment and drying shrinkage strain of the system is found to be approximately than 0.05 percent - an improvement of more than 6 to 8 folds over the current standard material system of acid gelled Binder B on Norton 7920 powder. However, part strength was found to be slightly lower than expected, therefore, a very practical printing saturation level should be approximately 70 to 75 percent.

Nyacol 9950 at 50 weight percent with 100 ppm PEG was found difficult to print through small orifices due to low stability at high concentration. Material deposition rate on the catcher was also found to be very high. Binder deposition alternatives such as spray deposition shall be a vital necessity for the binder in the future. In addition, part strength and shrinkage strain can be optimized in the future by adjusting the process parameters such as printing saturation below natural saturation level, layer spacing, and the binder deposition pattern and its distribution in the powder bed. This optimization shall be proven very essential when large casting shells are made with Three-Dimensional Printing process.

BIBLIOGRAPHY

[1] Suzuki M., *Description of Particulate Assemblies*, Powder Technology Handbook, Ed by Linoya K., Gotoh K., Higashitani K., Marcel Dekker, 1991

[2] Scott G., *Radial Distribution of the Ramdom Close Packing of Equal Spheres*, Nature, 194, pp. 956-957, 1962

[3] Scott G., Mader D., *Angular Distribution of Ramdom Close-Packed Equal Spheres*, Nature, 201, pp. 382-383, 1964

[4] Scott G., Charlesworth A, Mak M., *On the Random Packing of Spheres*, J. Chem. Phys., 40 [1], pp. 611-612, 1964

[5] Levine M., Chernick J., *A Numerical Model of Random Packing of Spheres*, Nature, 208, pp.68-69, 1965

[6] Gotoh K., *J. Soc. Powder Technol. Jpn.*, 15:220, 1978

[7] Gotoh K., *J. Soc. Powder Technol. Jpn.*, 16: 709, 1979

[8] Suzuki M., Makino K., Tamamura T, Linoya K., *Kagaku Kogaku Ronbunshu*, 5:616: 1979

[9] Chandrasekhar S., *Rev. Mod. Phys.*, 15: 1, 1943

[10] Bansal P., Ardel A., *Metallography*, 5: 97, 1972

[11] Bredt J., *Binder Stability and Powder\Binder Interaction in Three Dimensional Printing*, MIT PhD Thesis, Dept. of Mechanical Engineering, Supervised by E. M. Sachs, 1995.

Chapter 9

Conclusion

9.1 SHRINKAGE IN THREE-DIMENSIONAL PRINTING OF CERAMICS

Current Three-Dimensional Printing of ceramics depends on acid gelled Binder B and Norton 7920 lamella alumina powder. At present, the process yields approximately 0.5 percent linear shrinkage after heat treatment to 900°C. Half of the shrinkage occurs during drying of binder and the rest takes place during sintering at elevated temperature. The focus of this research is on drying shrinkage.

A new optical measurement technique reviewed that drying shrinkage depends on 1) Gellation method of the binders, and 2) Packing and morphological effect of the powder. Silica binder can be gelled by several means such as by a surfactant or drying. Gellation governs the liquid content at the point of gel which defines the shrinkage potential of the gel body during drying. On the other hand, powder morphology controls the deformation response of the powder under isostatic stress. To minimize drying shrinkage, gelation should take place at minimal liquid content with a powder of high resistance to isostatic deformation.

The experiment has revealed that Nyacol 9950 at 50 weight percent solid loading results in minimal shrinkage deformation when gelled by drying. In addition, powders with aspect ratio close to 1 (such as spherical or equi-ax) are naturally packed at a tighter formation than lamella powder with much higher resistance to isostatic stress. Nyacol 9950 gelled by drying with CB-A30S spherical powder results in an improvement in drying shrinkage by a factor of 6 over acid gelled Binder B with Norton 7920 powder based on saturated printing.

9.2 PHYSICS OF DRYING AND SHRINKAGE MINIMIZATION STRATEGIES

Drying shrinkage deformation of gels takes place only during saturation drying starting when the liquid-vapor interface reaches the pore entrances. Wetting causes the liquid-vapor interface to bend and forces the liquid to be under tension. In the case where the network is deformable, the liquid starts to flow from the interior to the liquid-vapor interface at the exterior. The pressure (tension) gradient in the liquid is described by Darcy's law. Not only must the liquid flow rate be equal to the rate at which the network contracts such that no vapor is formed, but it must also be equal to the evaporation rate at the liquid-vapor interface. The network deformation continues until the network strength is sufficient to withstand the liquid tension. At this point the liquid-vapor interface reaches its maximum tension and recedes into the interior marking the end of drying deformation and saturation drying. There are three strategies to minimize drying shrinkage:

1) Minimize the liquid content at gel point

   Level of liquid content at gel point governs the shrinkage potential of the gel. Therefore, reducing the liquid content at the gel point directly lowers the shrinkage capacity.

2) Increase the strength of the network

   Strengthen the network reduces the deformation which is driven by the liquid tension under capillarity.

3) Lower the liquid tension

   The magnitude of liquid tension is the only network deformation driving force. Liquid tension is governed by the surface physics of the pore liquid and the network solid as well as the method of drying (natural or supercritical drying).

9.3 POWDER DEFORMATION RESPONSE TO ISOSTATIC STRESS

Powder experiences isostatic (omni-direction) compression induced by the shrinkage stress of the binder. In the range of compression stress experienced by Three-Dimensional Printing parts, the deformation is governed by restacking and rearrangement of the particles in the powder bed. It was found that powder strain varies linearly with the level of isostatic stress, and the change of powder strain per an increment of isostatic stress was a strong function of initial packing density as well as the aspect ratio of the powder.

9.4 POWDER-BINDER INTERACTION

Binder consolidates during drying and sintering and pulls attached particles along with shrinkage stress. The particles are, however, mechanically constrained with their neighbors, thus the movement induced compressive stress in the powder is known as resistant stress. At all times, the forces developed from both shrinkage and resistance stress must be equal such that the powder-binder always remain under static equilibrium.

The relation of binder strain and powder (or composite) strain is governed by the magnitude of mean particle separation which is the average free distance from one particle to others in the first-layer neighbors. Powders with an aspect ratio close to unity (such as spherical or equi-ax) apparently have small mean particle separation due to morphological superiority. It was found experimentally that the mean particle separation of Norton 7920 is slightly more than twice that of CB-A30S spherical alumina. Since CB-A30S spherical powder naturally packs to a tighter formation than Norton 7920, its shrinkage level is approximately half that of the lamella powder

When the printing saturation level is below the natural saturation of the powder, binder distribution has a strong impact on both shrinkage deformation and part strength. Improper binder distribution may result in a reduction of shrinkage deformation at a cost of much lower part strength.

9.5 CONTRIBUTION

The achievements and contribution of this thesis work are:

- Binder stress-strain relationship in one-dimension
- Powder deformation characteristics under low isostatic stress
- The concept of powder-binder shrinkage interaction

9.6 FUTURE WORK

• HEAT TREATMENT SHRINKAGE

Heat treatment shrinkage of Three-Dimensional Printing of ceramics parts has not been thoroughly quantified in this thesis work. After drying shrinkage is reduced, heat treatment shrinkage presents a large portion of total shrinkage especially for binders with high silica loading.

• OPTIMIZATION OF SHRINKAGE WITH RESPECT TO PART STRENGTH

The requirement for low shrinkage always conflicts with the requirement for high part strength. Future study should include an optimization of drying and heat treatment shrinkage with respective to part strength by means of alternating the binder distribution and printing saturation level (printing pattern, line and layer spacing, binder materials and flow rate). The optimization is essential for the case where a low printing saturation level is desired.

• DEVELOP THREE-DIMENSIONAL POWDER-BINDER SHRINKAGE INTERACTION MODEL

The powder-binder shrinkage interaction model in this thesis work is based on the one-dimension shrinkage model of a simple cubic cellular structure. Although the model captures the essence of powder-binder shrinkage interaction, the model is unrealistically constrained to the requirement of orthogonal arrays of binder bonds between ordered

polygon particles. In fact, the model should be improved to apprehend the interaction of powder and binder in a randomly packed three-dimensional powder bed. This involves intensive numerical simulation.

- SHRINKAGE ANISOTROPY

Future development shall include shrinkage anisotropy within and between layers to give a better understanding of warpage and internal stress in the powder. If possible, a predictive model on interlayer stress can be further developed to explain interlayer cracking and delamination.

APPENDIX A.

WAXES FOR PATTERN MAKING IN INVESTMENT CASTING

The most widely used waxes for patterns are parafins and microcrystalline waxes. Parafin waxes are available with closely controlled grades and melting points (increment of 2.8°C from 52-68°C). Its low cost, highly availability, high lubricity, and low melting viscosity make parafin waxes very popular for the investment casting process. However, parafin waxes exhibit high shrinkage and brittleness which limit their use [3].

Microcrystalline waxes are highly plastic and tougher and available with higher melting points than parafin wax. Generally, parafin and microcrystalline waxes are used in combination. Other alternative waxes are:

Fisher-Tropsch waxes are synthetic hydrocarbons which resembles parafins, but are much harder and having higher melting points. They improve hardness and rigidity. A good example of wax in this class is polyethylene wax which has a melting point of 132°C.

Candelilla is a hard and tacky vegetable wax. It has low thermal expansion and is normally used to raise the softening point of hydrocarbon waxes. Carnauba is another vegetable wax with a igh melting point of 83°C and with low thermal expansion.

Beeswax is a natural wax which melts at 64°C. It is widely used for modeling and pattern blends. Beeswax has very similar characteristic to microcrystalline waxes. The first investment casting is believed to have been made out of beeswax. Today's beeswax is quite expensive due to its limited availability.

Palmitic and stearic acids are fatty acids that have good properties. They have low melting viscosity and very low thermal expansion.

APPENDIX B.

COMMON REFRACTORIES IN INVESTMENT CASTING

[L. O'Bannon, Dictionary of Ceramic Science and Engineering, Plenum Press, New York, 1984]

FUSED SILICA

Fused silica is a glass made by melting silica, quartz, or sand which is also known as fused quartz or quartz glass. In addition, fused silica can be made by flame hydrolysis of silicon tetrachloride

ZIRCON

Zircon has a chemical formula of $ZrO_2 \cdot SiO_2$ with a molecular weight of 182.9. It is used in porcelain enamels and glazes as an opacifier and to improve color stability and crazing resistance. Zircon has a softening point of 850°C-950°C with a melting point of 2250°C.

ZIRCONIA

ZrO_2 with molecular weight of 123.2 and melting point about 2700°C. Zirconia is used primarily for opacifier in porcelain enamels and glazes as well as an abrasive in polish and grinding compounds.

CHROMITE

Chromite is a mineral compound of the oxides of chromium, iron, aluminum, and magnesium. It is utilized as refractories and pigments.

OLIVINE

Olivine has a chemical formula of $(Mg, Fe_2)SiO_4$. It is used in refractories, cement, and foundry sand. Purer grade are used in electronic components.

QUARTZ

Quartz has a chemical formula of SiO_2 with a molecular weight of 60.1 and a melting point of 1710°C. Quartz appears as a natural crystal in many varieties such as agate, chalcedony, chert, flint, opal, etc. It is abundant and widely spread of all minerals.

MULLITE

$3Al_2O_3 \cdot 2SiO_2$ with a molecular weight of 425.9 and a melting point of 1810°C, mullite is highly resistant to corrosion and heat. It is used as a refractory for high temperature applications and as a strength-producing element in stoneware and procelain.

KYANITE

$Al_2O_3 \cdot SiO_2$ is a natural silicate of aluminum with the same composition as silimanite and andalusite but differs in structure and physical properties. Kyamite decomposes to mullite and cristobalite at about 1300°C. It is used in refractories, sanitary porcelains, precision-casting molds, brake disc because of its superior mechanical strength.